# MODELING AND OPTIMISATION OF ONE DIMENSIONAL PHOTONIC CRYSTAL WAVEGUIDES AND DEVICES

THESIS

*Submitted in fulfilment of the requirement of the degree of*

DOCTOR OF PHILOSOPHY

*to*

*J.C BOSE UNIVERSITY OF SCIENCE & TECHNOLOGY*

*by*

VINOD CHACKO

YMCAUST/PH-06/2011

*Under the Supervision of*

Dr. SONIA

Associate Professor


Department of Physics

Faculty of Sciences

J.C.BOSE University of Science & Technology

YMCA, Sector-6, Mathura Road, Faridabad, Haryana, India

**September, 2020**

DEDICATED

to

God and his Glory

My parents, My wife Susan and son Joel

# DECLARATION

I hereby declare that this Thesis entitled "**MODELING AND OPTIMISATION OF ONE DIMENSIONAL PHOTONIC CRYSTAL WAVEGUIDES AND DEVICES**" by **VINOD CHACKO**, being submitted in fulfilment of the requirements for the Degree of Doctor of Philosophy in DEPARTMENT OF PHYSICS under Faculty of Sciences of J.C.Bose University of Science & Technology , YMCA Faridabad, during the academic year 2020-21, is a bona fide record of my original work carried out under guidance and supervision **of DR. SONIA, ASSOCIATE PROFESSOR , DEPARTMENT OF PHYSICS** and has not been presented elsewhere.

I further declare that the thesis does not contain any part of any work which has been submitted for the award of any degree either in this university or in any other university.

Vinod Chacko

YMCAUST/PH06/2011

# CERTIFICATE

This is to certify that this Thesis entitled **"MODELING AND OPTIMISATON OF ONE DIMENSIONAL PHOTONIC CRYSTAL WAVEGUIDES AND DEVICES"** by **VINOD CHACKO**, submitted in fulfillment of the requirement for the Degree of Doctor of Philosophy in **DEPARTMENT OF PHYSICS**, under Faculty of Sciences of J.C.BOSE University of Science & Technology, YMCA Faridabad, during the academic year 2020-21, is a bonafide record of work carried out under my guidance and supervision.

I further declare that to the best of my knowledge, the thesis does not contain any part of any work which has been submitted for the award of any degree either in this university or in any other university.

Dr.Sonia
Associate Professor
Department of Physics
Faculty of Sciences
J.C.Bose University of Science & Technology, YMCA Faridabad.

Dated:

# ACKNOWLEDGEMENT

I would like to express my sincere gratitude to my Supervisor Dr Sonia for giving me the opportunity to work in this area. It would never be possible for me to take this thesis to this level without his/her innovative ideas and his/her relentless support and encouragement.

I would also like to express gratitude to Dr A.K Hafiz, Jamia Millia Islamia for giving me support and suggestion in carrying out this work.

I would like to thank my fellow researchers of nanophotonics lab of J.C Bose University of Science and Technology for providing valuable suggestions time to time.

Finally I would like to thank my wife Susan and son Joel for their unconditional support and patience for carrying out this work.

VINOD CHACKO

YMCAUST/PH06/2011

# ABSTRACT

In this work the selected one dimensional photonic crystal structures are studied and their photonic band gap is theoretically computed by solving the wave equation in multilayered periodic media using the transfer matrix method. The mathematical modeling of one dimensional photonic crystal is used to calculate the effect of design parameters on the optical response of these structures .The analytical expression of density of states, effective index and group velocity is used to comparatively study the optical properties of selected photonic crystals. The application of one dimensional photonic crystal as omnidirectional reflector is mathematically designed which can be tuned by changing the design parameters. The comparative study of effect of material dispersion on the Omni-directional Reflector (ODR) properties is examined. One dimensional photonic crystal based microcavity chemical sensors are also designed using anisotropic effects.

The first chapter deals with the introduction and literature review of work and various applications of 1DPC. The second chapter represents the mathematical modelling of linear 1DPC for obtaining the dispersion relation and transmission coefficients. The effect of design parameters on the optical response of 1DPCs is analysed in this chapter. The third chapter deals with application of 1DPCs as (ODRs). The optimisation of ODR has been analysed on the basis of design parameters in this chapter. We have designed 1DPC microcavity based anisotropic and isotropic bio-chemical sensors. The theory of design, mathematical modelling and comparison of sensitivity is mentioned in fourth chapter.The design of Metallo-Dielectric 1DPCs and its applications are discussed fifth chapter. In the sixth chapter, conclusion and future scope of work has been discussed.

# TABLE OF CONTENTS

# LIST OF TABLES

**Table**

# LIST OF FIGURES

Figure (2.5) The reflectance spectrum plotted for N=20 and normal incidence with $n_1$=3.42, $n_2$=1.45, $d_1$=58.48 nm, $d_2$= 137.93 nm.

Figure (2.6) Dispersion relation for $TiO_2/SiO_2$ multilayered structure with N=20 for normal incidence, the refractive index of the alternating medium are $n_1 = 2.67$, $n_2 = 1.45$, and their thickness are $74.90$ nm, $d_2 = 137.93$ nm respectively.

Figure (2.7) Reflectance curve for multilayered $TiO_2/SiO_2$ structure with $n_1 = 2.67$, $n_2 = 1.45$, $d_1 = 74.90$ nm, $d_2 = 137.93$ nm with $\lambda_0 = 800$ nm. The above curve is plotted for N=20 and normal incidence.

Figure (2.8) Dispersion relation for Ge / $Na_3AlF_6$ multilayered structure with N = 20 for normal incidence, the refractive index of the alternating medium are $n_1 = 4.2$, $n_2 = 1.34$, and their thickness are $d_1 = 47.61\ nm, d_2 = 149.25\ nm$, respectively.

Figure (2.9) Reflectance curve for $n_1 = 4.2, n_2 = 1.34$, $d_1 = 47.61\ nm$, $d_2 = 149.25\ nm$ with $\lambda_0 = 800\ nm$. The above curve is plotted for N = 20 and normal incidence.

Figure (2.10) Dispersion relation for Te / Cryolite multilayered structure with N = 20 for normal incidence, the refractive index of the alternating medium are $n_1 = 4.6$, $n_2 = 1.34$, and their thickness are $d_1 = 43.47$ nm, $d_2 = 149.25$ nm, respectively.

Figure (2.11) Reflectance curve for $n_1 = 4.6, n_2 = 1.34$, $d_1 = 43.47$ nm, $d_2 = 149.25$ nm with $\lambda_0 = 800$ nm. The above curve is plotted for N = 20 and normal incidence.

Figure (2.12) Dispersion relation for Si / Cryolite multilayered structure with N = 20 for normal incidence, the refractive index of the alternating medium are $n_1 = 3.42$, $n_2 = 1.34$, and their thickness are $d_1 = 58.48$ nm, $d_2 = 149.25$ nm, respectively.

Figure (2.13) Reflectance curve for $n_1 = 3.42, n_2 = 1.34$, $d_1 = 58.48$ nm, $d_2 = 149.25$ nm with $\lambda_0 = 800$ nm. The above curve is plotted for N = 20 and normal incidence.

# LIST OF ABBREVIATIONS

| | |
|---|---|
| PC | Photonic Crystal |
| PBG | Photonic Band Gap |
| 1DPC | One Dimensional Photonic Crystal |
| 2DPC | Two Dimensional Photonic Crystal |
| 3DPC | Three Dimensional Photonic Crystal |
| QPM | Quasi Phase Matched |
| PBGF | Photonic Band Gap Fibers |
| 1D | One Dimensional |
| 2D | Two Dimensional |
| 3D | Three Dimensional |
| PCF | Photonic Crystal Fiber |
| TMM | Transfer Matrix Method |
| PWE | Plane Wave Expansion |
| FDTD | Finite Difference Time Domain |
| ODR | Omnidirectional reflector |
| 1DMDPC | One dimensional Metallo-Dielectric Photonic Crystal |
| R | Reflectance |
| T | Transmittance |
| DOS | Density of States |
| EFS | Equi-Frequency Surfaces |
| TE | Transverse Electric |
| TM | Transverse Magnetic |
| NIR | Near Infra Red |
| NPS | Nano Porous Silicon |

| | |
|---|---|
| BEMA | Bruggeman's Effective Medium Approximation |
| GVD | Group Velocity Dispersion |
| FWHM | Full Width Half Maximum |
| 1DPSMC | One Dimensional Porous Silicon Micro-Cavity |
| PS | Porous Silicon |
| E-ray | Extraordinary Ray |
| O-ray | Ordinary Ray |

# CHAPTER-I

# INTRODUCTION

## 1.1 PHOTONIC NANOSTRUCTURES

The beginning of research on periodic nanostructures in photonics has unwrapped new scenarios in various fields with unique optical properties of light-matter interaction. Nano-photonics is a promising field in optics which deals with interaction of light with thin nanostructures of different optical constants. The thickness of each layer of the nanostructure is of the order of wavelength of interacting radiation. The structure shows interesting optical properties at this thickness scale due to superposition effects of light within a small volume. This has led to realization of optical devices like micro-lasers, antireflection coatings, optical switches, optical storage devices, biosensors and many more novel applications.

Optical properties of these periodic nanostructures can be observed throughout the natural world, from changing colours of an opal held to the observed reflection patterns on a butterfly's wings. Nature has been exploiting photonic crystals for millions of years, but humans have only recently started to realise their potential. Photonic Crystals (PC) or Photonic Band Gap (PBG) materials are periodic nanostructures composed of periodically arranged low and high refractive index materials with thickness comparable to wavelength of incident light [1.1]. They are characterized by allowed photonic energy bands and electromagnetic forbidden bandgaps or PBGs. In other words, the propagation of electromagnetic waves, whose frequencies lie within the PBGs, is prohibited. This property of PCs to mould photons led to many potential applications [1.2].

An optical system possessing a periodic modulation of dielectric constant on wavelength scale can be considered as a PC in the same way as periodic distribution of one or more atoms or ions constitutes a solid-state crystal. The atomic distribution scatters the electrons in a solid-state crystal and breaks the free energy electron dispersion relation into allowed bands and gaps. In the same way the periodic modulation of dielectric constant in a PC breaks the free photon energy dispersion relation into allowed photonic bands and gaps [1.3]. The scattering centres in PC are the periodic regions of high dielectric constant and this periodic refractive index in PC is equivalent to the periodic potential of ions in solid state crystals. If a complete gap is there in the photonic dispersion relation which means

photons within this frequency range will not be able to enter in this PC from outside and will not be able to leave the crystal from inside, irrespective of the direction of propagation of light. Frequencies of photons which are allowed to travel through this crystal are called modes and groups of allowed modes are called photonic bands and disallowed frequency bands are called gaps or PBGs [1.4].

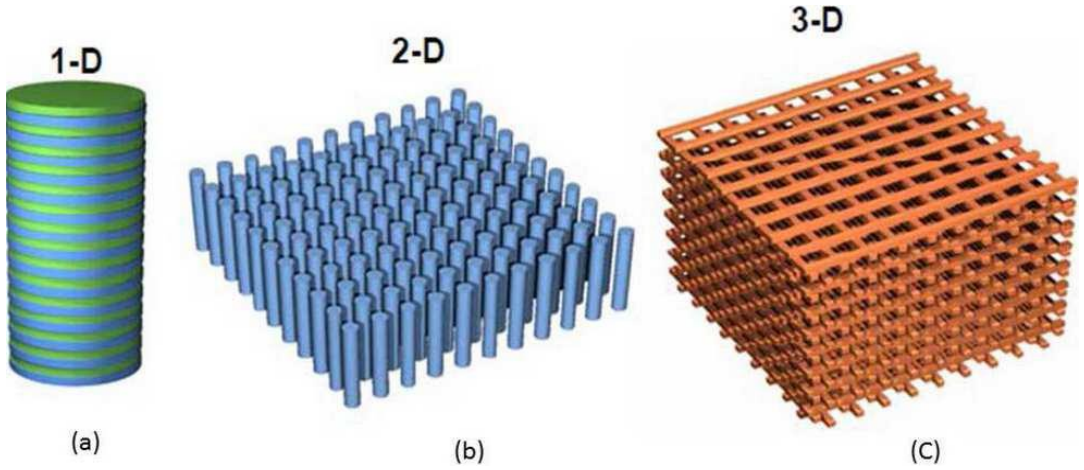


Figure 1.1: (a) One dimensional photonic crystal (b) Two-dimensional photonic crystal (c) Three-dimensional photonic crystal.

In these PC structures the refractive index is a periodic function in space and if the refractive index is periodic only in one dimension, then the structure is called one dimensional photonic crystal (1DPC). With periodicity in two and three dimensions, the structures are known as two dimensional photonic crystals (2DPC) and three-dimensional photonic crystals (3DPC), respectively, as shown in Fig 1.1. The classification of PCs depends not only on the nature of periodic modulation but also depends on phase matching requirements and nature of materials forming the layers. A 1DPC can be purely periodic, where the linear optical constant is alternately modulated or quasi periodic like Quasi-phase matched (QPM) structure or a Fibonacci quasi-crystal.

## 1.2 MAXWELL'S EQUATION IN PERIODIC MEDIA

Felix Bloch in 1928 studied propagation of waves in three-dimensional periodic media. Bloch proved that in such a medium the wave travels without scattering and they are characterised by a periodic envelope function multiplied by a plane wave. Bloch studied quantum mechanics and according to it the electrons in a conductor are scattered by the imperfections and not by the periodic ions, the same method can be applied to electromagnetism by putting Maxwell's equation as an eigenvalue problem in analogue

with Schrödinger equation. By combining the Faraday's law and Ampere's law at a fixed frequency we get:

$$\vec{\nabla} \times \frac{1}{\varepsilon} \vec{\nabla} \times \vec{H} = \left(\frac{\omega}{c}\right)^2 \vec{H}, \tag{1.1}$$

where ε is the dielectric function and c is the speed of light. A photonic crystal corresponds to a periodic dielectric function $\varepsilon(\vec{x}) = \varepsilon(\vec{x} + \vec{R_i})$ for some primitive lattice vectors $\vec{R_i}$ (i = 1, 2, 3 for all three dimensions). In this case the Bloch theorem states that the solution to Eq. (1.1) can be chosen of the form $\vec{H}(\vec{x}) = e^{i\vec{k}.\vec{x}} \vec{H}_{n,\vec{k}}(\vec{x})$ with eigenvalues $\omega_n(\vec{k})$, where $\vec{H}_{n,\vec{k}}(\vec{x})$ is the periodic envelope function satisfying

$$(\vec{\nabla} + i\vec{k}) \times \frac{1}{\varepsilon} (\vec{\nabla} \times i\vec{k}) \times \vec{H}_{n,k}(\vec{x}) = \left(\frac{\omega_n(\vec{k})}{c}\right)^2 \vec{H}_{n,\vec{k}}(\vec{x}), \tag{1.2}$$

yielding a different eigenvalue problem over the primitive cell of the lattice at each Bloch vector $\vec{k}$. These eigenvalues $\omega_n(\vec{k})$ are continuous functions of $\vec{k}$, forming the discrete bands when plotted versus $\vec{k}$ in a dispersion diagram. The eigensolutions are periodic functions of $\vec{k}$ as well, the eigensolution at $\vec{k}$ is same at $\vec{k} + G_j$ , where $G_j$ is the primitive reciprocal lattice vector defined by $R_i . G_j = 2\pi\delta_{i,j}$. Due to periodicity, one considers the set of equivalent wave vectors closest to origin $\vec{k} = 0$, a region called the first Brillouin zone. In one dimensional system, where $R_1 = a$ for some periodicity a, $G_1 = 2\pi/a$, the first Brillouin zone is the region $\vec{k} = -\frac{\pi}{a}$ to $\vec{k} = \frac{\pi}{a}$, all the other wavevectors are equivalent to some points on this zone under translation by a multiple of $G_1$. The familiar dispersion relations of uniform waveguides arise as a special case of Bloch formalism, such translational symmetry corresponds to a period $a \to 0$. In this case, the Brillouin zone of wavevector $\vec{k}$ (also called β) is unbounded and the envelope function $\vec{H}_{n,\vec{k}}(\vec{x})$ is a function only of the transverse coordinates.

## 1.3 ORIGIN OF PHOTONIC BAND GAP

A complete photonic gap is a range of frequencies for which there are no propagating solutions of Maxwell's Eq. (1.2) for any $\vec{k}$ , surrounded by propagating states above and below the gap. There is also incomplete bandgap, which exist over a subset of all possible wavevectors, polarisations and / or symmetries. Consider a one-dimensional system with uniform medium, which has plane wave eigen solutions $\omega = ck$ as depicted in Fig. 1.2 (left). We can label the states in terms of Bloch envelope function and wave vectors for $a > 0$, the bands for $|k| > \pi/a$ are translated (folded) into the first Brillouin zone as shown by the dashed lines in Fig. 1.2 (Left). In place of writing these wave solutions with electric field $\vec{E}(x) \sim e^{\pm \pi x/a}$, we can equivalently write in terms of linear combinations $e(x) = \cos(\pi x/a)$ and $o(x) = \sin(\pi x/a)$ both at $\omega = \frac{c\pi}{a}$ as shown in Fig.1.3.

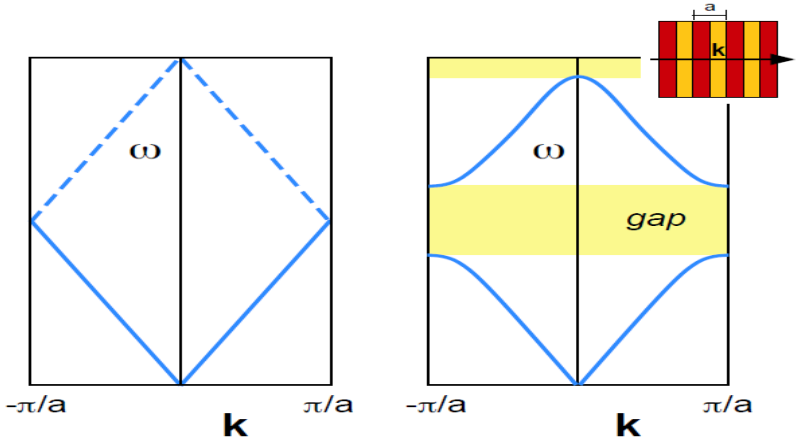


Figure 1.2: Left: Dispersion relation (ω verses k) for a uniform one dimensional region, where the dashed lines show the folding effect of applying the Bloch theorem with periodicity a. Right: Dispersion relation in a periodic dielectric variation where a gap has been opened by splitting the degeneracy at $k = \pm\pi/a$ Brillouin zone boundaries.

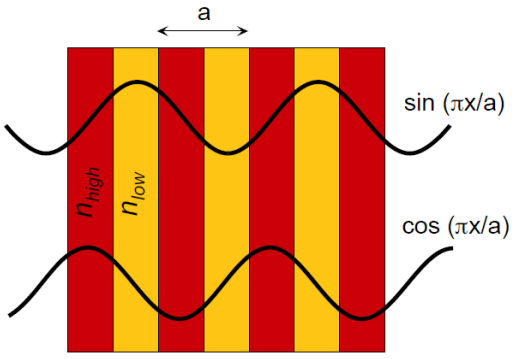

Figure 1.3: Schematic origin of bandgap in one dimension. The degenerate $k = \pm\pi/a$ plane waves of a uniform medium are split into $\cos(\pi x/a)$ and $\sin(\pi x/a)$ standing waves by the dielectric periodicity, forming the lower and upper edges of bandgap, also $\cos(\pi x/a)$ has electric field peaks at higher dielectric medium so will lie at lower frequency than the $\sin(\pi x/a)$ which peaks at lower dielectric medium.

By the same arguments, it follows that any periodic dielectric variation in one dimension will lead to bandgap. In order to get a complete bandgap to arise in two and three dimensions, bandgaps in each symmetry direction must overlap in frequency. In order that they overlap, the gaps must be sufficiently large which requires high dielectric contrast. The periodicity should also be the same in different directions. The largest gap arises for hexagonal lattices in 2D and fcc lattices in 3D which have nearly circular / spherical Brillouin zones. The fabrication of 3DPC in the optical wavelength range is one of the difficult challenges to nanotechnology. Even accurate fabrication of 1DPC and 2DPC with nanometre size variations still possess serious manufacturing challenges. The PCs provide promising possibilities to be used in various optoelectronic applications so the research activities in PCs have increased exponentially in the last decade. Many analytical and numerical techniques have been developed for analysing the wave propagation in inhomogeneous media and in general case when the inhomogeneity is in three dimensions, the exact solution of the problem is extremely hard to obtain and one is forced to use some approximation scheme [1.5]. In the cases where the inhomogeneity is one dimensional, however, there exist several theoretical methods that allow exact solutions of the problem in some simple situations [1.6]. This can be used to obtain exact solutions for the reflection and transmission coefficients of incoming waves and the electric and magnetic field amplitudes inside arbitrarily inhomogeneous media [1.7].

## 1.4 LITERATURE REVIEW

### 1.4.1 Brief History of Photonic Crystals

Historically, the property of periodic medium was introduced by Lord Rayleigh in the end of the 18th century. After a long time, the property of periodic medium was theoretically explored by F. Bloch in 1928. In 1972, Bykov explained that the spontaneous emission of atoms at optical wavelengths can be reduced by placing them in periodic lattice of dielectrics with pitches smaller than the wavelength of radiation [1.5]. In 1976, P.Yeh et. al., gave an idea of light behaviour in the periodic media with dispersion relation, and the band structure in analogue with Bloch phases [1.6]. The idea was implemented by E. Yablonovitch [1.1] and S. John [1.7] in 1987. Thereafter, an era of research in photonic crystals and its applications began. Yablonovitch focussed on designing three dimensional photonic crystals to enhance the density of optical states and hence to control the spontaneous emission of materials embedded within photonic crystals. The tools of classical electromagnetic theory can be used to explain the behaviour of light in these periodic media. Propagation of light in photonic crystals is analogous to the flow of electrons in crystalline atomic lattice, where periodic potential of the electron wavefunction produces electronic bandgap. The concept of defect lattice and light localisation was introduced by John [1.7]. A lot of research work was done around this period but most of them were theoretical studies and little experimental work was reported in micron scale. The reason behind this was the difficulty to achieve the experimental realisation of nano-scale structuring with the existing fabrication technology.

A theoretical investigation using plane wave expansion method for Maxwell's equations predicted the existence of photonic band structure of a face centred cubic lattice [1.8]. In 1992, a two-dimensional photonic crystal was fabricated using GaAs / InGaAs [1.9]. The existence of complete photonic band gap was experimentally verified in a three-dimensional photonic crystal fabricated using layer by layer method in wood pile structure [1.10]. The application-based research on photonic crystals flourished towards the end of the 20th century. It has also been reported that the nonlinear interactions are enhanced in a periodic high Q cavity medium [1.11]. First integrated optical device using photonic crystals was designed in 1996 [1.12]. This device had a transmission waveguide designed with a line defect in photonic crystal and it realised high transmission and 90° bends which could never be attained by conventional waveguides. The main drawback with

conventional waveguides based on total internal reflection was to bend the light to large angles and this difficulty was overcome by the use of photonic crystal waveguides. Super-prism effects have also been observed in photonic crystals [1.13]. A 2DPC defect mode laser was invented in 1996 [1.14]. Currently photonic band gap fibers (PBGF) designed from 2DPC promises important applications in optical communications. PBGF has the advantage over conventional single mode fiber as it can guide the light by phenomena of diffraction rather than total internal reflection. PBGF provides data delivery without nonlinear effects and material damage [1.15]. Plasmonics is another field of nano-photonics in which nonlinear optical materials with periodicity in wavelength scale are integrated with metal nano-particles. Presently research in plasmonics has attained considerable attention [1.16].

The first experimental realisation of three-dimensional photonic crystal with photonic band gap in near infrared region was reported in 1996 [1.17]. A full three-dimensional photonic crystal fabricated using wafer–fusion technique exhibited complete photonic band gap at optical communication wavelengths [1.18]. A defect in the 3D structure provides strong localisation of resonant photons in it and this effect allows perfect control of light propagation through such a structure. The recent advances in fabrication techniques encourage the development of photonic devices with applications including optical communication, photovoltaic and bio-photonics. It has been observed that a 3D photonic crystal can absorb more solar light than conventional thin films. Increased solar absorption leading to enhanced photocurrent density with an ultra-thin (100-300 nm) layer of gallium arsenide has been reported [1.19]. The metallic photonic crystals can be employed for an emission spectrum useful for solar thermo-photovoltaic applications as they exhibit high spectral emissivity compared to unstructured metals [1.20].

The 1DPC has been subject of interest to large theoretical and experimental research, because of its simplest design and complicated practical realization due to fabrication accuracy. One of the main applications of 1DPC is the omnidirectional reflector. In 1999, the first omnidirectional reflector was designed experimentally [1.21]. This designing was later extended to waveguide formation, where the core was filled with lossless high index material, so that light is confined to the core of the omnidirectional reflector thus enabling high power laser guidance at various wavelengths in visible – IR region. These structures can exhibit high gain nonlinear effects [1.22]. One dimensional nonlinear photonic crystal has been explored extensively for various nonlinear phenomena like higher harmonic

generation, self-focussing, self-steepening, pulse trapping and self-phase modulation. These effects are explored in designing of devices including higher harmonic generation [1.23] and pulse shaping mechanism like pulse compression [1.24-1.25]. These structures offer soliton propagation with balancing of non-linearity with dispersion effects [1.26]. One dimensional photonic crystal with defect exhibits high nonlinear gain and such structures can be used as a micro cavity for optical applications [1.27].

### 1.4.2 Introduction of Defects to the Periodic Structures

The periodicity in photonic crystals produces allowed energy bands and forbidden energy gaps and in the bandgap region no electromagnetic waves are allowed. A defect or imperfection in the otherwise perfect crystal sustains modes in the bandgap region [1.28 - 1.34]. In analogy with semiconductor crystals where the dopant and acceptor impurities create localized electromagnetic levels like donor level and acceptor level, intentional impurities added in photonic crystals creates localised modes inside the bandgap region [1.35–1.43]. This gives the possibility of confining light within the localised modes and to be used at sharp bends without losses in photonic integrated circuits [1.12, 1.44 - 1.48]. The defect introduced in an otherwise perfect crystal can be one dimensional (1D), two dimensional (2D) or three dimensional (3D). In 1D defect, light can be confined to a single defect plane whereas in 2D defect, light can be localized along a linear defect while in 3D defect, light can be trapped at a single point known as “cage of photon” [1.49]. Figure (1.4) shows the various types of inserted defects. One of the imperfections is changing the dielectric medium at a place in a photonic crystal or modifying its size or simply removing it [1.50]. A defect mode appears in the bandgap region leading to a strong localised state. By removing the dielectric medium at a place in a photonic crystal creates a cavity which is surrounded by reflecting walls. If the cavity is of sufficient size to support a mode, then the light is strongly confined in this cavity, which is also called resonant cavity.

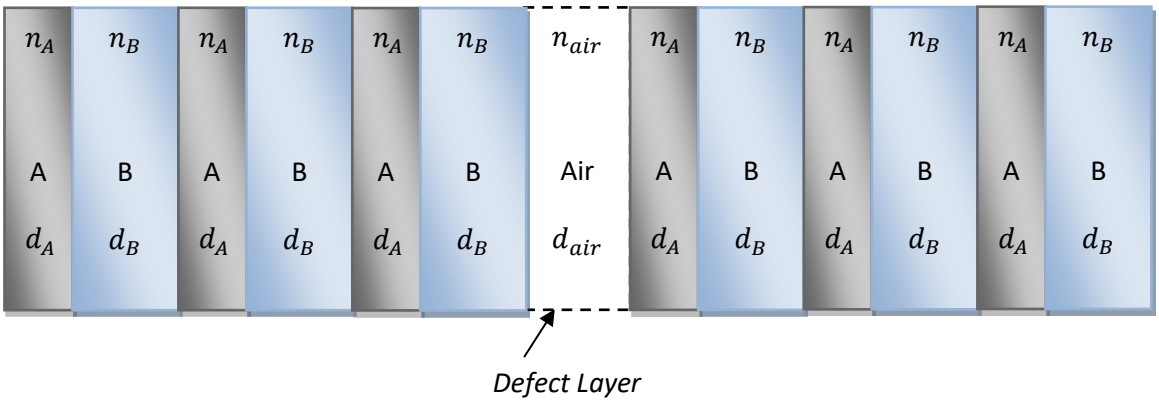


Figure 1.4 (a) One dimensional photonic crystal with defect layer of air in between a multi-layered $(AB)^{12}$ structure. The refractive index and the thickness of the two dielectric mediums being $n_A$, $n_B$ and $d_A$, $d_B$ respectively.

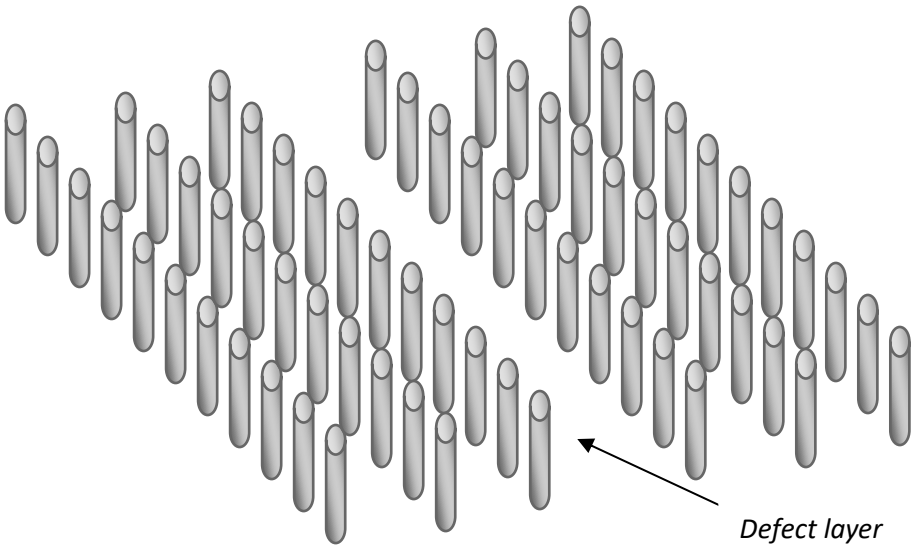


Figure 1.4 (b) Two-dimensional photonic crystal with a line defect layer

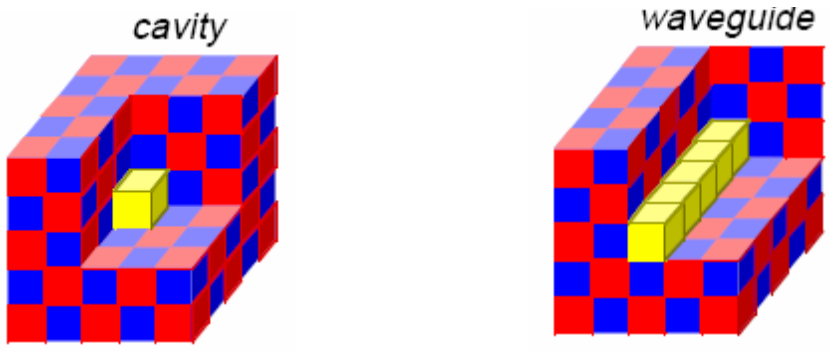


Figure 1.4 (c) Three-dimensional photonic crystal with a cavity point defect and waveguide inside the bulk

The resonant cavity mode inside the bandgap can be tuned by removing the dielectric or adding impurity [1.51-1.53]. This flexibility of tuning the defect modes makes microcavity photonic crystals useful in many applications including various optical sensors, filters, couplers, laser micro cavities with high Q value, etc. Line defect in otherwise perfect crystals creates a waveguide in which light is confined and directed along the waveguide. This resonant cavity waveguide has advantage over conventional dielectric waveguides like optical fiber in which light travels by phenomena of total internal reflection. In an optical fiber there is too much loss when it is bent at sharp corners because the condition of total internal reflection is not fulfilled. However, in resonant cavity waveguides, light travels through the defect mode in the bandgap region such that it can bend at sharp corners. Photonic crystal resonant cavity waveguides bring compactness to the photonic integrated circuits.

### 1.4.3 Applications of Photonic Crystals

The photonic crystals have the unique ability of controlling the photons, which make them useful in many future optical and photonic applications. Photonic crystals can improve the performance of waveguides [1.12, 1.40-1.42, 1.54 -1.58]. Photonic crystal waveguide is basically a photonic crystal with defect mode which allows the propagation of light in a specific direction. Photonic waveguides are superior to dielectric and metallic waveguides because of the photonic bandgap properties that make them lossless. A straight photonic crystal waveguide with discrete periodicity can produce mode coupling whenever Bragg's condition is satisfied. Photonic crystal waveguides can be easily created by removing a row of air holes or embedding dielectric waveguides in photonic crystal slabs [1.12, 1.44, 1.61].

Photonic crystals are used to make resonant microcavities where light is trapped in intentionally created defects leading to strong localisation of electric field inside the small volume of micro-cavities [1.49, 1.50, 1.62]. Photonic crystals with defects cause the concentration of high electric fields in the defect mode which give rise to enhancement of nonlinear optical phenomena [1.59, 1.60, 1.63-1.65]. Photonic crystals can be inserted in conventional waveguides to create optical filters with special transmission characteristics which can create optical systems with small volume, instantaneous response and consume small amounts of power [1.65-1.67]. One of the important needs in optics is to create omnidirectional reflectors which can reflect light irrespective of the angle of incidence and state of polarisation. Photonic crystals are used to create tuneable omnidirectional reflectors with desired frequency ranges [1.22, 1.68-1.76]. Photonic crystal microcavities with defect modes are used as optical sensors for sensing refractive index, pressure, temperature, etc. One of the most successful applications of photonic crystals is in the development of photonic crystal fibers (PCFs) [1.51, 1.77-1.81]. PCF is different from conventional optical fiber because PCF light travels in a hollow core with the property of photonic crystals. PCF is finding applications in optical communication, fiber laser, nonlinear devices, high power transmission, sensitive gas sensors and other areas. PCF are categorised into photonic-bandgap fiber, holey fiber (PCF with air holes in the cross-sections), Bragg fiber (PCF formed by concentric rings of multilayer films). 1DPCs are very much used in thin film optics from low reflection and high reflection coatings on lenses and mirrors to colour changing paints and inks. 2DPCs are used in nonlinear devices and to guide exotic wavelengths. 3DPCs can lead to efficient photovoltaic devices.

The fabrication of photonic crystals with full 3D band gap in the optical wavelength range is one of the most difficult challenges for the micro-system and nano-system technologies. Even accurate fabrication of 1D and 2D structures with nanometre-size features often possess serious manufacturing challenges. In recent years, much effort has been made to demonstrate the localization of light experimentally [1.82]. Another important area of research has been created from an analogy with the electronic band structure problem in condensed matter physics. In media where the dielectric permeability varies periodically in space, a series of photonic band gaps can appear in their frequency spectra. Because of the promising possibility that the number of devices based on this phenomenon can be used in various optoelectronic applications, research activity in photonic crystals has increased exponentially in the last decade. A number of analytical and numerical techniques have

been developed for analysing the wave propagation in inhomogeneous media. In the most general cases where the inhomogeneity is three dimensional, the exact solution of the problem is extremely hard to obtain and one is forced to use some approximation scheme. In the cases where the inhomogeneity is one dimensional, however, there exist several theoretical methods that allow exact solutions of the problem in some simple situations. It can be used to obtain exact solutions for the reflection and transmission coefficients of incoming waves and the electric and magnetic field amplitudes inside arbitrarily inhomogeneous media.

## 1.5 THEORETICAL TOOLS TO STUDY THE INTERACTION OF LIGHT WITH PHOTONIC CRYSTALS

There are some effective tools to study the propagation of light through a periodic medium. The widely used methods are Transfer Matrix Method (TMM), Plane Wave Expansion Method (PWE) and Finite Difference Time Domain (FDTD) method.

### 1.5.1 Plane Wave Expansion Method:

The PWE method is one of the most extensively used methods to calculate band structure because of its convenience [1.83]. Kushwaha et al. [1.84] firstly obtained the band structure of a PC by PWE. The PWE method includes expansion of all parameters such as modulus, density, and Poisson's ratio as the Fourier series in the reciprocal space. The equations of motion are transformed into the standard eigenvalue problem based on the Bloch theorem. The band structure of the dispersion relations between the frequency and wave vector is obtained by solving the eigenvalue equation. It is a convenient assumption that the wave vector just needs to traverse along the boundary of the irreducible region of the first Brillouin zone. The PWE shows great advantages in dealing with scatterers of different geometries and different arrangements, because it does not require meshing and reconstructing the finite element matrix. But the conventional PWE has a disadvantage of the slow convergence rate, especially for systems of either very high or very low filling ratios or of large elastic mismatch. The fictitious band gaps always appear as redundant lines in the band structure. Nevertheless, an improved PWE has a good convergence and can provide much more accurate numerical results [1.85, 1.86].

### 1.5.2 Finite Difference Time Domain Method

It can be shown from Maxwell's differential equations that the time derivative of the E-field is dependent on the H-field across the space. This gives the basic FDTD relation that at any point in space, the change in E-field with time is dependent on the stored value of the E-field and the curl of the local distribution of H-field in space. Similarly, the H-field is time stepped, at any point in space the change in H-field with time is dependent on the stored value of the H-field and the curl of the local distribution in E-field in space. In this technique the finite differences of the temporal and spatial derivatives of the E-fields and H-fields are computed using central difference approximations. At a particular instant the magnetic field vector components are solved and then the electric field vector components are calculated at the next instant. This process is repeated for the whole problem area till the exact picture of propagation analysis is completed. This method was introduced by Taflove [1.87] for analysing wave propagation in bulk medium. Chan et. al. [1.88] implemented this method to compute the band structure of multi-layered structures of high complexity. This method is a time domain method hence the solution covers a wide range of frequencies. This method has emerged as a commercial tool for device designing using photonic crystal structure.

### 1.5.3 Transfer Matrix Method

This method is used in optics and acoustics to study the propagation of electromagnetic and acoustic waves through multi-layered medium. The Transfer Matrix method is based on the fact that according to Maxwell's equations and the boundary conditions, the components of electric field and magnetic field are continuous across the boundaries from one medium to another. In case of a multi-layered system the field components at the starting layer are related to the field components at the end layer through transfer matrix operation [1.89]. The transmission and reflection coefficients of this multi-layered system can be derived from the field components. Abeles [1.90-1.91] studied the propagation of electromagnetic waves through multi-layered medium and framed this method. Later P. Yeh [1.6] extended this method for periodically stratified medium and the conditions of photonic band gap (PBG) were derived. This method is then proposed to find the dispersion relation and electrostatic potential calculations in multi-layered systems. The transfer matrix method to calculate the reflection and transmission coefficients in a thin

film is described here. Transfer matrix method correlates the amplitude of incoming wave and outgoing wave.

The TMM is a very useful method for calculation of reflection and transmission coefficients in multi-layered systems. It can analyse real and complex refractive index so it can be used to study lossless, absorptive and amplifying mediums. There is no restriction on the number of layers in this method for multi-layered structures. All these layers can be ordered in any manner and there is no essential requirement of periodicity. If the structure has periodicity, then the unit cell can be composed of any number of layers. The thickness and refractive index of the periodic layers can be defined independently. There is no restriction on thickness and refractive index of layers which makes this method suitable for modelling different periodic multilayer structures stacked together. This method can handle high refractive index contrast between the constituent layers, hence suitable for modelling multilayer structures, which usually have a high index contrast between their composite materials.

The TMM method assumes the plane perpendicular to the direction of propagation of the wave to be infinite, which means the multilayer structures extends infinitely in the other two dimensions, which is not realistic. So, the layers which are used have to be wide enough to avoid errors from this assumption. This method calculates the field throughout the multilayer structure by matrix multiplication, so it depends on the computation speed and therefore is limited by it. This method is limited to continuous wave propagation and cannot handle pulse propagation. This method is combined with the Fourier Transform method to deal with pulse propagation.

## 1.6 MOTIVATION

Photonic crystal is a composite dielectric with periodic modulation of refractive index that brings about a unique photonic band-gap effect by which light could be totally reflected on the surface of such material regardless of any incident angle or mode. Many applications based on this mechanism have been developed and introduced into new waveguides. Such band-gap effect could be understood by investigating the optical performance of one-dimensional photonic crystals. The wave-guides from 1DPCs are superior to conventional waveguides because of the bandgap property which makes them lossless. 1DPCs also work as optical filters that can be tuned in the desired wavelength

range. These optical filters are useful in optical networks and photonic circuits. Omnidirectional reflectors (ODR) formed by 1DPCs are superior over dielectric and metallic mirrors because of low absorption. ODRs find applications in photonic integrated circuits. 1DPCs with porous silicon layers are used for making microcavity sensors which can sense, liquid and gaseous chemical and biological analytes and environmental pollutants. These sensors are highly sensitive to change in refractive index due to the analytes inside its pores. The designed 1D-metallo-dielectric photonic crystals structures find applications in radio and microwave shields, transparent conductors, laser safety goggles, sunglasses for protection from UV rays etc.

## 1.7 PROBLEM STATEMENT

The bandgap of 1DPCs is controlled by its design parameters. The design parameters of 1DPCs like thickness, refractive index contrast, ambient medium index and number of layers helps us to tune the PBG in the desired wavelength range. 1DPCs are used in a wide variety of applications like wavelength filters, optical switches, omnidirectional reflectors, microcavity and waveguides, wavelength multiplexers, optical sensors, colour displays and photovoltaic. ODR is a perfect mirror and is very useful in photonic integrated circuits. These reflectors are superior over the conventional dielectric and metallic mirrors. There is a need for highly efficient ODRs with optimised design parameters. The width of the ODR band can be tuned to the desired wavelength range of application by selecting different materials and by changing the design parameters.

1DPCs with introduction of defect layer creates a microcavity structure which is widely used in waveguide and sensing applications. High precision optical sensing of chemical-analytes, bio-analytes, gases and environmental pollutants is the need of the hour. One of the applications of 1DPC microcavity structure is in designing of chemical and gas sensors with high sensitivity. Porous silicon based 1DPC microcavity sensors are superior over conventional sensors and have high sensitivity. 1DPCs with metallo-dielectric layers find application in microwave shielding and transparent conductors and UV-filters.

## 1.8 RESEARCH OBJECTIVES

- To characterize the photonic crystals using matrix approach.
- The emphasis of work will be on 1DPC waveguides and devices with different design parameters.
- To design and propose new designs of photonic crystal waveguides and optoelectronic devices.
- To study the analytical treatment for the density of states in 1DPC.
- To compare the analytical expression for the density of states with the results of direct numerical calculations.

## 1.9 ORGANIZATION OF THESIS

**Chapter 1: Introduction**

This chapter deals with the introduction of photonic crystals and its literature review. The development of PCs over the years along with its utility in various applications is studied. Advantages of 1DPC over 2DPC, 3DPC and other conventional waveguides are discussed through literature review. The mathematical models like PWE, FDTD method and TMM are studied to characterize the spectral response of 1DPCs. The versatility of 1DPCs to be used in opto-electronic devices and sensing applications gives the motivation for work

**Chapter 2: Mathematical Modeling and Effect of Design Parameters on Optical Response of 1DPC**

In this chapter the mathematical modelling of 1DPC is done by solving the wave equation in a multi-layered periodic medium. The dispersion relation is obtained by applying boundary conditions and Bloch theorem. The reflection and transmission coefficients in 1DPC are calculated using TMM where the thickness of constituent layers is taken from quarter wave stack condition.

**Chapter 3: Omnidirectional Reflection Band in 1DPC**

This chapter deals with one of the applications of 1DPC as ODR. An ODR is a perfect reflector which has high reflectance in a specific wavelength range irrespective of the angle of incidence and state of polarization of the incident wave.

**Chapter 4: Microcavity Defect in 1DPC**

This chapter deals with simulation study of single defects in 1DPC to make resonant microcavities. PCs with defects lead to localised electromagnetic modes inside the bandgap region. Many useful devices are designed using impurities in the PCs e.g., micro-

cavities, linear waveguides, etc. Impurities destroy the perfect translational symmetry in the photonic crystals. This can be achieved in a periodic dielectric structure by various methods e.g., adding impurity dielectric materials to a unit cell, removing dielectric materials from a unit cell, changing the dielectric constant of materials in a cell and by changing the size/geometry of materials in a cell in the lattice. The total effect will be a localized change of the average dielectric constant of the medium. Impurities at a single site serve as high quality factor microcavities. Such structures bind resonantly localized cavity modes about themselves having a frequency in a stop band of the photonic crystal. Since no light in the stop band can pass through the surrounding bulk materials, the impurity mode will be evanescent in the bulk material. Thus, a resonance occurs in a very narrow frequency range inside the stop band. The structure is then called a resonant microcavity, and the confined resonant mode about the structure is called the resonant excitation. The efficiency of the resonant cavity is characterized by a quality factor or Q value, a measure of the number of oscillations of light in the cavity before damping eventually causing the original excitation to decay away. The resonant excitations in such cavities are the basis of laser systems, Fabry-Perot oscillators, and photonic microcavities.

**Chapter 5: Metallo-Dielectric 1DPC**

In this chapter the transmission characteristics of 1D-Metallo-Dielectric PC (1DMDPC) with formation of structural and plasmonics bandgaps are studied. The structural bandgap is due to interference effects whereas the plasmonics bandgap is due to the bulk metal property. Transparent 1DMDPCs find applications in devices like microwave open door cavity, solar heat shields, laser safety goggles, sunglasses for protection from UV rays, and Radio waves shields.

**Chapter 6**: **Conclusion and Future Scope of Work**

This chapter presents the conclusions of the whole thesis and describes the expectations for further work in this area.

# CHAPTER-II

# MATHEMATICAL MODELING AND EFFECT OF DESIGN PARAMETERS ON OPTICAL RESPONSE OF 1DPC

**INTRODUCTION:**

In this chapter the mathematical modelling of 1DPC is done by solving the wave equation in a multi-layered periodic medium. The dispersion relation is obtained by applying boundary conditions and Bloch theorem. The reflection and transmission coefficients in 1DPC are calculated using TMM where the thickness of constituent layers is taken from quarter wave stack condition.

## 2.1 KRONIG PENNY MODEL

Electrons trapped inside a one-dimensional periodic rectangular potential well give rise to allowed energy bands and forbidden energy gaps. This model is known as the Kronig Penny Model. This model is also applicable for photons where the periodic potential is replaced by the periodic refractive index of the structure [2.1-2.8]. In the case of one-dimensional photonic crystal there is a periodic variation of refractive index where the periodicity is of the order of wavelength. Fig. (2.1) below shows the periodic variation of refractive index with distance inside the crystal

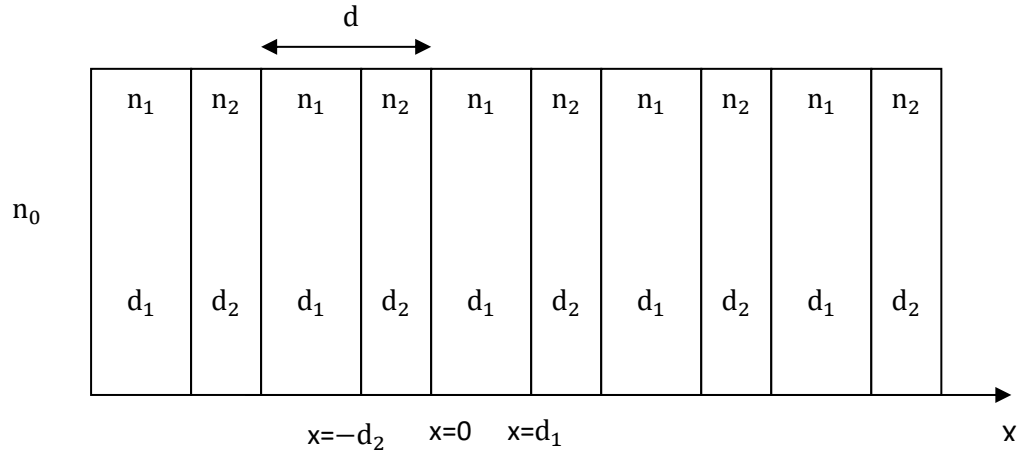


Figure (2.1): Periodic variation of refractive index in one dimensional photonic crystal

The periodic refractive index can be expressed as

$$n(x) = \begin{cases} n_1, & 0 \le x \le d_1 \\ n_2, & -d_2 \le x \le 0 \end{cases} \quad (2.1)$$

where $d_1$ and $d_2$ are thickness of the two medium and the corresponding refractive indices are $n_1$ and $n_2$, respectively. The periodicity of the structure is

$d = d_1 + d_2$ , such that $n(x) = n(x + d)$.

We have the one-dimensional wave equation for the electromagnetic eigen-mode $\psi_k(x)$ as

$$\frac{\partial^2 \psi_k(x)}{\partial x^2} + \frac{n^2(x)\omega^2{}_k}{c^2}\psi_k(x) = 0. \quad (2.2)$$

Using Eq. (2.1) , the above equation yields

$$\frac{\partial^2 \psi_k(x)}{\partial x^2} + \frac{{n_1}^2(x)\omega^2{}_k}{c^2}\psi_k(x) = 0, \qquad 0 \le x \le d_1 \quad (2.3)$$

$$\frac{\partial^2 \psi_k(x)}{\partial x^2} + \frac{{n_2}^2(x)\omega^2{}_k}{c^2}\psi_k(x) = 0, \qquad -d_2 \le x \le 0 \quad (2.4)$$

Let $\alpha = \frac{n_1}{c}\omega_k$, $\beta = \frac{n_2}{c}\omega_k$

$$\frac{\partial^2 \psi_k(x)}{\partial x^2} + \alpha^2\psi_k(x) = 0, \qquad 0 \le x \le d_1 \quad (2.5)$$

$$\frac{\partial^2 \psi_k(x)}{\partial x^2} + \beta^2\psi_k(x) = 0, \qquad -d_2 \le x \le 0 \quad (2.6)$$

Now according to Bloch's theorem, the wavefunction in a periodic potential can be written as $\psi_k(x) = u_k(x)e^{ikx}$ so

$$\psi_k(x) = u_1(x)e^{ikx} , \qquad 0 \le x \le d_1 \quad (2.7)$$

$$\psi_k(x) = u_2(x)e^{ikx} , \qquad -d_2 \le x \le 0 \quad (2.8)$$

Using the Bloch's theorem and applying the boundary conditions

$$u_1(x)|_{x=0} = u_2(x)|_{x=0} \tag{2.9}$$

$$\left.\frac{du_1}{dx}\right|_{x=0} = \left.\frac{du_2}{dx}\right|_{x=0} \tag{2.10}$$

$$u_1(x)|_{x=d_1} = u_2(x)|_{x=-d_2} \tag{2.11}$$

$$\left.\frac{du_1}{dx}\right|_{x=d_1} = \left.\frac{du_2}{dx}\right|_{x=-d_2} \tag{2.12}$$

We will get four equations with four unknown constants. To obtain a nontrivial solution of the equations the determinant of coefficient matrix of unknown constants must be zero.

$$\text{So} \begin{bmatrix} A_{11} & A_{12} & A_{13} & A_{14} \\ A_{21} & A_{22} & A_{23} & A_{24} \\ A_{31} & A_{32} & A_{33} & A_{34} \\ A_{41} & A_{42} & A_{43} & A_{44} \end{bmatrix} = 0. \tag{2.13}$$

Where

$A_{11} = A_{12} = A_{13} = A_{14} = 1$

$A_{21} = i(\alpha - k), \quad A_{22} = i(\alpha + k), \quad A_{23} = i(\beta - k), \qquad A_{24} = -i(\beta + k)$

$A_{41} = i(\alpha - k)e^{id_1(\alpha - k)},$

$A_{42} = -i(\alpha - k)e^{-id_1(\alpha + k)}, A_{43} = i(\beta - k)e^{-id_2(\beta - k)} A_{31} = e^{id_1(\alpha - k)},$

$A_{32} = e^{-id_1(\alpha + k)}, \quad A_{33} = e^{-id_2(\beta - k)}, A_{34} = e^{id_2(\beta + k)}$

$A_{44} = -i(\beta + k)e^{id_2(\beta + k)}.$

Here, k is the wave-number related to frequency $\omega$. After solving Eq. (2.13), we get the dispersion relation,

$$k(\omega) = \frac{1}{d}\cos^{-1}\left[\cos\left(\frac{n_1 \omega d_1}{c}\right)\cos\left(\frac{n_2 \omega d_2}{c}\right) - \frac{1}{2}\left(\frac{n_1}{n_2} + \frac{n_2}{n_1}\right)\sin\left(\frac{n_1 \omega d_1}{c}\right)\sin\left(\frac{n_2 \omega d_2}{c}\right)\right] \tag{2.14}$$

## 2.2 TRANSFER MATRIX METHOD

### 2.2.1 Application of TMM in a Thin Film

Let us consider a plane wave incident on a thin dielectric film as shown in Fig. (2.3). Let ($A_1$, $A_2'$, $A_2$, $A_3'$) represent the amplitude of the wave progressing towards right side and ($B_1$, $B_2'$, $B_2$, $B_3'$) represent the amplitude of the wave progressing towards left side.

$$n(x) = \begin{cases} n_1 & x < 0 \\ n_2 & 0 < x < d \\ n_3 & d < x \end{cases} \tag{2.15}$$

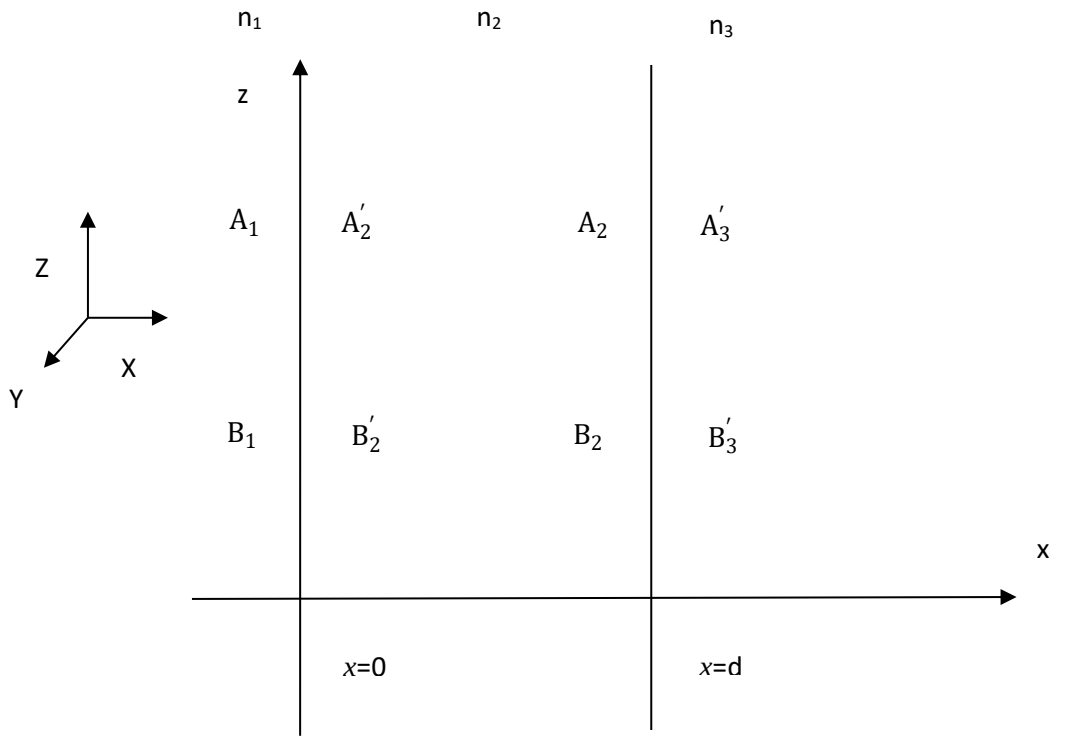


Figure (2.2): Block diagram of two dielectric interfaces

Where $n_1$, $n_2$, $n_3$ are the refractive indices of layers 1, 2, 3 respectively and d is the thickness of film. The medium is homogenous in z-direction so the solution to the classical wave equation is

$$E = E(x)e^{i(\omega t - \beta z)} \tag{2.16}$$

Where β is representing the z-component of wave vector and ω is the angular frequency. Since the wave is travelling along x-z plane and for s-wave, $\vec{E}$ is parallel to y-axis and for p-wave, $\vec{H}$

is parallel to y-axis. The total electric field $\mathrm{E}(x)$ can be written as sum of Right side travelling wave and Left side travelling wave.

$$\mathrm{E}(x) = \mathrm{R}e^{-\mathrm{i}xk_x} + \mathrm{L}e^{\mathrm{i}xk_x} = \mathrm{A}(x) + \mathrm{B}(x) \tag{2.17}$$

where $k_x$ is the x-component of wave-vector and R and L are homogenous constants for Right side and Left side travelling waves $\mathrm{A}(x)$ and $\mathrm{B}(x)$ are the amplitudes of Right and Left side travelling waves. To represent in matrix method, we use the following definitions

$$\mathrm{A}_1 = \mathrm{A}(0^-),\ \mathrm{B}_1 = \mathrm{B}(0^-), \mathrm{A}_2' = \mathrm{A}(0^+)\ , \mathrm{B}_2' = \mathrm{B}(0^+) \tag{2.18}$$

$$\mathrm{A}_2 = \mathrm{A}(\mathrm{d}^-), \mathrm{B}_2 = \mathrm{B}(\mathrm{d}^-), \mathrm{A}_3' = \mathrm{A}(\mathrm{d}^+), \mathrm{B}_3' = \mathrm{B}(\mathrm{d}^+) \tag{2.19}$$

where $0^-$ represent the left side of the interface at $x = 0$, and $0^+$ represent the right side of the interface at $x = 0$, similarly $\mathrm{d}^-$ represent the left side of interface at $x = \mathrm{d}$ and $\mathrm{d}^+$represent the right side of interface at $x = \mathrm{d}$.

The two amplitudes of $\mathrm{E}(x)$ can now be shown related through a column matrix form

$$\begin{pmatrix}\mathrm{A}_1\\ \mathrm{B}_1\end{pmatrix} = {\mathrm{D}_1}^{-1}\mathrm{D}_2\begin{pmatrix}\mathrm{A}_2'\\ \mathrm{B}_2'\end{pmatrix} = \mathrm{D}_{12}\begin{pmatrix}\mathrm{A}_2'\\ \mathrm{B}_2'\end{pmatrix} \tag{2.20}$$

$$\begin{pmatrix}\mathrm{A}_2'\\ \mathrm{B}_2'\end{pmatrix} = \mathrm{P}_2\begin{pmatrix}\mathrm{A}_2\\ \mathrm{B}_2\end{pmatrix} = \begin{pmatrix}e^{\mathrm{i}\emptyset_2} & 0\\ 0 & e^{-\mathrm{i}\emptyset_2}\end{pmatrix}\begin{pmatrix}\mathrm{A}_2\\ \mathrm{B}_2\end{pmatrix} \tag{2.21}$$

$$\begin{pmatrix}\mathrm{A}_2\\ \mathrm{B}_2\end{pmatrix} = {\mathrm{D}_2}^{-1}\mathrm{D}_3\begin{pmatrix}\mathrm{A}_3'\\ \mathrm{B}_3'\end{pmatrix} = \mathrm{D}_{23}\begin{pmatrix}\mathrm{A}_3'\\ \mathrm{B}_3'\end{pmatrix} \tag{2.22}$$

where $P_2$ is called the propagation matrix which represents the propagation through the bulk medium and the dynamical matrices$\mathrm{D}_1$, $\mathrm{D}_2$, $\mathrm{D}_3$ are given by

$$\mathrm{D}_l = \begin{cases}\begin{pmatrix}1 & 1\\ \mathrm{n}_l\cos\theta_l & -\mathrm{n}_l\cos\theta_l\end{pmatrix} & (\mathrm{s}-\mathrm{wave})\\ \begin{pmatrix}\cos\theta_l & \cos\theta_l\\ \mathrm{n}_l & -\mathrm{n}_l\end{pmatrix} & (\mathrm{p}-\mathrm{wave})\end{cases} \tag{2.23}$$

where $l$ = 1, 2, 3 and $\theta_l$ is the incident ray angle in $l$ th layer and is related to $\beta$ and $k_{lx}$ as

$$\beta = \mathrm{n}_l\frac{\omega}{\mathrm{c}}\sin\theta_l \tag{2.24}$$

$$k_{lx} = \mathrm{n}_l\frac{\omega}{\mathrm{c}}\cos\theta_l \tag{2.25}$$

and $\emptyset_2$is given by

$$\emptyset_2 = k_{2x}\mathrm{d} \tag{2.26}$$

The matrices $D_{12}$ and $D_{23}$ are transmission matrices which relates the amplitudes of waves on two sides of the interface and are given by

$$D_{12} = \begin{pmatrix} \frac{1}{2}\left(1+\frac{k_{2x}}{k_{1x}}\right) & \frac{1}{2}\left(1-\frac{k_{2x}}{k_{1x}}\right) \\ \frac{1}{2}\left(1-\frac{k_{2x}}{k_{1x}}\right) & \frac{1}{2}\left(1+\frac{k_{2x}}{k_{1x}}\right) \end{pmatrix} \quad s-\text{wave} \tag{2.27}$$

and

$$D_{12} = \begin{pmatrix} \frac{1}{2}\left(1+\frac{n_2^2\,k_{2x}}{n_1^2\,k_{1x}}\right) & \frac{1}{2}\left(1-\frac{n_2^2\,k_{2x}}{n_1^2\,k_{1x}}\right) \\ \frac{1}{2}\left(1-\frac{n_2^2\,k_{2x}}{n_1^2\,k_{1x}}\right) & \frac{1}{2}\left(1+\frac{n_2^2\,k_{2x}}{n_1^2\,k_{1x}}\right) \end{pmatrix} \quad p-\text{wave} \tag{2.28}$$

Similarly

$$D_{23} = \begin{pmatrix} \frac{1}{2}\left(1+\frac{k_{3x}}{k_{2x}}\right) & \frac{1}{2}\left(1-\frac{k_{3x}}{k_{2x}}\right) \\ \frac{1}{2}\left(1-\frac{k_{3x}}{k_{2x}}\right) & \frac{1}{2}\left(1+\frac{k_{3x}}{k_{2x}}\right) \end{pmatrix} \quad s-\text{wave} \tag{2.29}$$

$$D_{23} = \begin{pmatrix} \frac{1}{2}\left(1+\frac{n_3^2\,k_{3x}}{n_2^2\,k_{2x}}\right) & \frac{1}{2}\left(1-\frac{n_3^2\,k_{3x}}{n_1^2\,k_{1x}}\right) \\ \frac{1}{2}\left(1-\frac{n_3^2\,k_{3x}}{n_2^2\,k_{2x}}\right) & \frac{1}{2}\left(1+\frac{n_3^2\,k_{3x}}{n_2^2\,k_{2x}}\right) \end{pmatrix} \quad p-\text{wave} \tag{2.30}$$

$D_{12}$ can now be written as

$$D_{12} = \frac{1}{t_{12}}\begin{pmatrix} 1 & r_{12} \\ r_{12} & 1 \end{pmatrix} \tag{2.31}$$

where $t_{12}$ and $r_{12}$ are Fresnel transmission and reflection coefficients and are given by

$$r_{12} = \begin{cases} \frac{k_{1x}-k_{2x}}{k_{1x}+k_{2x}}, & s-\text{wave} \\ \frac{n_1^2\,k_{1x}-n_2^2\,k_{2x}}{n_1^2\,k_{1x}+n_2^2\,k_{2x}} & p-wave \end{cases} \tag{2.32}$$

and

$$t_{12} = \begin{cases} \frac{2k_{2x}}{k_{1x}+k_{2x}} & s-\text{wave} \\ \frac{2n_2^2\,k_{2x}}{n_1^2\,k_{1x}+\,n_2^2\,k_{2x}} & p-\text{wave} \end{cases} \tag{2.33}$$

The amplitudes of incidence medium $A_1, B_1$ and exit medium $A_3', B_3'$ are related as

$$\begin{pmatrix} A_1 \\ B_1 \end{pmatrix} = {D_1}^{-1} D_2 P_2 {D_2}^{-1} D_3 \begin{pmatrix} A_3' \\ B_3' \end{pmatrix} \tag{2.34}$$

Each side of the interface is represented by dynamic matrix and each bulk medium is represented by propagation matrix. This method can be applied to multi-layered systems with the matrix multiplication in sequential order of the exact system.

### 2.2.2: Application of TMM in Multilayer system

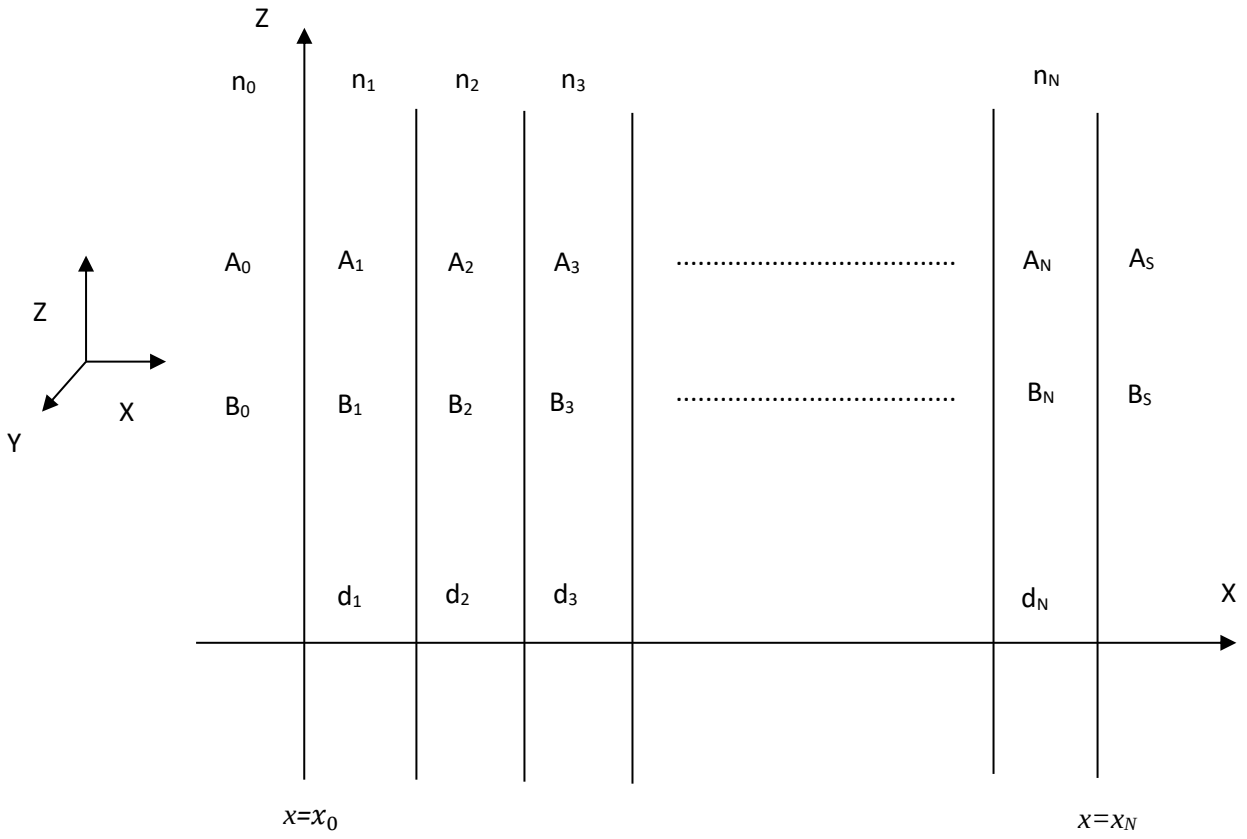


Figure (2.3): Block diagram of N layered dielectric medium

Let us consider a one-dimensional multi-layered dielectric structure with refractive index variation along x-axis. We assume that all the mediums are homogenous, isotropic and infinitely extended as shown in Fig. (2.3). The total number of layers is considered as N. The refractive index profile of the system can be described by

$$n(x) = \begin{cases} n_0, & x < 0 \\ n_1, & 0 < x \leq x_1 \\ n_2, & x_1 < x \leq x_2 \\ . & \\ . & \\ . & \\ . & \\ n_N, & x_{N-1} < x \leq x_N \\ n_s, & x_N < x \end{cases} \quad (2.35)$$

Here $n_p$ is the refractive index of $p^{th}$ layer($1 < p < N$), the refractive index of surrounding medium layer is $n_0$ and the refractive index of $N^{th}$ layer is $n_N$. The refractive index of substrate is $n_s$. The thickness of layers is given by

$d_1 = x_1 - x_0$

$d_2 = x_2 - x_1$

$d_3 = x_3 - x_2$

$d_N = x_N - x_{N-1}$

The electric field of the plane wave solution of Maxwell's equations can be written as

$E = E(x)e^{i(\omega t - \beta z)}$, where β is z-component of wavevector and ω is the angular frequency.

$$E(x) = \begin{cases} A_0 e^{-ik_{0x}(x-x_0)} + B_0 e^{ik_{0x}(x-x_0)}, & x < x_0 \\ . & \\ . & \\ . & \\ A_P e^{-ik_{px}(x-x_p)} + B_p e^{ik_{px}(x-x_p)}, & x_{p-1} < x < x_p \\ . & \\ . & \\ A_N e^{-ik_{xN}(x-x_{N-1})} + B_N e^{ik_{xN}(x-x_{N-1})}, & x_{N-1} < x < x_N \\ A_s e^{-ik_{xs}(x-x_N)} + B_s e^{ik_{xs}(x-x_N)}, & x_N < x \end{cases} \quad (2.36)$$

Where $k_{px}$is the x-component of wave-vector of $p^{th}$ layer given by

$$k_{px} = \left(\left(\frac{n_p \omega}{c}\right)^2 - \beta^2\right)^{\frac{1}{2}} = n_p \frac{\omega}{c} \cos\theta_p \quad , (p = 1,2,3,4, \ldots . N, s)$$

Here $A_0, A_1, \ldots A_p, \ldots A_N, A_s$ are the amplitudes of waves travelling towards (+x) direction and $B_0, B_1, \ldots . B_p, \ldots B_N, B_s$ are the amplitude of waves travelling towards (-x) direction. The amplitudes of plane waves at the interface are related with matrix as

$$\begin{pmatrix} A_0 \\ B_0 \end{pmatrix} = {D_0}^{-1} D_1 \begin{pmatrix} A_1 \\ B_1 \end{pmatrix} \tag{2.37}$$

$$\begin{pmatrix} A_p \\ B_p \end{pmatrix} = P_1 {D_p}^{-1} D_{p+1} \begin{pmatrix} A_{p+1} \\ B_{p+1} \end{pmatrix} \qquad (p = 1,2, \ldots\ldots\ldots\ldots N) \tag{2.38}$$

Here (p+1) is the substrate layer s, i.e., $A_{p+1} = A_s$ and $B_{p+1} = B_s$

$$D_p = \begin{pmatrix} 1 & 1 \\ n_p \cos\theta_p & -n_p \cos\theta_p \end{pmatrix} \quad TE - \text{wave} \tag{2.39}$$

$$\text{also } D_p = \begin{pmatrix} \cos\theta_p & \cos\theta_p \\ n_p & -n_p \end{pmatrix} \qquad TM - \text{ wave} \tag{2.40}$$

$$\text{and } P_p = \begin{pmatrix} e^{i\emptyset_p} & 0 \\ 0 & e^{-i\emptyset_p} \end{pmatrix} \tag{2.41}$$

$$\text{where } \emptyset_p = k_{px} d_p \tag{2.42}$$

The amplitude of plane wave $A_0, B_0$ at the ambient medium $(x = x_0)$ and $A_s, B_s$ at the substrate medium $(x = x_N)$ are correlated now by a matrix as

$$\begin{pmatrix} A_0 \\ B_0 \end{pmatrix} = \begin{pmatrix} M_{11} & M_{12} \\ M_{21} & M_{22} \end{pmatrix} \begin{pmatrix} A_s \\ B_s \end{pmatrix} \tag{2.43}$$

where the matrix is given by

$$\begin{pmatrix} M_{11} & M_{12} \\ M_{21} & M_{22} \end{pmatrix} = {D_0}^{-1} D_s \prod_{p=1}^{N} D_p \, P_p {D_p}^{-1} \tag{2.44}$$

### 2.2.3 Quarter Wave Stack Condition

There is a specific condition in designing the 1D multi-layered photonic crystal which is called quarter wave condition where the thickness of each layer is made equal to quarter of wavelength of incident light. Take for example the refractive index of the two layers are $n_1 = 3.6, n_2 = 1.5$ for $\lambda_0$ as central wavelength of incident wave, the corresponding thickness of the two layers will be $d_1 = \frac{\lambda_0}{4n_1}$, $d_2 = \frac{\lambda_0}{4n_2}$. The phase corresponding to a path length of quarter wave length is $\frac{\pi}{2}$. So $\emptyset_p = \frac{\pi}{2}$ , and the propagation matrix from Eq. (2.41) becomes

$$P_p = \begin{pmatrix} i & 0 \\ 0 & i \end{pmatrix} \tag{2.45}$$

If light is incident form the ambient medium $n_0$ with amplitudes $A_0, B_0$ and the exit medium (substrate) have amplitudes $A_s, B_s$ , the reflection coefficient of the system is defined as

$$r = \frac{B_0}{A_0}\Big|_{B_s=0} \tag{2.46}$$

and the transmission coefficient is defined as

$$t = \frac{A_s}{A_0}\Big|_{B_s=0} \tag{2.47}$$

Using the matrix Eq. (2.44), the reflection and transmission coefficient can be written as

$$r = \frac{M_{21}}{M_{11}} \tag{2.48}$$

$$t = \frac{1}{M_{11}} \tag{2.49}$$

From Eqs. (2.49 and 2.50) , the reflectance (R) and transmittance (T) is given by

$$R = |r|^2 = \left|\frac{M_{21}}{M_{11}}\right|^2 \tag{2.50}$$

$$T = |t|^2 = \frac{n_s \cos\theta_s}{n_0 \cos\theta_0}\left|\frac{1}{M_{11}}\right|^2 \tag{2.51}$$

### 2.2.4 Dispersion Relation and Bloch's Theorem

Dispersion relation can be obtained in an infinite periodic multi-layered structure by using Bloch's theorem. Since the multi-layered structure is periodic in x –direction and is invariant under lattice translation. Under the translational symmetry with a translational operator 'T' we can write

$$T\,E(x) = E(x + \Lambda l) \tag{2.52}$$

where $l$ is an integer and Λ is the periodicity.

The electric field can be written in form of Bloch waves as

$$E = E_K(x)e^{-iKx}e^{-i(\omega t - k_x x)} \tag{2.53}$$

where $E_K(x)$ is periodic with Λ

$$E_K(x) = E_K(x + \Lambda) \tag{2.54}$$

The constant K is known as Bloch wave number. Using Eq. (2.38) and Eq. (2.54) we have the eigenvalue equation

$$\begin{pmatrix} A_m \\ B_m \end{pmatrix} = e^{-iK\Lambda} \begin{pmatrix} A_{m-1} \\ B_{m-1} \end{pmatrix} \tag{2.55}$$

From Eq. (2.45) and Eq. (2.55) the eigenvalue equation can be written as

$$\begin{pmatrix} M_{11} & M_{12} \\ M_{21} & M_{22} \end{pmatrix} \begin{pmatrix} A_m \\ B_m \end{pmatrix} = e^{iK\Lambda} \begin{pmatrix} A_m \\ B_m \end{pmatrix} \tag{2.56}$$

Eq. (2.56) leads to

$$\begin{vmatrix} M_{11} - e^{iK\Lambda} & M_{12} \\ M_{21} & M_{22} - e^{iK\Lambda} \end{vmatrix} = 0 \tag{2.57}$$

The solutions are

$$e^{iK\Lambda} = \frac{1}{2}(M_{11} + M_{22}) \pm \left\{ \left( \frac{1}{2}(M_{11} + M_{22}) \right)^2 - 1 \right\}^{1/2} \tag{2.58}$$

Eq.(2.59) gives the dispersion relation between $\omega$, $k_x$ and K as

$$K(k_x, \omega) = \frac{1}{\Lambda} \cos^{-1} \left[ \frac{1}{2}(M_{11} + M_{22}) \right] \tag{2.59}$$

Here, if the value of $\left[\frac{1}{2}(M_{11} + M_{22})\right] < 1$, then this corresponds to real values of Bloch vector K, hence this condition will correspond to propagating waves i.e. allowed modes or allowed photonic bands. If the value of $\left[\frac{1}{2}(M_{11} + M_{22})\right] > 1$, then this corresponds to imaginary values of Bloch vector K, hence no propagating solution exists in this condition and this region is called photonic bandgap. The value of $\left[\frac{1}{2}(M_{11} + M_{22})\right] = 1$ corresponds to the band edges.

From Eq. (2.59) , the dispersion relation can also be written as

$$\cos K\Lambda = \cos k_1 d_1 \cos k_2 d_2 - \frac{1}{2}\left(\frac{n_2}{n_1} + \frac{n_1}{n_2}\right) \sin k_1 d_1 \sin k_2 d_2 \tag{2.60}$$

## 2.3 SIMULATION RESULTS OF PHOTONIC BANDGAP REGION IN 1DPC

### 2.3.1 Silicon/Silicon-Dioxide ($Si/SiO_2$)

The plot between the normalised Bloch wave-vector $\frac{K\Lambda}{\pi}$ and normalised frequency $\frac{\omega\Lambda}{2\pi c}$ using Eq. (2.60) is called dispersion relation curve. Fig. (2.4) shows the dispersion relation with allowed bands and photonic bandgap for 20 layered Si / $SiO_2$ with $n_1 = 3.42, n_2 = 1.45,\ d_1 = \frac{\lambda_0}{4n_1} = 58.48$ nm, $d_2 = \frac{\lambda_0}{4n_2} = 137.93$ nm and considering central wavelength $\lambda_0 = 800$ nm . Fig. (2.5) shows the reflectance curve according to Eq. (2.50) for the same above design parameters.

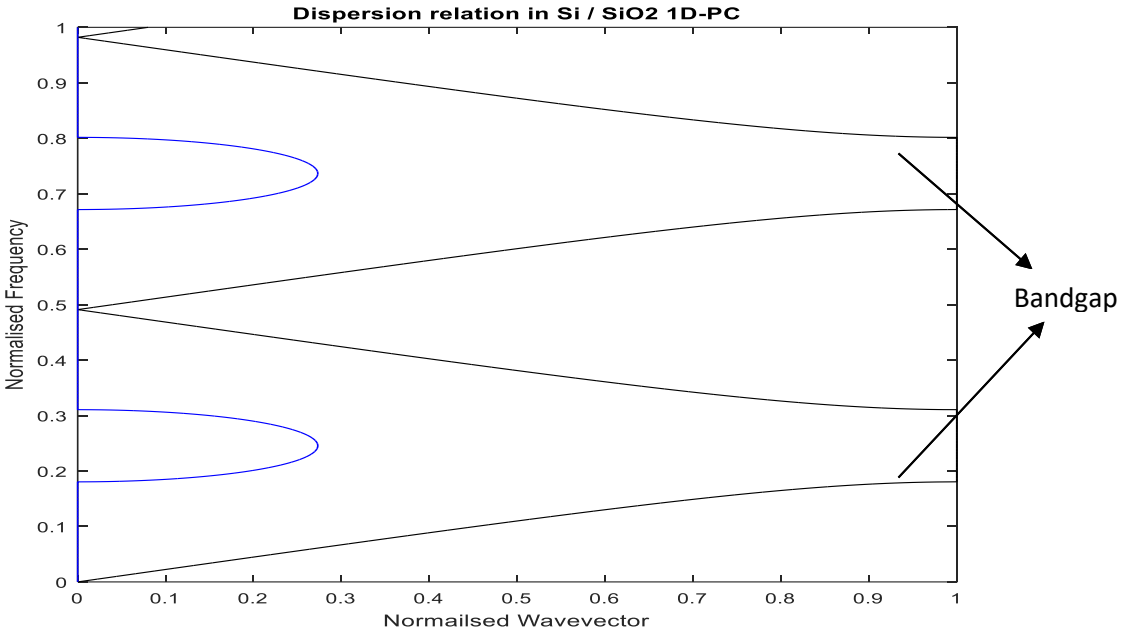


Figure (2.4): The Dispersion relation curve plotted for N = 20 and normal incidence. $n_1$=3.42, $n_2$=1.45, $d_1$=58.48 nm, $d_2$= 137.93 nm. The blue curve shows the imaginary part of normalised wave-vector

From the dispersion relation curve Fig. (2.4), the first bandgap exists with the bandgap edges from normalised frequency 0.1798, to 0.3097. The lower bandgap edge $\lambda_L$ in terms of wavelength will be

$$\lambda_L = \frac{\Lambda}{\text{normalised frquency}} = \frac{(137.93 + 58.48)}{0.3097} = 634 \text{ nm}$$

The upper bandgap edge $\lambda_U$ will be

$$\lambda_U = \frac{\Lambda}{\text{normalised frquency}} = \frac{(137.93 + 58.48)}{0.1798} = 1092 \text{ nm}$$

So, the first photonic bandgap edges lie between 634 nm and 1092 nm and the bandgap = 1092 nm-634 nm= 458 nm. Waves of this wavelength range from 1092 nm-634 nm will not be allowed to pass through this multi-layered structure and these waves will be reflected from the multi-layered structure. The blue curve in Fig. (2.4) shows the imaginary values of normalised Bloch wave-vector where no propagating solution exists. The blue curve shows the maximum at the middle of the photonic bandgap. The ambient medium and substrate is taken as air in all calculations.

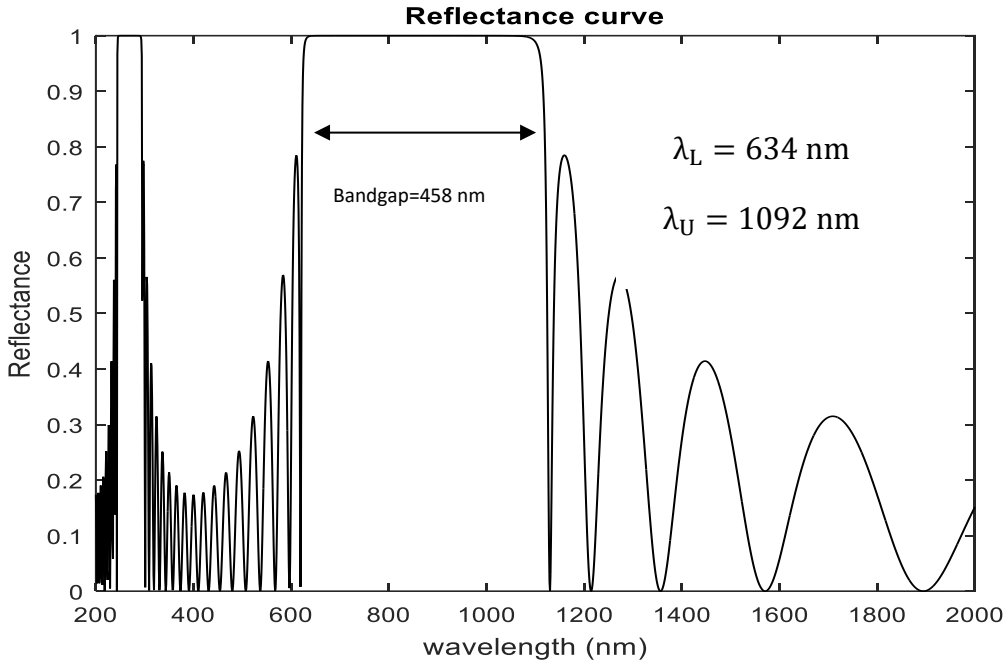


Figure (2.5): The reflectance spectrum plotted for N=20 and normal incidence with $n_1$=3.42, $n_2$=1.45, $d_1$=58.48 nm, $d_2$= 137.93 nm.

We present here simulation results for our TMM model for few 1DPC with dielectric layers. The ambient medium and the substrate medium is taken as air in all calculations and for simplicity the normal angle of incidence is considered. We are considering N number of layers with periodicity $\Lambda$, and the thickness of each layer is given by the quarter wave stack condition. Since normal incidence is considered, the Transverse Electric (TE) and Transverse Magnetic (TM) polarisation results will be same.

### 2.3.2 Titanium Oxide / Silicon-Dioxide ($TiO_2$ / $SiO_2$)

One dimensional photonic crystal consisting of 20 layers of alternate layers of high refractive index ($TiO_2$=2.67) and low refractive index ($SiO_2$=1.45) at 800 nm is used for simulations. The material dispersion effects are ignored in this calculation. The refractive index of ambient medium and substrate is taken as 1 in all calculations. The thickness of the two layers is according to quarter wave stack condition. If $d_1, d_2$ are thicknesses of $TiO_2$ layers and $SiO_2$ layers, respectively, then according to quarter wave stack condition:

$$d_1 = \frac{800}{4n_1} = \frac{800}{4 \times 2.67} = 74.90 \text{ nm},$$

$$d_2 = \frac{800}{4n_1} = \frac{800}{4 \times 1.45} = 137.93 \text{ nm}.$$

The periodicity $\Lambda = (74.90 \text{ nm} + 137.93 \text{ nm}) = 212.83 \text{ nm}$ Now according to mathematical model of TMM from Eq. (2.60), the dispersion relation is shown in Fig. (2.6).

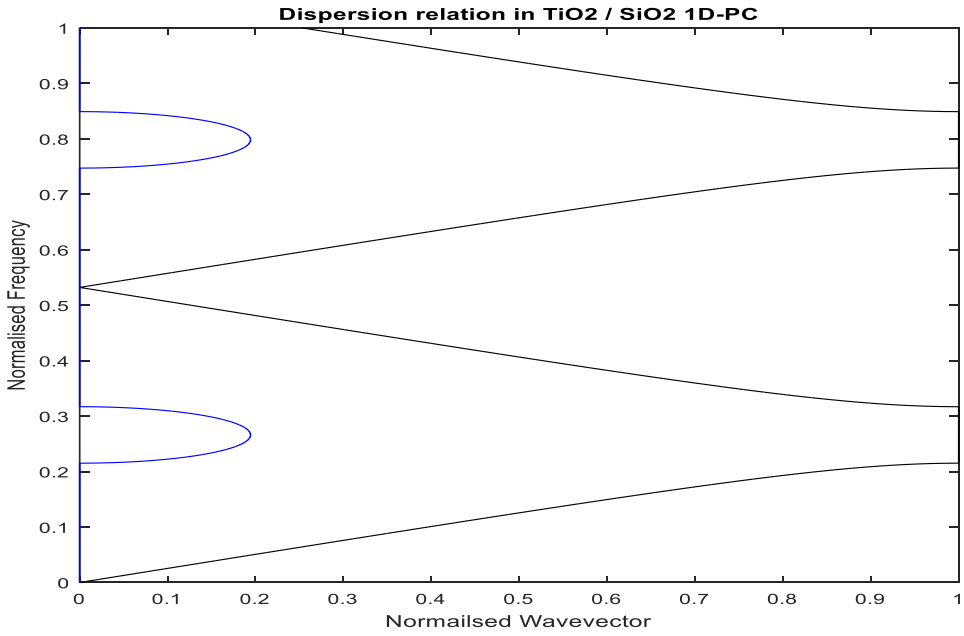


Figure (2.6): Dispersion relation for $TiO_2$/$SiO_2$ multi-layered structure with N=20 for normal incidence, the refractive index of the alternating medium is $n_1 = 2.67,\ n_2 = 1.45$, and their thickness are $d_1 = 74.90 \text{ nm}, d_2 = 137.93 \text{ nm}$ respectively.

The bandgap edges are at normalised frequency =0.2161 and 0.3161 so the bandgap edges in terms of wavelength are at

$$\lambda_L = \frac{\Lambda}{\text{normalised frquency}} = \frac{212.83}{0.3161} = 673.29 \text{ nm}$$

The upper bandgap edge $\lambda_U$ will be

$$\lambda_U = \frac{\Lambda}{\text{normalised frquency}} = \frac{212.83}{0.2161} = 984.86 \text{ nm}$$

$$\text{Bandgap} = 984.86 - 673.29 = 311.57 \text{ nm}$$

In Fig. (2.6) the blue lines represent the imaginary part of the normalised wave-vector. These values of Bloch wave-vector are not allowed so no propagating states exists for these K values. Fig. (2.7) shows the reflection spectrum for this multi-layered structure with the bandgap edges at $\lambda_L = 673$ nm; $\lambda_U = 984$ nm, bandgap $= 984 - 673 = 311$ nm. The waves with this range of wavelength will be reflected from the multi-layered structure.

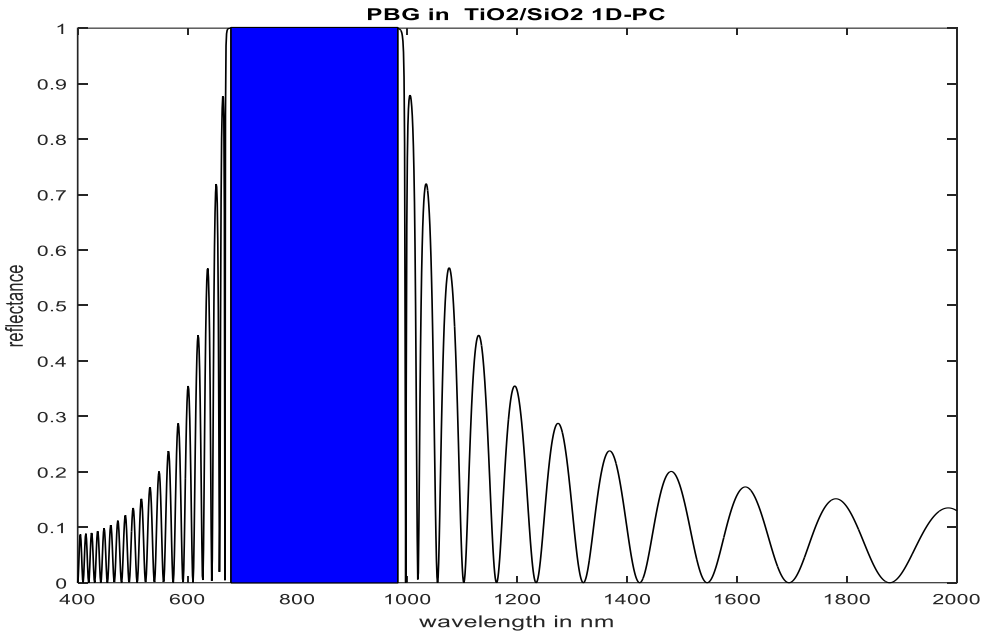


Figure (2.7) Reflectance curve for multi-layered $TiO_2/SiO_2$ structure with $n_1 = 2.67$, $n_2 = 1.45$, $d_1 = 74.90$ nm, $d_2 = 137.93$ nm with $\lambda_0 = 800$ nm. The above curve is plotted for N=20 and normal incidence

### 2.3.3 Germanium / Cryolite (Ge / $Na_3AlF_6$)

Another example of one-dimensional photonic crystal is using Cryolite ($Na_3AlF_6$) films. A 1D-PC consisting of 20 alternate layers of high refractive index (Ge = 4.2) and low refractive index (Cryolite = 1.34) at 800 nm is used for simulations. The material dispersion effects are ignored in this calculation. The thickness of the two layers is according to quarter wave stack condition. If $d_1$, $d_2$ are thicknesses of Ge layer and Cryolite layer, respectively, then according to quarter wave stack condition

$$d_1 = \frac{800}{4n_1} = \frac{800}{4 \times 4.2} = 47.61 \text{ nm}$$

$$d_2 = \frac{800}{4n_1} = \frac{800}{4 \times 1.34} = 149.25 \text{ nm}$$

The periodicity $\Lambda = (47.61 + 149.25) = 196.86$ nm . Now according to mathematical model of TMM from Eq. (2.60), the dispersion relation is shown in Fig. (2.8).

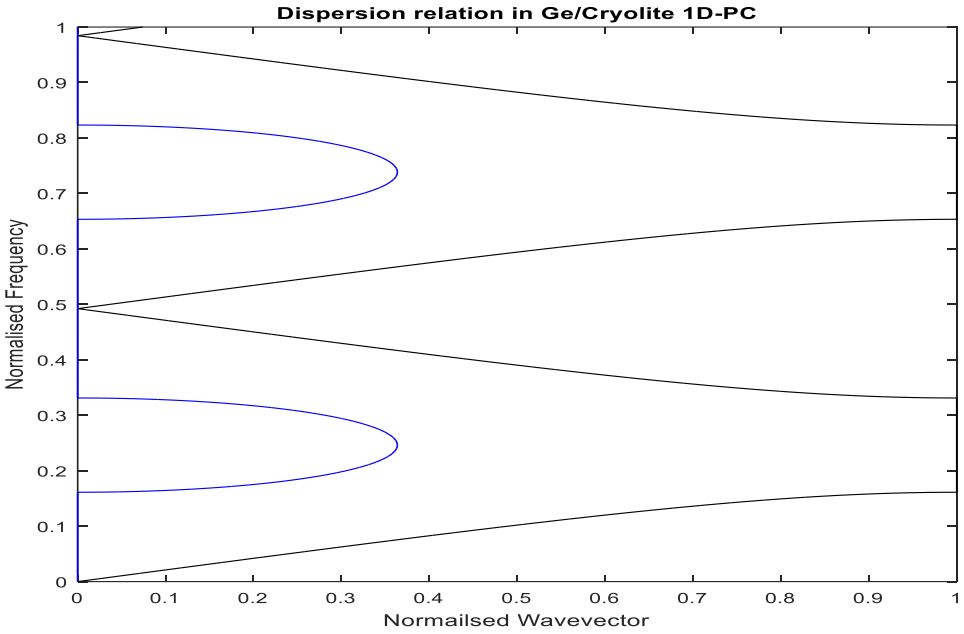


Figure (2.8): Dispersion relation for Ge / $Na_3AlF_6$ multi-layered structure with N = 20 for normal incidence, the refractive index of the alternating medium are $n_1 = 4.2$, $n_2 = 1.34$, and their thickness are $d_1 = 47.61\ nm, d_2 = 149.25\ nm$, respectively.

The first bandgap edges are at normalised frequency =0.1621 and 0.3301 so the bandgap edges in terms of wavelength are at

$$\lambda_L = \frac{\Lambda}{\text{normalised frquency}} = \frac{196.86}{0.3301} = 596.36 \text{ nm}$$

The upper bandgap edge $\lambda_U$ will be

$$\lambda_U = \frac{\Lambda}{\text{normalised frquency}} = \frac{196.86}{0.1621} = 1214.43 \text{ nm}$$

$$\text{Bandgap} = 1214.43 - 596.36 = 618.07 \text{ nm}$$

In Fig. (2.8) the blue lines represent the imaginary part of the normalised wave-vector. These values of Bloch wave-vector are not allowed so no propagating states exists for these K values. Fig. (2.9) shows the reflection spectrum for this multi-layered structure with the bandgap edges at $\lambda_L = 596.36$ nm; $\lambda_H = 1214.43$ nm, Bandgap $= 1214.43 - 596.36 = 618.07$ nm. The waves with this range will be reflected from the multi-layered structure.

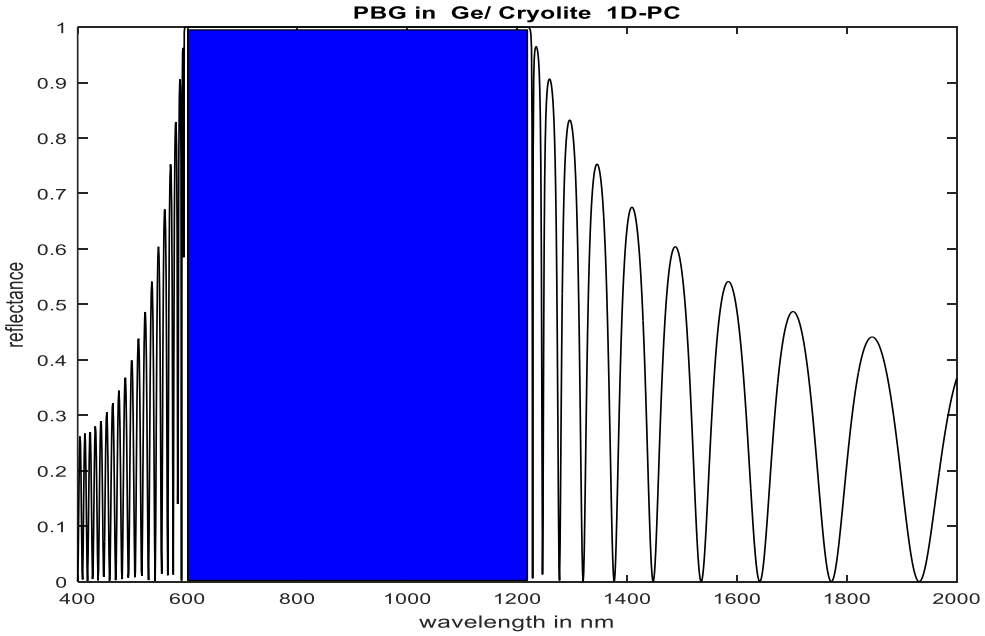


Figure (2.9) Reflectance curve for $n_1 = 4.2, n_2 = 1.34,\ d_1 = 47.61\ nm,\ d_2 = 149.25\ nm$ with $\lambda_0 = 800\ nm$. The above curve is plotted for N = 20 and normal incidence

### 2.3.4 Tellurium-Cryolite (Te / $Na_3AlF_6$)

Another example of one-dimensional photonic crystal is using Cryolite ($Na_3AlF_6$) films. A 1D-PC consisting of 20 alternate layers of high refractive index (Te = 4.6) and low refractive index (Cryolite = 1.34) at 800 nm is used for simulations. The material dispersion effects are ignored in this calculation. The refractive index of ambient medium and substrate is taken as 1 in all calculations. The thickness of the two layers is according to quarter wave stack condition. If $d_1, d_2$ are thickness of Te layer and cryolite layer respectively, then according to quarter wave stack condition

$$d_1 = \frac{800}{4n_1} = \frac{800}{4 \times 4.6} = 43.47\ nm$$

$$d_2 = \frac{800}{4n_1} = \frac{800}{4 \times 1.34} = 149.25\ nm$$

The periodicity $\Lambda = (43.47 + 149.25) = 192.72\ nm$. Now according to mathematical model of TMM from Eq. (2.60), the dispersion relation is shown in Fig. (2.10).

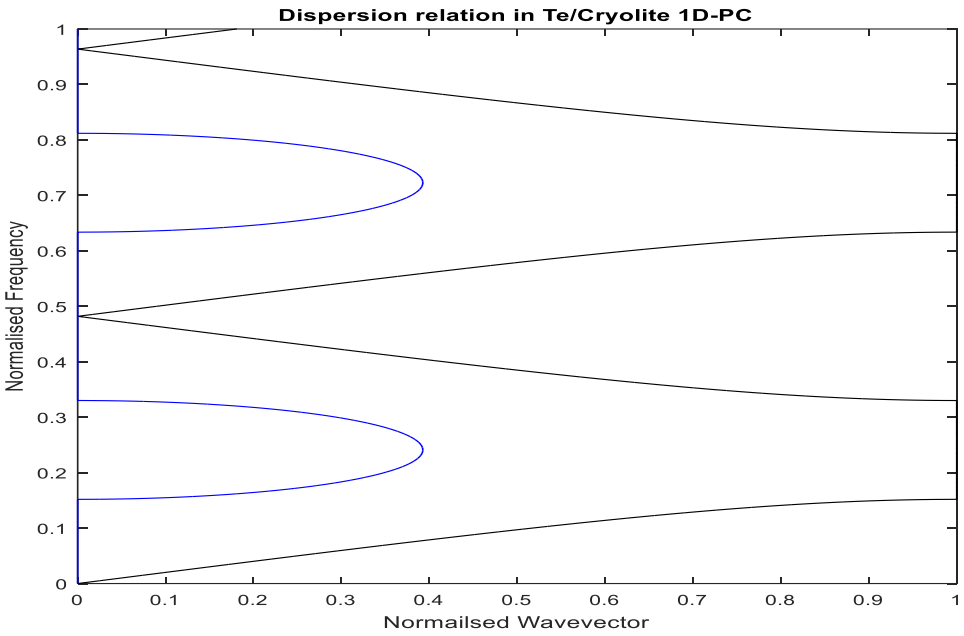


Figure (2.10): Dispersion relation for Te / Cryolite multi-layered structure with N = 20 for normal incidence, the refractive index of the alternating mediums are $n_1 = 4.6,\ n_2 = 1.34$, and their thickness are $d_1 = 43.47$ nm, $d_2 = 149.25$ nm, respectively.

The first bandgap edges are at normalised frequency = 0.1521 and 0.3291 so the bandgap edges in terms of wavelength are at

$$\lambda_L = \frac{\Lambda}{\text{normalised frquency}} = \frac{192.72}{0.3291} = 585.59 \text{ nm}$$

The upper bandgap edge $\lambda_U$ will be

$$\lambda_U = \frac{\Lambda}{\text{normalised frquency}} = \frac{192.72}{0.1521} = 1267.06 \text{ nm}$$

$$\text{Bandgap} = 1267.06 - 585.59 = 681.47 \text{ nm}$$

In Fig. (2.10) the blue lines represent the imaginary part of the normalised wave-vector. These values of Bloch wave-vector are not allowed so no propagating states exists for these K values. Fig. (2.11) shows the reflection spectrum for this multi-layered structure with the bandgap edges at $\lambda_L = 585.59$ nm, $\lambda_U = 1267.06$ nm, Bandgap $= 1267.06 - 585.59 = 681.47$ nm. The waves with this range will be reflected from the multi-layered structure.

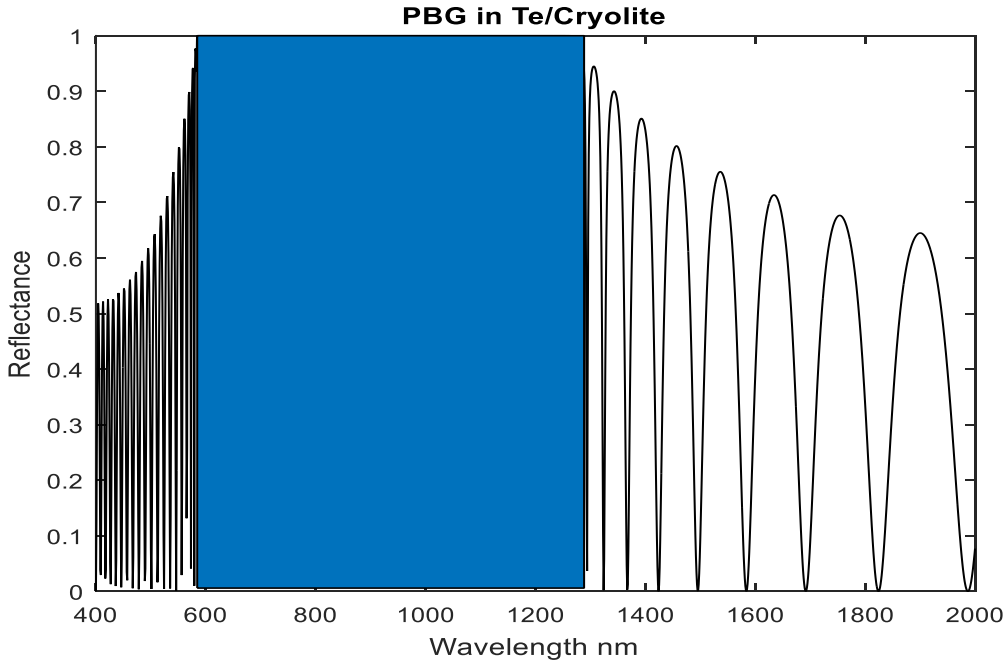


Figure (2.11) Reflectance curve for $n_1 = 4.6, n_2 = 1.34$, $d_1 = 43.47$ nm, $d_2 = 149.25$ nm with $\lambda_0 = 800$ nm. The above curve is plotted for N = 20 and normal incidence.

### 2.3.5 Silicon-Cryolite (Si / $Na_3AlF_6$)

A 1D-PC consisting of 20 alternate layers of high refractive index (Si = 3.42) and low refractive index (Cryolite = 1.34) at 800 nm is used for simulations. The material dispersion effects are ignored in this calculation. The refractive index of ambient medium and substrate is taken as 1 in all calculations. The thickness of the two layers is according to quarter wave stack condition. If $d_1, d_2$ are thickness of Si layer and cryolite layer respectively, then according to quarter wave stack condition

$$\mathrm{d_1} = \frac{800}{4\mathrm{n_1}} = \frac{800}{4 \times 3.42} = 58.48 \text{ nm}$$

$$\mathrm{d_2} = \frac{800}{4\mathrm{n_1}} = \frac{800}{4 \times 1.34} = 149.25 \text{ nm}$$

The periodicity $\Lambda = (58.48 + 149.25) = 207.73$ nm, Now according to mathematical model of TMM from Eq. (2.60), the dispersion relation is shown in Fig. (2.12). First bandgap edges are at normalised frequency = 0.1851 and 0.3341 so the bandgap edges in terms of wavelength are at

$$\lambda_\mathrm{L} = \frac{\Lambda}{\text{normalised frquency}} = \frac{207.73}{0.3341} = 621.76 \text{ nm.}$$

The upper bandgap edge $\lambda_U$ will be

$$\lambda_\mathrm{U} = \frac{\Lambda}{\text{normalised frquency}} = \frac{207.73}{0.1851} = 1122.25 \text{ nm.}$$

$$\text{Bandgap} = 1122.25 - 621.76 = 500.49 \text{ nm.}$$

In Fig. (2.12) the blue lines represent the imaginary part of the normalised wave-vector. These values of Bloch wave-vector are not allowed so no propagating states exists for these K values. Fig. (2.13) shows the reflection spectrum for this multi-layered structure with the bandgap edges at $\lambda_\mathrm{L} = 621.76$ nm, $\lambda_\mathrm{U} = 1122.25$ nm, $\text{Bandgap} = 1122.25 - 621.76 = 500.49$ nm. The waves with this range will be reflected from the multi-layered structure.

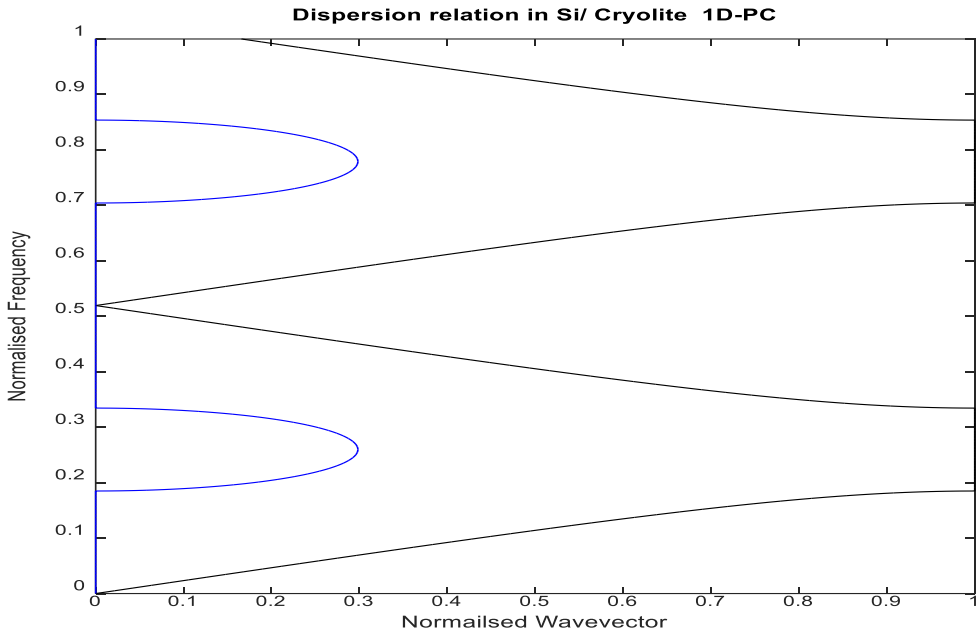


Figure (2.12): Dispersion relation for Si / Cryolite multi-layered structure with N = 20 for normal incidence, the refractive index of the alternating medium is $n_1 = 3.42,\ n_2 = 1.34$, and their thickness are $d_1 = 58.48$ nm, $d_2 = 149.25$ nm, respectively.

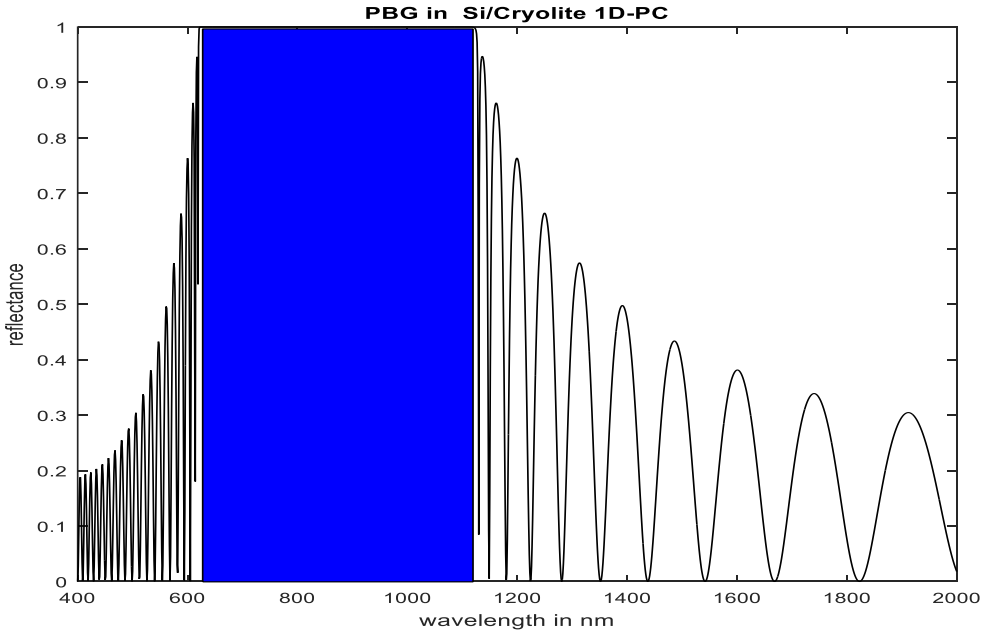


Figure (2.13) Reflectance curve for $n_1 = 3.42, n_2 = 1.34,\ d_1 = 58.48$ nm, $d_2 = 149.25$ nm with $\lambda_0 = 800$ nm. The above curve is plotted for N = 20 and normal incidence

### 2.3.6 Gallium Arsenide / Cryolite (GaAs / $Na_3AlF_6$)

A 1D-PC consisting of 20 alternate layers of high refractive index (GaAs = 3.6) and low refractive index (Cryolite = 1.34) at 800 nm is used for simulations. The material dispersion effects are ignored in this calculation. The refractive index of ambient medium and substrate is taken as 1 in all calculations. The thickness of the two layers is according to quarter wave stack condition. If $d_1, d_2$ are thickness of GaAs layer and cryolite layer respectively, then according to quarter wave stack condition

$$\mathrm{d_1} = \frac{800}{4\mathrm{n_1}} = \frac{800}{4 \times 3.6} = 55.55 \text{ nm}$$

$$\mathrm{d_2} = \frac{800}{4\mathrm{n_1}} = \frac{800}{4 \times 1.34} = 149.25 \text{ nm}$$

The periodicity $\Lambda = (55.55 + 149.25) = 204.8$ nm. Now according to mathematical model of TMM from Eq. (2.60), the dispersion relation is shown in Fig. (2.14). The first bandgap edges are at normalised frequency = 0.1791 and 0.3331 so the bandgap edges in terms of wavelength are at

$$\lambda_\mathrm{L} = \frac{\Lambda}{\text{normalised frquency}} = \frac{204.8}{0.3331} = 614.83 \text{ nm}$$

The upper bandgap edge $\lambda_U$ will be

$$\lambda_\mathrm{U} = \frac{\Lambda}{\text{normalised frquency}} = \frac{204.8}{0.1791} = 1143.49 \text{ nm}$$

$$\text{Bandgap} = 1143.49 - 614.83 = 528.66 \text{ nm}$$

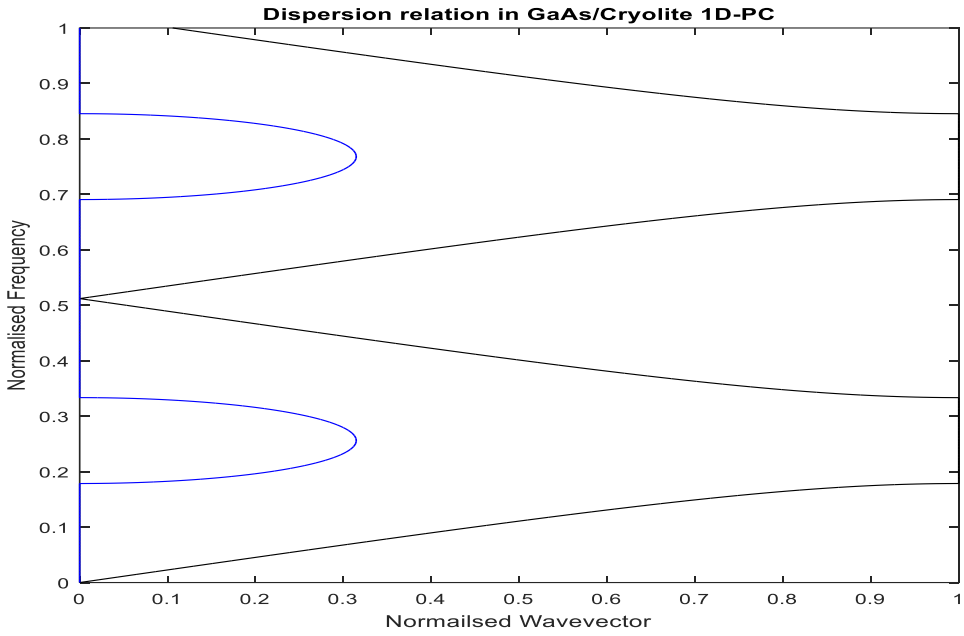


Figure (2.14): Dispersion relation for GaAs / Cryolite multi-layered structure with N=20 for normal incidence, the refractive index of the alternating medium are $n_1 = 3.6,\ n_2 = 1.34$, and their thickness are $d_1 = 55.55$ nm, $d_2 = 149.25$ nm, respectively.

In Fig. (2.14) the blue dotted lines represent the imaginary part of the normalised wave-vector. These values of Bloch wave-vector are not allowed so no propagating states exists for these K values. Fig. (2.15) shows the reflection spectrum for this multi-layered structure with the bandgap edges at $\lambda_L = 614.83$ nm, $\lambda_U = 1143.49$nm, Bandgap $= 1143.49 - 614.83 = 528.66$ nm. The waves with this range will be reflected from the multi-layered structure.

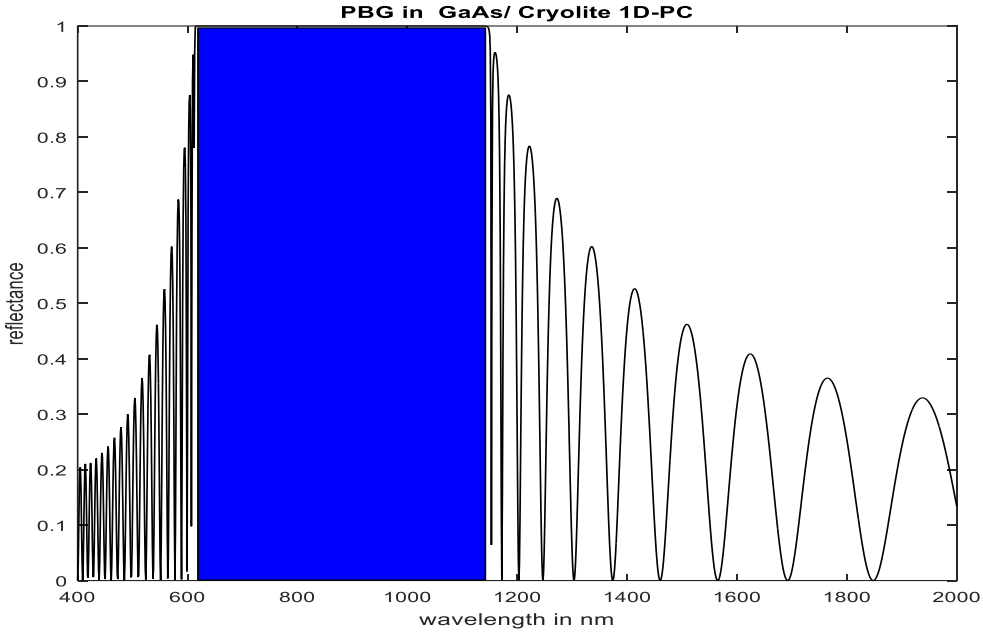


Figure (2.15) Reflectance curve for $n_1 = 3.6, n_2 = 1.34,\ d_1 = 55.55$ nm, $d_2 = 149.25$ nm with $\lambda_0 = 800$ nm. The above curve is plotted for N = 20 and normal incidence

### 2.3.7 Zinc Oxide / Silicon Dioxide (ZnO / $SiO_2$)

A 1D-PC consisting of 20 alternate layers of high refractive index (ZnO = 2.08) and low refractive index ($SiO_2$ = 1.45) at 800 nm is used for simulations. The material dispersion effects are ignored in this calculation. The refractive index of ambient medium and substrate is taken as 1 in all calculations. The thickness of the two layers is according to quarter wave stack condition. If $d_1, d_2$ are thickness of ZnO layer and $SiO_2$ layer respectively, then according to quarter wave stack condition

$$d_1 = \frac{800}{4n_1} = \frac{800}{4 \times 2.08} = 96.15 \text{ nm}$$

$$d_2 = \frac{800}{4n_1} = \frac{800}{4 \times 1.45} = 137.93 \text{ nm}$$

The periodicity $\Lambda = (96.15 + 137.93) = 234.08$ nm. Now according to mathematical model of TMM from Eq. (2.60), the dispersion relation is shown in Fig. (2.16). The first bandgap edges are at normalised frequency = 0.2601 and 0.3251 so the bandgap edges in terms of wavelength are at

$$\lambda_L = \frac{\Lambda}{\text{normalised frquency}} = \frac{234.08}{0.3251} = 720 \text{ nm.}$$

The upper bandgap edge $\lambda_U$ will be

$$\lambda_U = \frac{\Lambda}{\text{normalised frquency}} = \frac{234.08}{0.2601} = 900 \text{ nm.}$$

$$\text{Bandgap} = 900 - 720 = 180 \text{ nm.}$$

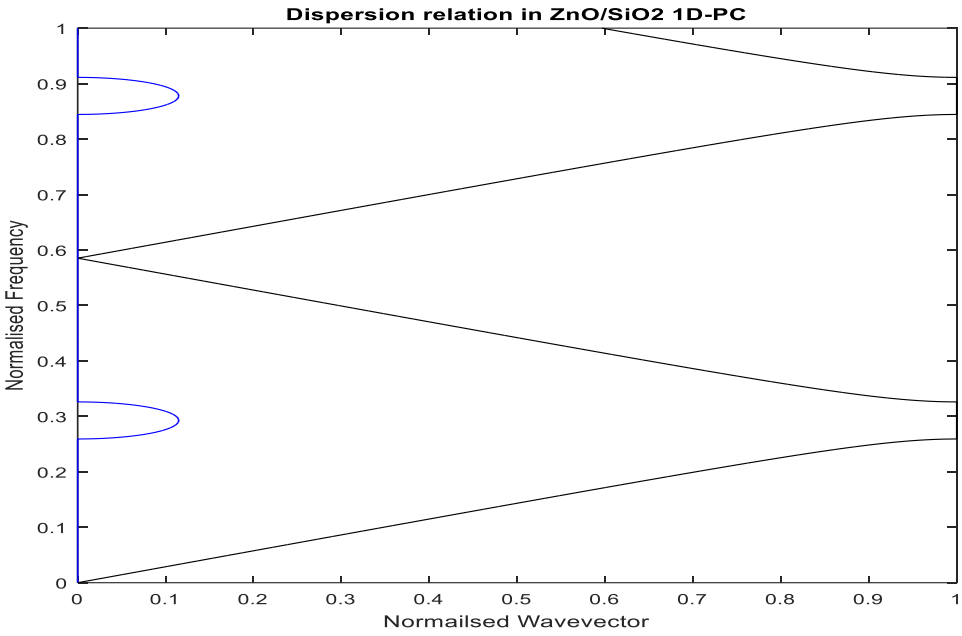


Figure (2.16): Dispersion relation for $ZnO/SiO_2$ multi-layered structure with N = 20 for normal incidence, the refractive index of the alternating medium is $n_1 = 2.08,\ n_2 = 1.45$, and their thickness are $d_1 = 96.15$ nm, $d_2 = 137.93$ nm respectively.

In Fig. (2.16) the blue dotted lines represent the imaginary part of the normalised wave-vector. These values of Bloch wave-vector are not allowed so no propagating states exists for these K values. Fig. (2.17) shows the reflection spectrum for this multi-layered structure with the bandgap edges at $\lambda_L = 720$ nm, $\lambda_U = 900$ nm, $\text{Bandgap} = 900 - 720 = 180$ nm. The waves with this range will be reflected from the multi-layered structure.

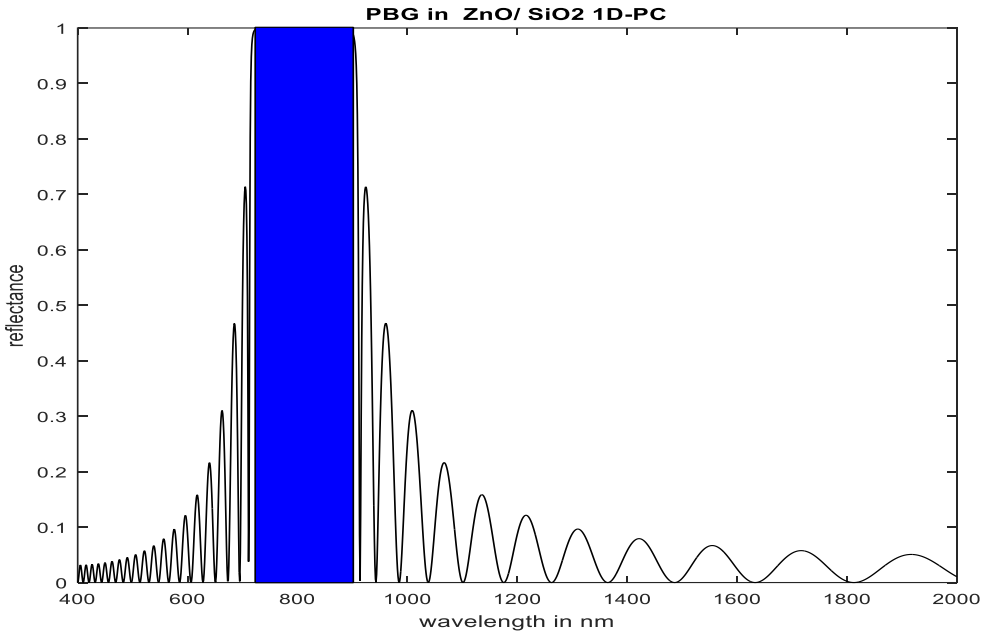


Figure (2.17) Reflectance curve for $n_1 = 2.08, n_2 = 1.45,\ d_1 = 96.15$ nm, $d_2 = 137.93$ nm with $\lambda_0 = 800$ nm. The above curve is plotted for N = 20 and normal incidence

## 2.4 DENSITY OF STATES

Photonic crystals attract lot of research investigations due to their ability to control the properties of photons [2.9-2.12]. Let us consider a collimated light ray of wavelength λ and angle of incidence $\theta_{in}$ falling on the surface of a 1DPC from air reaches the surface of the 1DPC. We assume that the wave propagates in x-y plane and we match the frequency and the tangential component of wave-vector for the incident and refracted wave across the interfaces.

Using relation Eq. (2.61) and Eq. (2.62), we can find the wave-vector in the incident medium.

$$\varepsilon_r \omega^2 = {k_x}^2 + {k_y}^2 \tag{2.61}$$

$$\tan\theta_{in} = \frac{k_y}{k_x} \tag{2.62}$$

where $\omega = 2\pi f$ is the angular frequency ( $f$ is the frequency of light), $\varepsilon_r$ is the relative permittivity of the incident medium, $k_x$ and $k_y$ are the components of wave-vector perpendicular and parallel, respectively, to the interface between the homogeneous medium and the photonic crystal. We have assumed here $k_z = 0$ for simplicity. The dispersion relation from the transfer matrix method is computed from Eq. (2.62), and from the dispersion relation we can calculate the group velocity using the relation

$$v_g = \nabla_k \omega_k = \left( \frac{\partial \omega_k}{\partial k_x}, \frac{\partial \omega_k}{\partial k_y}, \frac{\partial \omega_k}{\partial k_z} \right) \tag{2.63}$$

Photonic crystals have the ability to modify the DOS due to which they are getting significant attention in high Q value, small mode volume cavities. An increase in DOS of the lasing mode causes significant enhancement in the spontaneous emission rate [2.3]. The DOS is defined as

$$N(\omega) = \sum_m \frac{1}{A_{BZ}} \int_{BZ} \delta\big(\omega - \omega_m(k)\big)\, d^2k, \tag{2.64}$$

where, the integral is over m$^{th}$ band and $A_{BZ}$is the area of the Brillouin zone (BZ). Eq. (2.64) can also be written as

$$N(\omega) = \sum_m \frac{1}{A_{BZ}} \int_{EFS_m} \left\| \frac{dk}{d\omega} \right\| ds, \tag{2.65}$$

where the integral is taken along the m$^{th}$ equi-frequency surfaces (EFS) at frequency $\omega$. The DOS was first used in analysing the modification of spontaneous emission in photonic crystals. DOS plays an important role in mode confinement in photonic crystal structures and light trapping of solar cells. Fig. (2.18) shows the variation of DOS with the normalised frequency for a multi-layered Si / $SiO_2$ 1DPC with $n_1 = 3.42, n_2 = 1.45$. It can be seen here that at bandgap edges the DOS show sharp rise to maximum value and at other values it is almost zero. The comparative study of DOS is shown for different 1DPC structures are shown in Fig. (2.19).

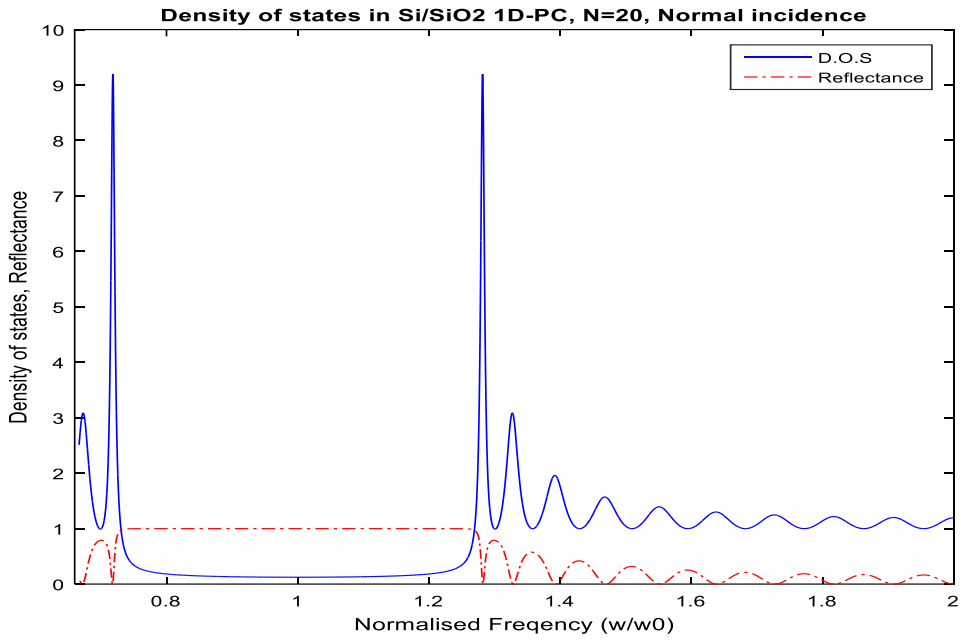


Figure (2.18): The density of states in Si / $SiO_2$ 1DPC for N = 20 and normal incidence, $n_1$ = 3.42, $n_2$ = 1.45, $d_1$ = 58.48 nm, $d_2$ = 137.93 nm.

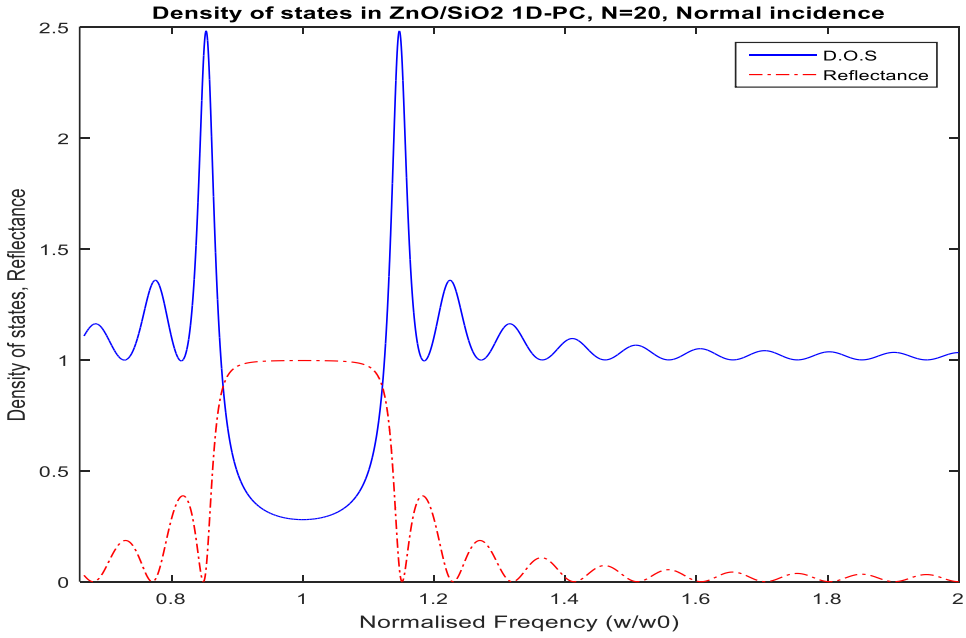


(a)

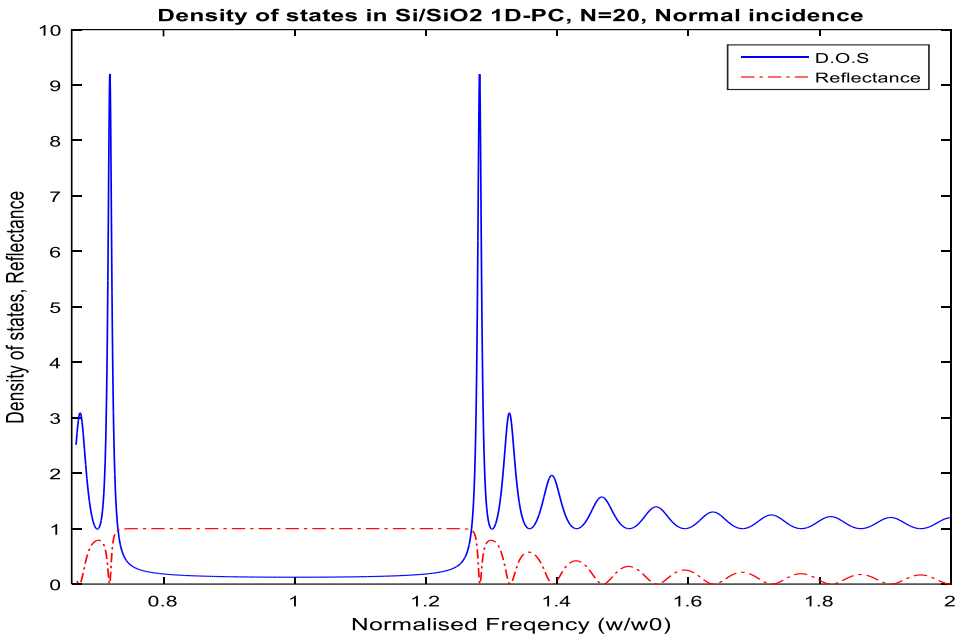
Density of states in Si/SiO2 1D-PC, N=20, Normal incidence
D.O.S
Reflectance
Density of states, Reflectance
Normalised Freqency (w/w0)
0
1
2
3
4
5
6
7
8
9
10
0.8
1
1.2
1.4
1.6
1.8
2

(b)

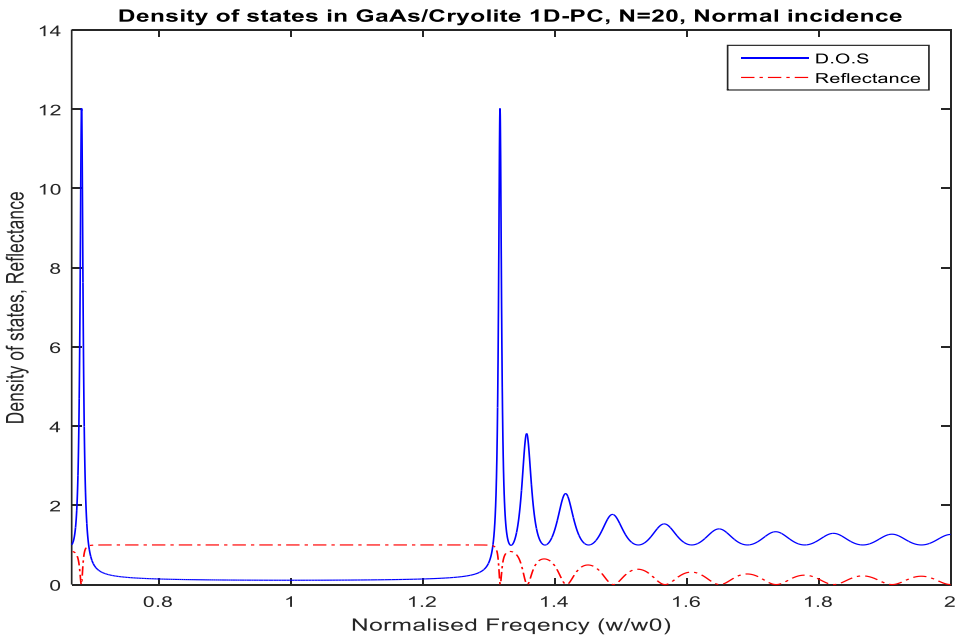
Density of states in GaAs/Cryolite 1D-PC, N=20, Normal incidence
D.O.S
Reflectance
Density of states, Reflectance
Normalised Freqency (w/w0)
0
2
4
6
8
10
12
14
0.8
1
1.2
1.4
1.6
1.8
2

(c)

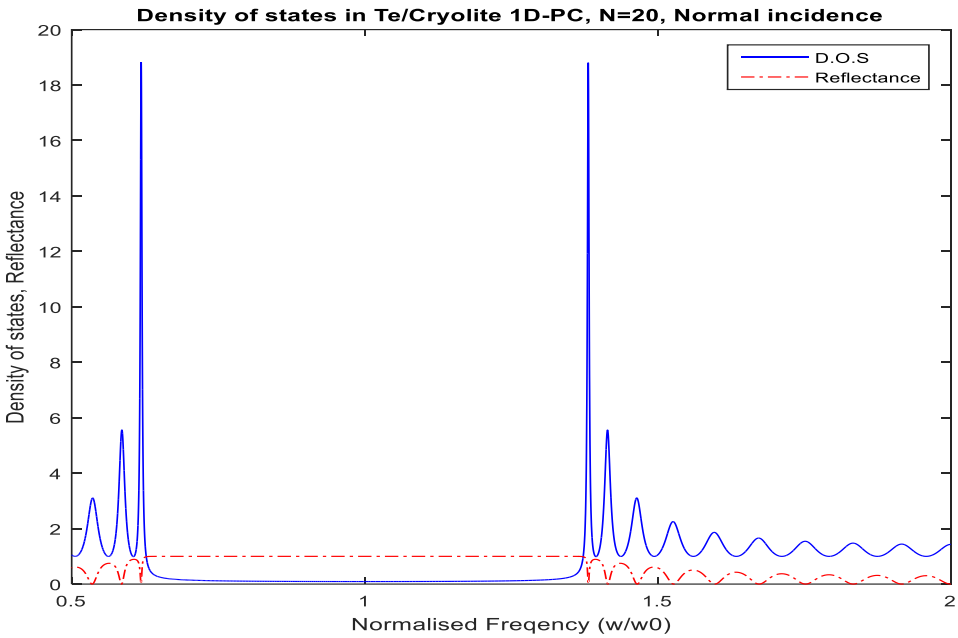
Density of states in Te/Cryolite 1D-PC, N=20, Normal incidence
D.O.S
Reflectance
Density of states, Reflectance
Normalised Freqency (w/w0)
0
2
4
6
8
10
12
14
16
18
20
0.5
1
1.5
2

(d)

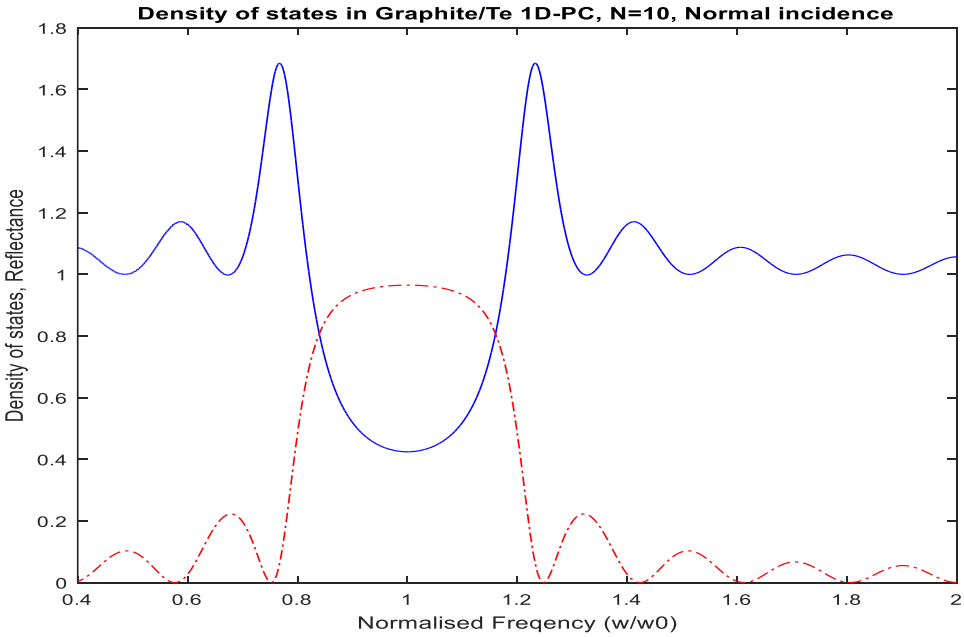
Density of states in Graphite/Te 1D-PC, N=10, Normal incidence
Density of states, Reflectance
Normalised Freqency (w/w0)
0
0.2
0.4
0.6
0.8
1
1.2
1.4
1.6
1.8
0.4
0.6
0.8
1
1.2
1.4
1.6
1.8
2

(e)

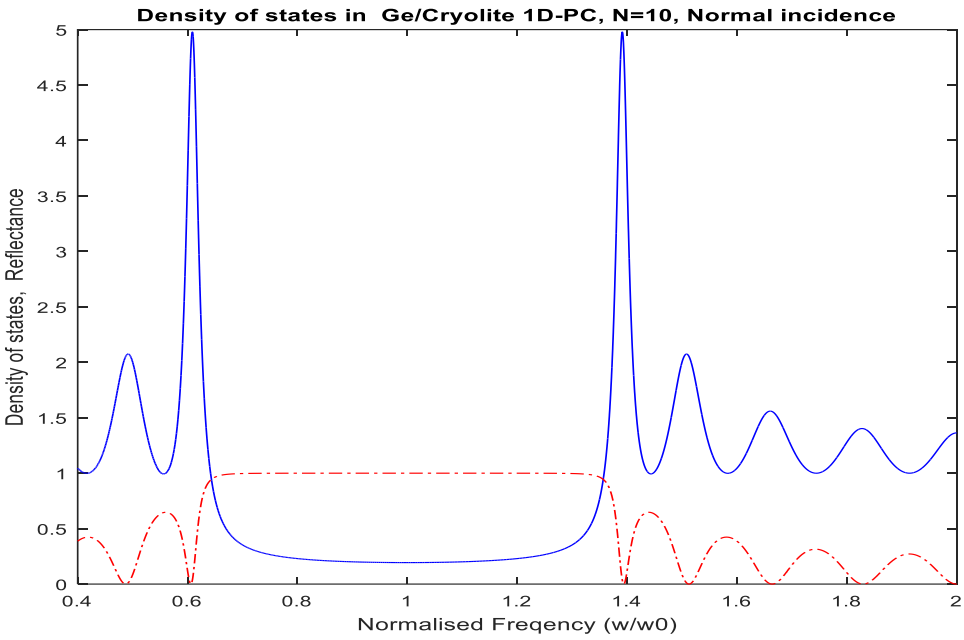


(f)

Figure (2.19): The density of states in 1DPC (a) ZnO/$SiO_2$ (b) Si / $SiO_2$ (c) GaAs/Cryolite (d) Te/ Cryolite (e) Graphite /Te (f) Ge/ Cryolite , for N = 20 and normal incidence.

## 2.5 EFFECTIVE INDEX AND GROUP VELOCITY

Photonic crystal devices which work on the principle of band gap edges have greater advantages over conventional waveguides because they offer very high operating speed, greater lifetime, tolerance to temperature fluctuations, and capability of high repetition rates. All light sources in actual practice are wave-packets and have some frequency spread. When we define effective index in terms of group velocity we get some very interesting results. For example the effective index of refraction becomes negative for certain frequency ranges and it becomes zero at some points and it even becomes much higher than the constituent refractive index of the two mediums($n_1$ and $n_2$). This concept of group velocity lead to lasing without inversion [2.13-2.14]. By using the concept of group velocity some very interesting results were obtained which show potential applications of PBG materials in photonic technology.

From the dispersion relation Eq. (2.61), we obtain the group velocity $(v_g)$ as

$$v_g = \left(\frac{d\omega}{dk}\right) = \left(\frac{dk}{d\omega}\right)^{-1} \tag{2.66}$$

Using Eq. (2.60) we can write

$$v_g = \frac{\left[1 - \left[\cos A \cos B - \frac{1}{2}\eta \sin A \sin B\right]^2\right]^{1/2} \Lambda}{\cos A \sin B \left[\left(\frac{n_2 d_2}{c}\right) + \frac{1}{2}\left(\frac{n_1 d_1}{c}\right)\eta\right] + cos\, B\, sin\, A \left[\left(\frac{n_1 d_1}{c}\right) + \frac{1}{2}\left(\frac{n_2 d_2}{c}\right)\eta\right]}, \quad (2.67)$$

where,

$$A = \frac{n_1 \omega d_1}{c}, \qquad B = \frac{n_2 \omega d_2}{c}, \qquad \eta = \left(\frac{n_1}{n_2} + \frac{n_2}{n_1}\right), \qquad \Lambda = d_1 + d_2.$$

The expression for the effective index of refraction $(n_{eff})$ can be written as

$$n_{eff} = \frac{c}{v_g} \quad (2.68)$$

Using Eq. (2.68) and Eq. (2.69), we can write

$$n_{eff} = \frac{\cos A \sin B \left[\left(\frac{n_2 d_2}{c}\right) + \frac{1}{2}\left(\frac{n_1 d_1}{c}\right)\eta\right] + cos\, B\, sin\, A \left[\left(\frac{n_1 d_1}{c}\right) + \frac{1}{2}\left(\frac{n_2 d_2}{c}\right)\eta\right]}{\left[1 - \left[\cos A \cos B - \frac{1}{2}\eta \sin A \sin B\right]^2\right]^{1/2}} \left(\frac{c}{\Lambda}\right) \quad (2.69)$$

The variation of normalised group velocity with the normalised frequency is shown in Fig. (2.20) for Si/SiO2 with N=10 and normal incidence. The comparative study of variation of normalised group velocity in various 1DPC's is shown in Fig.( 2.21) . We have found the normalised group velocity drops to minimum value at the band gap edges.

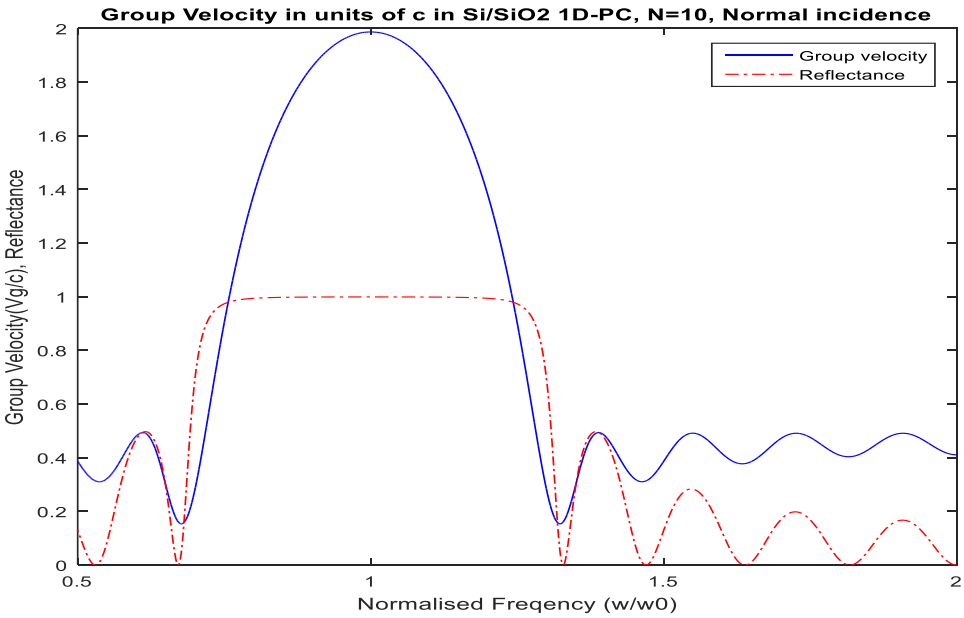


Figure (2.20): The group velocity in Si / $SiO_2$ 1D-PC for N = 10 and normal incidence, $n_1$=3.42, $n_2$=1.45, $d_1$=58.48 nm, $d_2$= 137.93 nm

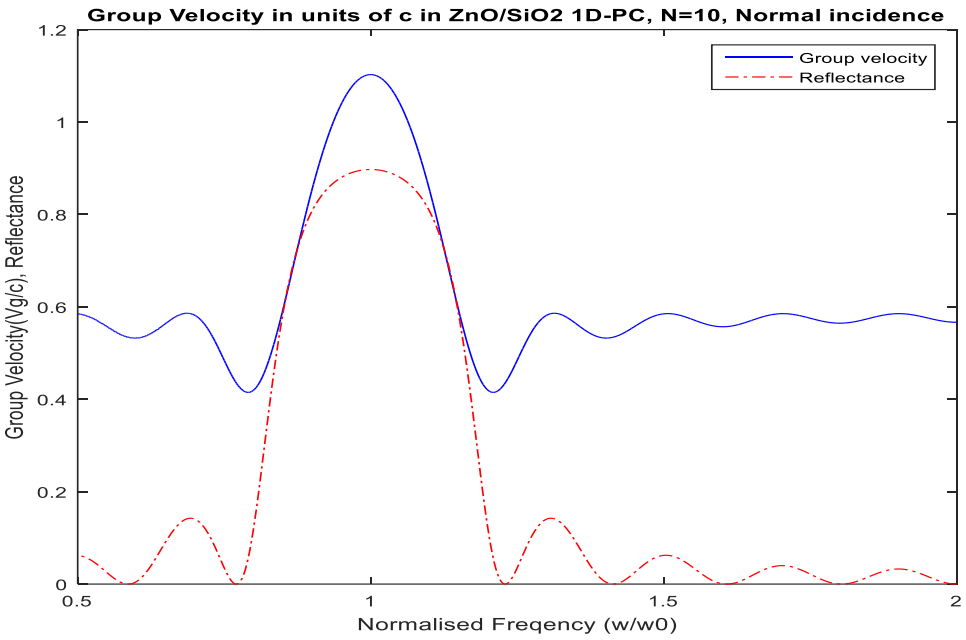
Group Velocity in units of c in ZnO/SiO2 1D-PC, N=10, Normal incidence
Group velocity
Reflectance
Group Velocity(Vg/c), Reflectance
Normalised Freqency (w/w0)
0
0.2
0.4
0.6
0.8
1
1.2
0.5
1
1.5
2

(a)

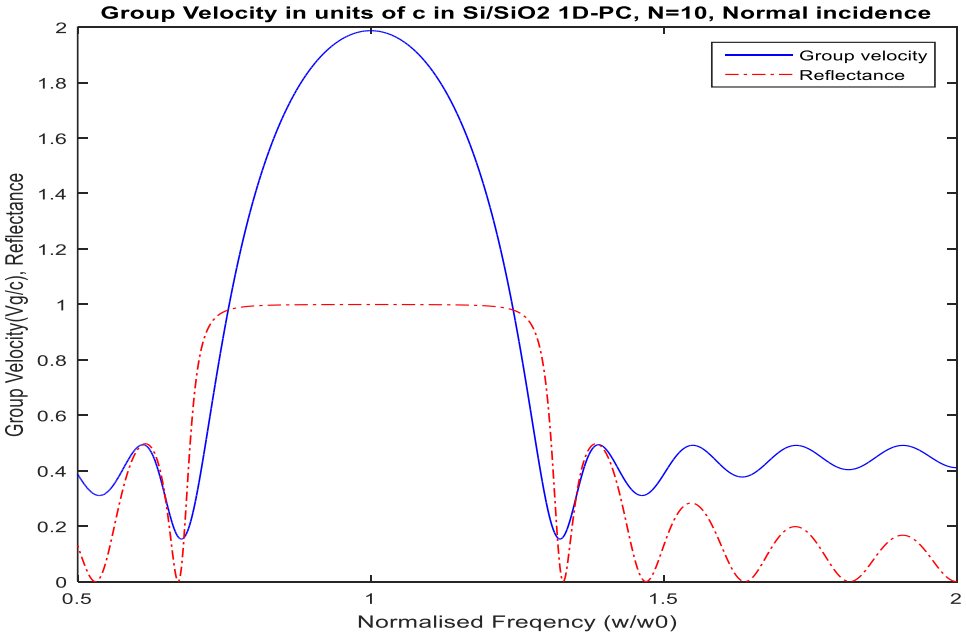
Group Velocity in units of c in Si/SiO2 1D-PC, N=10, Normal incidence
Group velocity
Reflectance
Group Velocity(Vg/c), Reflectance
Normalised Freqency (w/w0)
0
0.2
0.4
0.6
0.8
1
1.2
1.4
1.6
1.8
2
0.5
1
1.5
2

(b)

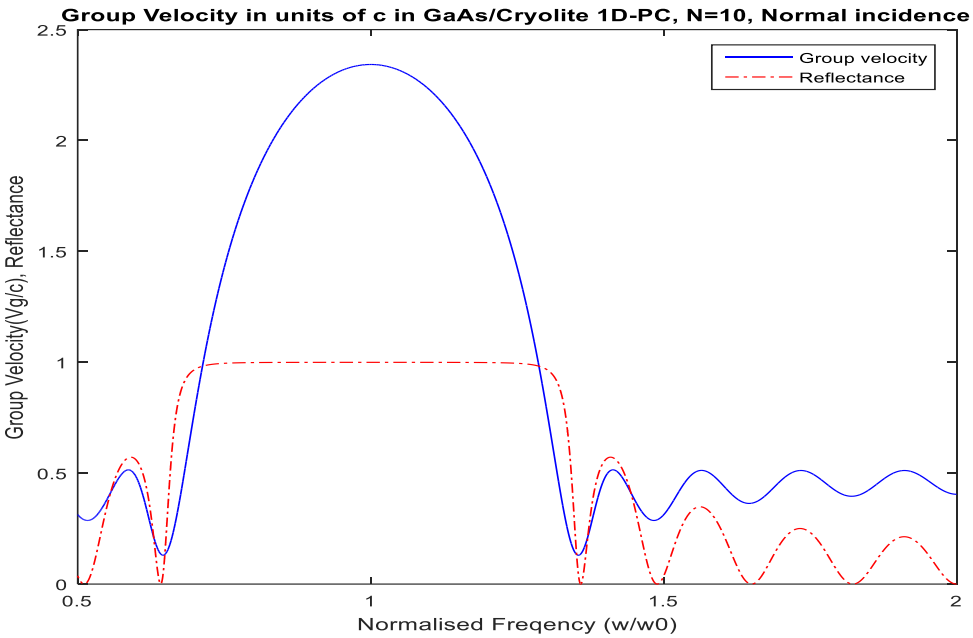
Group Velocity in units of c in GaAs/Cryolite 1D-PC, N=10, Normal incidence
Group velocity
Reflectance
Group Velocity(Vg/c), Reflectance
Normalised Freqency (w/w0)
0
0.5
1
1.5
2
2.5
0.5
1
1.5
2

(c)

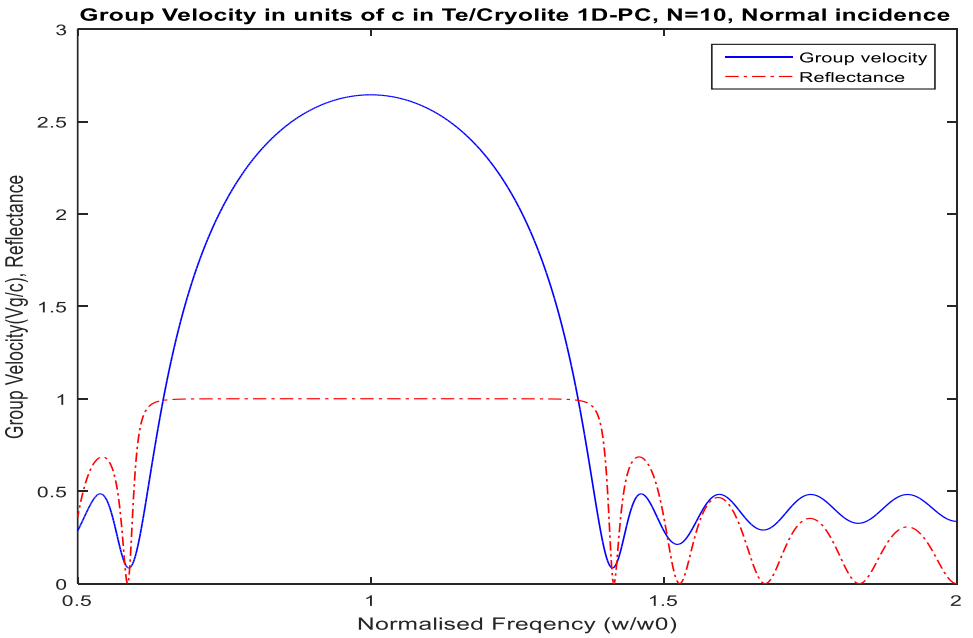
Group Velocity in units of c in Te/Cryolite 1D-PC, N=10, Normal incidence
Group velocity
Reflectance
Group Velocity(Vg/c), Reflectance
Normalised Freqency (w/w0)
0
0.5
1
1.5
2
2.5
3
0.5
1
1.5
2

(d)

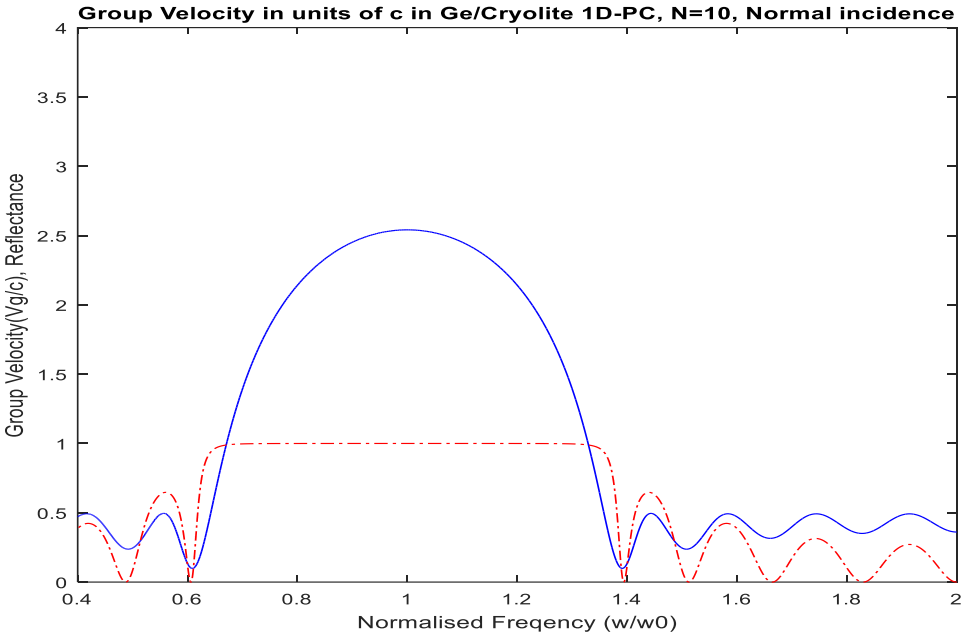


(e)

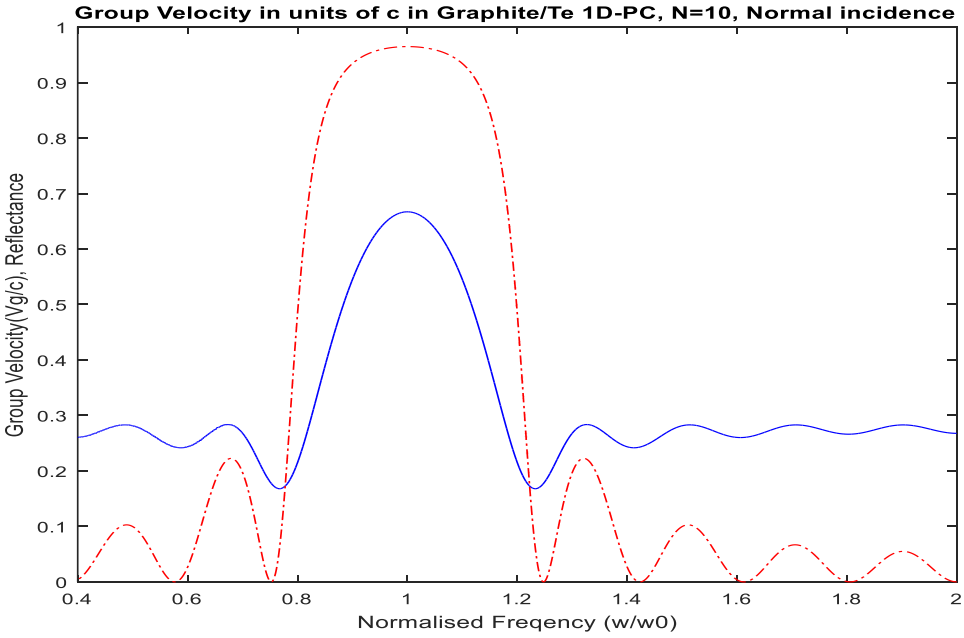


(f)

Figure (2.21): The normalised group velocity in 1DPC (a) $ZnO/SiO_2$ ,(b) Si / $SiO_2$ , (c) GaAs/Cryolite, (d) Te/ Cryolite, (e) Ge/ Cryolite, (f) Graphite /Te for N = 10 and normal incidence.

The variation of effective index of refraction with wavelength is shown in Fig. (2.22) for $Si/SiO_2$ with N=10 and normal incidence. The comparative study of variation of effective index of refraction in various 1DPC's is shown in Fig.( 2.23) . We have found that the effective index of refraction shows drastic variation at the band gap edges.

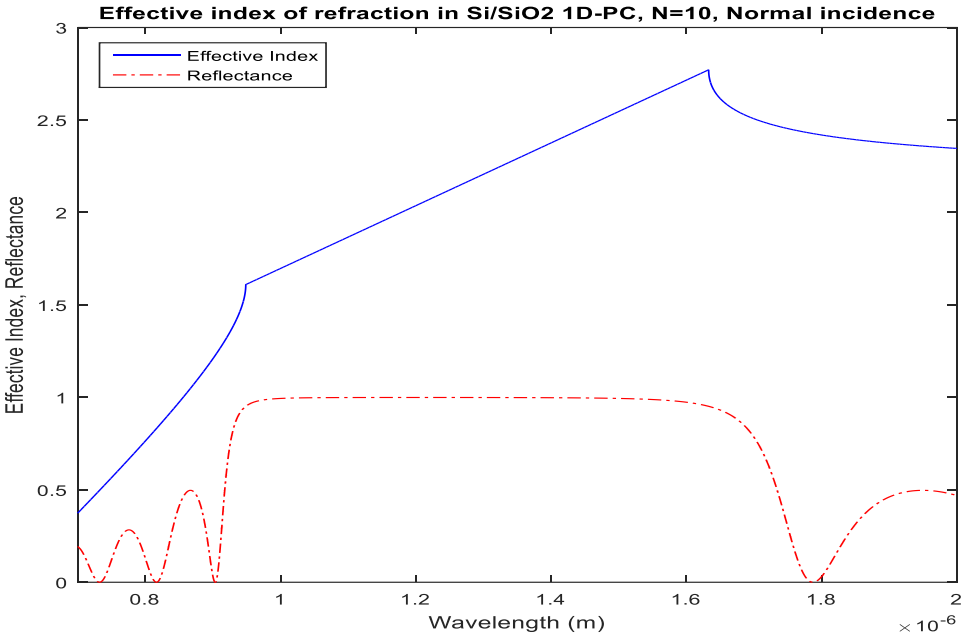


Figure (2.22): The effective index of refraction in $Si/SiO_2$ 1D-PC for N=10 and normal incidence, $n_1$=3.42, $n_2$=1.45, $d_1$=58.48 nm, $d_2$= 137.93 nm

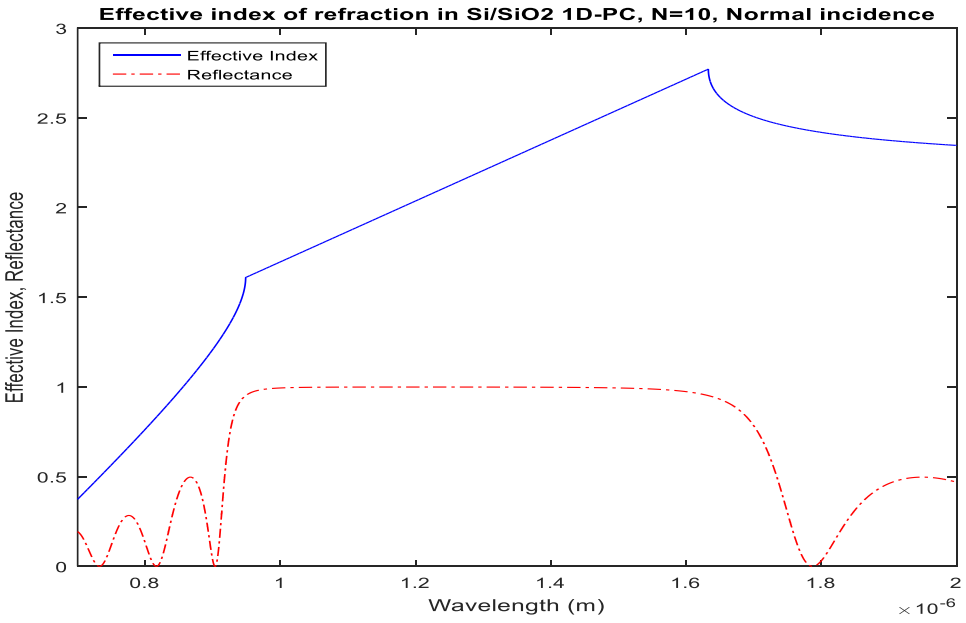


(a)

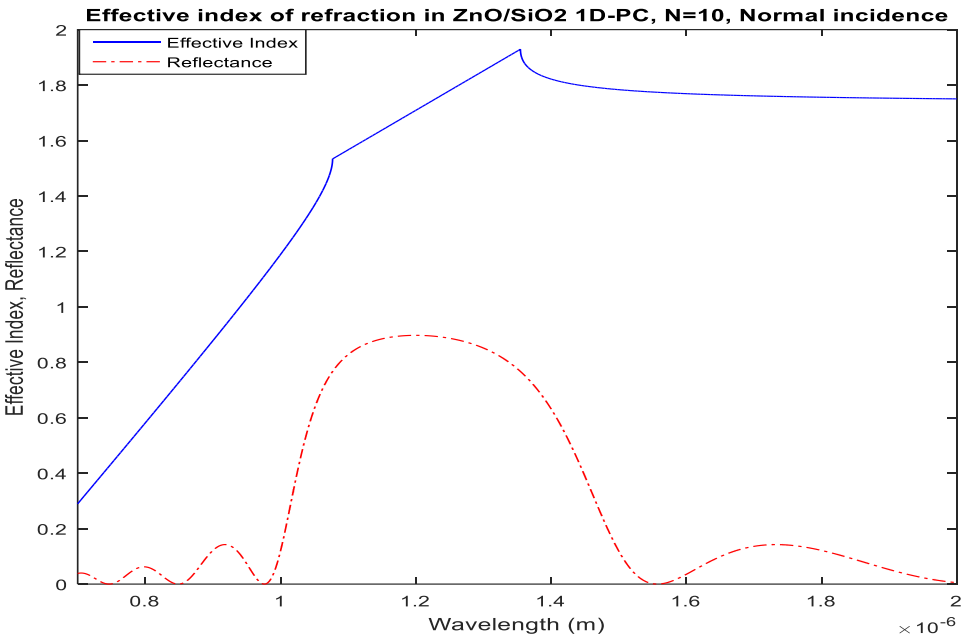
Effective index of refraction in ZnO/SiO2 1D-PC, N=10, Normal incidence
Effective Index
Reflectance
Effective Index, Reflectance
Wavelength (m)
×10^-6

(b)

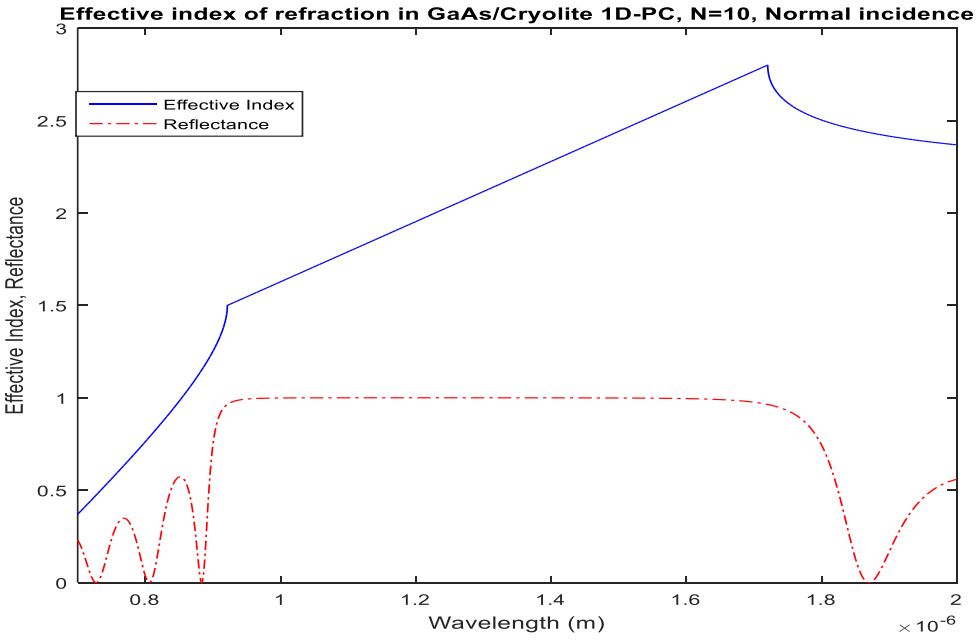
Effective index of refraction in GaAs/Cryolite 1D-PC, N=10, Normal incidence
Effective Index
Reflectance
Effective Index, Reflectance
Wavelength (m)
×10^-6

(c)

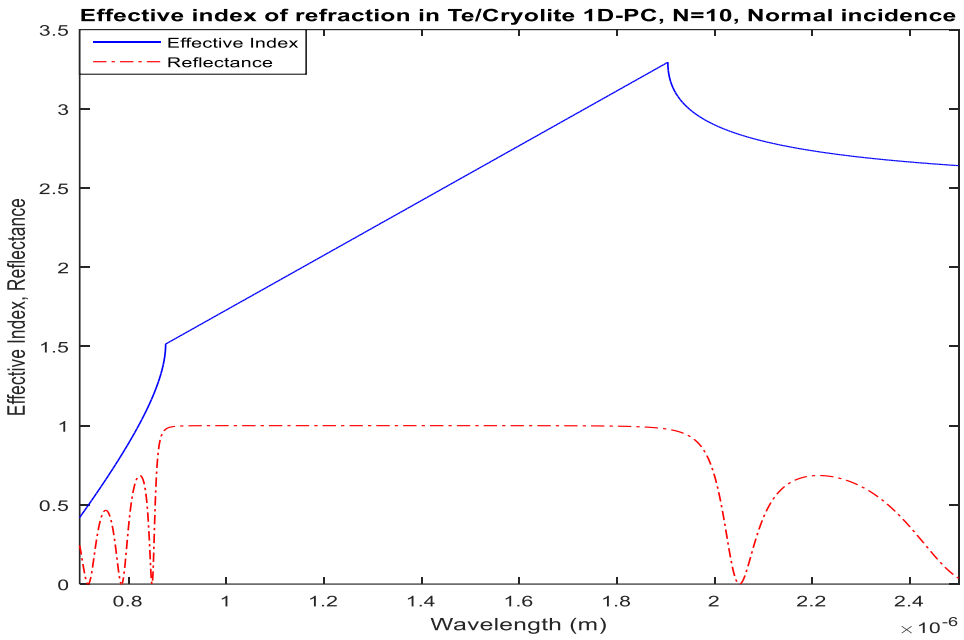
Effective index of refraction in Te/Cryolite 1D-PC, N=10, Normal incidence
Effective Index
Reflectance
Effective Index, Reflectance
Wavelength (m)
×10^-6

(d)

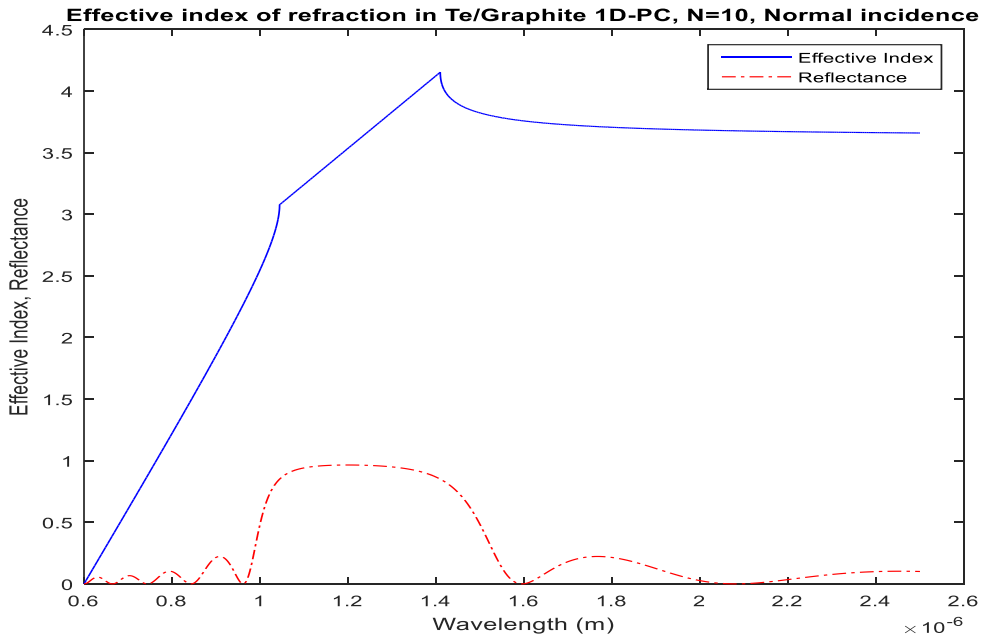
Effective index of refraction in Te/Graphite 1D-PC, N=10, Normal incidence
Effective Index
Reflectance
Effective Index, Reflectance
Wavelength (m)
×10^-6

(e)

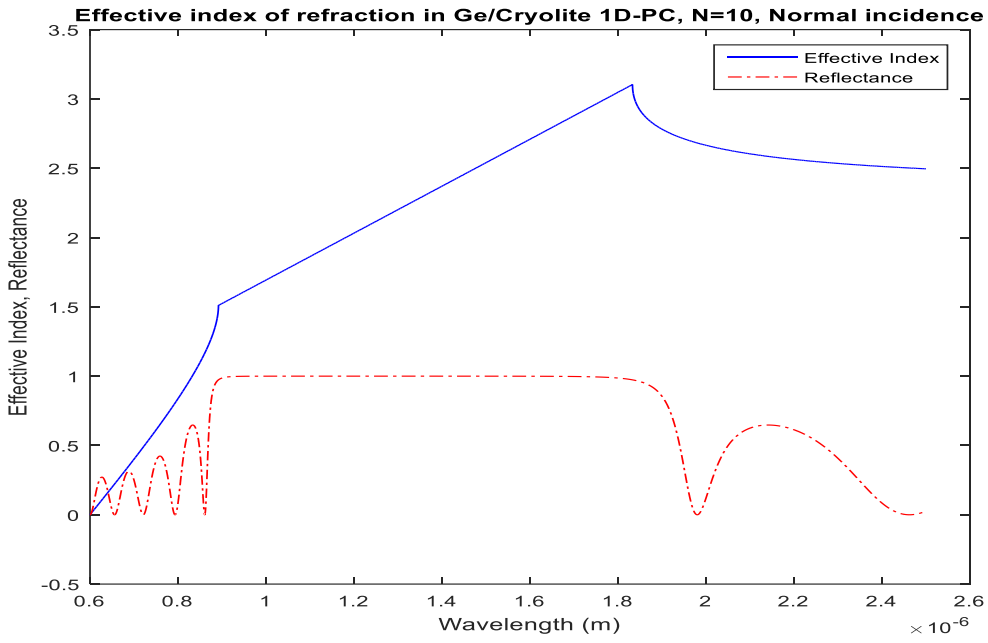


(f)

Figure (2.23): The effective index of refraction in 1DPC (a) Si / $SiO_2$, (b) ZnO/$SiO_2$ ,(c) GaAs/Cryolite, (d) Te/ Cryolite, (e) Graphite /Te, (f) Ge/ Cryolite, for N = 10 and normal incidence.

## 2.6 EFFECT OF REFRACTIVE INDEX CONTRAST ON REFLECTION SPECTRUM OF 1DPC

The variation in the PBG due to change in refractive index contrast for 1DPCs has been simulated and shown in Table (2.1). It was found from the observed results that the refractive index contrast is an important design parameter for optical characterisation of 1D-PC. The increase in refractive index contrast increases the width of PBG, causing red shift in upper wavelength edge ($\lambda_U$) of PBG and blue shift in the lower wavelength edge ($\lambda_L$) of PBG. The reflection spectrum of 1DPC's corresponding to Table (2.1) is shown in Fig. (2.24).

Table-2.1: Variation of PBG with refractive index contrast for N=20 and normal incidence

| **Material (N=20)** | **$n_1$** | **$n_2$** | **$d_1$ (nm)** | **$d_2$ (nm)** | **$\lambda_L$ (nm)** | **$\lambda_U$ (nm)** | **PBG (nm)** |
|---|---|---|---|---|---|---|---|
| $ZnO/SiO_2$ | 2.08 | 1.45 | 96.15 | 137.93 | 719 | 901 | 182 |
| $TiO_2/SiO_2$ | 2.67 | 1.45 | 74.90 | 137.93 | 673.29 | 984.86 | 311.57 |
| $Si/SiO_2$ | 3.42 | 1.45 | 58.48 | 137.93 | 633.58 | 1091.16 | 457.58 |
| $Si/ Na_3AlF_6$ | 3.42 | 1.34 | 58.48 | 149.25 | 621.76 | 1122.25 | 500.49 |
| $GaAs/ Na_3AlF_6$ | 3.6 | 1.34 | 55.55 | 149.25 | 614.83 | 1143.49 | 528.66 |
| $Ge/Na_3AlF_6$ | 4.2 | 1.34 | 47.61 | 149.25 | 596.36 | 1214.43 | 618.07 |
| $Te/ Na_3AlF_6$ | 4.6 | 1.34 | 43.47 | 149.25 | 585.59 | 1267.06 | 681.47 |

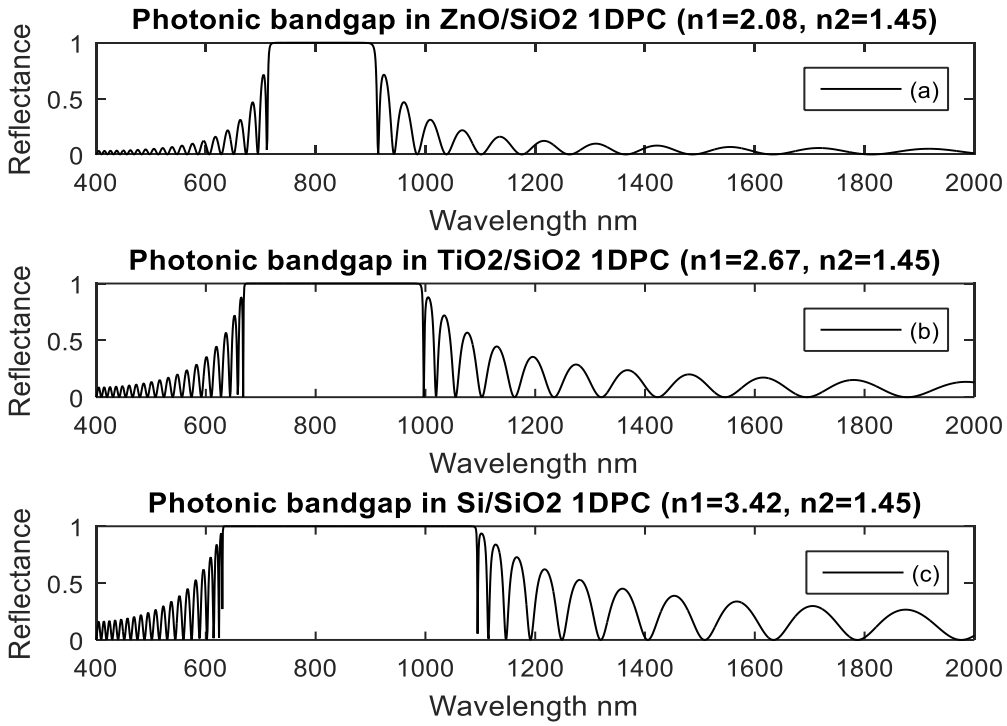

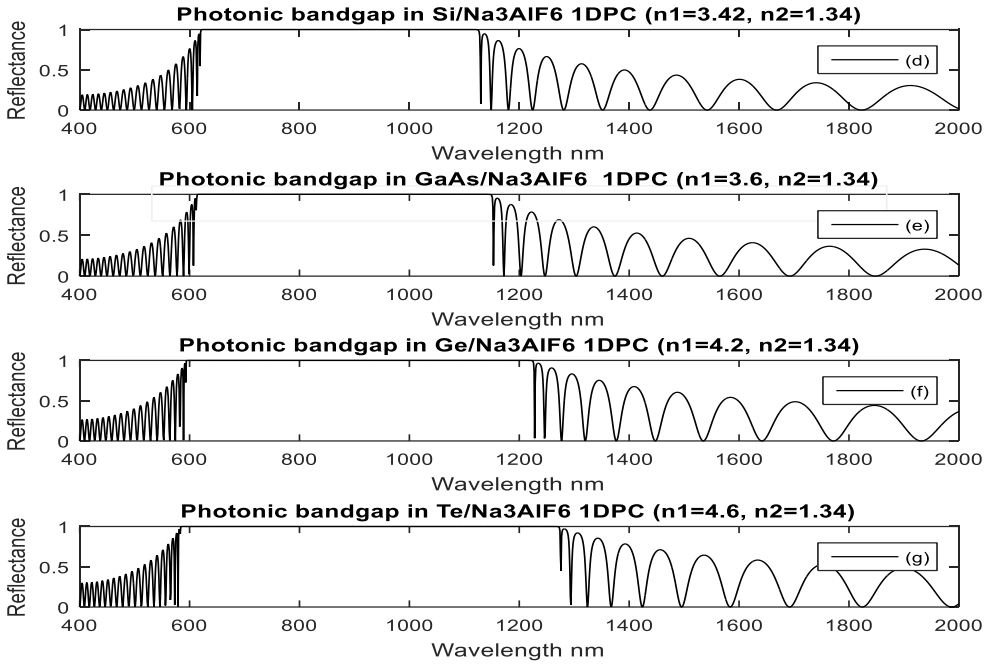


Figure (2.24): Effect of refractive index contrast on reflection spectrum of 1DPC for N=20, and θ=0°, (a) $ZnO/SiO_2$ , (b) $TiO_2/SiO_2$ , (c) $Si/SiO_2$, (d) $Si/Na_3AlF_6$ , (e) $GaAs/Na_3AlF_6$ , (f) $Ge/Na_3AlF_6$ , (g) $Te/Na_3AlF_6$.

## 2.7 EFFECT OF OBLIQUE INCIDENCE ON REFLECTION SPECTRUM OF 1DPC

The effect of angle of incidence on the PBG is studied for 20 layered (Graphite-Te) 1DPC structures. It was found that as the angle of incidence increases, there is blue shift in upper PBG edge ($\lambda_U$) and lower PBG edge ($\lambda_L$) for both TE and TM modes [63]. The width of PBG for TE modes increases whereas that for TM modes decreases with increase in the angle of incidence as shown in Table-2.2. The value of $n_1$ for graphite is 2.87 and that of $n_2$ for Te is 4.6 and the corresponding thickness of layers are $d_1$=69.7 nm, $d_2$=43.5 nm respectively from quarter wave stack condition [1.2]. The reflection spectrum for TE modes and TM modes for N=20 is shown in Fig. (2.25) and Fig. (2.26) respectively.

Table-2.2: Variation of PBG with angle of incidence for both polarizations. Graphite-Te 1D-PC and N=20.

| [Graphite-Te] N=20 | TE | | | TM | | |
|---|---|---|---|---|---|---|
| | Lower Bandgap Edge $\lambda_L$(nm) | Upper Bandgap Edge $\lambda_U$(nm) | Bandgap (nm) | Lower Bandgap Edge $\lambda_L$(nm) | Upper Bandgap Edge $\lambda_U$(nm) | Bandgap (nm) |
| $\Theta=0^0$ | 697 | 939 | 242 | 697 | 939 | 242 |
| $\Theta=30^0$ | 688 | 932 | 244 | 691 | 926 | 235 |
| $\Theta=60^0$ | 669 | 919 | 250 | 680 | 899 | 219 |
| $\Theta=89^0$ | 660 | 912 | 252 | 674 | 885 | 211 |

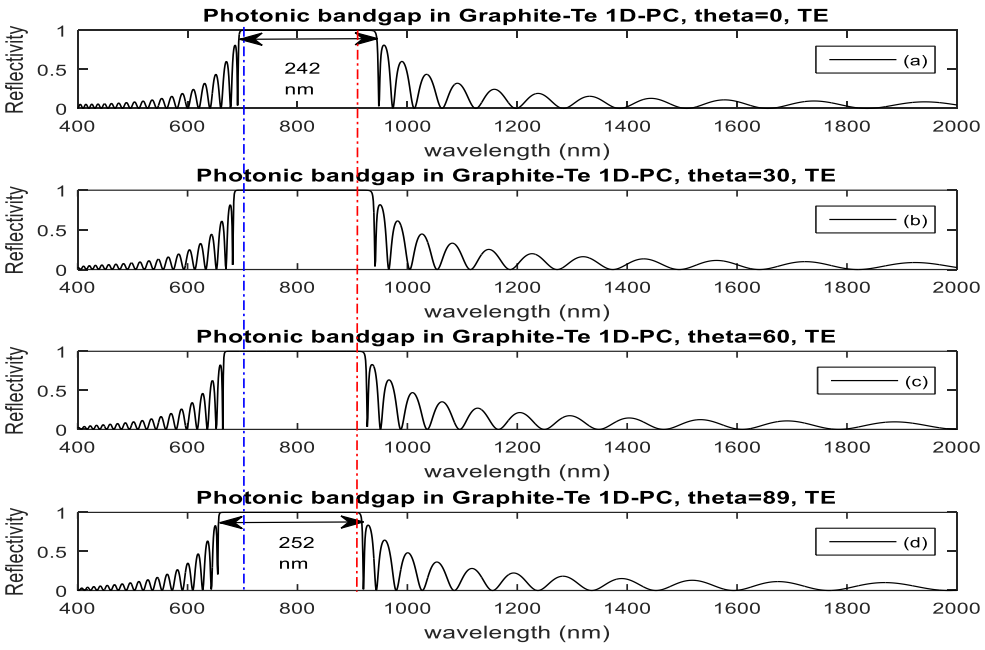

Figure (2.25): The reflectance spectra for [Graphite-Te] for TE modes for various incident angles (a) θ=0° (b) θ=30°, (c) θ= 60°, (d) θ=89°

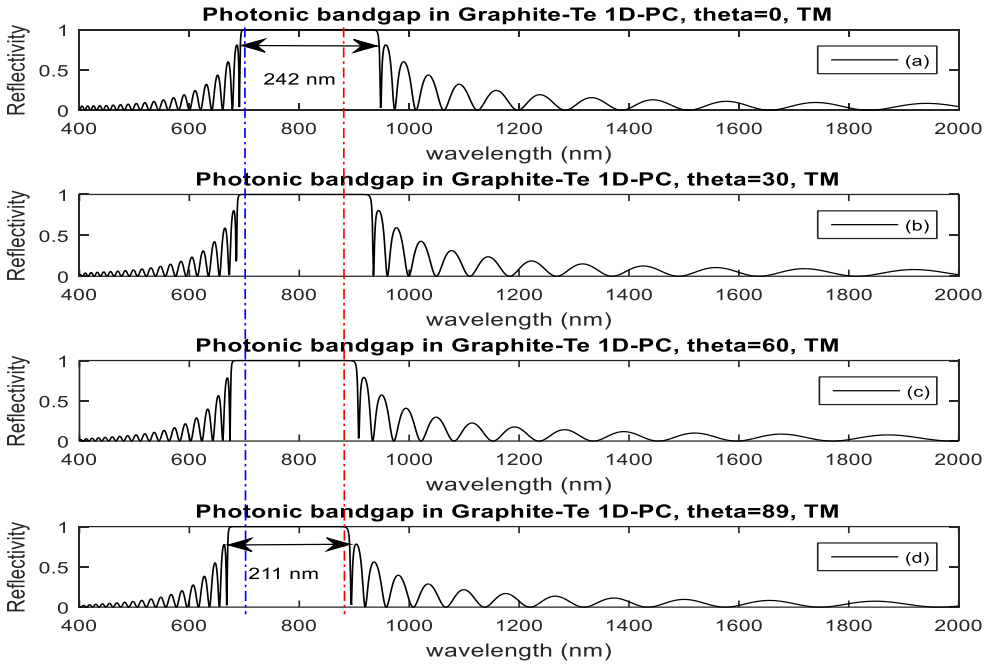


Figure (2.26): The reflectance spectra for [Graphite-Te] for TM modes for various incident angles (a) θ=0° (b) θ=30°, (c) θ= 60°, (d) θ=89°

## 2.8 EFFECT OF AMBIENT MEDIUM ON REFLECTION SPECTRUM OF 1DPC

The role of ambient medium in the spectral response is simulated for 20 layered Si/$SiO_2$ 1D-PC structure. There was a blue shift in lower and upper PBG edges for both TE and TM modes with the increase in refractive index of ambient medium as shown in Table-2.3. The corresponding reflection spectrum for TE modes and TM modes is shown in Fig. (2.27) and Fig. (2.28), respectively.

Table-2.3: Variation of PBG with refractive index of ambient medium for both polarizations, θ=30°.

| $Si/SiO_2$ N=20 | TE | | | TM | | |
|---|---|---|---|---|---|---|
| | Lower Bandgap Edge (nm) | Upper Bandgap Edge (nm) | Bandgap (nm) | Lower Bandgap Edge (nm) | Upper Bandgap Edge (nm) | Bandgap (nm) |
| $n_a$=1 | 602.6 | 1071 | 468.4 | 617.3 | 1028 | 410.7 |
| $n_a$=1.2 | 590 | 1063 | 473 | 611 | 999 | 388 |
| $n_a$=1.4 | 573 | 1054 | 481 | 603 | 965 | 362 |
| $n_a$=1.6 | 554 | 1043 | 489 | 594 | 924 | 330 |

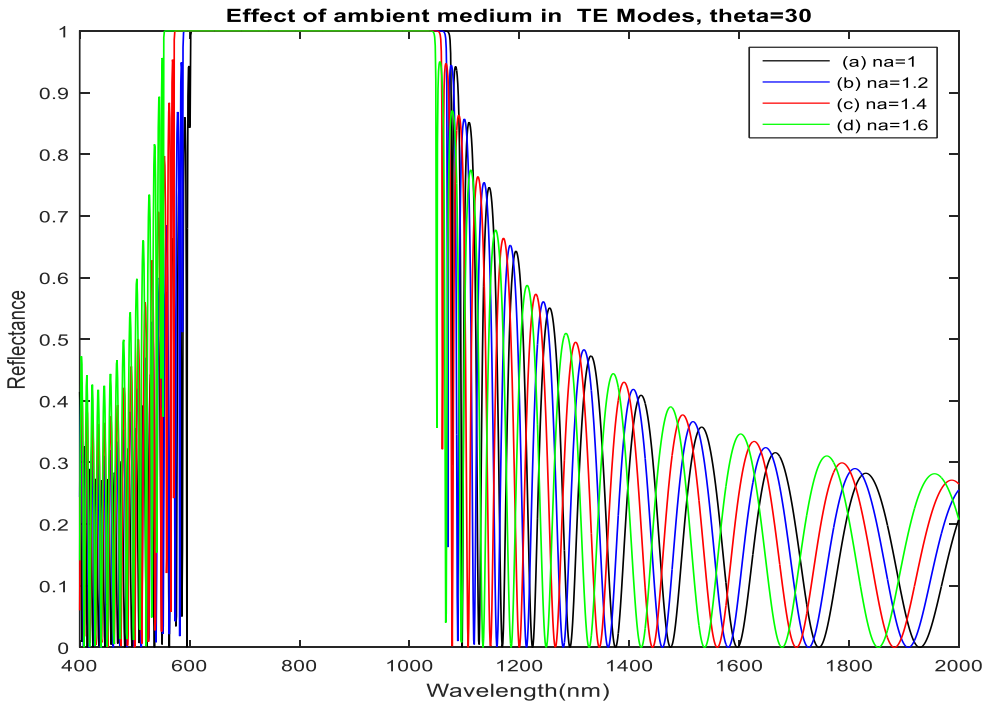

Figure (2.27): Reflection band for $Si/SiO_2$ 1D-PC with N=20, TE, θ=30°. The incident ambient medium varies as (a) $n_a$=1 (b) $n_a$=1.2 (c) $n_a$=1.4 (d) $n_a$=1.6.

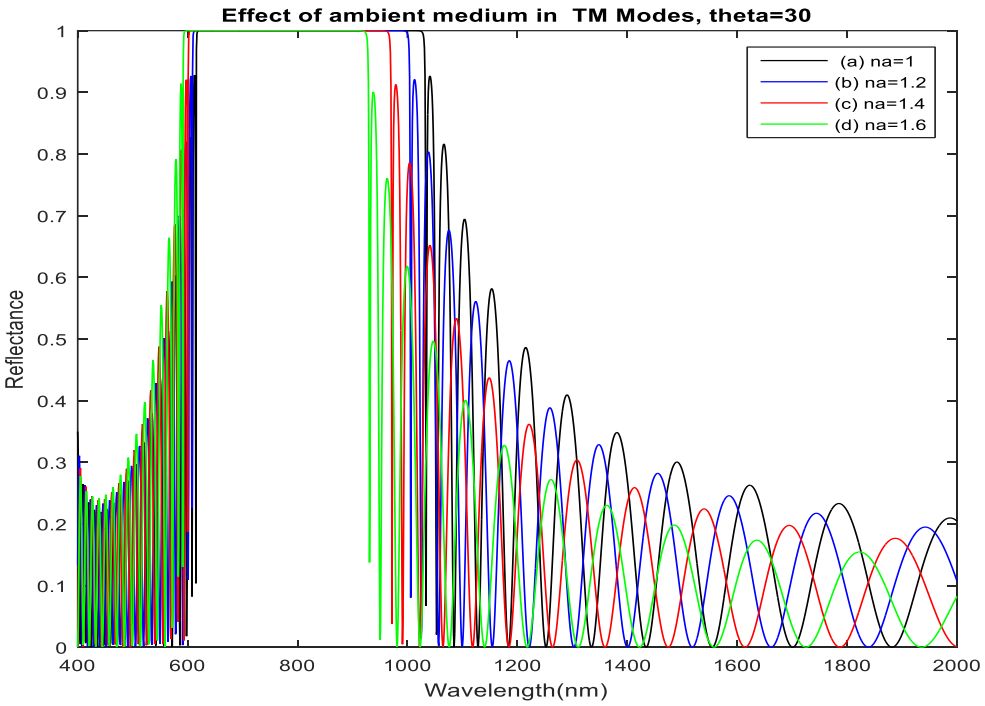


Figure (2.28): Reflection band for $Si/SiO_2$ 1D-PC with N=20, TM, θ=30° . The incident ambient medium varies as (a) $n_a$=1 (b) $n_a$=1.2 (c) $n_a$=1.4 (d) $n_a$=1.6.

## 2.9 EFFECT OF NUMBER OF LAYERS ON REFLECTION SPECTRUM OF 1DPC

Investigations on the impact of number of layers of 1DPC on the spectral response is carried out for $Si/SiO_2$ 1DPC structure with number of layers varying from N=2, 4, 6, 10 and it was found that as the number of layers increases, the PBG narrows with increase in 100% reflection regions as shown in Fig. (2.29).

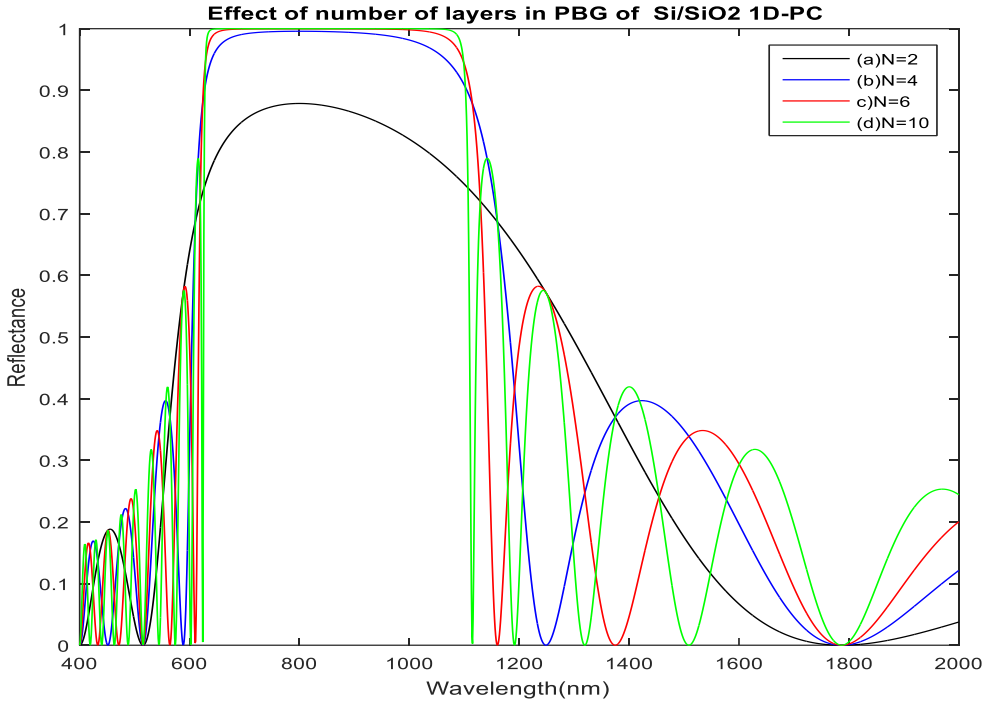


Figure (2.29): Reflection band for $Si/SiO_2$ 1D-PC at normal incidence for TE modes at (a) N=2 (b) N=4 (c) N=6 (d) N=10

**CONCLUSION:**

PBG is simulated by using dispersion relation and reflection spectrum for 20 layered 1D-PCs with constituent layers mentioned as in Table-2.1 at central wavelength of 800 nm and normal incidence. The analytical expression for DOS is obtained and the optical response of 1DPCs is analysed through DOS for all 1DPCs mentioned in Table-2.1. The variation of group velocity and effective refractive index is studied for all 1DPCs mentioned in Table-2.1. The variation in the PBG due to change in refractive index contrast for 1D-PCs has been simulated and shown in Table 2.1. It was found from the observed results that the refractive index contrast is an important design parameter for optical characterisation of 1DPC. The increase in refractive index contrast increases the width of PBG, causing red shift in upper wavelength edge of PBG and blue shift in the lower wavelength edge of PBG. The effect of angle of incidence on the PBG is studied for 20 layered (Graphite-Te) 1DPC structures. It was found as the angle of incidence increases, there is blue shift in upper PBG edge and lower PBG edge for both TE and TM modes. The width of PBG for TE modes increases whereas that for TM modes decreases with increase in the angle of incidence as shown in Table-2.2. The role of ambient medium in the spectral response is simulated for 20 layered $Si/SiO_2$ 1D-PC structure. There was a blue shift in lower and upper PBG edges for both TE and TM modes with the increase

in refractive index of ambient medium as shown in Table-2.3. Investigations on the impact of number of layers of 1D-PC on the spectral response is carried out for $Si/SiO_2$ 1DPC structure with number of layers varying from N=2, 4, 6, 10 and it was found that as the number of layers increases, the PBG narrows with increase in 100% reflection regions as shown in Fig. (2.29).

# CHAPTER- III

# OMNIDIRECTIONAL REFLECTION BAND IN 1DPC

## INTRODUCTION

This chapter deals with one of the applications of 1DPC as ODR. An ODR is a perfect reflector which has high reflectance in a specific wavelength range irrespective of the incident angle and the state of polarization. Depending on the potential usage the ODR's can be designed in the wavelength range of interest. One of the applications of ODR is in coating of an enclosure which can work as optical cavity. Other applications are in designing of low loss broadband waveguide and efficient heat barriers in thermoelectric devices [3.1-3.4].

Metallic mirrors reflect over broad range of frequencies at arbitrary incident angles and are widely used in imaging, solar energy collection and laser cavities. However, these mirrors have absorption losses at infrared and optical frequencies. On the other hand, the dielectric mirrors are low loss and their ability to reflect light for arbitrary angle of incidence will depend on the existence of complete three 3D bandgap which is a function of periodicity in all the three dimensions. The necessary condition for ODR at a given frequency is the absence of propagating states existing inside the light cone of ambient medium [3.5-3.7].

There is no difference in TE modes and TM modes for normal incidence however at increasingly oblique incidence, the width of TE bandgap increases whereas that of TM modes decreases. There is also considerable blue shift in the central wavelength of bandgap region. The criterion for existence of ODR can now be stated as the occurrence of frequency overlap of bandgap region for TE modes at normal incidence and TM modes at 90° incidence. The thickness of the layers in dielectric mirror is determined by the quarter wave stack condition.

## 3.1. DESIGNING OF ODR WITH 1DPC

We consider a multi-layered 1DPC structure with 20 alternating layers of Si and $SiO_2$ coupled to a homogenous ambient medium $n_0$. The refractive index profile of the structure is shown in Fig. 3.1. The refractive index ($n_1$) and thickness ($d_1$) of Si layer is taken as 3.42 and 58.48 nm and that for $SiO_2$ layer is 1.45 ($n_2$) and 138 nm ($d_2$), respectively from the quarter wave stack condition. The periodicity of structure is $d = (d_1+d_2)$.

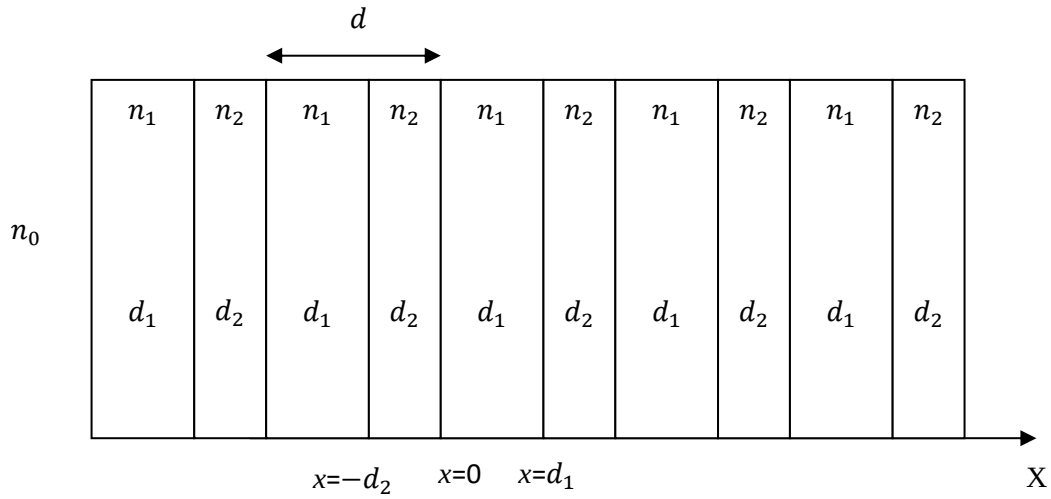


Figure (3.1): Refractive index profile of 1D-PC structure

The variation of PBG in the structure is shown in Table 3.1 at various angles of incidence for both TE and TM modes. The width of TE bandgap increases from 458 nm to 511 nm with increase in angle of incidence. However, the width of TM bandgap decreases from 458 nm to 246 nm. There is considerable blue shift in the band edges of bandgap in both TE and TM modes as shown in Fig. 3.2 (a & b). The ODR band is between the lower bandgap edge at normal incidence for TE mode (633 nm) and upper bandgap edge at θ=90° for TM mode (818 nm) as shown in Fig. 3.3. The proposed structure gives 100% reflection within a wide range of wavelengths in the visible – NIR region and can be used effectively in wavelength filters, optical resonators and mirrors in desired wavelength range.

Table (3.1): ODR in $Si/SiO_2$ 1DPC, $n_1 = 3.42$, $n_2 = 1.45$, $d_1 = 58.48$ nm, $d_2 = 138$ nm, N = 20

| **$Si/SiO_2$** | **TE** | | | **TM** | | |
|---|---|---|---|---|---|---|
| N=20 | Lower Bandgap Edge (nm) | Upper Bandgap Edge (nm) | Bandgap (nm) | Lower Bandgap Edge (nm) | Upper Bandgap Edge (nm) | Bandgap (nm) |
| Θ=0º | 633 | 1091 | 458 | 633 | 1091 | 458 |
| Θ=30º | 603 | 1071 | 468 | 618 | 1027 | 409 |
| Θ=60º | 540 | 1036 | 496 | 587 | 893 | 306 |

| | | | | | | |
|---|---|---|---|---|---|---|
| Θ=90º | 507 | 1018 | 511 | 572 | 818 | 246 |
| ODR= 818 nm-633 nm= 185 nm | | | | | | |

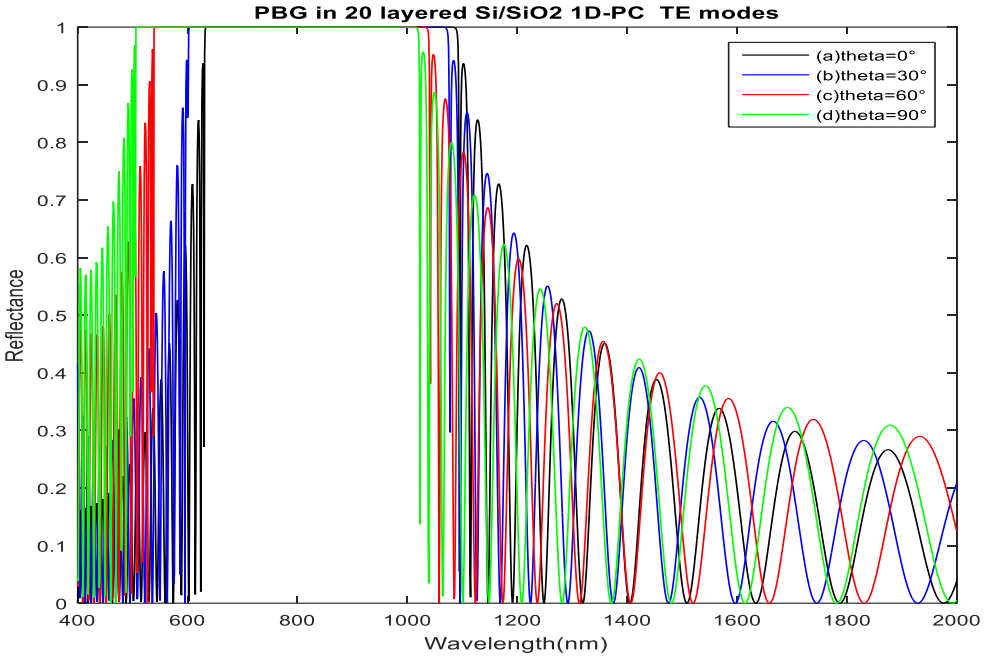


Figure (3.2) (a): The reflectance spectra for $Si/SiO_2$ 1DPC for TE modes at incident angles (a) θ = 0° (b) θ = 30° (c) θ = 60° (d) θ=90°

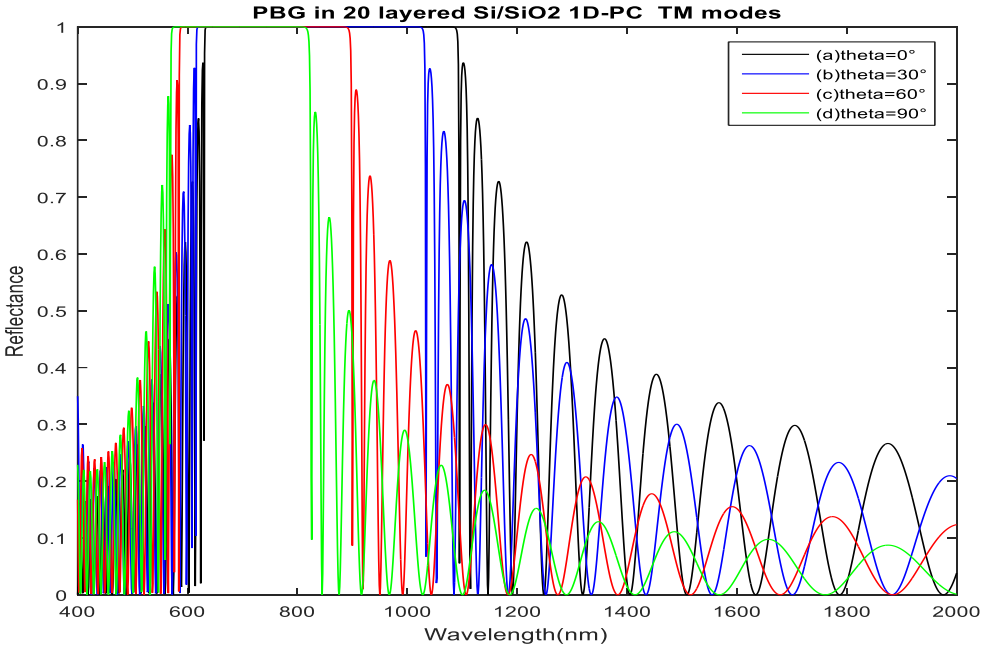


Figure (3.2) (b) The reflectance spectra for $Si/SiO_2$ 1DPC for TM modes at incident angles (a) θ = 0° (b) θ = 30° (c) θ = 60° (d) θ=90°

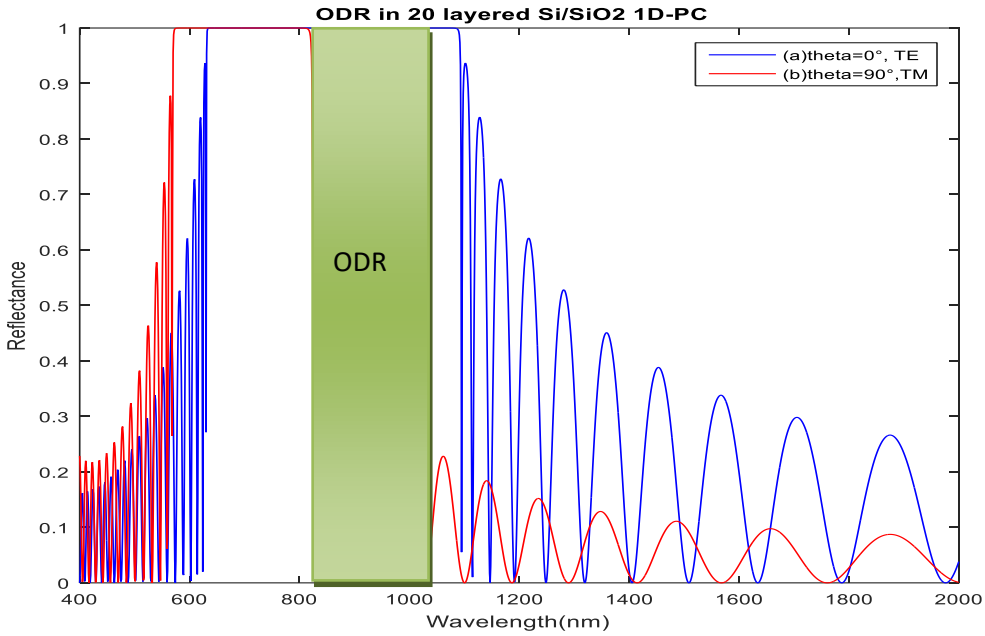


Figure (3.3): ODR in $Si/SiO_2$ 1D-PC for $n_1 = 3.42$, $n_2 = 1.45$, $d_1 = 58.48$ nm, $d_2 = 138$ nm and N = 20.

### 3.2 EFFECT OF REFRACTIVE INDEX CONTRAST ON ODR PROPERTY OF 1DPC

The increase in refractive index contrast $(n_1/n_2)$ increases the photon confinement in periodic refractive index profile structure. This increases the bandgap regions in both TE and TM modes. We have investigated the effect of refractive index contrast on the ODR property of 1DPC by considering four different 1DPC structures namely Si-$Na_3AlF_6$, GaAs-$Na_3AlF_6$, Ge-$Na_3AlF_6$, and Te-$Na_3AlF_6$. The thickness of each layer is calculated by quarter wave stack condition and the number of alternate layers in all 1D-PCs is taken as 20. The refractive index contrast of all four 1DPCs is shown in Table 3.2. We have calculated the PBG edges of all four 1DPCs for both TE and TM modes for normal incidence and $\theta = 90°$. The PBG is found to increase with increase in refractive contrast for both TE and TM modes. ODR is also found to increase with refractive index contrast as shown in Table 3.2. The variation of ODR with refractive index contrast is also shown in Fig. (3.4).

Table (3.2): Effect of refractive index contrast on ODR of 1D-PC for $N = 20$, for (a) Si-$Na_3AlF_6$ (b) GaAs-$Na_3AlF_6$ (c) Ge-$Na_3AlF_6$ (d) Te-$Na_3AlF_6$

| **N=20** | **$n_1$** | **$n_2$** | **$d_1$ (nm)** | **$d_2$ (nm)** | **TE** | | | | | **TM** | | | **ODR (nm)** |
|---|---|---|---|---|---|---|---|---|---|---|---|---|---|
| | | | | | Angle of incidence | Lower Band Edge (nm) | Upper Band Edge (nm) | Band gap (nm) | Angle of incidence | Lower Band Edge (nm) | Upper Band Edge (nm) | Band gap (nm) | |
| Si-$Na_3AlF_6$ | 3.42 | 1.34 | 58.48 | 149.25 | Θ=0º | 624 | 1123 | 499 | Θ=90º | 558 | 777 | 219 | 153 |
| GaAs-$Na_3AlF_6$ | 3.6 | 1.34 | 55.55 | 149.25 | Θ=0º | 616 | 1150 | 534 | Θ=90º | 551 | 794 | 243 | 178 |
| Ge-$Na_3AlF_6$ | 4.2 | 1.34 | 47.61 | 149.25 | Θ=0º | 600 | 1223 | 623 | Θ=90º | 537 | 846 | 309 | 246 |
| Te-$Na_3AlF_6$ | 4.6 | 1.34 | 43.47 | 149.25 | Θ=0º | 585 | 1271 | 686 | Θ=90º | 528 | 878 | 350 | 293 |

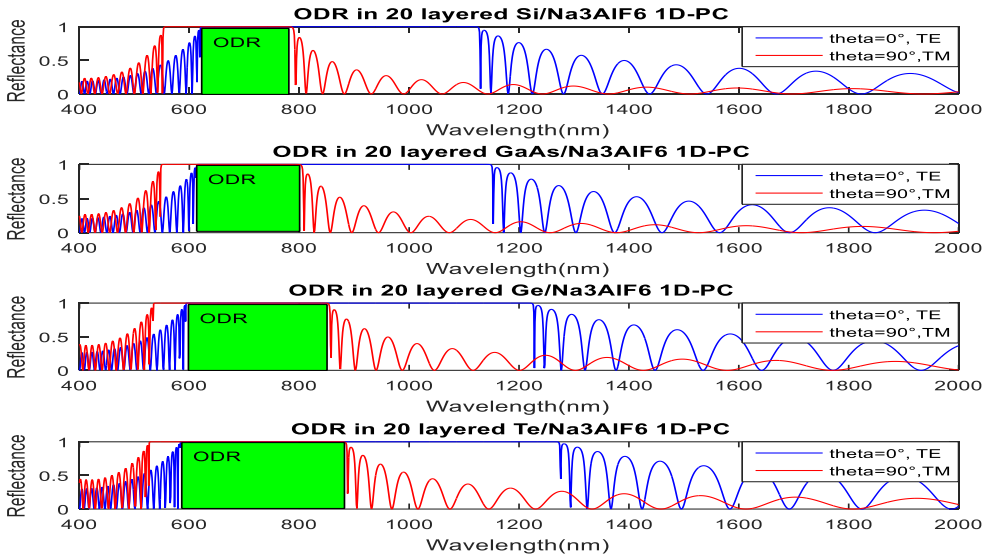


Figure (3.4): Effect of refractive index contrast on ODR of 1D-PC for $N = 20$, for (a) Si-$Na_3AlF_6$ (b) GaAs-$Na_3AlF_6$ (c) Ge-$Na_3AlF_6$ (d) Te-$Na_3AlF_6$

### 3.3 EFFECT OF AMBIENT MEDIUM ON ODR BAND

The effect of ambient medium on ODR is investigated with 20 layered Si-$SiO_2$ 1D-PC structure with variation of refractive index of ambient medium ($n_a$) from 1 to 1.6. We have found that ODR width decreases with increase in refractive index of ambient medium as shown in Fig. 3.5. Also the ODR band disappears as the refractive of ambient medium approaches near to the lower refractive index of 1D-PC structure. Ambient medium plays important role in designing ODR from 1DPC structures.

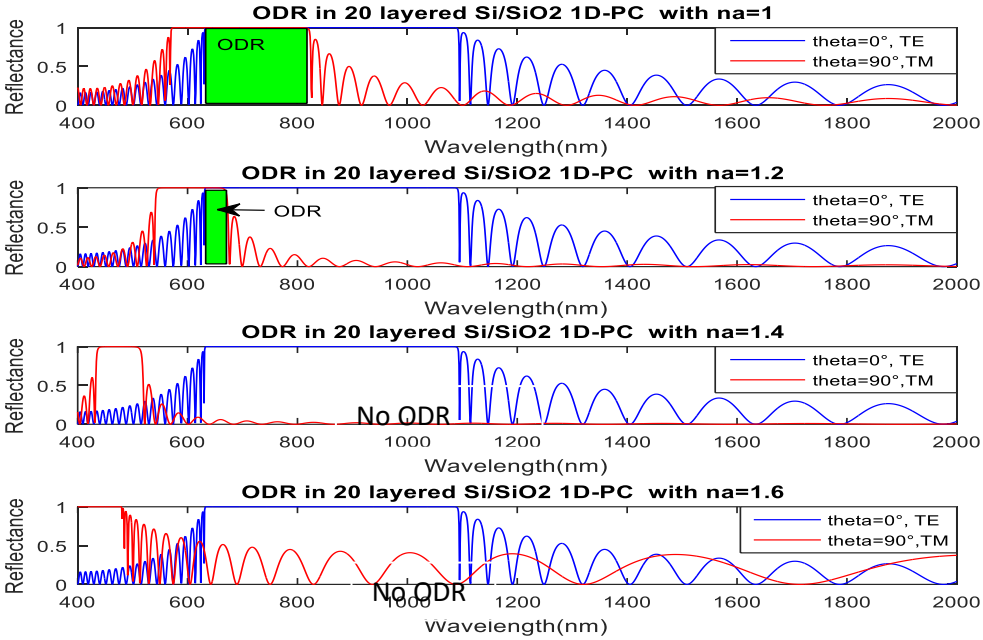


Figure (3.5): Variation of ODR in Si/$SiO_2$ 1D-PC with refractive index of ambient medium (a) $n_a = 1$ (b) $n_a = 1.2$ (c) $n_a = 1.4$ (d) $n_a = 1.6$.

### 3.4 EFFECT OF NUMBER OF LAYERS ON ODR BAND

The study of the effect of number of layers on ODR is carried out for Si-$NaAlF_6$ 1D-PC structure. The number of layers in designing of 1DPC is varied from N = 2 to N = 10. We have found that the width of ODR band increases with increase in number of layers as shown in Fig. 3.6. The reflectance of 1DPC structure increases with number of layers in both TE and TM modes. The ODR band becomes sharper and wider with increase in number of layers.

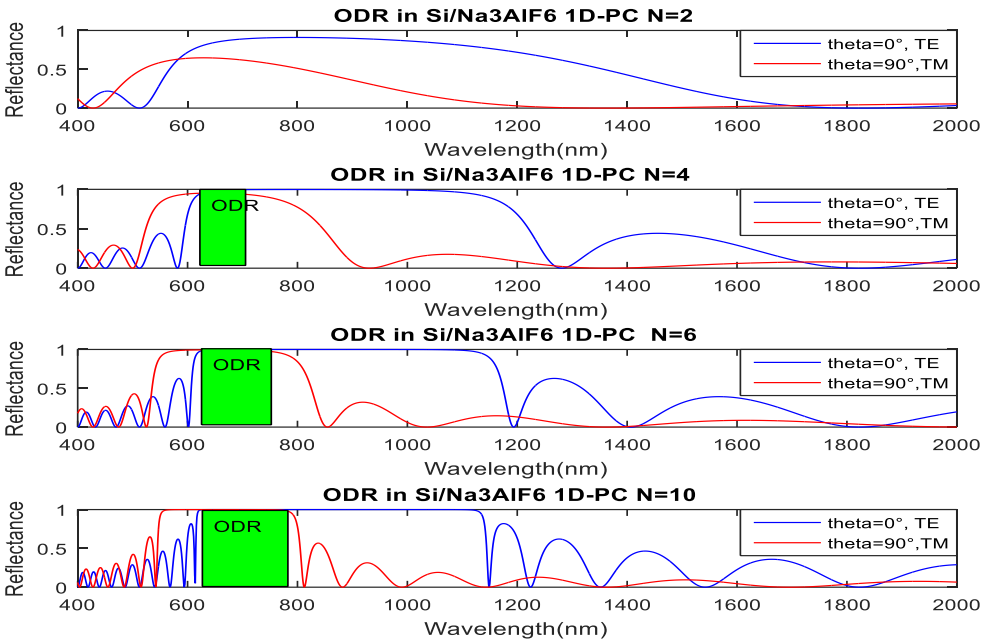


Figure (3.6): ODR in Si-$Na_3AlF_6$ 1D-PC for (a) N = 2 (b) N = 4 (c) N = 6 (d) N = 10.

## 3.5 ENHANCEMENT OF ODR IN 1DPC USING GRADUAL THICKNESS CONSTANT 'Y'

We also propose here the considerable enhancement of omnidirectional reflection band in near infrared region by changing the design parameters using a gradual constant 'Y'

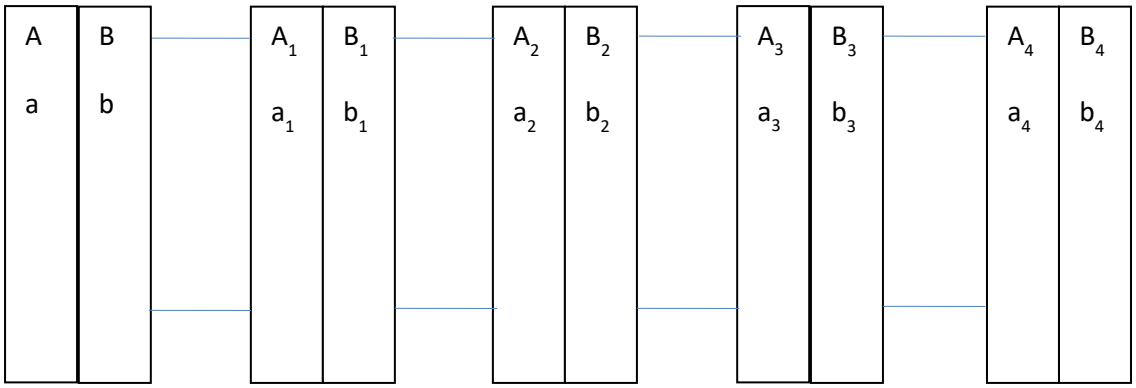


Figure (3.7): Schematic representation of proposed structure $(AB)^5(A_1B_1)^5(A_2B_2)^5(A_3B_3)^5(A_4B_4)^5$

Here we have considered the multi-layered 5 stacks of 5 alternate layers of Si as (A) and $SiO_2$ as (B). The structure shown in Fig.3.7 is described by the following sequence:

$$(AB)^5(A_1B_1)^5(A_2B_2)^5(A_3B_3)^5(A_4B_4)^5 \quad (3.1)$$

The refractive index of Si is taken as $n_1 = 3.42$ and that of $SiO_2$ is taken as $n_2 = 1.45$ in the wavelength range from 400 nm to 2000 nm.The central wavelength for computation is taken

as $\lambda_c = 800$ nm. According to quarter wave stack condition, in the stack (AB) the thickness of Si layer and $SiO_2$ is $a = 58.48$ nm, $b = 138$ nm, respectively. We have introduced a gradual multiplication constant $\Upsilon$ such that in stack ($A_1B_1$) the thickness of Si layer is $a_1 = \Upsilon a$ and the thickness of $SiO_2$ is $b_1 = \Upsilon b$. In stack ($A_2B_2$) the thickness of Si layer is $a_2 = \Upsilon a_1$ and the thickness of $SiO_2$ is $b_2 = \Upsilon b_1$. Similarly in stack ($A_3B_3$) the thickness of Si layer is $a_3 = \Upsilon a_2$ and that of $SiO_2$ is $b_3 = \Upsilon b_2$. Also in stack ($A_4B_4$) the thickness of Si layer is $a_4 = \Upsilon a_3$ and that of $SiO_2$ is $b_4 = \Upsilon b_3$. There is blue shift in the edges of PBG when we increase the angle of incidence and at Brewster's angle, TM mode will not be reflected and we will not get a complete ODR. The incident wave from outside cannot couple to Brewster window if the maximum refracted angle from ambient medium $n_0$ is less than the Brewster's angle for the photonic structure and this will result in reflection of TM modes as well which will give the reflection at all angle of incidence. At the $n_0$ and $n_1$ interface, by Snell's law

$$n_0 \sin\theta_0 = n_1 \sin\theta_1 \quad (3.2)$$

where $\theta_0$ is the angle of incidence in ambient medium, $\theta_1$ is the angle of refraction in 1st medium, So maximum refracted angle will be

$$\theta_{1max} = \sin^{-1}(n_0/n_1) = \sin^{-1}(1/3.42) = 16.97° \quad (3.3)$$

Also from Brewster's law at $n_1$ and $n_2$ interface

$$\theta_B = \tan^{-1}(n_2/n_1) = \tan^{-1}(1.45 / 3.42) = 22.9° \quad (3.4)$$

Since ($\theta_B > \theta_{1max}$) condition is satisfied by our design parameters so the incident wave from the ambient medium will not get coupled to Brewster's window, and we will still get ODR band. For complete periodicity we take $\Upsilon$ =1 in our proposed structure and Fig.3.8 shows reflectivity for both TE waves at $\theta = 0°$ and TM waves at $\theta = 89°$ and the ODR is also shown. The upper and lower edges for omnidirectional band gap is found to be $\lambda_U = 818$ nm and $\lambda_L = 633$ nm, respectively so the ODR is 185 nm which is 7.4 % of the total considered wavelength range as shown in Table 3.3. We have changed the design parameter by considering $\Upsilon = 1.02$, the reflectivity diagram and omnidirectional reflection band is shown in Fig. 3.8. The upper and lower edges for ODR are found to be $\lambda_U = 857$ nm and $\lambda_L = 650$ nm so the ODR width is 207 nm which is 25.88% of the total considered wavelength range. We have further increased this band by taking $\Upsilon = 1.04$, as shown in Fig. 3.8. The upper and lower edges of ODR are found to be $\lambda_U = 924$ nm and $\lambda_L = 653$ nm with ODR width of 271 nm which is 33.88% of the total considered wavelength range. To further increase the ODR we have considered $\Upsilon$=1.06, the upper and lower edges for ODR are found to be $\lambda_U = 992$ nm and $\lambda_L = 658$ nm

so the ODR is 334 nm which is 41.75% of the total considered wavelength range. It was found that by changing the design parameters of the proposed photonic structure by a gradual constant there is considerable increase in the ODR. The structure can be used as filter device in the visible and near infrared region of spectrum. It can also be tuned according to the design parameters. These types of optical filters may have potential applications in optical technology and optical communication.

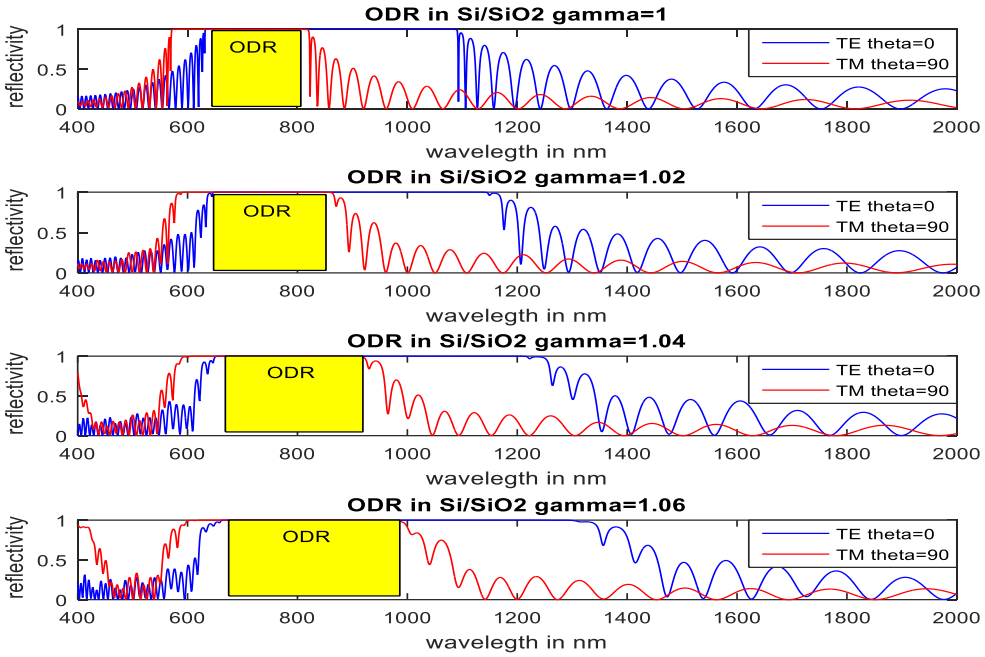


Figure (3.8): Enhancement of ODR in 50 layered $Si/SiO_2$ 1D-PC with gradual thickness constant for $n_1$=3.42, $n_2$=1.45, $d_1$=58.48 nm, $d_2$= 138 nm.

Table (3.3): Enhancement of ODR in 50 layered $Si/SiO_2$ 1D-PC with gradual thickness constant for $n_1$ = 3.42, $n_2$ = 1.45, $d_1$ = 58.48 nm, $d_2$ = 138 nm.

| S.No | Gradual constant (Y) | Lower bandgap edge of ODR ($\lambda_L$) | Upper bandgap edge of ODR ($\lambda_U$) | ODR ($\Delta\lambda$) | $\%\Delta\lambda/\lambda_C$ |
|---|---|---|---|---|---|
| | | (for $\theta$=0°, TE) | (for $\theta$ = 89°, TM) | | |
| 1 | 1 | 633 | 818 | 185 | 23.13% |
| 2 | 1.02 | 650 | 857 | 207 | 25.88% |
| 3 | 1.04 | 653 | 924 | 271 | 33.88% |
| 4 | 1.06 | 658 | 992 | 334 | 41.75% |

### 3.6: ODR IN POROUS SILICON MULTI-LAYERED STRUCTURES

Nano-porous silicon (NPS) has become a promising candidate for design of 1D PC optical sensors due to tremendous advantages [3.8]. Its large surface to volume ratio, easy fabrication, controllable pore sizes and ability of refractive index modulation with depth [3.9] makes it suitable for many applications. NPS is now widely used in making 1D PC with defect layers for sensing gas, chemicals, biochemical, bio-analytes [3.10-3.11]. The optical characteristic of NPS is highly sensitive to the presence of these analytes due to large number of pores inside [3.12-3.15]. We have probed the ODR band properties in the 1D PC structure consisting of 10 periods of alternate layers of NPS and Si. The theoretical analysis is based on the Bruggeman's effective medium approximation (BEMA) [3.16, 3.17] and transfer matrix method (TMM) [3.18]. Here we have used alternate layers of NPS as low refractive index and Si as high refractive index. In the present study, we have neglected field absorption as the constituent materials have negligible absorption coefficients in the wavelength range of interest.

Nano-porous silicon is a two-phase composite mixture of air and silicon solid phase containing silicon walls and nano-pores. The sponge like structure of NPS makes it a useful candidate for sensing applications in optical technology. In nano-porous silicon the key parameters for modelling are the refractive index $n_1$, the thickness $d_1$ and the porosity P. Considering the nano-porous silicon layer is developed on a Si substrate and air as the medium inside the pores, the refractive index is related to porosity according to BEMA model by the equation

$$(1-\mathrm{P})\frac{n_{Si}^2-n_{NPS}^2}{n_{Si}^2-2n_{NPS}^2}+\mathrm{P}\frac{n_{Air}^2-n_{NPS}^2}{n_{Si}^2-n_{NPS}^2}=0. \tag{3.5}$$

Where $n_{Si}$ is the refractive index of Si substrate, $n_{NPS}$ is the refractive index of nanoporous silicon and $n_{Air}$ is the refractive index of air or medium inside the pores and P is the porosity of NPS. This approximation is reasonable because the size of pores is much smaller than the wavelength of incident light so the electromagnetic light waves cannot distinguish between Si and pores in NPS and it will treat it as a homogenous medium [3.17]. In the present study we have considered 10 periods of alternate layers of NPS and Si. The refractive index and porosity are related by BEMA as explained in Eq. (3.5). The NPS structure can be easily fabricated by electrochemical etching of p-type Si wafer ($<100>, 0.01-0.02\ \Omega\, cm, 275\mu m,\ 20\ \mathrm{cm}^2$) [3.17]. In electrochemical etching, the applied current density (J) and the etching time (t) is responsible for the variation of refractive index $n_1$ and thickness $d_1$ of NPS. The refractive index $n_1$ and $n_2$ for NPS and Si, respectively, is taken as $n_1 = 1.7$ and $n_2 = 3.6$ in the wavelength

range 400 nm to 2000 nm. The structure of interest is designed around a central wavelength $\lambda_0 = 1200$ nm. This wavelength regime is of high interest as most of optical based device applications have been proposed and implemented in this range. The thickness of the individual layers is considered according to the quarter wave stack condition. The desired thickness of NPS layer is a $= \frac{\lambda_0}{4n_1} = 176.47$ nm and the thickness of Si layer is b $= \frac{\lambda_0}{4n_2} = 83.33$ nm .The fabrication parameters for this refractive index and thickness of NPS are $J = 70\text{mA/cm}^2$, etching time t = 2.5 sec [3.17]. The transmission spectrum of 10 period NPS-Si for TE and TM modes and the corresponding ODR is shown in Figs (3.9-3.11). The PBG for TE and TM mode is represented in Figs. (3.12-3.13), for various angles of incidence. The PBG edges in TE mode and TM mode is summarized in Table 3.4

At the $n_0$ and $n_1$ interface, maximum refracted angle will be

$$\theta_1{}^{\max} = \sin^{-1}\frac{n_0}{n_1} = \sin^{-1}\frac{1}{1.7} = 36.01^\circ \tag{3.6}$$

Also from Brewster's law at $n_1$ and $n_2$ interface

$$\theta_B = \tan^{-1}\frac{n_2}{n_1} = \tan^{-1}\frac{3.6}{1.7} = 64.72^\circ \tag{3.7}$$

Since ($\theta_B > \theta_1{}^{max}$ ) condition is satisfied by our design parameters so the incident wave from the ambient medium will not be coupled in the Brewster's window, and we will still get ODR. The lower bandgap edge for TE mode at $\theta = 0^\circ$ is $\lambda_L$ = 982 nm and the upper bandgap edge for TM mode at $\theta = 89^\circ$ is $\lambda_U$ = 1270 nm. So, the total ODR band is (1270 nm-982 nm) = 288 nm which is considerable and can be used in potential applications in near- infrared frequencies.

Table (3.4) : Photonic bandgap variation with incidence angle in multi-layered NPS-Si. Omni-direction band (1270 nm-982 nm) =288 nm.

| Angle | TE | | | TM | | |
|---|---|---|---|---|---|---|
| | Lower bandgap edge (nm) | Upper bandgap edge (nm) | Bandgap (nm) | Lower bandgap edge (nm) | Upper bandgap edge (nm) | Bandgap (nm) |
| 0° | 982 | 1544 | 562 | 982 | 1544 | 562 |
| 30° | 947 | 1525 | 578 | 964 | 1481 | 517 |
| 60° | 873 | 1485 | 612 | 930 | 1344 | 414 |
| 90° | 835 | 1464 | 629 | 914 | 1270 | 356 |

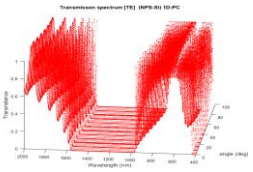

Figure (3.9) : Transmission spectrum in NPS-Si 1DPC, $n_1$=1.7, $n_2$=3.6, $d_1$=176.47 nm, $d_2$= 83.33 nm , $\lambda_o$=1200 nm at normal incidence for TE modes.

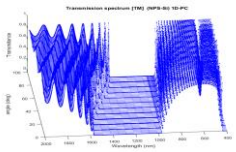

Figure (3.10): Transmission spectrum in NPS-Si 1DPC, $n_1$=1.7, $n_2$=3.6, $d_1$=176.47 nm, $d_2$= 83.33 nm , $\lambda_o$=1200 nm at normal incidence for TM modes

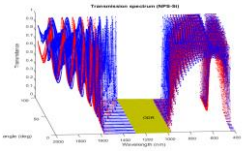

Figure (3.11): ODR in NPS-Si, $n_1$=1.7, $n_2$=3.6, $d_1$=176.47 nm, $d_2$= 83.33 nm , $\lambda_o$=1200 nm

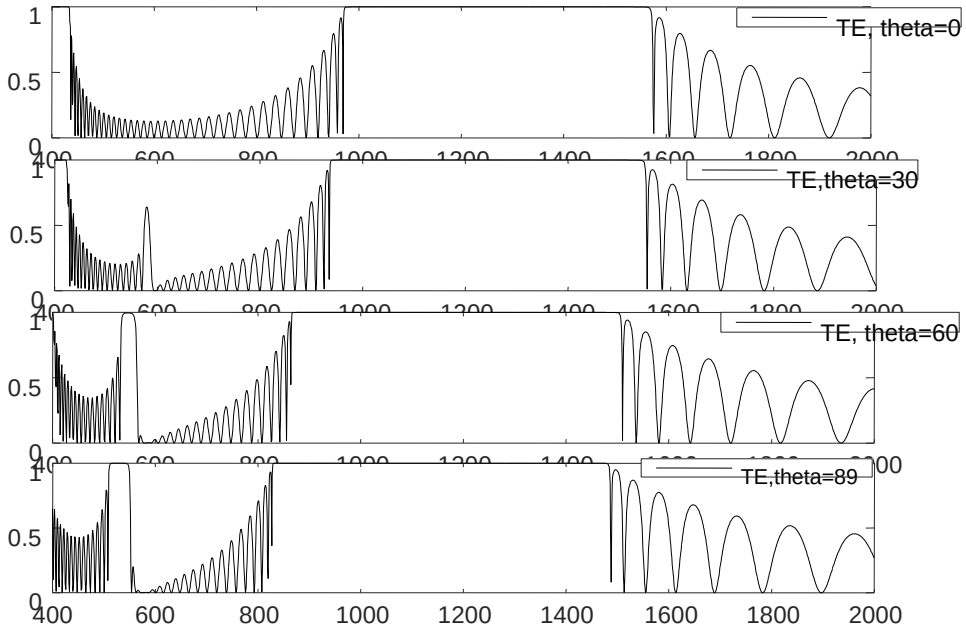


Figure (3.12)**:** Variation of reflectance with wavelength at different angle of incidence for TE modes in multi-layered NPS-Si.

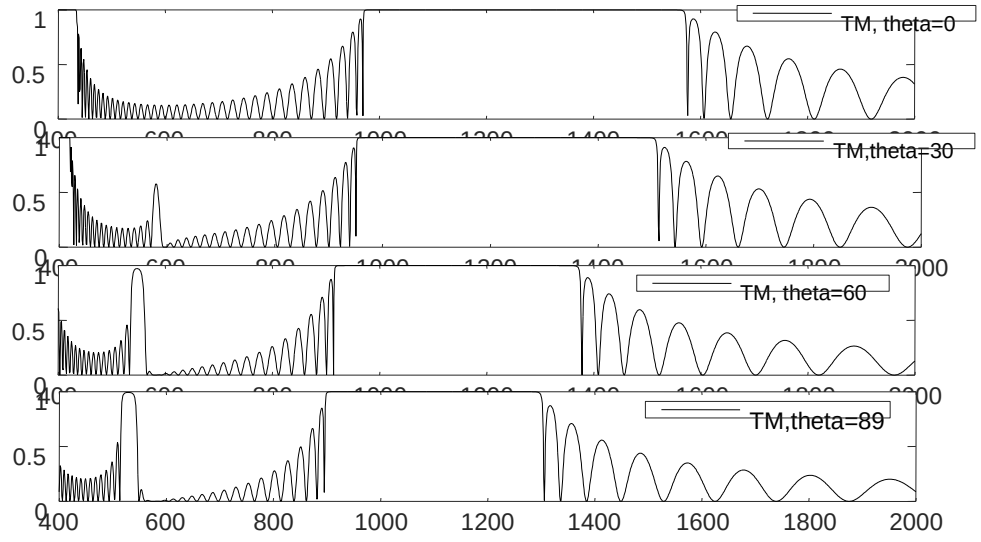


Figure (3.13)**:** Variation of reflectance with wavelength at different angle of incidence for TM modes in multi-layered NPS-Si.

### 3.6.1: Effect of Infiltration of Chemicals/ Analytes inside Pores:

In this section we consider the effect of infiltration of liquids in pores of NPS layers of multi-layered NPS-Si 1DPC. The infiltration of variety of materials into the porous silicon matrix, including polymers [3.19] and biological species [3.20] has already been reported. The modulation in reflection spectrum of synthetic opal with liquid crystals in void spaces was

recently observed [3.21]. The effective refractive index of NPS layer is defined by the porosity and the refractive index of medium inside the pores ($n_{void}$) as shown in Eq. (3.5). As the refractive index of pores increases, the effective index of refraction of NPS increases, which changes the PBG for both TE and TM modes. The PBG in TE and TM modes are found to be decreased with increase in $n_{void}$ as shown in Fig (3.14-3.15) and Table (3.5). The ODR is also found to be decreased from 284 nm to 250 nm for an increase in $n_{void}$ from 1 to 1.3 as shown in Fig. (3.16)

Table (3.5): Variation of ODR with $n_{void}$ in NPS-Si 1D-PC.

| S.No. | nvoid | TE (θ=0°) | | | TM (θ=89°) | | | ODR |
|---|---|---|---|---|---|---|---|---|
| | | Lower Bandgap Edge (nm) | Upper Bandgap Edge (nm) | Bandgap (nm) | Lower Bandgap Edge (nm) | Upper Bandgap Edge (nm) | Bandgap (nm) | |
| 1 | 1 | 982 | 1535 | 553 | 909 | 1266 | 357 | 284 |
| 2 | 1.1 | 997 | 1507 | 510 | 924 | 1272 | 348 | 275 |
| 3 | 1.2 | 1009 | 1481 | 472 | 939 | 1272 | 333 | 263 |
| 4 | 1.3 | 1020 | 1458 | 438 | 953 | 1270 | 317 | 250 |

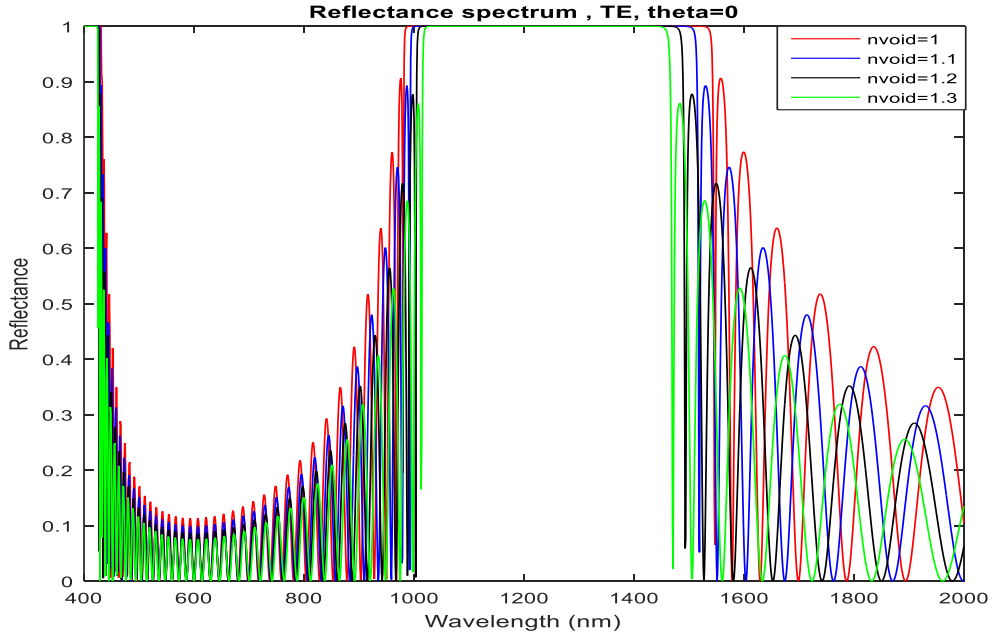

Figure (3.14): Reflection spectrum for TE modes in NPS-Si, $n_1$=1.7, $n_2$=3.6, $d_1$=176.47 nm, $d_2$= 83.33 nm, $\lambda_o$ = 1200 nm , with $n_{void}$ = 1, 1.1 ,1.2 ,1.3

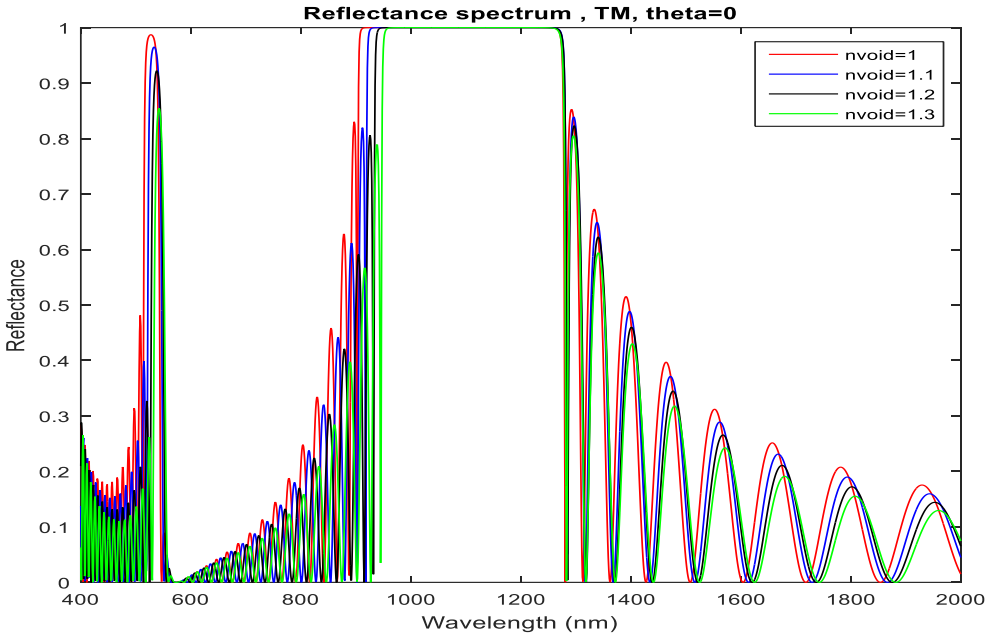


Figure (3.15): Reflection spectrum for TM modes in NPS-Si, $n_1$=1.7, $n_2$=3.6, $d_1$=176.47 nm, $d_2$= 83.33 nm , $\lambda_o$=1200 nm , with $n_{void}$=1, 1.1 ,1.2 ,1.3

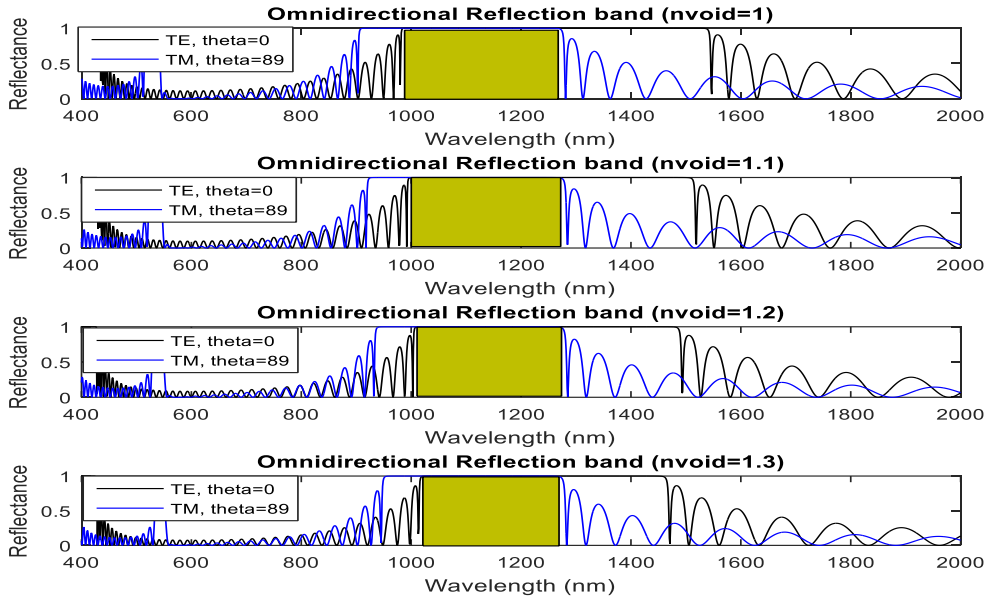


Figure (3.16): ODR band in NPS-Si, $n_1$=1.7, $n_2$=3.6, $d_1$=176.47 nm, $d_2$= 83.33 nm , $\lambda_o$=1200 nm , with $n_{void}$=1, 1.1 ,1.2 ,1.3

We have observed that NPS based photonic crystal structures can be tuned and used as wavelength filters in the near infrared spectrum which is very useful in many imaging sensors.

## 3.7: EFFECT OF MATERIAL DISPERSION IN ODR PROPERTIES OF ZnO-$SiO_2$ 1DPC

### 3.7.1 ZnO-SiO2 1DPC without Material Dispersion Effects

We have investigated the effect of dispersion on the omnidirectional reflection band properties in the 1D PC structure consisting of 25 periods of alternate layers of ZnO and $SiO_2$. The theoretical analysis is based on TMM. We have taken alternate layers of ZnO as high refractive index medium and $SiO_2$ as low refractive index medium. In the study, we have neglected field absorption / attenuation as the constituent materials have negligible absorption coefficients in the wavelength range of interest. The index of refraction $n_1$ and $n_2$ for ZnO and $SiO_2$, respectively, ignoring material dispersion, is taken as $n_1 = 2.08$ and $n_2 = 1.46$ in the wavelength range 400 nm to 2000 nm. The structure of interest is designed around a central wavelength $\lambda_0 = 1200$ nm. This wavelength regime around 1200 nm is of high interest as most of optical device applications have been proposed and implemented in this range [3.22-3.24]. This wavelength range is very near to wavelength of optical fiber communication systems and infrared light with a wavelength around 1330 nm (least dispersion), 1550 nm (best transmission) are the best choices for standard silica fibers. The wavelength range of interest is also close to the region where optical fibers have small transmission loss (1260 nm to 1625 nm). The thickness of the individual layers is considered according to the quarter wave stack condition. The thickness of ZnO layer is $d_1 = \frac{\lambda_0}{4n_1} = 144.2$ nm and the thickness of SiO2 layer is $d_2 = \frac{\lambda_0}{4n_2} = 205.48$ nm. The PBG for TE and TM mode is represented in Figs. (3.17 & 3.18), respectively, for various angles of incidence without the inclusion of material dispersion effects. In TE mode there is considerable blue shift of PBG edges as we increase the angle of incidence together with a decrease in the bandwidth of PBG. Similar type of blue shift of PBG edges is also observed for TM modes as we increase the angle of incidence but PBG width increases. The PBG edges in TE mode and TM mode is summarized in Table (3.6).

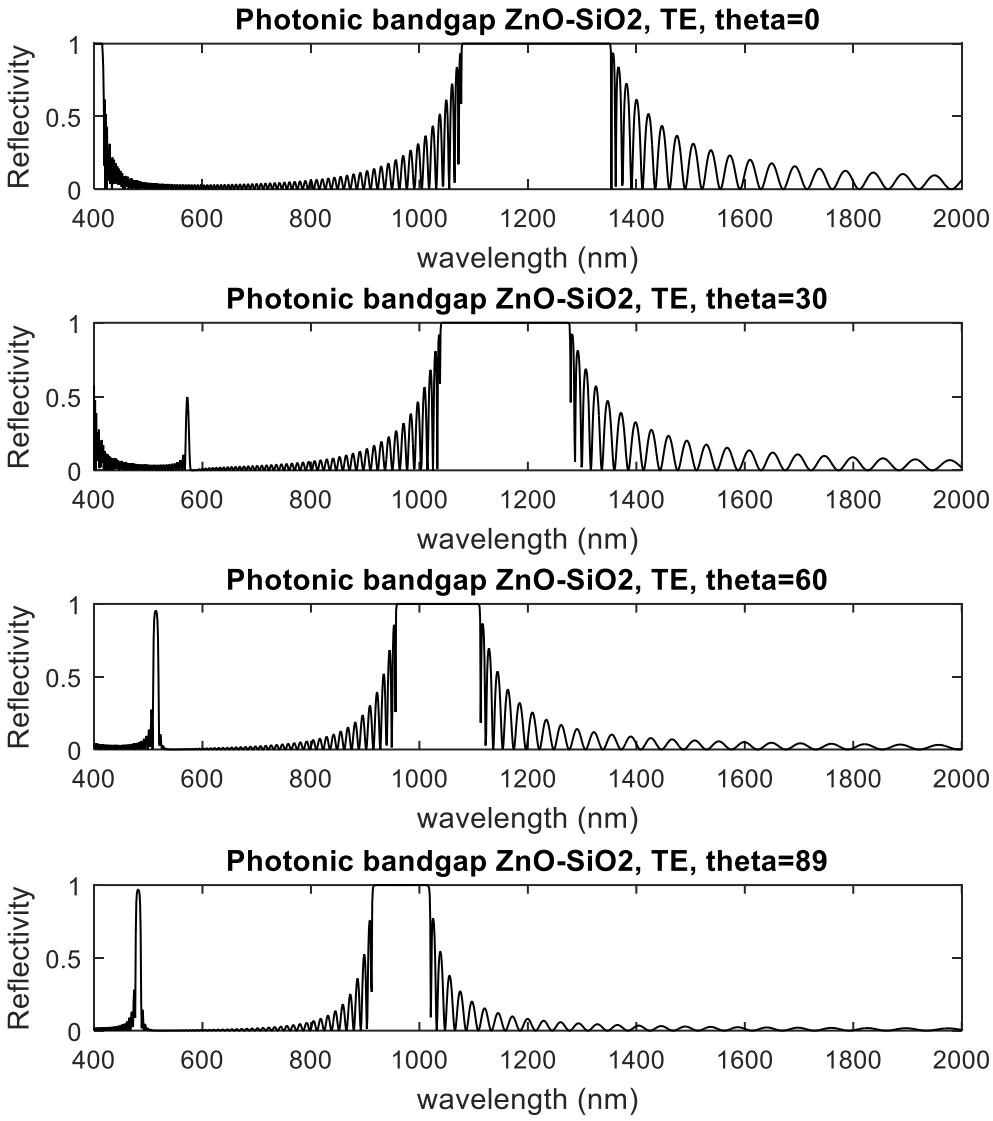


Figure (3.17): Reflectivity variation with wavelength at different angle of incidence for TE modes in multi-layered ZnO-$SiO_2$ without dispersion effects.

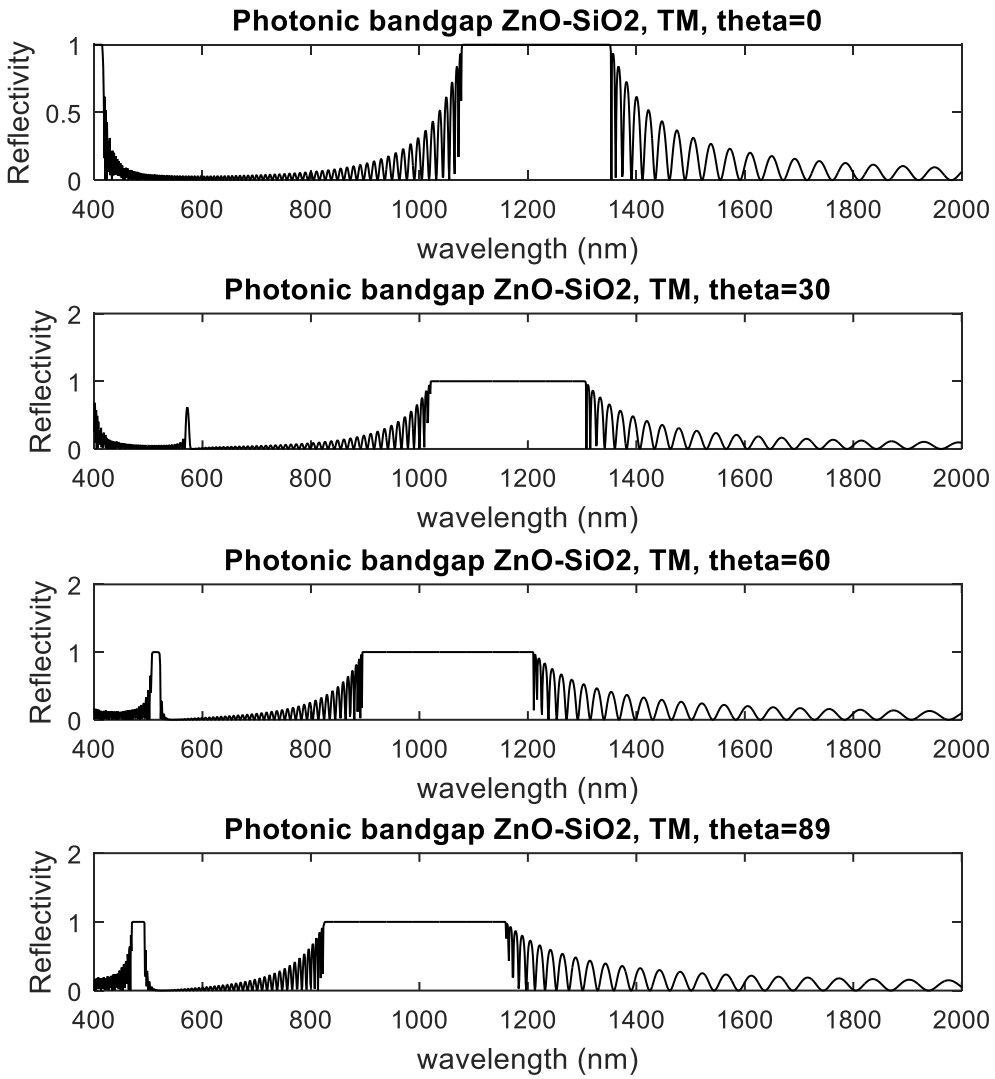


Figure (3.18): Reflectivity variation with wavelength at different angle of incidence for TM modes in multi-layered ZnO-$SiO_2$ without dispersion effects.

Table (3.6): Photonic bandgap variation with incidence angle in multi-layered ZnO-$SiO_2$ without dispersion effects. ODR band (1079 nm -1158 nm = 79 nm).

| Angle | TE | | | TM | | |
|---|---|---|---|---|---|---|
| | Lower bandgap edge (nm) | Upper bandgap edge (nm) | Bandgap (nm) | Lower bandgap edge (nm) | Upper bandgap edge (nm) | Bandgap (nm) |
| 0° | 1079 | 1351 | 272 | 1079 | 1351 | 272 |
| 30° | 1041 | 1275 | 234 | 1022 | 1303 | 281 |

| | | | | | | |
|---|---|---|---|---|---|---|
| 60° | 960 | 1110 | 150 | 896 | 1209 | 313 |
| 89° | 915 | 1016 | 101 | 827 | 1158 | 331 |

The ODR in ZnO-$SiO_2$ multi-layered photonic structure ignoring the dispersion effects is shown in Figs. (3.19-3.21), and bandgap edges are mentioned in Table (3.6). The lower bandgap edge for TE mode at $\theta = 0°$ is $\lambda_L$ = 1079 nm and the upper bandgap edge for TM mode at $\theta = 89°$ is $\lambda_U$ = 1158 nm. So the total ODR bandwidth is (1158nm-1079nm) = 79 nm which is considerable and can be used in potential applications in near- infrared frequencies.

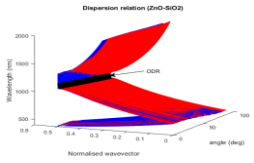


Figure (3.19): Dispersion relation with variation of angle of incidence for TE modes (Red lines) and TM modes (Blue lines) for $ZnO_2$-$SiO_2$.

In Fig. (3.19), we observe the dispersive characteristics of the 25-period ZnO-$SiO_2$ 1DPC which shows large overlap of the properties for both TE and TM waves. The ODR region observed around 1100 nm is highly prominent. The transmission profile for the structure of interest is given in Fig. (3.20). One can observe shifts in the PBG with change in angle of incidence for both TE and TM modes of the field. Fig.(3.21) shows the reflection profile for both polarizations together with the region for ODR.

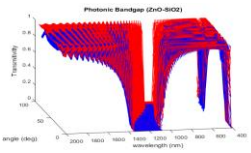

Figure (3.20): Transmissivity variation with wavelength and angle of incidence for TE modes (Red lines) and TM modes (Blue lines) in multi-layered ZnO-$SiO_2$ .

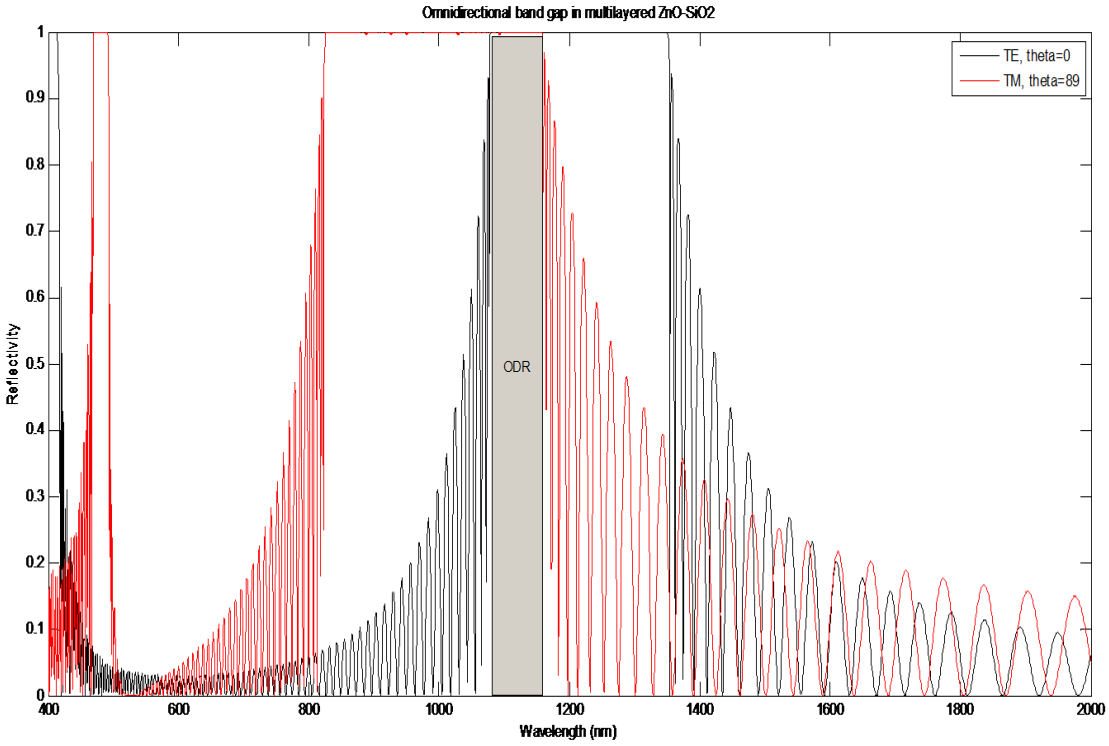


Figure (3.21): Reflectivity variation with wavelength for TE modes at θ = 0° and TM modes θ = 89° in multi-layered ZnO-$SiO_2$ without dispersion effects. ODR band (1079 nm -1158 nm = 79 nm).

### 3.7.2 Effect of Material Dispersion

In this section we consider the effect of material dispersion on the electromagnetic wave propagation properties across a 1DPC consisting of 25-periods of alternating layers of ZnO and SiO2. In order to include material dispersion in our formalism we use the Sellmeier equations cited in reference [3.25]. The Sellmeier equation for the refractive index of ZnO is expressed as

$$n_1{}^2(\lambda) = A + \frac{B\lambda^2}{\lambda^2 - C^2} + \frac{D\lambda^2}{\lambda^2 - E^2}, \tag{3.8}$$

where A, B, C, D and E are Sellmeier coefficients, λ is the wavelength of light in (nm). We have taken the value of parameters cited in reference [3.26].

Table (3.7): Sellmeier coefficients for ZnO thin film.

| A | B | C (nm) | D | E (nm) |
|---|---|---|---|---|
| 2.0065 | $1.5748\times10^6$ | $10^7$ | 1.5868 | 260.63 |

The refractive index of $SiO_2$ is given by the Sellmeier equation as

$$n_2{}^2(\lambda) = 1 + \frac{B_1\lambda^2}{\lambda^2 - C_1} + \frac{B_2\lambda^2}{\lambda^2 - C_2} + \frac{B_3\lambda^2}{\lambda^2 - C_3}, \tag{3.9}$$

where, $B_1$, $B_2$, $B_3$, $C_1$, $C_2$, and $C_3$ are Sellmeier coefficients and we have taken the value of these coefficients as cited in reference in [3.25, 3.27].

Table (3.8): Sellmeier coefficients for $SiO_2$.

| $B_1$ | $B_2$ | $B_3$ | $C_1$ ($nm^2$) | $C_2$ ($nm^2$) | $C_3$ ($nm^2$) |
|---|---|---|---|---|---|
| 0.6694 | 0.43458 | 0.8716 | 4480.1 | 13284 | 95341000 |

Under the influence of material dispersion, the reflection band of the desired structure undergoes changes such that for both TE modes and TM modes, we observe red shift in the lower bandgap edge and a blue shift in upper bandgap edge. At normal incidence ($\theta = 0°$), the lower edge of bandgap was at 1079 nm in the absence of material dispersion. The edge got red shifted to 1103 nm with dispersion effects. The upper bandgap edge was at 1351 nm without dispersion and with the inclusion of material dispersion, it blue shifts to 1315 nm. Similar properties such as decrease in the width of photonic bandgap, for higher angles of incidence, are observed for both TE and TM modes. The photonic bandgap edges for TE and TM modes are summarized in Table 4.The comparative shift due to dispersion for both TE and TM modes

is shown in Fig. (3.22) and Fig. (3.23), respectively. Figs. (3.24 & 3.25) show the dispersive characteristics and transmission profile of the 25-period ZnO-$SiO_2$ 1DPC structure, respectively. The effective group velocity for the structure is

$$v_g = \frac{d\omega}{dK} = \left[\frac{dK}{d\omega}\right]^{-1} = \left[-\frac{\lambda^2}{c}\frac{dK}{d\lambda}\right]^{-1}.$$

Putting $d = d_1 + d_2$ and using Eqs. (3.8-3.9) and Eq. (2.61), we get,

$$\frac{dK}{d\lambda} = -\frac{1}{d\sin Kd}\left[\sin\frac{n_1d_1}{\lambda}\cos\frac{n_2d_2}{\lambda}\left(-\frac{1}{2}\frac{d_2}{\lambda}\frac{dn_2}{d\lambda}\left(\frac{n_1}{n_2}+\frac{n_2}{n_1}\right)+\frac{1}{2}\frac{d_2}{\lambda^2}\left(n_1+\frac{{n_2}^2}{n_1}\right)+d_1\left(-\lambda\frac{dn_1}{d\lambda}+n_1\right)\right)+\cos\frac{n_1d_1}{\lambda}\sin\frac{n_2d_2}{\lambda}\left(-\frac{1}{2}\frac{d_1}{\lambda}\frac{dn_1}{d\lambda}\left(\frac{n_1}{n_2}+\frac{n_2}{n_1}\right)+\frac{1}{2}\frac{d_1}{\lambda^2}\left(n_2+\frac{{n_1}^2}{n_2}\right)+d_2\left(-\lambda\frac{dn_2}{d\lambda}+n_2\right)\right)+\sin\frac{n_1d_1}{\lambda}\sin\frac{n_2d_2}{\lambda}\left(\frac{1}{2}\frac{dn_2}{d\lambda}\left(\frac{n_1}{{n_2}^2}-\frac{1}{n_1}\right)+\frac{1}{2}\frac{dn_1}{d\lambda}\left(\frac{n_2}{{n_1}^2}-\frac{1}{n_2}\right)\right)\right], \quad (3.10)$$

$$\frac{dn_1}{d\lambda} = -\frac{\lambda}{n_1}\left[\frac{BC^2}{(\lambda^2-C^2)^2}+\frac{DE^2}{(\lambda^2-E^2)^2}\right], \quad (3.11)$$

$$\frac{dn_2}{d\lambda} = -\frac{\lambda}{n_2}\left[\frac{B_1C_1}{(\lambda^2-C_1)^2}+\frac{B_2C_2}{(\lambda^2-C_2)^2}+\frac{B_3C_3}{(\lambda^2-C_3)^2}\right]. \quad (3.12)$$

Table (3.9): Photonic bandgap variation with incidence angle in ZnO-$SiO_2$ 1DPC with dispersion effects. The region of ODR (1103 nm -1133nm = 30 nm).

| Angle | TE | | | TM | | |
|---|---|---|---|---|---|---|
| | Lower bandgap edge (nm) | Upper bandgap edge (nm) | Bandgap (nm) | Lower bandgap edge (nm) | Upper bandgap edge (nm) | Bandgap (nm) |
| 0° | 1103 | 1315 | 212 | 1103 | 1315 | 212 |
| 30° | 1058 | 1239 | 181 | 1041 | 1263 | 222 |
| 60° | 960 | 1075 | 115 | 906 | 1156 | 250 |
| 89° | 914 | 984 | 70 | 831 | 1133 | 302 |

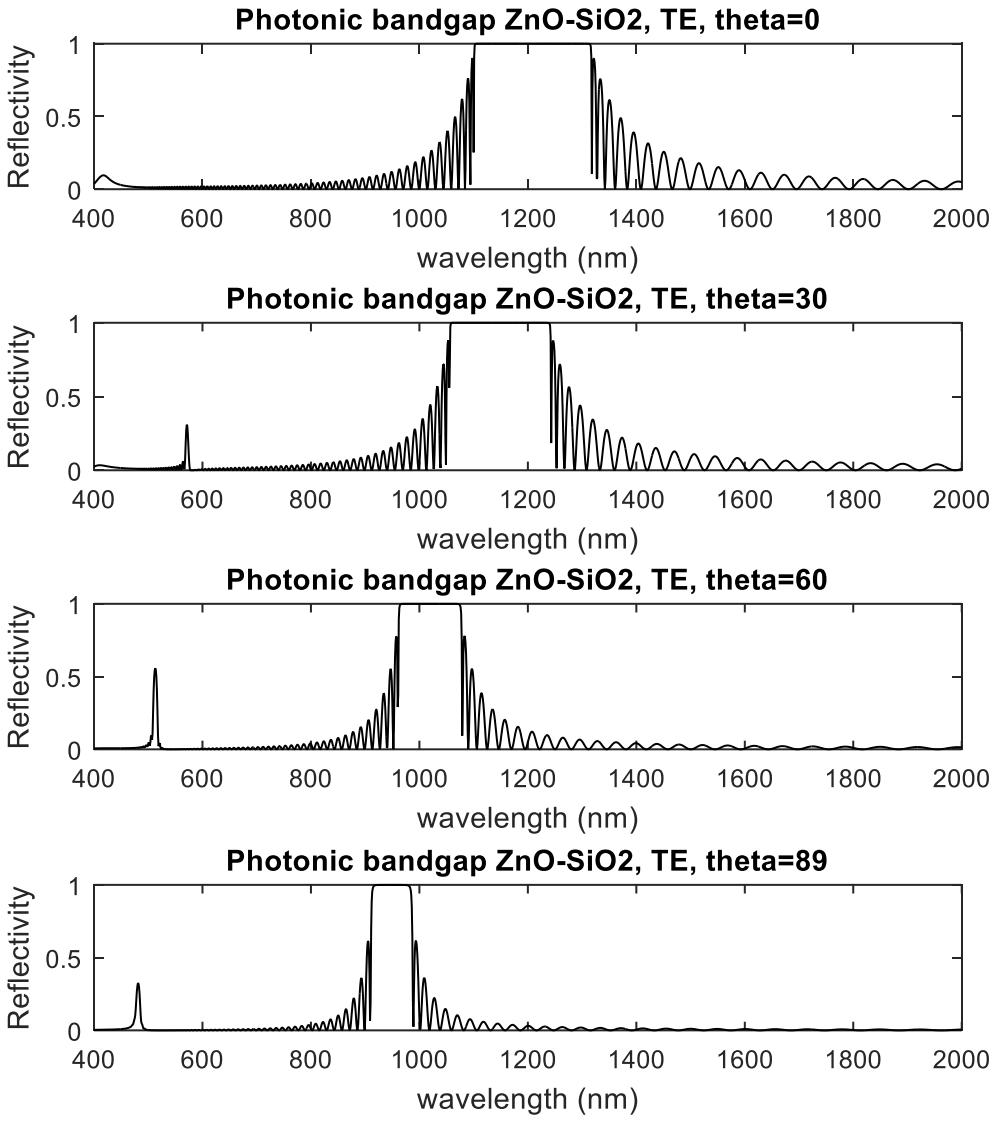


Figure (3.22): Reflectivity variation with wavelength for TE modes at θ = 0°, 30°, 60°, and 89° in ZnO-$SiO_2$ 1DPC with material dispersion effects.

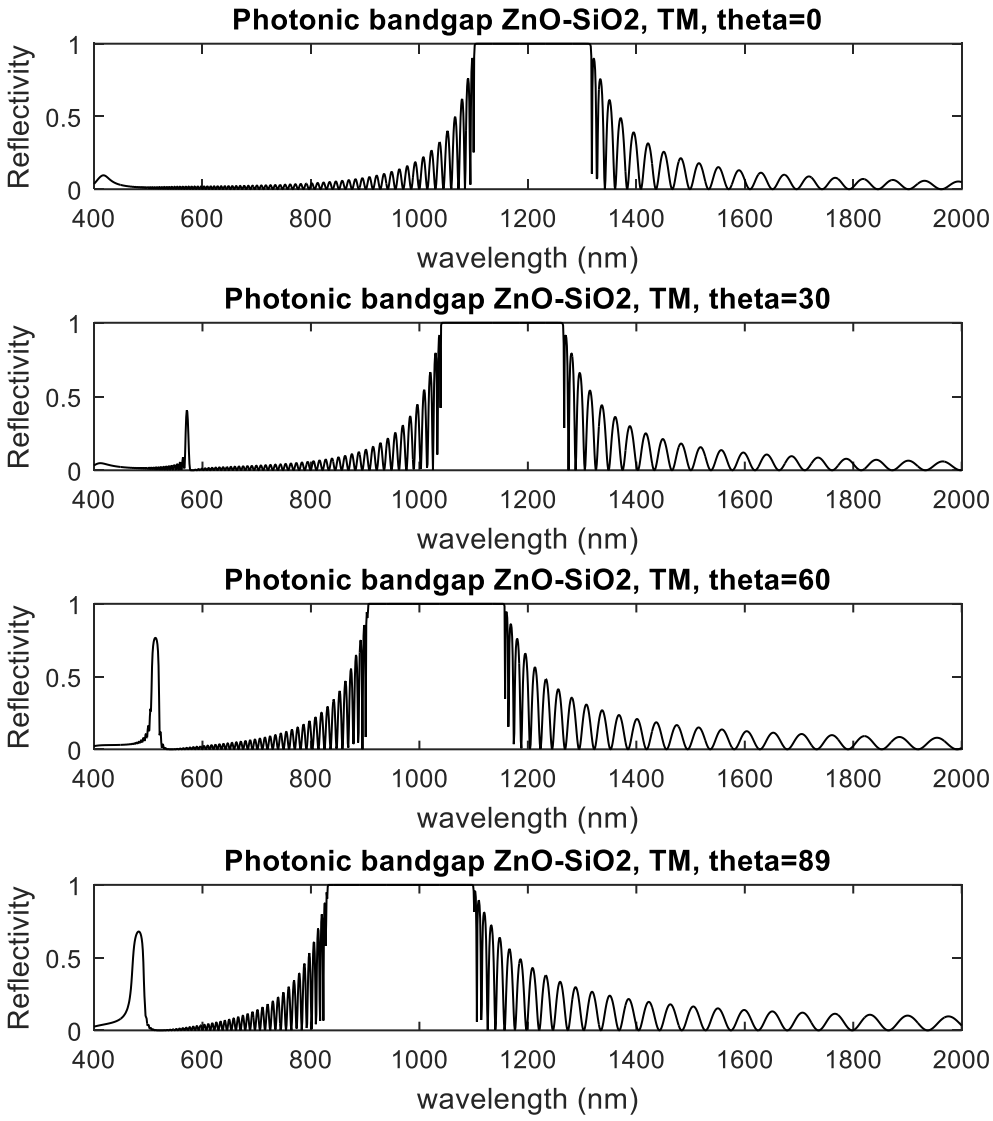


Figure (3.23): Reflectivity variation with wavelength for TM modes at θ=0°, 30°,60°, and 89° in ZnO-$SiO_2$ 1DPC with material dispersion effects.

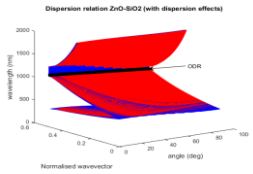


Figure (3.24): Dispersion relation with variation of angle of incidence for TE modes (Red lines) and TM modes (Blue lines) for $ZnO_2$-$SiO_2$ 1DPC with material dispersion.

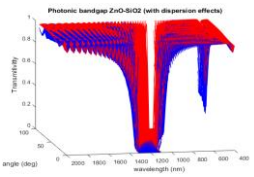


Figure (3.25): Transmissivity variation with wavelength and angle of incidence for TE modes (Red lines) and TM modes (Blue lines) in ZnO-$SiO_2$ 1DPC with material dispersion effects.

Table (3.10): Omnidirectional bandgap in ZnO-$SiO_2$ 1DPC with dispersion effects.

| TE | | | TM | | | Omnidirectional bandgap |
|---|---|---|---|---|---|---|
| Angle | Lower bandgap edge (nm) | Upper bandgap edge (nm) | Angle | Lower bandgap edge (nm) | Upper bandgap edge (nm) | |
| 0° | 1103 | 1315 | 89° | 831 | 1133 | 1133 nm-1103 nm=30 nm |

From Eqs. (3.10-3.12) one can infer that in presence of material dispersion, the effective group velocity as well as the group velocity dispersion (GVD) = $\frac{\partial}{\partial\omega}\left(\frac{1}{v_g}\right) = \frac{\partial^2 K}{\partial\omega^2}$, get highly sensitive to the changes in the refractive indices for each wavelength. This in turn results in the enhancement of both $v_g$ and GVD. As a consequence, we observe that the omnidirectional bandgap reduces considerably due to material dispersion effects. The photonic band edges for TE modes at θ = 0° are at lower bandgap edge at 1103 nm and upper bandgap edge at 1315 nm. Similarly, the photonic bandgap edges for TM modes at θ = 89° are at lower bandgap edge at 831 nm and upper band gap edge at 1133 nm. So, we obtain a reduced omnidirectional gap of 30 nm (1133 nm -1103 nm) due to material dispersion effects. With ZnO films being the material of choice for high refractive index, one can perform extensive tuning of the bandgap properties by appropriately varying the dopant element and level together with the material dispersion properties. The dopants create additional mode or microcavity in the bandgap region which can be tuned by the concentration of dopant and temperature [3.28-3.36]. In the present case, the inclusion of the material dispersion properties of the constituent layers results in a red shift in the ODR band position and bandgap. This interplay of the structural characteristics together with the material properties in the case of 25-period ZnO based 1DPC makes it a unique candidate for designing of novel optical / opto-electronic devices.

**CONCLUSIONS:**

1DPC structures mentioned in Table (3.2) are designed to be used as ODR to get the reflection spectrum in the desired wavelength range using Transfer Matrix Method. In 20 layered Si/$SiO_2$, ODR band is found to be from 818 nm to 633 nm as shown in Table (3.1). The proposed structure gives 100% reflection within a wide range of wavelengths in the visible-N IR region and can be used effectively in wavelength filters, optical resonators and mirrors in desired wavelength range. The variation in the ODR band due to change in refractive index contrast

for 1DPCs has been simulated and shown in Table (3.2). It was found from the observed results that the refractive index contrast is an important design parameter for optical characterisation of ODR. The width of ODR increases with the increase in refractive index contrast. As the refractive index contrast increases, the lower ODR band edge is blue shifted and the upper ODR band edge is red shifted, which widens the ODR band. The role of ambient medium in the optical response of ODR is simulated for 20 layered $Si/SiO_2$ 1DPC structure. The width of ODR band is found to be decreased and blue shifted with increase in the refractive index of ambient medium. When the refractive index of ambient medium approaches the lower refractive index of constituent layer, the ODR band disappears as shown in Fig.(3.5). The effect of number of layers is simulated for the designing of ODR. The number of layers in ODR is an important parameter due to fabrication challenges. The width of ODR is found to be sharpened with increase in the higher reflectance region in $Si/Na_3AlF_6$ 1DPC with the increase in number of layers as shown in Fig.(3.6). There is a considerable enhancement of ODR band in 25 layered $Si\text{-}SiO_2$ 1DPC by changing the thickness parameters using a gradual constant 'Y' around central wavelength of 800 nm as shown in Table (3.3).The proposed structure gives high reflection within a wide range of wavelengths in the visible and near infrared region and can be used effectively in wavelength filters, optical resonators and mirrors.

Based on theoretical framework of BEMA and TMM, ODR band in PS/Si 1D-PC is studied. The effect of infiltration of liquids/chemicals inside pores of PS on ODR is simulated. There is enhancement of ODR in PS based 1D-PC with increase in refractive index of infiltrated liquids in pores as shown in Table (3.5). The structure gives broad inhibition of transmission frequencies within a wide range of wavelengths in the near infrared region (1269 nm- 985 nm) which can be tuned according to the design parameters and porosity.

The numerical study of the effect of material dispersion on the ODR properties in the case of 1D-PC consisting of alternate layers of ZnO and $SiO_2$ is investigated. Taking into account the material dispersion properties, shift in the wavelength range for ODR from (1079 − 1158 nm) to (1133 − 1103 nm) is observed as shown in Table-9 and 10. This shows the narrowing of the bandwidth for ODR from 79 nm to 30 nm as a result of material dispersion. The wavelength range of interest is close to optical communication wavelengths and is useful in many optical device applications. The effect of material dispersion on the spectral response of ODR is included and it is found that it plays an important role in designing and analysis of 1DPC .

# CHAPTER- IV

# MICROCAVITY DEFECT IN 1DPC

**INTRODUCTION:**

This chapter deals with simulation study of single defects in 1DPC to make resonant microcavities. PCs with defects lead to localised electromagnetic modes inside the bandgap region [4.1-4.5]. Many useful devices are designed using impurities in the PCs, e.g. micro-cavities, linear waveguides, etc. Impurities destroy the perfect translational symmetry in the photonic crystals. This can be achieved in a periodic dielectric by a number of different methods e.g. adding impurity dielectric materials to a unit cell, removing dielectric materials from a unit cell, by changing the dielectric constant of materials in a cell and by changing the size/geometry of materials in a cell in the lattice [4.6-4.10]. The overall effect will be a localized change of the average dielectric constant of the medium. Impurities at single site serve as high Q microcavities. Such structures bind resonantly localized cavity modes in the stop band of the photonic crystal. Since no light in the stop band can pass through the surrounding periodic regions, the impurity mode will be evanescent outside the defect layer. Thus a resonance occurs in a very narrow frequency range inside the stop band. The structure is then called a resonant microcavity, and the confined resonant mode about the structure is called the resonant excitation. The efficiency of the resonant cavity is characterized by a quality factor or Q value, which is a measure of the number of oscillations of light in the cavity before damping eventually, causes the original excitation to decay away. The resonant excitations in such cavities are the basis of laser systems, Fabry-Perot oscillators, and photonic microcavities. The Q-value for resonant cavity is defined as

$$Q = \frac{\lambda_0}{\Delta\lambda}. \tag{4.1}$$

Where $\lambda_0$ is the central wavelength of resonant cavity and $\Delta\lambda$ is the full width at half maxima (FWHM) of resonant cavity.

**4.1. DESIGN OF 1DPC MICROCAVITY**

Microcavities with $Si/SiO_2$ and Si/Air with defect in the form of doubled thickness of middle layer were simulated with parameters shown in Fig. 4.1 and Tables (4.1- 4.2). The introduction of defect layer creates localised photonic state in the bandgap region. The incident light coupled with the defect mode is transmitted by the structure. This represents a sharp transmission peak in the bandgap region for the 1DPC structure [4.11-4.16]. The position of this peak can be controlled by changing the refractive index or thickness of the defect layer. We have done

comparative analysis of the transmission spectrum of $Si/SiO_2$ 1DPC with defect layer of double thickness of $SiO_2$ and Si layer, respectively at the middle of the structure for wavelength range 1000 nm to 3000 nm with the central wavelength at 1550 nm as shown in Figs.4.2 and 4.3.

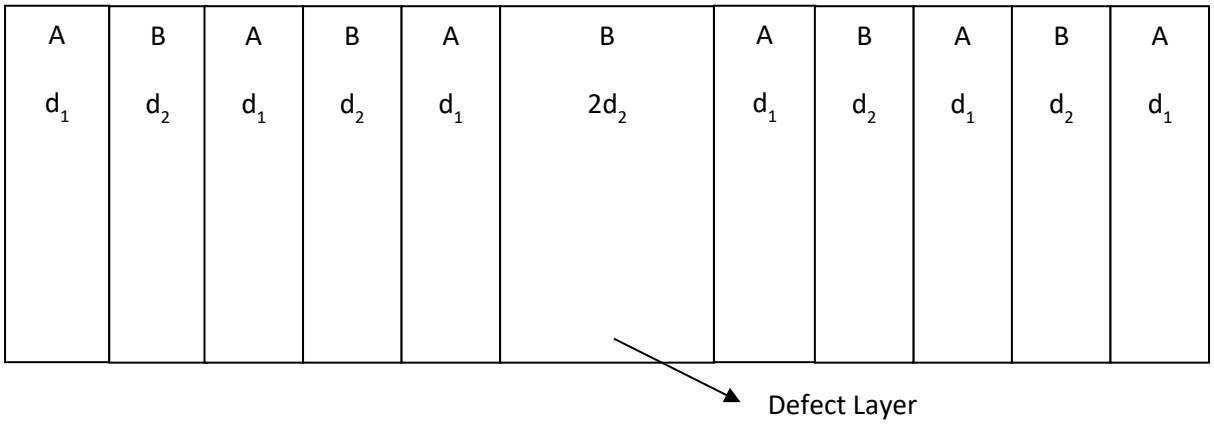


Figure 4.1: Design parameters of a $Si/SiO_2$ 1DPC microcavity with double width of defect layer at resonant wavelength $\lambda_o$=1550 nm.

Table 4.1: Parameters of a quarter wavelength stack comprising $SiO_2$ low index layers and Si high index layers and with double width of $SiO_2$ layer to be the defect at resonant wavelength $\lambda_o$=1550 nm

| Layer | Material | Refractive Index | Thickness |
|---|---|---|---|
| A | $SiO_2$ | 1.45 | 267.24 nm |
| B | Si | 3.42 | 113.30 nm |
| Defect | $SiO_2$ | 1.45 | 534.48 nm |

Table 4.2: Parameters of a quarter wavelength stack comprising $SiO_2$ low index layers and Si high index layers and with double width of Si layer to be the defect at resonant wavelength $\lambda_o$=1550 nm

| Layer | Material | Refractive Index | Thickness |
|---|---|---|---|
| A | $SiO_2$ | 1.45 | 267.24 nm |
| B | Si | 3.42 | 113.30 nm |
| Defect | Si | 3.42 | 226.6 nm |

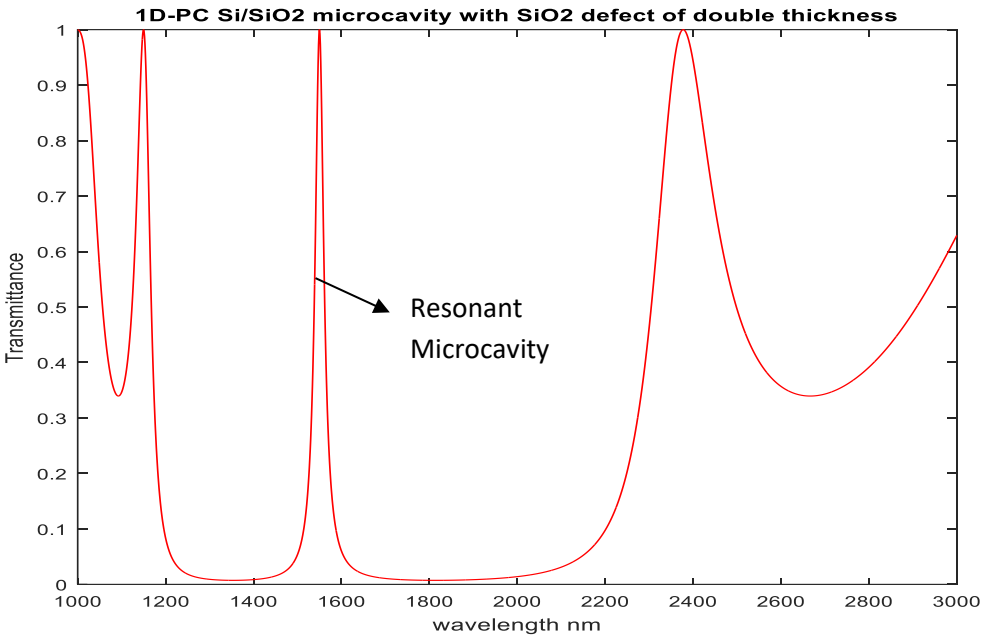


(a)

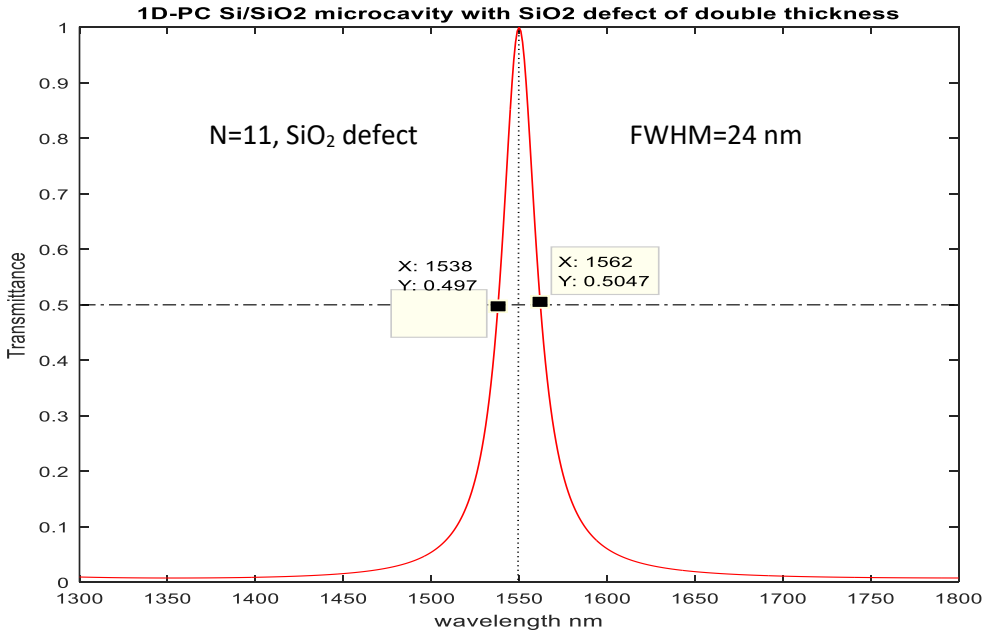


(b)

Figure 4.2: (a) Resonant microcavity mode in $Si/SiO_2$ 1D-PC with $SiO_2$ defect layer of double thickness with $n_1 = 1.45$, $n_2 = 3.42$, $d_1 = 267.24$ nm, $d_2 = 113.30$ nm, N = 11, $n_{defect} = 1.45$, $d_{defect} = 534.48$ nm. (b) Enlarged view of resonant cavity mode showing the full width at half maxima (FWHM).

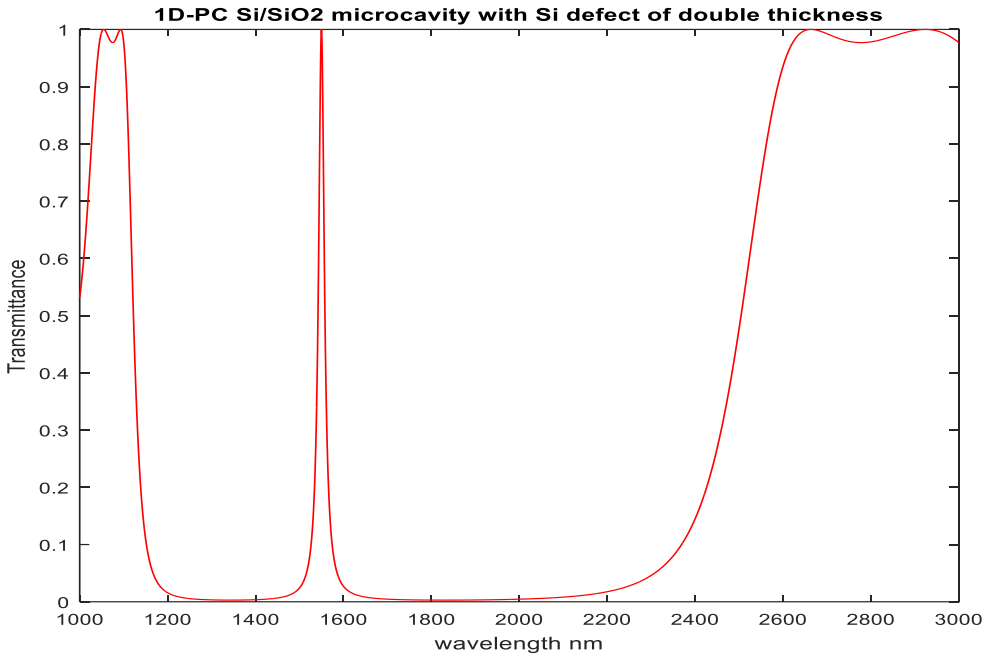


(a)

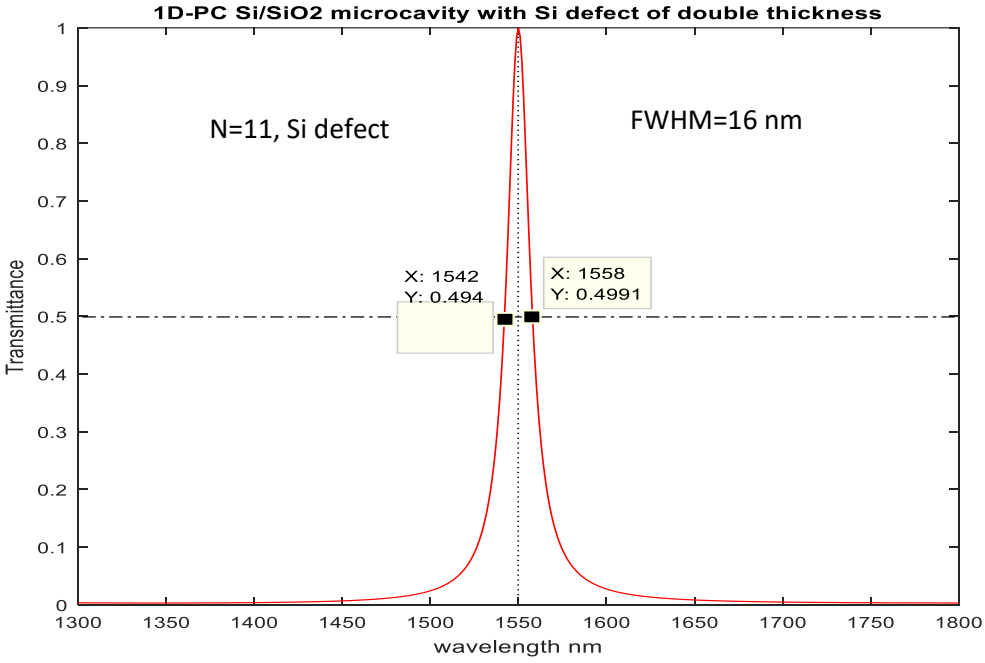


(b)

Figure-4.3: (a) Resonant microcavity mode in $Si/SiO_2$ 1D-PC with Si defect layer of double thickness with $n_1 = 1.45$, $n_2 = 3.42$, $d_1 = 267.24$ nm, $d_2 = 113.30$ nm, N = 11, $n_{defect} = 3.42$, $d_{defect} = 226.6$ nm. (b) Enlarged view of resonant cavity mode showing the full width at half maxima (FWHM).

## 4.2. OPTIMISING Q-VALUE FOR 1DPC MICROCAVITY

It is observed that increasing the number of constituent layers narrows the PBG and sharpens the bandgap edges. Q-value in the transmission peak is increased due to higher reflectivity of Bragg mirrors as number of layers is increased. In $Si/SiO_2$ 1DPC microcavity with Si as defect layer, the Q-value has increased from 15.9 to 258 for an increase of pair of layers from 7 to 13 as shown in Fig.(4.4). Similarly in $Si/SiO_2$ microcavity with $SiO_2$ as defect layer, the Q-value of defect mode has increased from 9.7 to 155 for an increase of pair of layers from 7 to 13 as shown in Fig. (4.5). Q-values for Si defect layer is much higher than the $SiO_2$ defect layer. In Si/Air 1DPC with defect layer as air, the Q-values increase from 6.5 to 258.3 for an increase in the number of pair of layers from 5 to 11 as shown in Fig.( 4.6). In Si/Air 1D-PC with defect layer as Si, the Q-value is found to increase from 11.5 to 517 as shown in Fig (4.7). It is observed that Si/Air 1DPC structures have higher Q values than $Si/SiO_2$ structures due to high refractive index contrast. So high refractive index contrast and high refractive index defect layer is required for creating a microcavity with high Q-values as shown in Fig.(4.8).

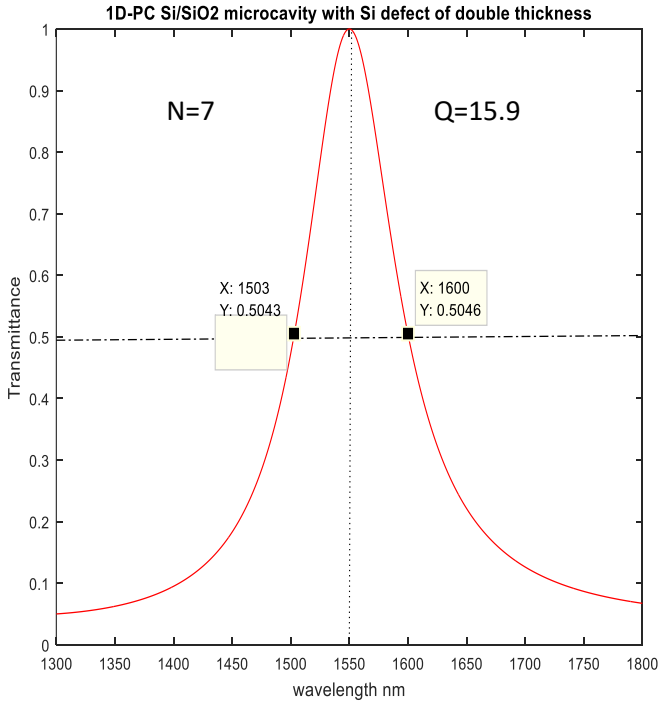


(a)

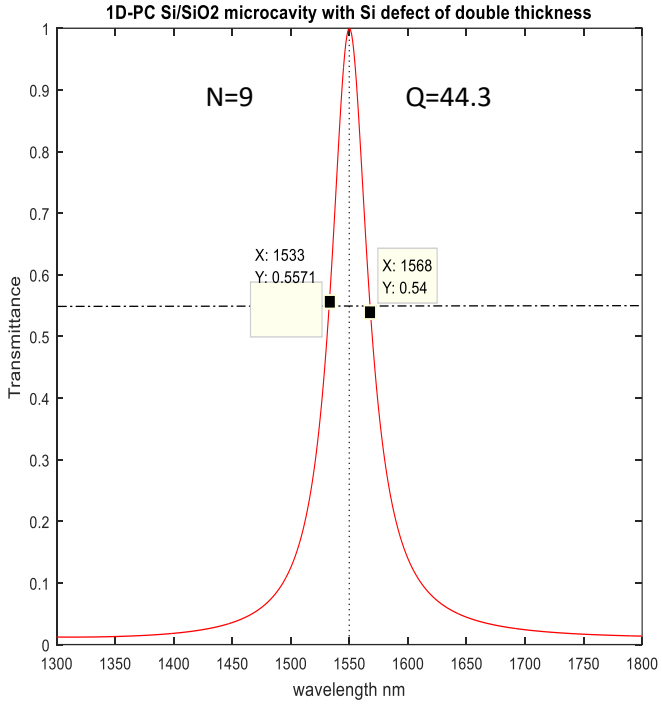
1D-PC Si/SiO2 microcavity with Si defect of double thickness
N=9
Q=44.3
X: 1533
Y: 0.5571
X: 1568
Y: 0.54
Transmittance
wavelength nm

(b)

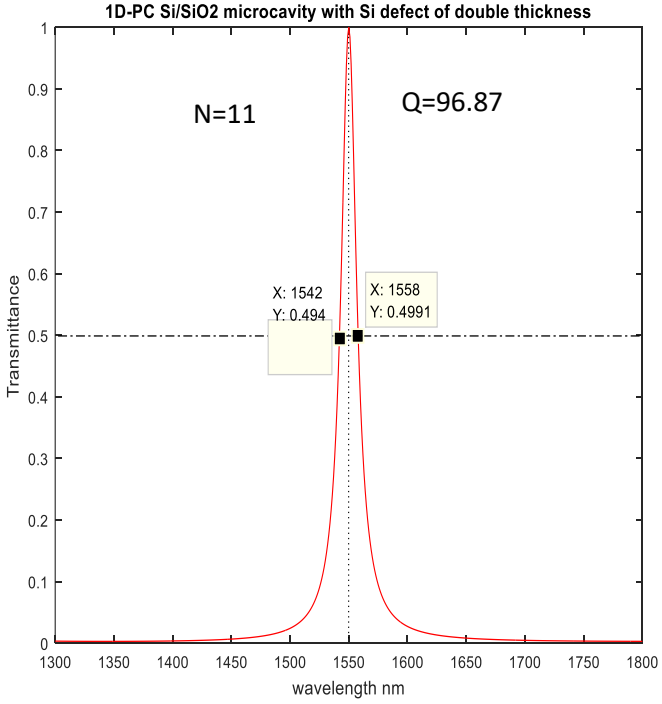
1D-PC Si/SiO2 microcavity with Si defect of double thickness
N=11
Q=96.87
X: 1542
Y: 0.494
X: 1558
Y: 0.4991
Transmittance
wavelength nm

(c)

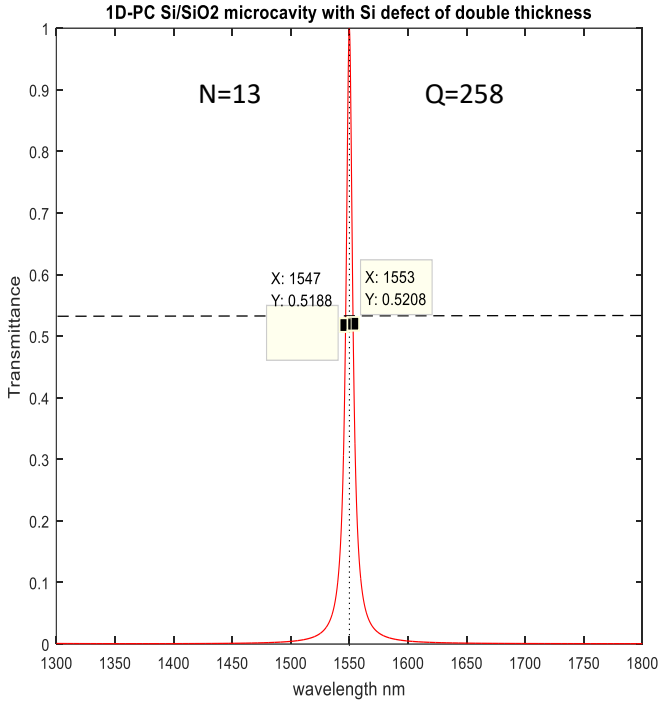


(d)

Figure 4.4: Resonant microcavity mode in $Si/SiO_2$ 1DPC with Si defect layer with $n_1 = 1.45$, $n_2 = 3.42$, $d_1 = 267.24$ nm, $d_2 = 113.30$ nm, $n_{defect} = 3.42$, $d_{defect} = 226.6$ nm, (a) N = 7, (b) N = 9, (c) N = 11, (d) N = 13.

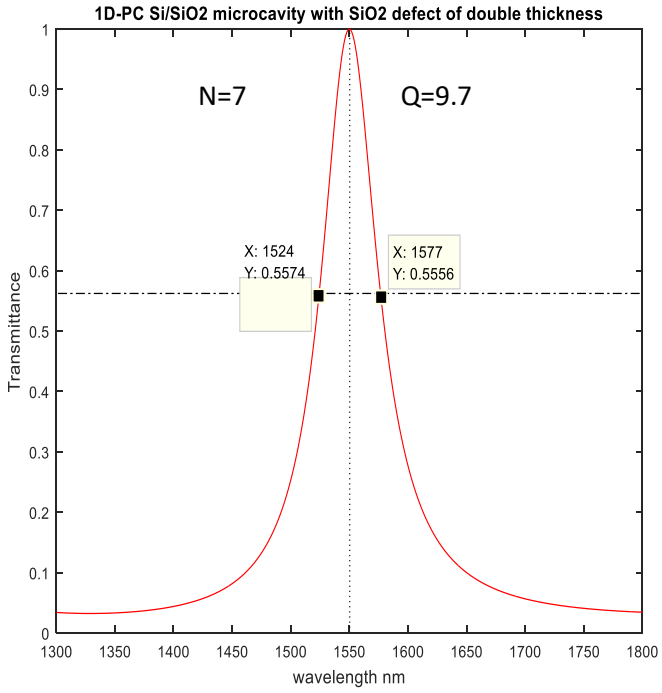


(a)

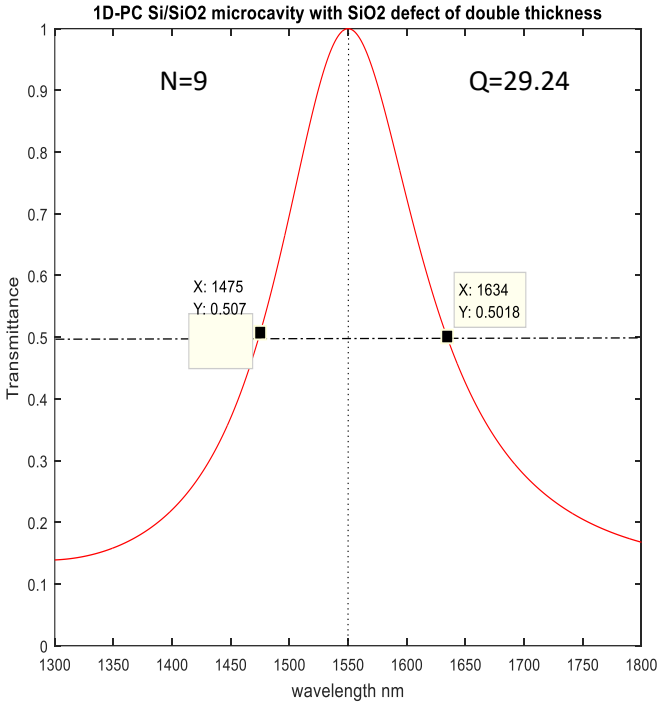
1D-PC Si/SiO2 microcavity with SiO2 defect of double thickness
N=9
Q=29.24
X: 1475
Y: 0.507
X: 1634
Y: 0.5018
Transmittance
wavelength nm

(b)

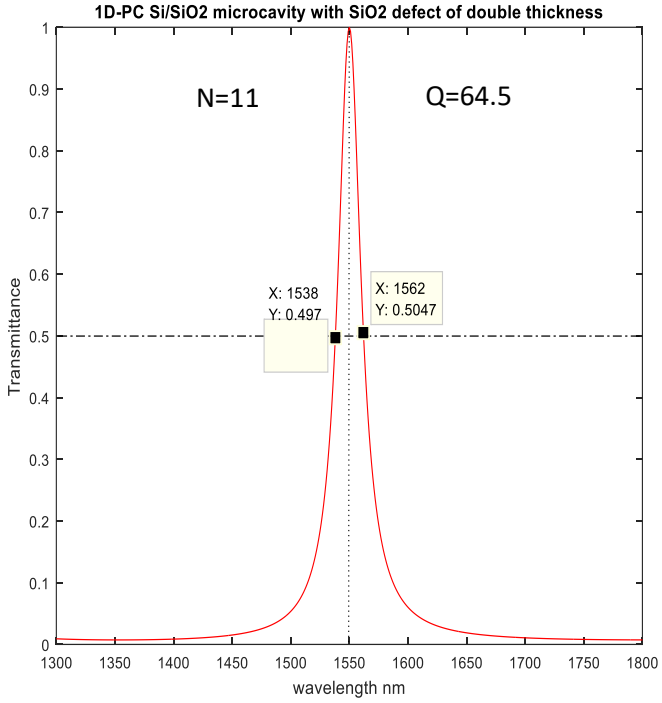
1D-PC Si/SiO2 microcavity with SiO2 defect of double thickness
N=11
Q=64.5
X: 1538
Y: 0.497
X: 1562
Y: 0.5047
Transmittance
wavelength nm

(c)

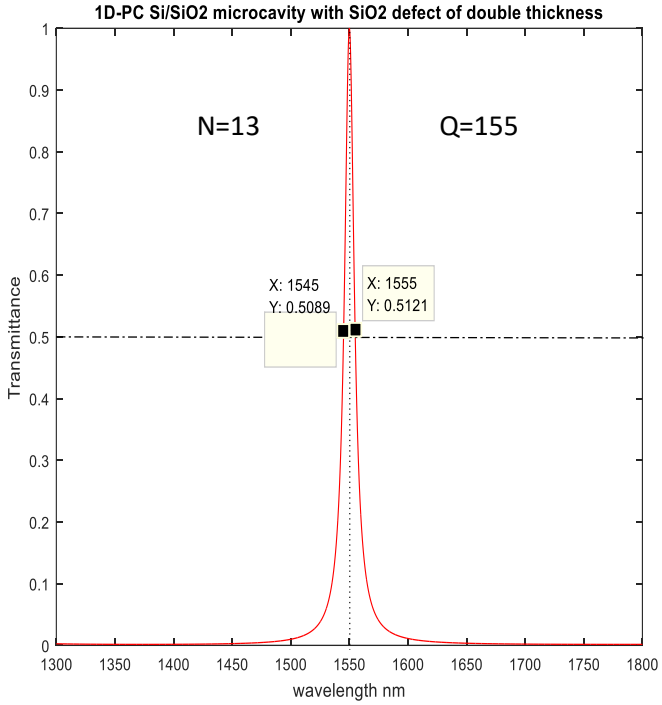


(d)

Figure 4.5: Resonant microcavity mode in $Si/SiO_2$ 1DPC with $SiO_2$ defect layer with $n_1 = 1.45$, $n_2 = 3.42$, $d_1 = 267.24$ nm, $d_2 = 113.30$ nm, $n_{defect} = 1.45$, $d_{defect} = 534.48$ nm, (a) N = 7, (b) N = 9, (c) N = 11, (d) N = 13.

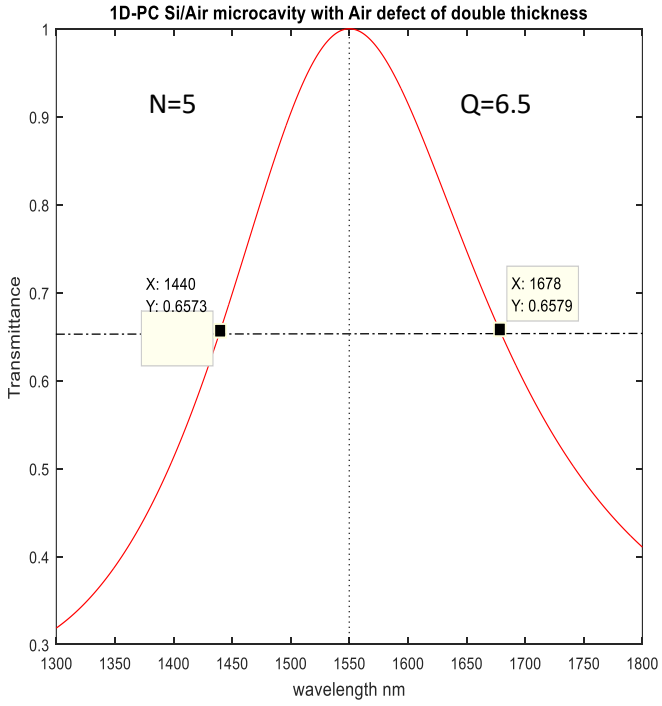


(a)

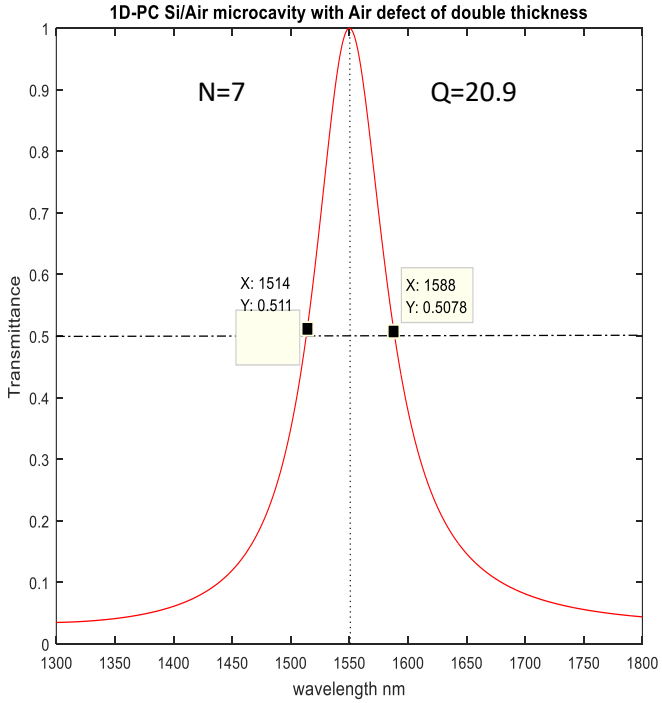
1D-PC Si/Air microcavity with Air defect of double thickness
N=7
Q=20.9
X: 1514
Y: 0.511
X: 1588
Y: 0.5078
Transmittance
wavelength nm

(b)

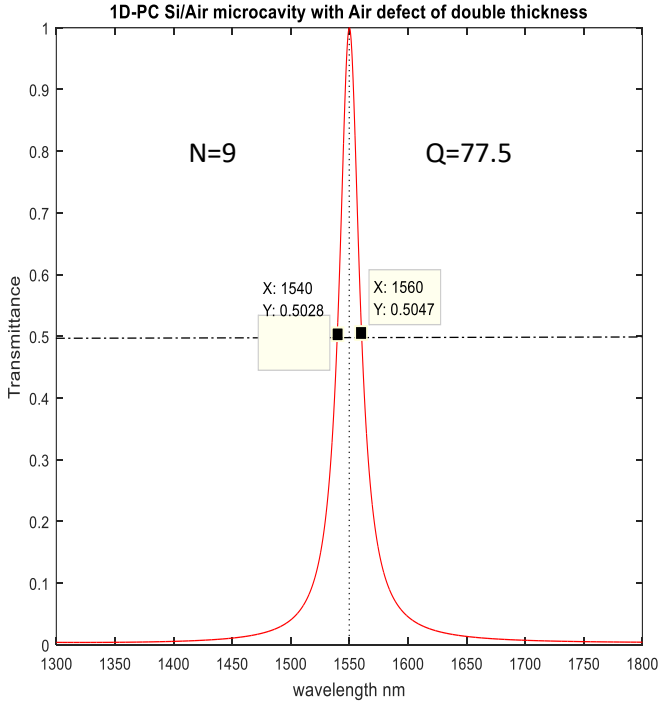
1D-PC Si/Air microcavity with Air defect of double thickness
N=9
Q=77.5
X: 1540
Y: 0.5028
X: 1560
Y: 0.5047
Transmittance
wavelength nm

(c)

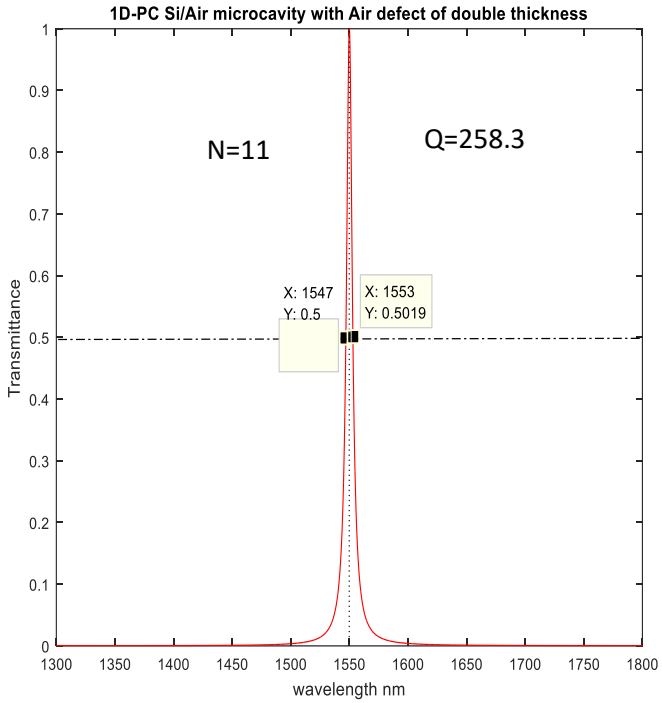


(d)

Figure 4.6: Resonant microcavity mode in Si/Air 1DPC with Air defect layer with $n_1 = 1$, $n_2 = 3.42$, $d_1 = 387.5$ nm, $d_2 = 113.30$ nm, $n_{defect} = 1$, $d_{defect} = 775$ nm, (a) N = 5, (b) N =7, (c) N = 9, (d) N = 11.

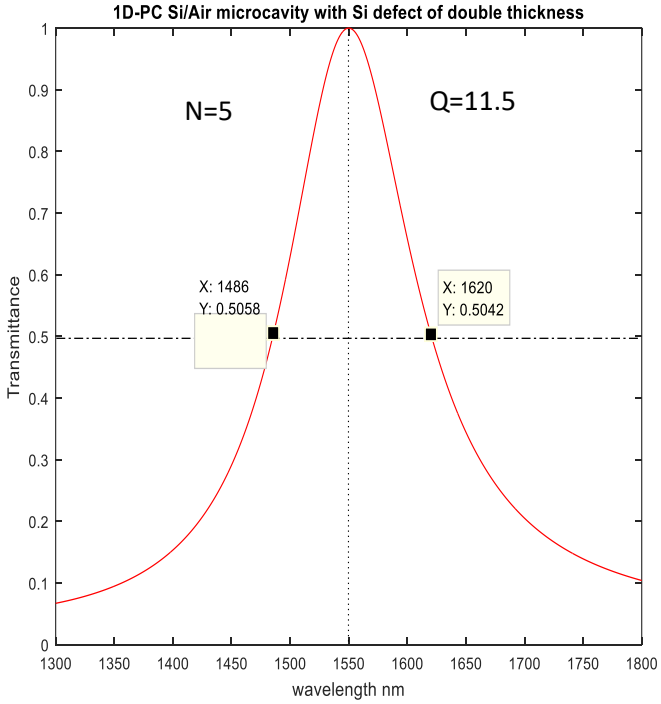


.

(a)

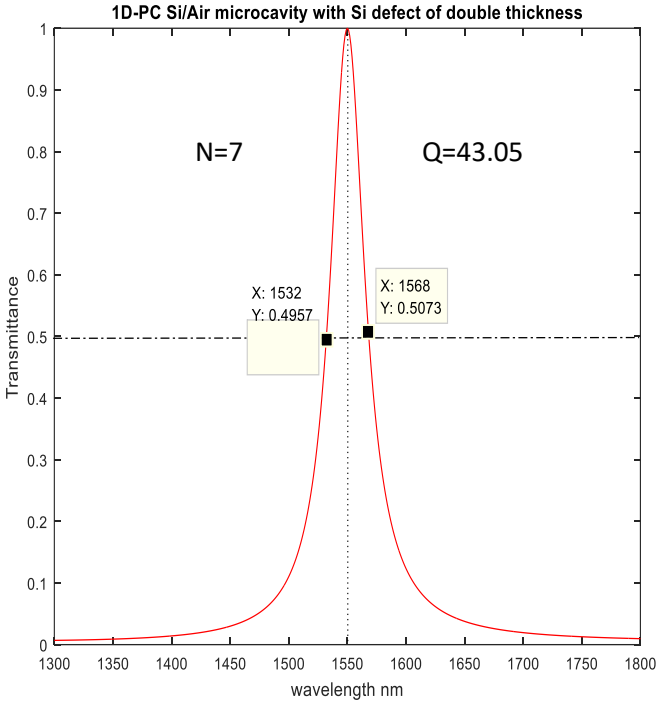
1D-PC Si/Air microcavity with Si defect of double thickness
N=7
Q=43.05
X: 1532
Y: 0.4957
X: 1568
Y: 0.5073
Transmittance
wavelength nm

(b)

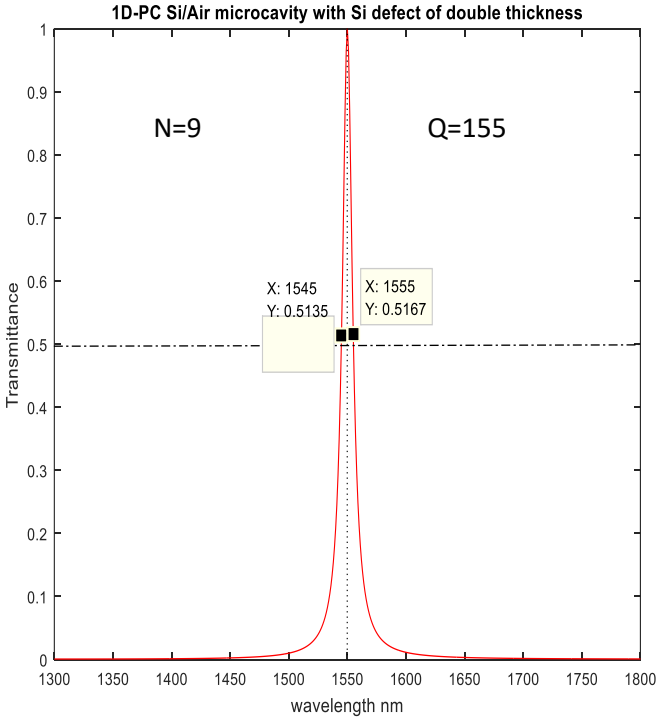
1D-PC Si/Air microcavity with Si defect of double thickness
N=9
Q=155
X: 1545
Y: 0.5135
X: 1555
Y: 0.5167
Transmittance
wavelength nm

(c)

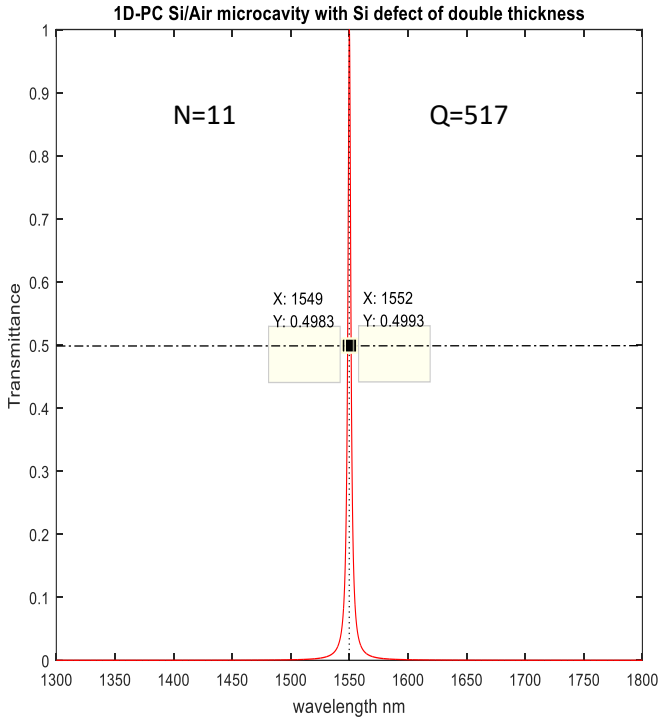


(d)

Figure 4.7: Resonant microcavity mode in Si/Air 1DPC with Si defect layer $n_1 = 1$, $n_2 = 3.42$, $d_1 = 387.5$ nm, $d_2 = 113.30$ nm, $n_{defect} = 3.42$, $d_{defect} = 226.6$ nm, (a) N = 5, (b) N = 7, (c) N = 9, (d) N = 11.

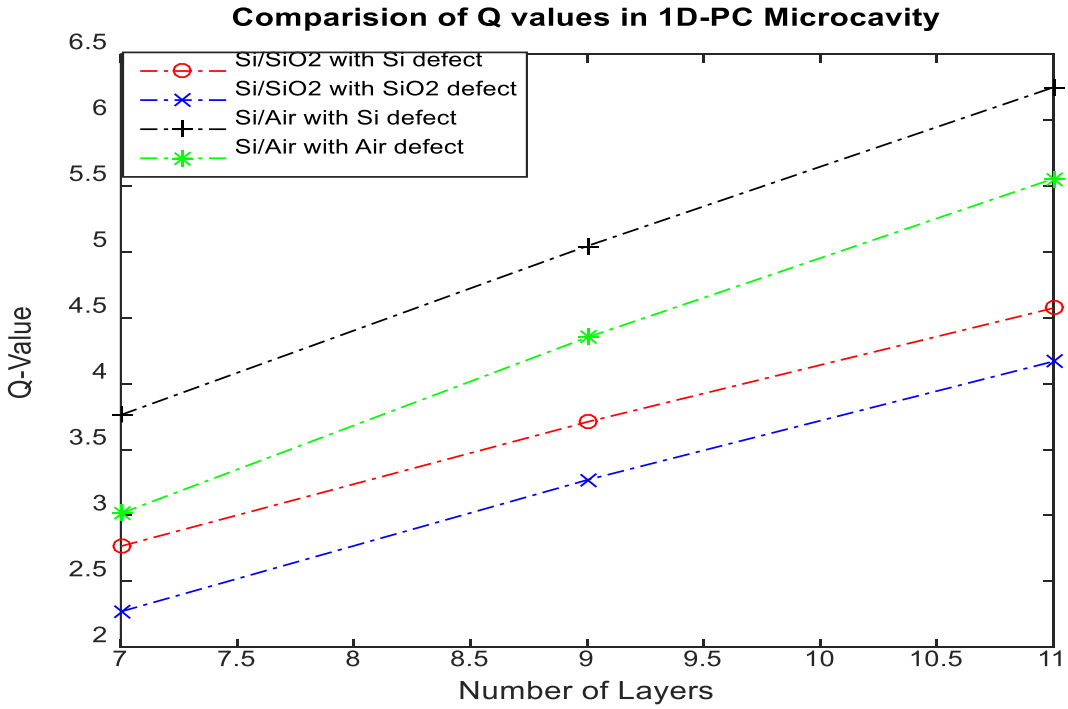

Figure 4.8: Variation of logarithmic Q-value with increasing the number of layers in $Si/SiO_2$ and Si/Air 1DPC with defect of constituent layers.

## 4.3 ONE DIMENSIONAL POROUS SILICON MICROCAVITY CHEMICAL SENSORS

We present a numerical study of the effect of anisotropy on the spectral characteristics of one dimensional porous silicon micro-cavity (1D-PSMC) with single defect layer. These structures have strong potential applications in optical sensing of chemicals and bio-analytes. Bruggeman's effective medium approximation (BEMA) and $(4 \times 4)$ general transfer matrix method (TMM) is used for theoretical modelling of the spectral response of anisotropic 1D-PSMC. The potential of this structure as a sensing material is illustrated by analysing wavelength shift in the defect mode induced by the infiltration of biochemical analytes of different refractive indices inside the pores. In recent years, porous silicon (PS) has become material of choice for designing of 1D-PC for sensing applications due to numerous advantages [4.17]. Its large surface to volume ratio, easy fabrication technology, controllable pore sizes, convenient surface chemistry and ability to modulate its refractive index as function of porosity makes it suitable for many applications [4.18].

Structures based on PS provide the necessary link between the silicon technology and optoelectronic devices. It facilitates the integration with standard micro-electronics platforms [4.19]. Porous silicon consists of many air voids (pores) and silicon residuals and can be described as a homogenous mixture of silicon and air. It is classified into three types based on porosity: nano-porous, mesoporous and macro-porous. In nano-porous and mesoporous silicon the size of the pores and the silicon residual is of the order of few to tens of nanometres so PS can be optically described as an 'effective medium' whose optical properties depend on the porosity [4.20]. 1DPC based on PS multilayer is formed by electrochemical etching where the porosity and hence the refractive index depends only on the current density once the other etching parameters are fixed. The thickness of these PS layers is controlled by etching exposure time [4.21-4.27]. Thus, by periodically varying the applied current density and the etching exposure time, a 1DPC as a dielectric multilayer structure is formed.

Bulk silicon is widely used as the target material for designing optical components because of its well-developed processing technology. Due to diamond like cubic crystalline structure, silicon offers inherent isotropic properties [4.28]. Nano-structuring can induce and control the birefringence in the bulk material. Porous silicon is known to exhibit large optical anisotropy

in the visible and infrared spectral regions [4.29]. Mesoporous silicon layers with pore dimensions of around 10nm to 30nm produced on the monocrystalline silicon substrate with low surface symmetry offers the properties of negative birefringence crystal whose birefringence magnitude can go up to $\Delta n = n_o - n_e = 0.24$, where $n_o$and $n_e$ are refractive index of ordinary ray (O-ray) and extraordinary ray (E-ray), respectively [4.30-4.31]. The magnitude of the birefringence depends on the pore size or porosity of the silicon. An increase in porosity decreases the effective index of both O-ray and E-ray but increases the difference between them resulting in an enhanced birefringence magnitude [4.32-4.33].

Large optical birefringence in (110) oriented mesoporous silicon layers was also observed [4.34]. The property of birefringence in mesoporous and nano-porous silicon enables us to develop anisotropic one dimensional porous silicon based photonic crystal (1D-PSPC) which can find potential applications as waveplates, polarization rotators, optical isolators, beam splitters and optical sensors [4.35]. The porous character of PS enables the infiltration of liquids and gases which allows further control of its optical properties and promotes its application in optical sensing devices [4.36-4.41]. Many researchers are working on the development of nano-optical devices and optical sensors using PS for the future applications because its optical properties are highly sensitive to the presence of biological or chemical specimens inside the pores. Fauchet et. al. developed optical biosensors using PS structures [4.42-4.43]. Solanki et. al. demonstrated the photovoltaic solar cell applications using PS [4.44]. Many research groups are working on characterisation and application of PS for the emerging nanotechnological applications [4.45-4.52]. Many researchers have worked theoretically and experimentally on porous silicon microcavity used for optical sensing applications [4.53-4.55].

Selective and accurate sensing of different chemical, biochemical and biological analytes is the need of the hour considering the ongoing effort to develop a sustainable environment. We present here a theoretical model of designing multi-layered 1D-PSMC with a defect layer also made up of PS for optical sensing of different chemicals, bio-chemicals and bio-analytes. We have analysed the sensitivity of this structure with and without anisotropic effects.

### 4.3.1 Theory

The sponge like structure of PS makes it suitable for optical sensing applications. The reflectance spectrum of a 1D-PSMC depends on the interferometric Fabry-Perot relationship [4.56-4.63]. Light reflected from the successive interfaces of 1D-PSMC constructively

interferes to give the reflection spectrum. The reflection spectrum fringes are governed by the thickness of layers $d$ and the effective refractive index of PS $n$, by the relation

$$\frac{m\lambda_0}{2} = n_L d_L + n_H d_H, \tag{4.2}$$

where, $m$ is an integer, $\lambda_0$ is resonance wavelength of micro-cavity, $n_L$ and $n_H$ are the low and high effective refractive index of PS and $d_L$and $d_H$ are the thickness of the layers of low and high effective refractive index of PS, respectively. When the pores of PS are filled with an analyte, the effective refractive index of PS increases from $n_{PS}$ to $n_{PS} + \Delta n$ and hence due to increased optical thickness of the structure we observe a red shift for the resonant wavelength of micro-cavity from $\lambda_0$ to $\lambda_0 + \Delta\lambda$ in the reflection spectrum. By analysing the wavelength shift $\Delta\lambda$ in the reflection spectrum, the refractive index of analyte can be estimated. The 1D-PSMC device structure depends on the effective refractive index of PS, thickness of layers $(d)$ and the porosity (P). The refractive index of PS is related to porosity by BEMA model, described by equation [4.58, 4.64-4.66]

$$(1 - \mathrm{P})\,\frac{\varepsilon_{\mathrm{Si}} - \varepsilon_{\mathrm{eff}}}{\varepsilon_{\mathrm{Si}} + 2\varepsilon_{\mathrm{eff}}} + \mathrm{P}\,\frac{\varepsilon_{\mathrm{void}} - \varepsilon_{\mathrm{eff}}}{\varepsilon_{\mathrm{void}} + 2\varepsilon_{\mathrm{eff}}} = 0. \tag{4.3}$$

Since $\varepsilon \propto n^2$ the above relation can also be written as

$$(1 - \mathrm{P})\,\frac{\mathrm{n}_{\mathrm{Si}}^2 - \mathrm{n}_{\mathrm{PS}}^2}{\mathrm{n}_{\mathrm{Si}}^2 + 2\,\mathrm{n}_{\mathrm{PS}}^2} + \mathrm{P}\,\frac{\mathrm{n}_{\mathrm{void}}^2 - \mathrm{n}_{\mathrm{PS}}^2}{\mathrm{n}_{\mathrm{void}}^2 + 2\,\mathrm{n}_{\mathrm{PS}}^2} = 0 \tag{4.4}$$

where $\varepsilon_{Si}$ and $\varepsilon_{eff}$ are the dielectric constant of silicon and PS, respectively, and $\varepsilon_{void}$ is the dielectric constant of medium inside the pores. The refractive index of silicon is $n_{Si}$ and $n_{void}$ is the refractive index of the medium inside the pores. This approximation becomes acceptable since the wavelength of incident light is near visible-NIR, which is much higher than the size of the pores so the electromagnetic radiation does not distinguish between silicon and void and treat the PS structure as a homogenous medium.

In an anisotropic layered media, the four magnetic and electric components of plane wave are no longer spatially independent and mode coupling occurs. Consequently a $4 \times 4$ matrix method is required to find the reflection and transmission coefficients. Berreman showed a general algorithm of finding reflection and transmission coefficients in an anisotropic slab using $4 \times 4$ matrix method by solving the Maxwell equations and applying boundary conditions at the interfaces [4.62]. This general algorithm can be used for both isotropic and anisotropic optical responses. Yeh [4.61] and Schubert [4.59-4.60] have developed a general

model for anisotropic and isotropic thin film systems based on Berreman's matrix formulation involving the incidence and exit medium transition matrices which is known as the general transfer matrix.

### 4.3.2 General Transfer Matrix

Consider an N layered system with parallel interfaces. Let us assume that the light wave of wave vector $k_a$ is coming from incident ambient medium $(-\infty < z < 0)$ of refractive index $n_a$ and $\Phi_a$ as the angle of incidence. Let x-z plane is the plane of incidence so $k_a$ will not have a component along y-direction. Let $A_p$ , $B_p$ represent the complex amplitudes of *p* –mode for incident and reflected waves and $A_s$ , $B_s$ represent the same for *s*-mode waves, as shown in Fig. 4.9. The exit substrate medium $(z_N < z < \infty)$ does not contain the back reflected amplitudes $(D_s = 0, D_p = 0)$, so there exist only two amplitudes $C_s$ and $C_p$ for the transmitted *s* and *p* modes.

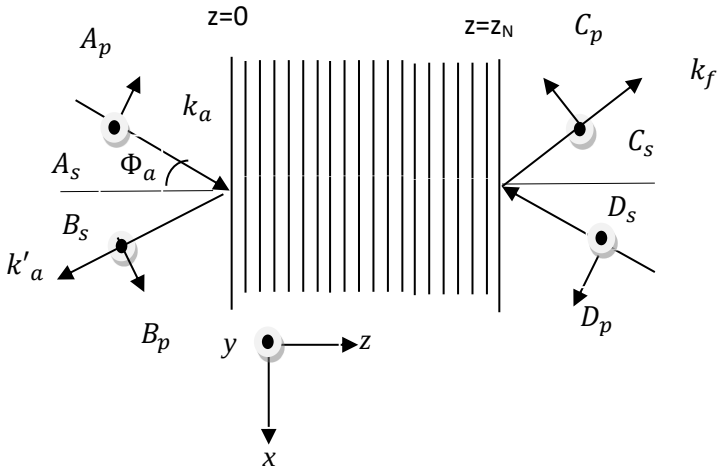


Figure 4.9: Incident, reflected and transmitted p and s modes of light wave with their wave vectors $k_a, k'_a, k_f$ , respectively.

The four complex amplitudes of incident medium and the two complex amplitudes of the exit medium are related by the general transfer matrix *T* for any multi-layered structure defined as

$$\begin{pmatrix} A_s \\ B_s \\ A_p \\ B_p \end{pmatrix} = T \begin{pmatrix} C_s \\ D_s \\ C_p \\ D_p \end{pmatrix} = \begin{pmatrix} T_{11} & T_{12} & T_{13} & T_{14} \\ T_{21} & T_{22} & T_{23} & T_{24} \\ T_{31} & T_{32} & T_{33} & T_{34} \\ T_{41} & T_{42} & T_{43} & T_{44} \end{pmatrix} \begin{pmatrix} C_s \\ 0 \\ C_p \\ 0 \end{pmatrix} \tag{4.5}$$

If $d_i$ is the thickness of $i^{th}$ layer, a partial transfer matrix $T_{ip}$ that connects the in-plane wave components at the interfaces at $z = z_i$ with those at the next interface at $z = z_i + d_i$ can be defined for both isotropic and anisotropic layers. Hence the ordered product of these partial matrices for all *N* layers connect the in-plane components from first interface $(z = 0)$ to last interface$(z = z_N)$. Similarly, the incident matrix $L_a$ projects the in-plane wave components of incident and reflected waves at the first interface and the exit matrix $L_f$ projects the transmitted amplitudes from last interface to the exit medium. The general transfer matrix *T* as defined in Eq. (4.5) can be obtained by Schubert's method [4.60] taking the product of all inverted partial matrices $T_{ip}$ for each layer and the incident matrix and exit matrix in order of their existence.

$$T = {L_a}^{-1} \prod_{i=1}^{N} \left[T_{ip}(d_i)\right]^{-1} \; L_f = {L_a}^{-1} \prod_{i=1}^{N} T_{ip}(-d_i) \; L_f \tag{4.6}$$

$T_{ip}$ does not require matrix inversion due to symmetry of coordinate system and the incident matrix and exit matrix is described as follows:

$${L_a}^{-1} = \frac{1}{2} \begin{pmatrix} 0 & 1 & -1/(n_a \cos \Phi_a) & 0 \\ 0 & 1 & 1/(n_a \cos \Phi_a) & 0 \\ 1/\cos \Phi_a & 0 & 0 & 1/n_a \\ -1/\cos \Phi_a & 0 & 0 & 1/n_a \end{pmatrix} \tag{4.7}$$

$$L_f = \begin{pmatrix} 0 & 0 & \sqrt{1 - \left[\left(n_a/n_f\right) \sin \Phi_a\right]^2} & 0 \\ 1 & 0 & 0 & 0 \\ -n_f \sqrt{1 - \left[\left(n_a/n_f\right) \sin \Phi_a\right]^2} & 0 & 0 & 0 \\ 0 & 0 & n_f & 0 \end{pmatrix} \tag{4.8}$$

where $n_f$ is the refractive index of exit medium. The partial transfer matrix $T_p$ is defined as follows

$$T_p = \exp\left(i \frac{\omega}{c} \Delta d\right) \tag{4.9}$$

This matrix connects the in-plane components of electric and magnetic field at interfaces separated by a distance $d$. The frequency of incident light is $\omega$ and velocity of light is $c$. The matrix $\Delta$ defined in Eq. (4.9) depends on the dielectric tensor $\varepsilon$ and the $x-$ component $k_x$ of wave vector $k_a$ as follows

$$\Delta = \begin{pmatrix} -k_x \frac{\varepsilon_{zx}}{\varepsilon_{zz}} & -k_x \frac{\varepsilon_{zy}}{\varepsilon_{zz}} & 0 & 1 - \frac{{k_x}^2}{\varepsilon_{zz}} \\ 0 & 0 & -1 & 0 \\ \varepsilon_{yz} \frac{\varepsilon_{zx}}{\varepsilon_{zz}} - \varepsilon_{yx} & {k_x}^2 - \varepsilon_{yy} + \varepsilon_{yz} \frac{\varepsilon_{zy}}{\varepsilon_{zz}} & 0 & k_x \frac{\varepsilon_{yz}}{\varepsilon_{zz}} \\ \varepsilon_{xx} - \varepsilon_{xz} \frac{\varepsilon_{zx}}{\varepsilon_{zz}} & \varepsilon_{xy} - \varepsilon_{xz} \frac{\varepsilon_{zy}}{\varepsilon_{zz}} & 0 & -k_x \frac{\varepsilon_{xz}}{\varepsilon_{zz}} \end{pmatrix} \tag{4.10}$$

where $\varepsilon_{nm}$ are the components of dielectric tensor. The reflection and transmission coefficients of the multi-layered system can be calculated using the general transfer matrix elements of $T$ as demonstrated by Yeh [4.61].

$$r_{ss} = \left(\frac{B_s}{A_s}\right) = \frac{T_{21}T_{33} - T_{23}T_{31}}{T_{11}T_{33} - T_{13}T_{31}} \tag{4.11}$$

$$r_{pp} = \left(\frac{B_p}{A_p}\right) = \frac{T_{11}T_{43} - T_{41}T_{13}}{T_{11}T_{33} - T_{13}T_{31}} \tag{4.12}$$

$$t_{ss} = \left(\frac{C_s}{A_s}\right) = \frac{T_{33}}{T_{11}T_{33} - T_{13}T_{31}} \tag{4.13}$$

$$t_{pp} = \left(\frac{C_p}{A_p}\right) = \frac{T_{11}}{T_{11}T_{33} - T_{13}T_{31}} \tag{4.14}$$

The reflectance R and transmittance ţ can be calculated as

$$R = |r|^2 \tag{4.15}$$

$$ţ = \frac{n_f}{n_a}|t|^2 \tag{4.16}$$

### 4.3.3 Isotropic Transfer Matrix

The $(4 \times 4)$ general transfer matrix reduces to $(2 \times 2)$ isotropic transfer matrix when we ignore the anisotropic effects. In an isotropic layered media, the p-modes (electric field vector parallel to the plane of incidence) and s- modes (electric field vector perpendicular to the plane of incidence) of a plane electromagnetic wave are uncoupled and they are dealt independently with $2 \times 2$ Abéles matrix method [4.72-4.75] for finding the reflection and transmission coefficients. The matrix $\Delta$ defined in Eq. (4.10) is now modified in isotropic 1D-PSMC as

$$\Delta = \begin{pmatrix} -k_x \frac{\varepsilon_{zx}}{\varepsilon_{xx}} & -k_x \frac{\varepsilon_{zy}}{\varepsilon_{xx}} & 0 & 1 - \frac{{k_x}^2}{\varepsilon_{xx}} \\ 0 & 0 & -1 & 0 \\ \varepsilon_{yz} \frac{\varepsilon_{zx}}{\varepsilon_{xx}} - \varepsilon_{yx} & {k_x}^2 - \varepsilon_{xx} + \varepsilon_{yz} \frac{\varepsilon_{zy}}{\varepsilon_{xx}} & 0 & k_x \frac{\varepsilon_{yz}}{\varepsilon_{xx}} \\ \varepsilon_{xx} - \varepsilon_{xz} \frac{\varepsilon_{zx}}{\varepsilon_{xx}} & \varepsilon_{xy} - \varepsilon_{xz} \frac{\varepsilon_{zy}}{\varepsilon_{xx}} & 0 & -k_x \frac{\varepsilon_{xz}}{\varepsilon_{xx}} \end{pmatrix} \quad (4.17)$$

The modified partial transfer matrix $T_p$ , and the isotropic transfer matrix T is calculated by Eq. (4.9) and Eq. (4.6), respectively. The reflection and transmission coefficients of the isotropic multi-layered system can be calculated using the Eqs. (4.11-4.14).

### 4.3.4 Results and Discussion

We have analysed and compared the effect of anisotropy on the spectral characteristics and sensitivity of two photonic bandgap microcavity sensors 1D-PSMC-1 and 1D-PSMC-2 of same constituent materials but different thickness parameters. Each structure consists of 12 alternate layers of porous silicon with different porosity and a defect layer of porous silicon in the middle of structure as shown in Fig. 4.10.

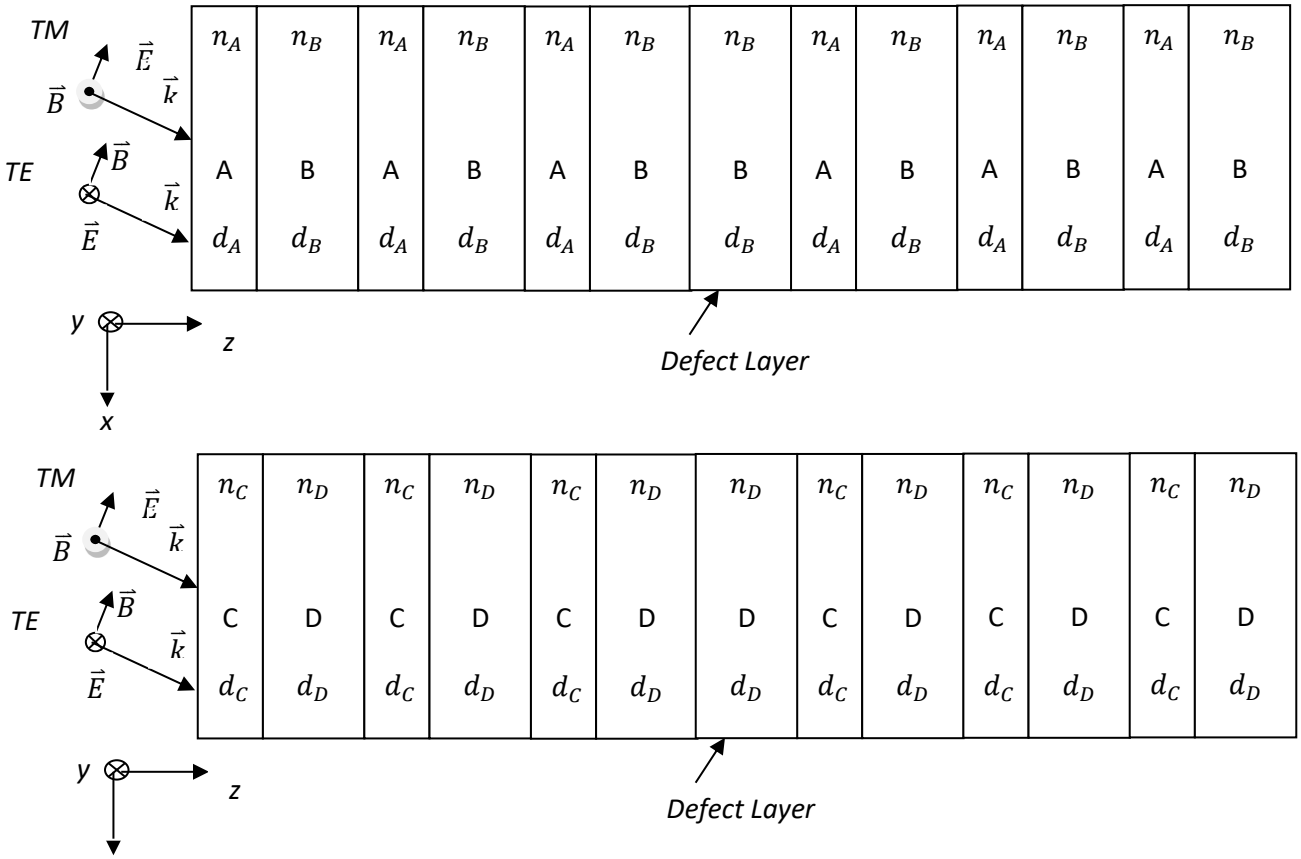


Figure 4.10: Schematic diagram of (a) 1D-PSMC-1 and (b) 1D-PSMC-2

### 4.3.5 Anisotropic 1D-PSMC Sensor

Optical anisotropy in porous silicon required anisotropic etching of Si where etching rate differs for different crystallographic directions. As a result, the pores in porous silicon are elongated in the direction of larger etching rate and are oriented in the direction perpendicular to the etching plane [4.73]. This leads to violation of cubic symmetry of Si single crystal. Etching (110) plane gives in-plane negative uniaxial anisotropy due to anisotropic dielectric nano-structuring. Both the anisotropic 1D-PSMC structures consists of 12 periodic alternating anisotropic negative uniaxial porous silicon layers A and C with porosity of 0.46 and B and D with porosity 0.72, respectively as shown in Fig. (4.10). The periodicity is broken by inserting a defect layer of porosity 0.72 in the middle of both the sensor structures. We assume the Cartesian principal axes of all the anisotropic porous silicon layers including the defect layer oriented parallel to the axes of the laboratory coordinate system so that the azimuthal angle for all the layers is zero in both the sensors. The refractive index of incident and exit medium is taken as air ($n_a = 1, n_f = 1$) and the angle of incidence for both sensor structures is taken as $\Phi_a = 10°$. The dielectric tensor of all the layers including the defect layers in both the sensors becomes diagonally anisotropic of the form

$$\varepsilon = \begin{pmatrix} \varepsilon_{xx} & 0 & 0 \\ 0 & \varepsilon_{yy} & 0 \\ 0 & 0 & \varepsilon_{zz} \end{pmatrix} \tag{4.18}$$

We have applied BEMA model to find the elements of dielectric tensor in both the anisotropic 1D-PSMC sensors. In the case of 1D-PSMC-1, the porosity of layer A and B gives the elements of dielectric tensor as $\varepsilon_{A_{xx}} = 5.01, \varepsilon_{A_{yy}} = 4.8, \varepsilon_{A_{zz}} = 5.01$ and $\varepsilon_{B_{xx}} = 2.25,\ \varepsilon_{B_{yy}} = 1.85, \varepsilon_{B_{zz}} = 2.25$ using Eqs. (4.4-4.5). In anisotropic 1D-PSMC -2, the porosity of constituent layers is same as of anisotropic 1D-PSMC-1, so the elements of dielectric tensor will be $\varepsilon_{C_{xx}} = 5.01, \varepsilon_{C_{yy}} = 4.8, \varepsilon_{C_{zz}} = 5.01$ and $\varepsilon_{D_{xx}} = 2.25,\ \varepsilon_{D_{yy}} = 1.85, \varepsilon_{D_{zz}} = 2.25.$ The dielectric tensor elements of defect layers are taken as $\varepsilon_{D_{xx}} = 2.25,\ \varepsilon_{D_{yy}} = 1.85, \varepsilon_{D_{zz}} = 2.25$ for both the anisotropic sensors. The refractive indices for ordinary and extraordinary rays for both layer A and layer C are 2.24 and 2.19, respectively. The refractive indices for ordinary and extraordinary rays for both layer B and layer D are 1.5 and 1.36, respectively [4.30]. In 1D-PSMC-1, the thickness of A layer is taken as 89.3 nm and the thickness of B layer and the defect layer is taken as 163 nm. In 1D-PSMC-2 sensor, the thickness of C layer is taken as 178.6 nm and the thickness of D layer and the defect layer is taken as 163 nm.

We have used General transfer matrix to calculate the reflectivity of both 1D-PSMC sensors. The selected wavelength range of interest is from 400 nm to 2000 nm. The numerically designed anisotropic 1D-PSMC-1 structure has micro-cavity mode at $\lambda = 833$ nm for s-polarization and at $\lambda = 895$ nm for p-polarization for air inside the pores ($n_{void} = 1$) as shown in Fig. (4.11). Designed anisotropic 1D-PSMC-2 structure has microcavity mode at $\lambda = 1137$ nm for s-polarization and at $\lambda = 1216$ nm for p-polarization for ($n_{void} = 1$) as shown in Fig. (4.12). When the biochemical analyte is introduced inside the pores, the refractive index of all porous silicon layers increases, thus increasing the optical path of the waves which corresponds to red shift in the micro-cavity wavelength ($\Delta\lambda$). We have observed a linear relationship between increase in refractive index inside the pores ($\Delta n$) and the red shift of micro-cavity wavelength $\Delta\lambda$ for both the polarizations. The estimated red shift $\Delta\lambda$ for different refractive index of the analyte is shown in Table-(4.3-4.6) for both anisotropic 1D-PSMC sensors. The observed wavelength shift with ($n_{void} > 1$) for both the anisotropic sensors is shown in Fig. (4.13-4.16) for both the polarizations. Thus, we get a fair idea of the refrative index of chemical or bio-analyte through our designed Anisotropic 1D-PSMC structures.

Table 4.3: Wavelength red-shift in anisotropic 1D-PSMC-1 with change in the refractive index of analyte inside the pores for s-polarization

Anisotropic 1D-PSMC-1, s-polarization ($\theta = 10°$)

| Refractive index of Analyte inside the pores | Micro-cavity wavelength (nm) with air in pores ( $n_{void}$ =1) | Micro-cavity wavelength (nm) with analyte in pores ( $n_{void} > 1$ ) | wavelength shift ($\Delta\lambda$) nm |
|---|---|---|---|
| 1.1 | 833 | 855 | 22 |
| 1.2 | 833 | 874 | 41 |
| 1.3 | 833 | 893 | 60 |
| 1.4 | 833 | 909 | 76 |
| 1.5 | 833 | 925 | 92 |

Table 4.4: Wavelength red-shift in anisotropic 1D-PSMC-1 with change in the refractive index of analyte inside the pores for p-polarization.

Anisotropic 1D-PSMC-1, p- polarization (θ = 10°)

| Refractive index of Analyte inside the pores | Micro-cavity wavelength (nm) with air in pores ( $n_{void}$ =1) | Micro-cavity wavelength (nm) with analyte in pores ( $n_{void} > 1$ ) | wavelength shift ($\Delta\lambda$) nm |
|---|---|---|---|
| 1.1 | 895 | 911 | 16 |
| 1.2 | 895 | 926 | 31 |
| 1.3 | 895 | 939 | 44 |
| 1.4 | 895 | 952 | 57 |
| 1.5 | 895 | 964 | 69 |

Table 4.5: Wavelength red-shift in anisotropic 1D-PSMC-2 with change in the refractive index of analyte inside the pores for s-polarization

Anisotropic 1D-PSMC-2, s-polarization (θ = 10°)

| Refractive index of Analyte inside the pores | Micro-cavity wavelength (nm) with air in pores ( $n_{void}$ =1) | Micro-cavity wavelength (nm) with analyte in pores ( $n_{void} > 1$ ) | wavelength shift ($\Delta\lambda$) nm |
|---|---|---|---|
| 1.1 | 1137 | 1166 | 29 |
| 1.2 | 1137 | 1192 | 55 |
| 1.3 | 1137 | 1216 | 79 |
| 1.4 | 1137 | 1238 | 101 |
| 1.5 | 1137 | 1258 | 121 |

Table 4.6: Wavelength red-shift in anisotropic 1D-PSMC-2 with change in the refractive index of analyte inside the pores for p-polarization

Anisotropic 1D-PSMC-2, p- polarization (θ = 10°)

| Refractive index of Analyte inside the pores | Micro-cavity wavelength (nm) with air in pores ( $n_{void}$ =1) | Micro-cavity wavelength (nm) with analyte in pores ( $n_{void} > 1$ ) | wavelength shift ($\Delta\lambda$) nm |
|---|---|---|---|
| 1.1 | 1216 | 1238 | 22 |
| 1.2 | 1216 | 1259 | 43 |
| 1.3 | 1216 | 1277 | 61 |
| 1.4 | 1216 | 1294 | 78 |
| 1.5 | 1216 | 1310 | 94 |

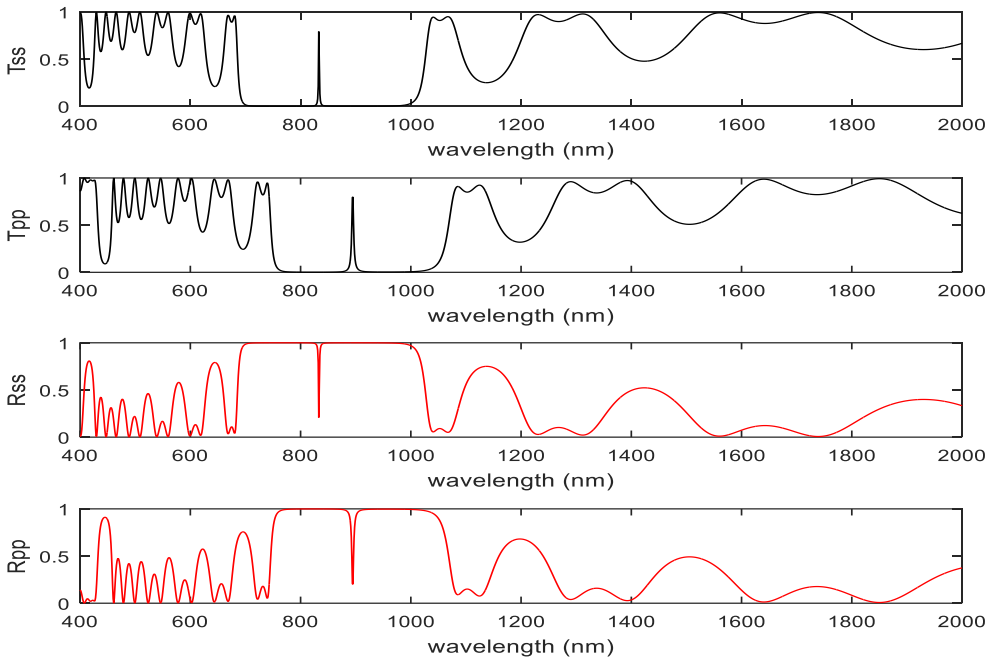


Figure 4.11: The reflectance (red lines) and transmittance (black lines) spectrum for s and p-polarizations for anisotropic 1D-PSMC-1 for $n_{void} = 1$

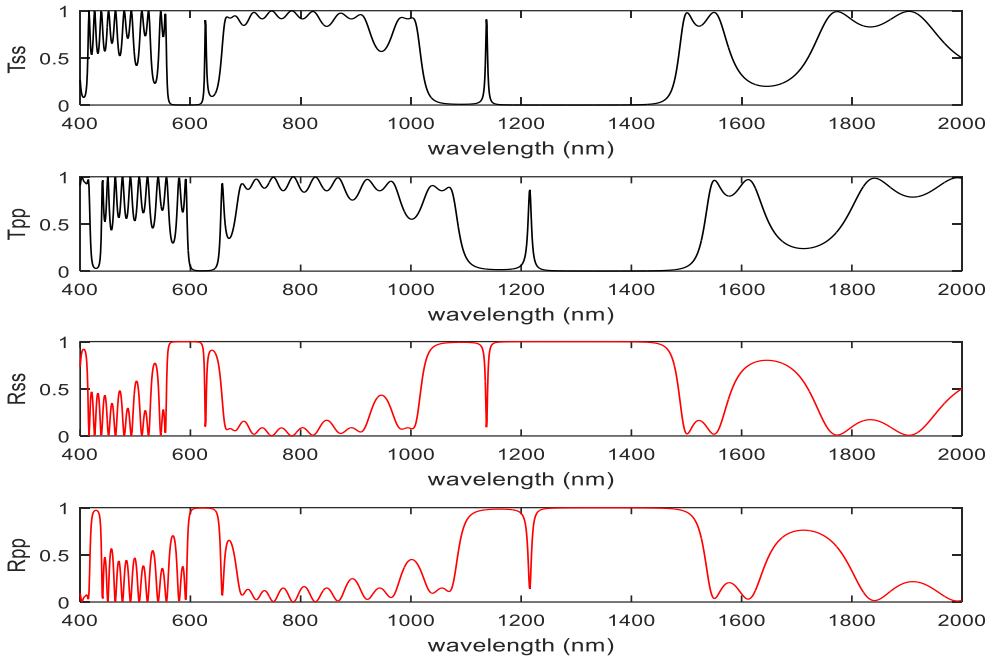


Figure 4.12: The reflectance (red lines) and transmittance (black lines) spectrum for s and p-polarizations for anisotropic 1D-PSMC-2 for $n_{void} = 1$

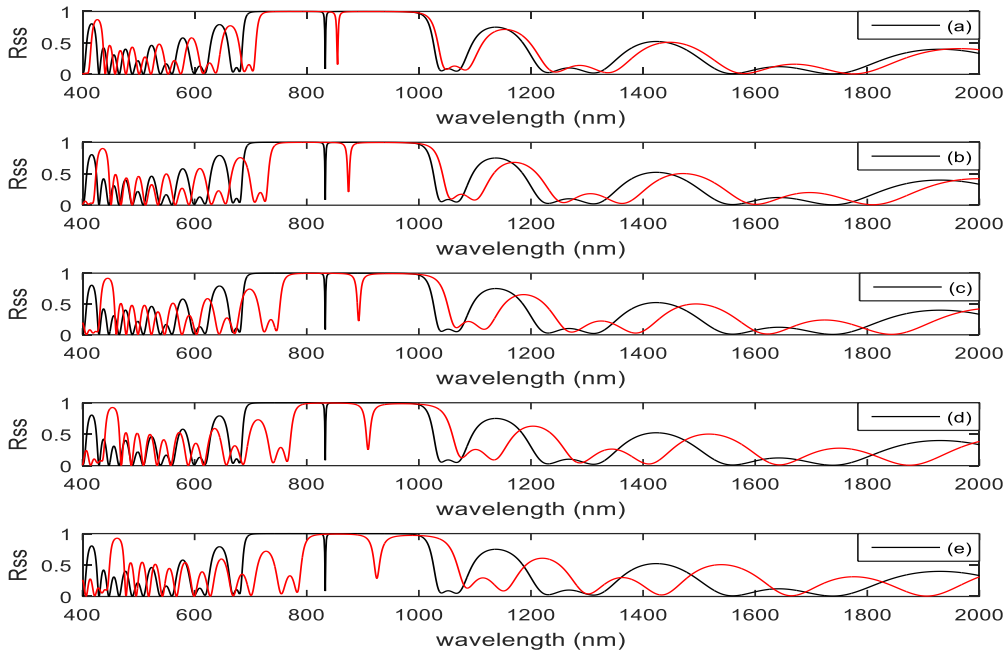


Figure 4.13: Reflection spectrum of anisotropic 1D-PSMC-1 sensor and wavelength red-shift observed with change in the refractive index of analyte inside the pores (red lines) (a) $n_{void} =$

1.1 (b) $n_{void} = 1.2$ (c) $n_{void} = 1.3$ (d) $n_{void} = 1.4$ (e) $n_{void} = 1.5$, with respect to air in pores ($n_{void} = 1$) for s-polarization (black lines).

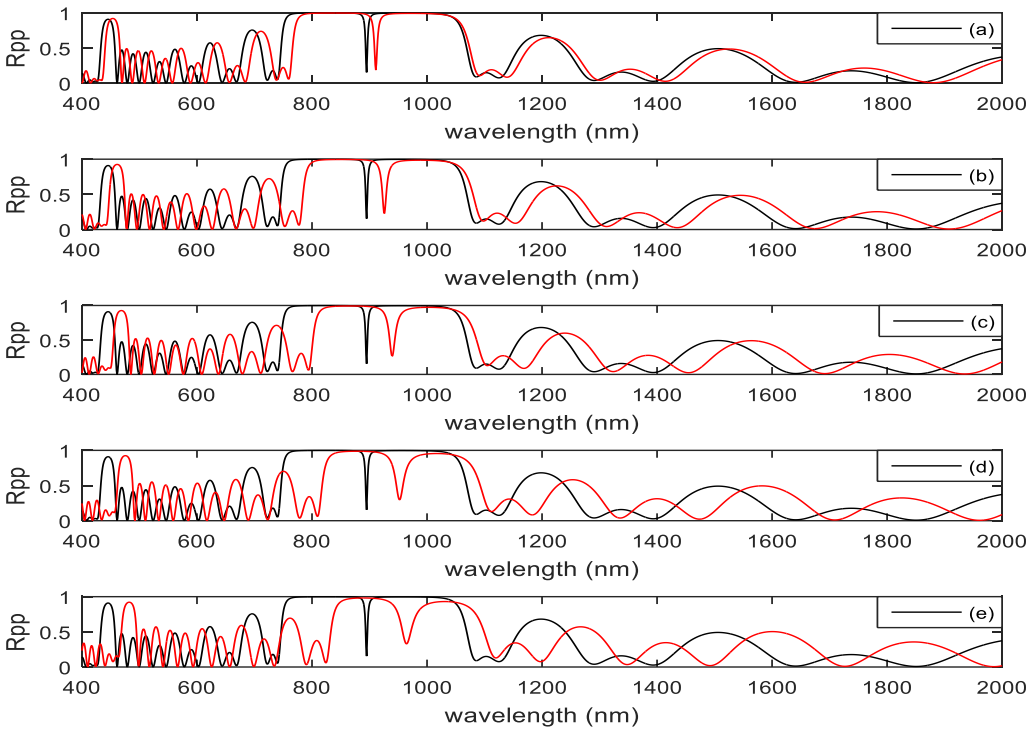


Figure 4.14: Reflection spectrum of anisotropic 1D-PSMC-1 sensor and wavelength red-shift observed with change in the refractive index of analyte inside the pores (red lines) (a) $n_{void} = 1.1$ (b) $n_{void} = 1.2$ (c) $n_{void} = 1.3$ (d) $n_{void} = 1.4$ (e) $n_{void} = 1.5$ with respect to air in pores ($n_{void} = 1$) for p-polarization (black lines).

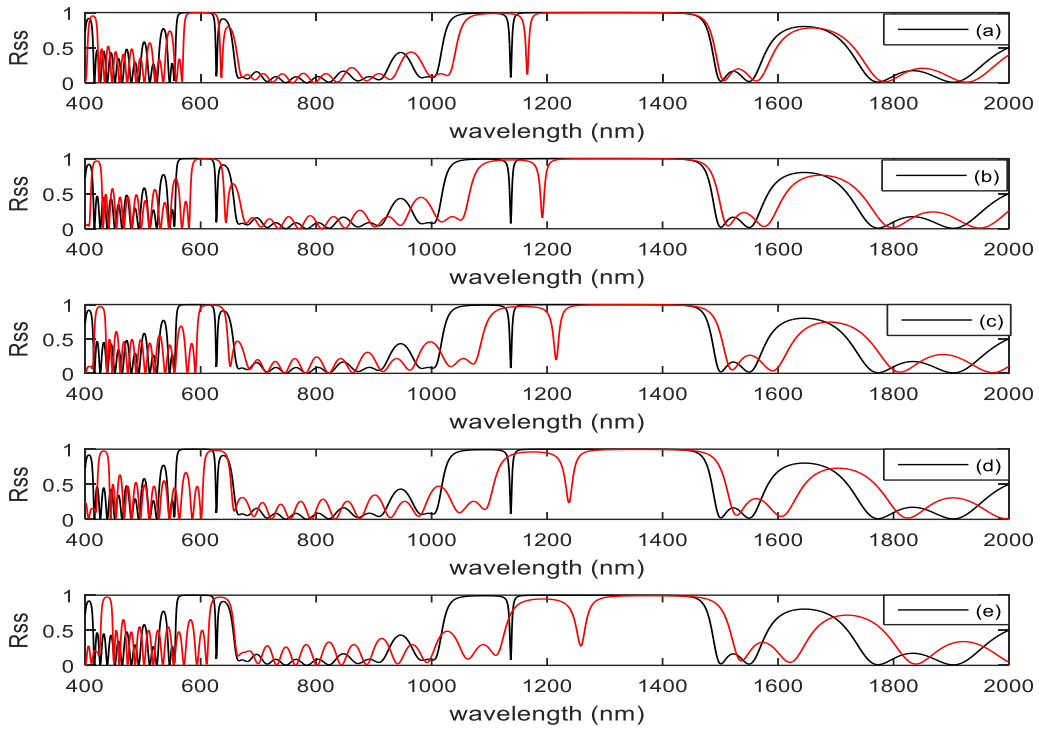


Figure 4.15: Reflection spectrum of anisotropic 1D-PSMC-2 sensor and wavelength red-shift observed with change in the refractive index of analyte inside the pores (red lines) (a) $n_{void} = 1.1$ (b) $n_{void} = 1.2$ (c) $n_{void} = 1.3$ (d) $n_{void} = 1.4$ (e) $n_{void} = 1.5$ with respect to air in pores ($n_{void} = 1$) for s-polarization (black lines).

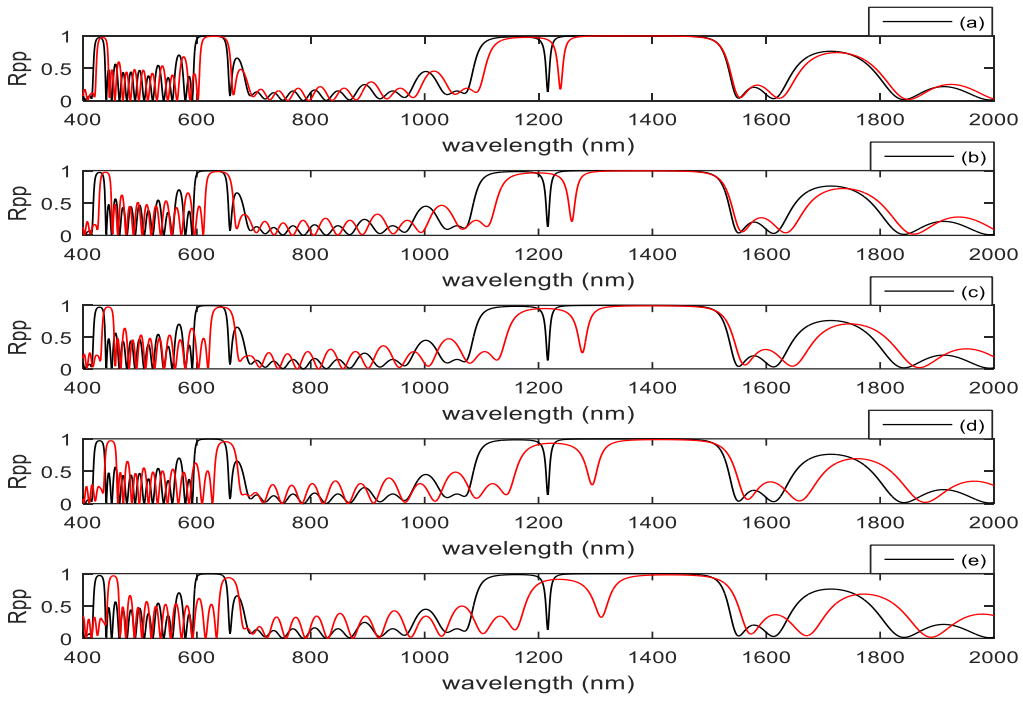

Figure 4.16: Reflection spectrum of anisotropic 1D-PSMC-2 sensor and wavelength red-shift observed with change in the refractive index of analyte inside the pores (red lines) (a) $n_{void} = 1.1$ (b) $n_{void} = 1.2$ (c) $n_{void} = 1.3$ (d) $n_{void} = 1.4$ (e) $n_{void} = 1.5$ with respect to air in pores ($n_{void} = 1$) for p-polarization (black lines).

### 4.3.6 Isotropic 1D-PSMC Sensor

Porous (100) Si surfaces have isotropic in-plane optical properties due to the equivalence of (010) and (001) crystallographic planes [4.31]. As a result, the pores in porous silicon are not elongated in a particular direction which leads to no violation of cubic symmetry of Si crystal. In our isotropic sensors 1D-PSMC-1 and 1D-PSMC-2 we have ignored the anisotropic effects and all the other design parameters of 1D-PSMC-1 and 1D-PSMC-2 remains the same as of anisotropic sensors. The refractive index of incidence and exit medium is taken as air ($n_a = 1, n_f = 1$). The angle of incidence on this structure is taken as $\Phi_a = 0°$. The dielectric tensor of all the layers of porous silicon including the defect layer for both the isotropic sensors is of the form

$$\varepsilon = \begin{pmatrix} \varepsilon_{xx} & 0 & 0 \\ 0 & \varepsilon_{xx} & 0 \\ 0 & 0 & \varepsilon_{xx} \end{pmatrix} \tag{4.19}$$

BEMA model as referred in previous section II is applied to calculate the elements of dielectric tensor in both isotropic sensors. In isotropic 1D-PSMC-1 sensor the porosity of layer A gives the elements of dielectric tensor of A as $\varepsilon_{A_{xx}} = \varepsilon_{A_{yy}} = \varepsilon_{A_{zz}} = 5.01$ and the porosity of B layer gives $\varepsilon_{B_{xx}} = \varepsilon_{B_{yy}} = \varepsilon_{B_{zz}} = 2.25$ and the dielectric tensor elements of defect layer is taken as $\varepsilon_{B_{xx}} = \varepsilon_{B_{yy}} = \varepsilon_{B_{zz}} = 2.25$ . In isotropic 1D-PSMC -2, the porosity of constituent layers is same as isotropic 1D-PSMC-1, so the elements of dielectric tensor will be $\varepsilon_{C_{xx}} = \varepsilon_{C_{yy}} = \varepsilon_{C_{zz}} = 5.01$ and $\varepsilon_{D_{xx}} = \varepsilon_{D_{yy}} = \varepsilon_{D_{zz}} = 2.25$. The dielectric tensor elements of defect layers are taken as $\varepsilon_{D_{xx}} = \varepsilon_{D_{yy}} = \varepsilon_{D_{zz}} = 2.25$ for both the isotropic sensors. In isotropic 1D-PSMC-1 sensor the refractive index of layer A, B and the defect layer is 2.24, 1.5, and 1.5 respectively to match with anisotropic 1D-PSMC-1. In isotropic 1D-PSMC-2 sensor the refractive index of layer C, D and defect layer is 2.24, 1.5, and 1.5 respectively to match with anisotropic 1D-PSMC-2. The thickness of A layer, B layer and the defect layer in isotropic 1D-PSMC -1 is $89.3\ nm, 163\ nm, 163\ nm$ respectively to match with anisotropic 1D-PSMC-1. The thickness of C layer, D layer and the defect layer in isotropic 1D-PSMC-2 is $178.6\ nm, 163\ nm, 163\ nm$ respectively to match with anisotropic 1D-PSMC-2.

We have used the isotropic transfer matrix referred in subsection B of section II to calculate the reflectivity of both isotropic 1D-PSMC sensors. The reflectivity for different polarizations $R_{ss}, R_{pp}$ and the transmissivity $T_{ss}$ , $T_{pp}$ for both sensors is shown in Figs. (4.17- 4.18) with air inside the pores ($n_{void} = 1$). The designed isotropic 1D-PSMC-1 structure is having the micro-cavity resonant wavelength at $\lambda_0 = 907$ nm for both s-polarization and p-polarization with $n_{void} = 1$ as shown in Fig. (4.17). The designed isotropic 1D-PSMC-2 sensor is having the microcavity wavelength at $\lambda_0 = 1234$ nm for both the polarizations with $n_{void} = 1$ as shown in Fig. (4.18). When the biochemical analyte is introduced inside the pores, the refractive index of constituent layers in both the sensors increases, thus increasing the optical path of the waves which corresponds to red shift in the micro-cavity wavelength ($\Delta\lambda$). We observed a linear relationship between the increase of refractive index inside the pores to the red shift of micro-cavity wavelength $\Delta\lambda$ in both the sensors for both the polarizations. It was also shown experimentally by Patel et.al. [4.57] that after the complete evaporation of chemical analyte, the micro-cavity wavelength returns to its initial position at $n_{void} = 1$. This implies that the wavelength shift is indicative of the presence of chemical analyte inside the pores.

The observed red shift in the microcavity wavelength with the change in refractive index inside the pores is shown in Tables (4.7-4.8) in both the isotropic sensors for both the polarizations. The observed wavelength shift for both isotropic sensors with ($n_{void} > 1$) is also shown in Figs. (4.19-4.20) for both the polarizations.

Table 4.7 : Wavelength red-shift observed in isotropic 1D-PSMC-1 with change in the refractive index of analyte inside the pores for s-polarization and p-polarization.

Isotropic 1D-PSMC-1, s-polarization and p-polarization ($\theta = 0^{\circ}$)

| Refractive index of Analyte inside the pores | Micro-cavity wavelength (nm) with air in pores ( $n_{void}$ =1) | Micro-cavity wavelength(nm) with analyte in pores ( $n_{void} > 1$ ) | wavelength shift ($\Delta\lambda$) nm |
|---|---|---|---|
| 1.1 | 907 | 924 | 17 |
| 1.2 | 907 | 939 | 32 |
| 1.3 | 907 | 953 | 46 |
| 1.4 | 907 | 966 | 59 |
| 1.5 | 907 | 979 | 72 |

Table 4.8 : Wavelength red-shift observed in isotropic 1D-PSMC-2 with change in the refractive index of analyte inside the pores for s-polarization and p-polarization.

Isotropic 1D-PSMC-2, s-polarization and p-polarization $(\theta = 0^{\circ})$

| Refractive index of Analyte inside the pores | Micro-cavity wavelength (nm) with air in pores ( $n_{void}$ =1) | Micro-cavity wavelength(nm) with analyte in pores ( $n_{void} > 1$ ) | wavelength shift ($\Delta\lambda$) nm |
|---|---|---|---|
| 1.1 | 1234 | 1256 | 22 |
| 1.2 | 1234 | 1277 | 43 |
| 1.3 | 1234 | 1296 | 59 |
| 1.4 | 1234 | 1314 | 80 |
| 1.5 | 1234 | 1330 | 96 |

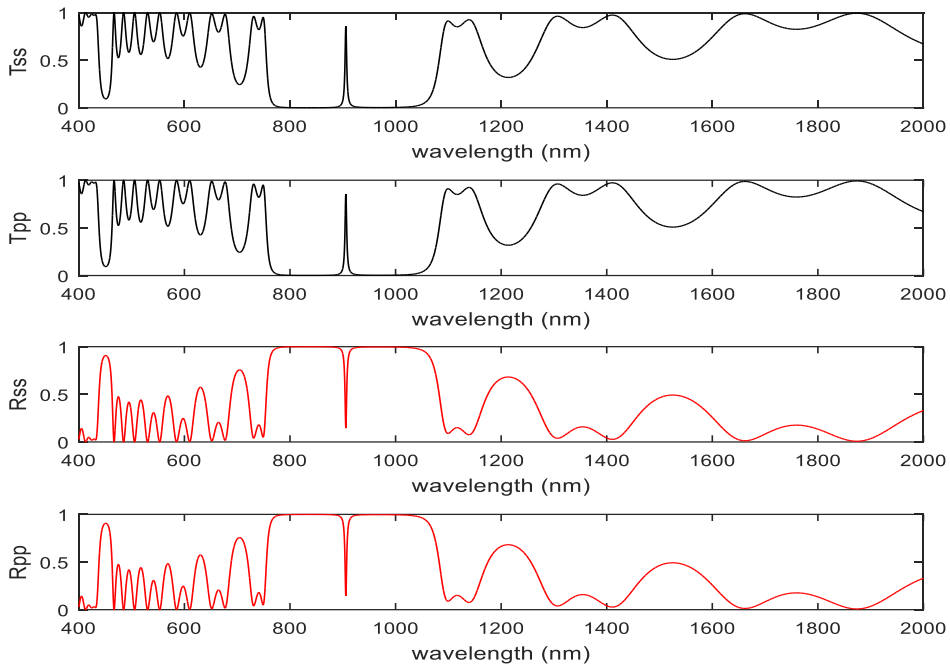


Figure 4.17: The reflectance spectrum (red lines) and transmittance spectrum (black lines) for s and p- polarization for isotropic 1D-PSMC-1 for $n_{void} = 1$

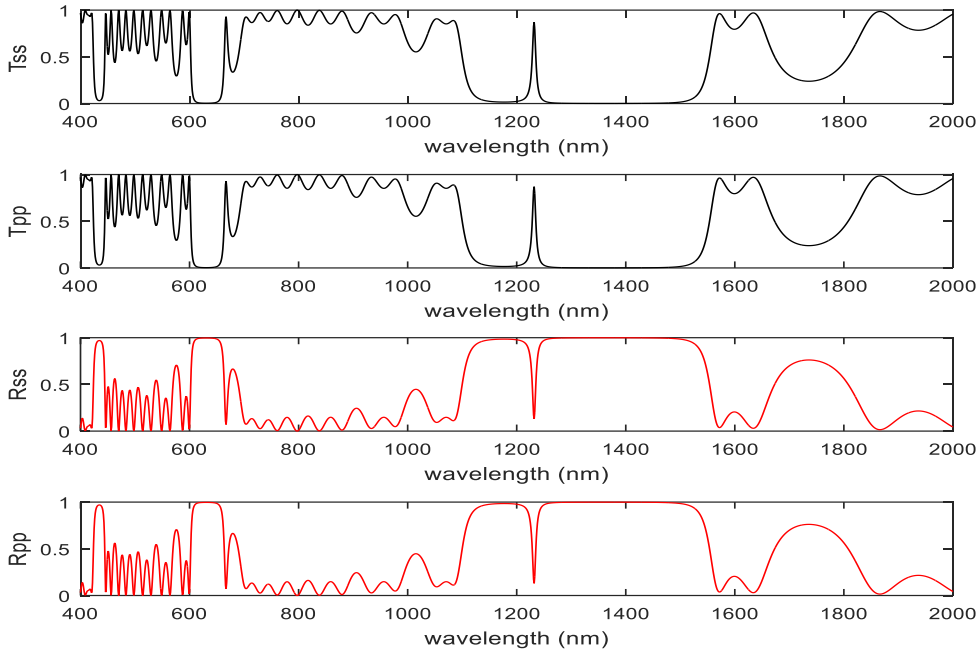


Figure 4.18: The reflectance spectrum (red lines) and transmittance spectrum (black lines) for s and p- polarization for isotropic 1D-PSMC-2 for $n_{void} = 1$

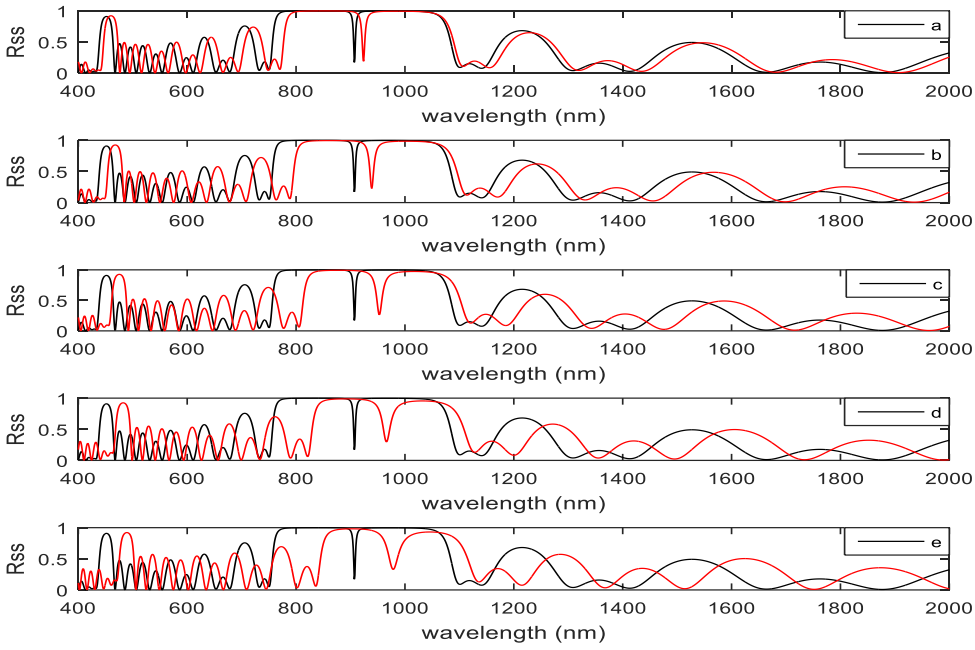


Figure 4.19: Reflection spectrum of isotropic 1D-PSMC-1 sensor and wavelength red-shift observed with change in the refractive index of analyte inside the pores (red lines) (a) $n_{void} =$

1.1 (b) $n_{void} = 1.2$ (c) $n_{void} = 1.3$ (d) $n_{void} = 1.4$ (e) $n_{void} = 1.5$ with respect to air in pores ($n_{void} = 1$)(black lines).

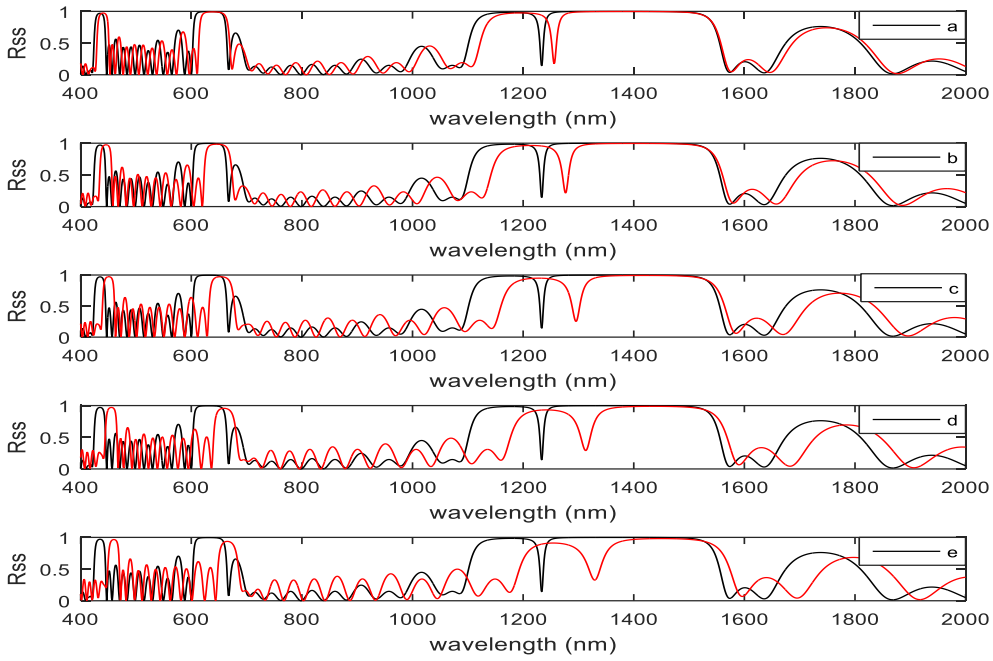


Figure 4.20: Reflection spectrum of isotropic 1D-PSMC-2 sensor and wavelength red-shift observed with change in the refractive index of analyte inside the pores (red lines) (a) $n_{void} = 1.1$ (b) $n_{void} = 1.2$ (c) $n_{void} = 1.3$ (d) $n_{void} = 1.4$ (e) $n_{void} = 1.5$ with respect to air in pores ($n_{void} = 1$)(black lines).

### 4.3.7 Sensitivity

In anisotropic and isotropic sensors referred in subsections (4.3.5 and 4.3.6) , it is observed that there is red-shift in micro-cavity wavelength as the refractive index of analyte in the pores of the sensor is increased as shown in Figs. (4.13-4.16) and Figs. (4.19-4.20). There is a linear relationship between the wavelength shift and the increase in refractive index of analyte for both the anisotropic and isotropic sensors as shown in Fig. (4.21). This is due to the variations in effective refractive index and optical path of the sensor device structure according to the change in refractive index of the biochemical analyte absorbed in its pores. Sensitivity is an important issue to evaluate the performance of the sensor. The sensitivity is calculated as the ratio of obtained red-shift in micro-cavity wavelength $\Delta\lambda$ due to a small change in the refractive index of chemical analyte $\Delta n$ inside the pores. Sensitivity S is defined as

$$S = \frac{\Delta\lambda}{\Delta n} \tag{4.20}$$

We have compared the sensitivity of anisotropic and isotropic sensors. The sensitivity of the sensors is dependent on the design parameters of its structure. The maximum sensitivity in anisotropic 1D-PSMC-2 sensor is found to be 260 and the same for isotropic 1D-PSMC-2 sensor is found to be 210 from the analysis of data of Table-(4.5) and Table-(4.8) respectively. The maximum sensitivity in anisotropic 1D-PSMC-1 sensor is found to be 190 and the same for isotropic 1D-PSMC-1 sensor is found to be 150 from the analysis of data of Table-(4.3) and Table-(4.7) respectively. Anisotropic sensors are found to be more sensitive than isotropic sensors. The reason being the *s*-polarization wave in anisotropic sensor is more sensitive to the variation in refractive index of the constituent layers of the sensor structure. It is also observed from Fig. (4.21) that the sensitivity of anisotropic 1D-PSMC-1 sensor is different from the sensitivity of anisotropic 1D-PSMC-2 sensor due to change in thickness of the two sensors. The observed sensitivity of isotropic ID-PSMC-1 sensor is also different from the sensitivity of isotropic 1D-PSMC-2 due to the difference in thickness of the two structures. The observed sensitivity in both the anisotropic and isotropic sensors decreases with increasing the refractive index of analyte in the pores of the structures.

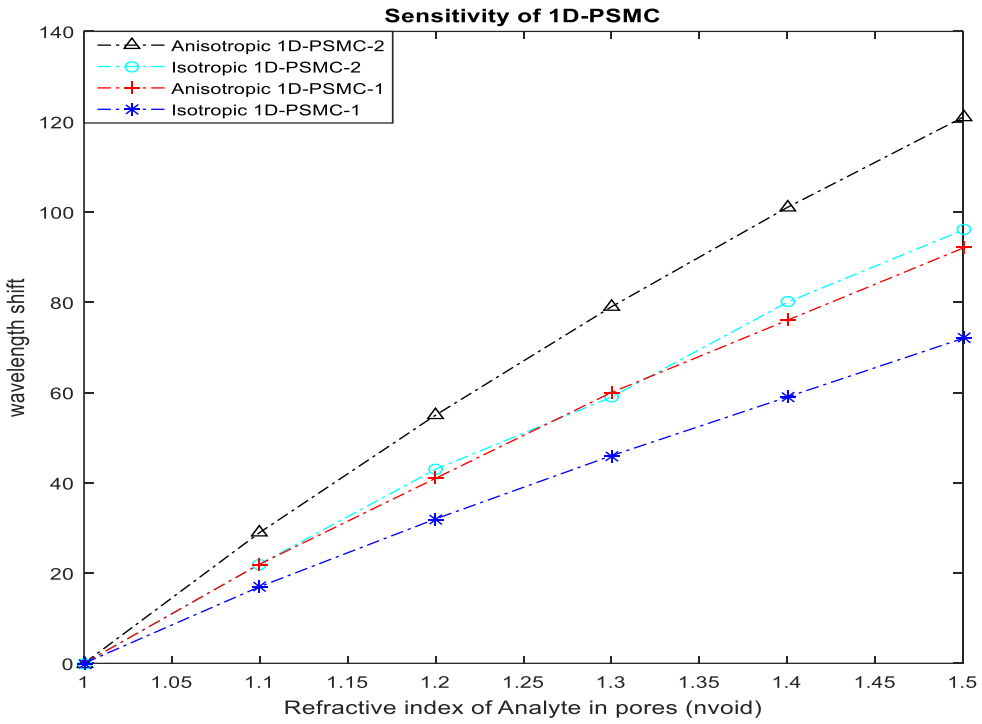

Figure 4.21: . Sensitivity comparision of anisotropic 1D-PSMC sensors and isotropic 1D-PSMC sensors

### 4.3.8 Conclusion

We have numerically designed two anisotropic sensors 1D-PSMC-1 and 1D-PSMC-2 with different thickness parameters in subsection (4.3.5). Numerical study was based on Bruggeman's effective medium approximation model and the $(4 \times 4)$ general transfer matrix method referred in subsection (4.3.2). In subsection (4.3.6), we have theoretically designed two isotropic sensors 1D-PSMC-1 and 1D-PSMC-2 ignoring the anisotropic effects. Simulations are done for the wavelength shift due to different analytes inside the pores. Both structures can be used for sensing the refractive index of chemicals or bio-analytes. Investigations were carried out on anisotropic and isotropic 1D-PSMC sensors for different analytes. We have found that wavelength shift $\Delta\lambda$ is linearly related to change in refractive index of chemical analyte $\Delta n$ inside the pores. A slight change of refractive index of chemical analyte inside the pores causes a significant red shift in the micro-cavity wavelength, which can be easily monitored by analysing the reflection spectrum with existing optical spectroscopy. Higher wavelength shift was observed for higher refractive index solvents inside the pores. The comparative analysis of sensitivity in section (4.3.7) shows that the anisotropic sensors are more sensitive than the isotropic sensors. Manipulation and control over the design parameters can effectively tune the sensitivity of 1D-PSMC sensors to the desired levels together with the tunability of the micro-cavity wavelength. The observed sensitivity in both the anisotropic and isotropic sensors decreases with increasing the refractive index of analyte in the pores of the structures. These 1D-PSMC sensor devices can be of potential applications in chemical, biochemical and bio-analyte sensing elements.

# CHAPTER-V

# METALLO-DIELECTRIC 1DPC

## INTRODUCTION

The interference effects in 1D-Metallo-Dieletric photonic crystals (1D-MDPC) give rise to tunable range of frequencies for transmission. Metals are highly reflective and absorptive in most part of EM spectrum including radio-waves, microwaves and ultraviolet. Metals are mostly used for their reflective and radiation shielding purposes. However, many dielectric structures are transparent in visible region and they provide minimal loss to propagation of light beam [5.1-5.6]. It is highly desirable to have access to structures which can reflect the longer wavelengths and be transparent in visible region i.e. transparent metallic structures. Most of the work on 1D-MDPCs is focussed on 2D and 3D structures where metal is embedded with dielectric to enhance the reflectivity [5.7-5.10]. We have found that metallo-dielectric periodic structures give controlled transmission in visible region and shield low and very low frequencies. Inside the metallic region the electromagnetic waves become evanescent wave and hence decay in amplitude. The characteristic distance in the metal within which the amplitude of the field reduces to $\left(\frac{1}{e}\right)^{th}$ of its value at surface of metal is known as skin depth ($\varsigma$). It is related to the imaginary part of complex refractive index($n_i$) as

$$\varsigma = \frac{c}{2n_i\omega} = \frac{\lambda}{4\pi n_i}. \quad (5.1)$$

Where c is the velocity of light in vacuum and λ is wavelength of incident wave. In case of silver (Ag), $n_i = 3$ for $\lambda = 5 \times 10^{-7}$m, so the skin depth from Eq. 5.1 turns out to be $\varsigma$ = 10 nm. For microwave frequencies the real and imaginary part of complex refractive index is of the order of $10^4$. The wavelength of microwaves inside the metal is $\lambda = \frac{1\,cm}{n} = 10^{-6}m$.

The optical path length of microwaves inside 10 nm thick metal layer is $10^{-4}$ m which is 100 times λ. Hence 10 nm metal layer is opaque to microwave radiations.

We have considered alternate layers of 1D-MDPC with Ag and cryolite as metal and dielectric layers respectively. The transmission characteristics of 1D-MDPC with formation of structural and plasmonics bandgaps are studied. The structural bandgap is due to interference effects whereas the plasmonics bandgap is due to the bulk metal property. The transmission properties of such structures as a number of factors like angle of incidence, number of layers and effect of variation of thickness of constituent layers is studied in this chapter. Transparent 1D-MDPCs

find applications in devices like microwave open door cavity, solar heat shields, laser safety goggles, sunglasses for protection from UV rays, and Radio waves shields.

## 5.1 DRUDE'S MODEL

This model provides a theoretical expression of dielectric constant and hence refractive index inside metal for low and high frequencies. The wave equation of oscillating free electrons in an oscillating electric field E (t) of light polarised in y- direction is given by

$$m_0 \frac{d^2x}{dt^2} + m_0\gamma \frac{dx}{dt} + e\,E(t) = 0 \tag{5.2}$$

Where $E(t) = E_0 e^{-i\omega t}$, $m_0$= mass of electron, γ = damping coefficient

Substituting $x = x_0 e^{-i\omega t}$ in Eq. (5.2) we will get

$$x = \frac{eE}{m_0(\omega^2 + i\gamma\omega)} \tag{5.3}$$

The Electric displacement vector $\vec{D}$ is expressed as

$$\vec{D} = \varepsilon_0\vec{E} + \vec{P} \tag{5.4}$$

$$\vec{D} = \varepsilon_0\vec{E} - \frac{Ne^2E}{m_0(\omega^2 + i\gamma\omega)} \tag{5.5}$$

Therefore

$$\varepsilon(\omega) = 1 - \frac{Ne^2}{\varepsilon_0 m_0(\omega^2 + i\gamma\omega)} \tag{5.6}$$

or

$$\varepsilon(\omega) = 1 - \frac{{\omega_p}^2}{(\omega^2 + i\gamma\omega)} \tag{5.7}$$

Where $\omega_p$ = plasma frequency given by

$${\omega_p}^2 = \left(\frac{Ne^2}{\varepsilon_0 m_0}\right)^{\frac{1}{2}} \tag{5.8}$$

## 5.2 DESIGN OF 1D-MDPC

1D-MDPC with metals of higher dielectric permittivity will result in lower number of periods to achieve PBG. We have designed 1D-MDPC structure with Cryolite and Silver layers and analysed its spectral response. The thickness of Cryolite layers and Silver layers are taken as 200 nm and 10 nm, respectively. The complex refractive index of Ag is calculated from its plasmonic frequency and damping coefficient. In case of Ag, $\omega_p = 2175$ THz and γ = 6.5 THz. It was found that the structural band gap in this structure exists from 300 nm to 570 nm and plasmonics band gap exists from 970 nm to very low frequencies. The resonance transmission band appears from 570 nm to 970 nm as shown in Fig.5.1. The corresponding profile of density of states is shown in Fig.5.2

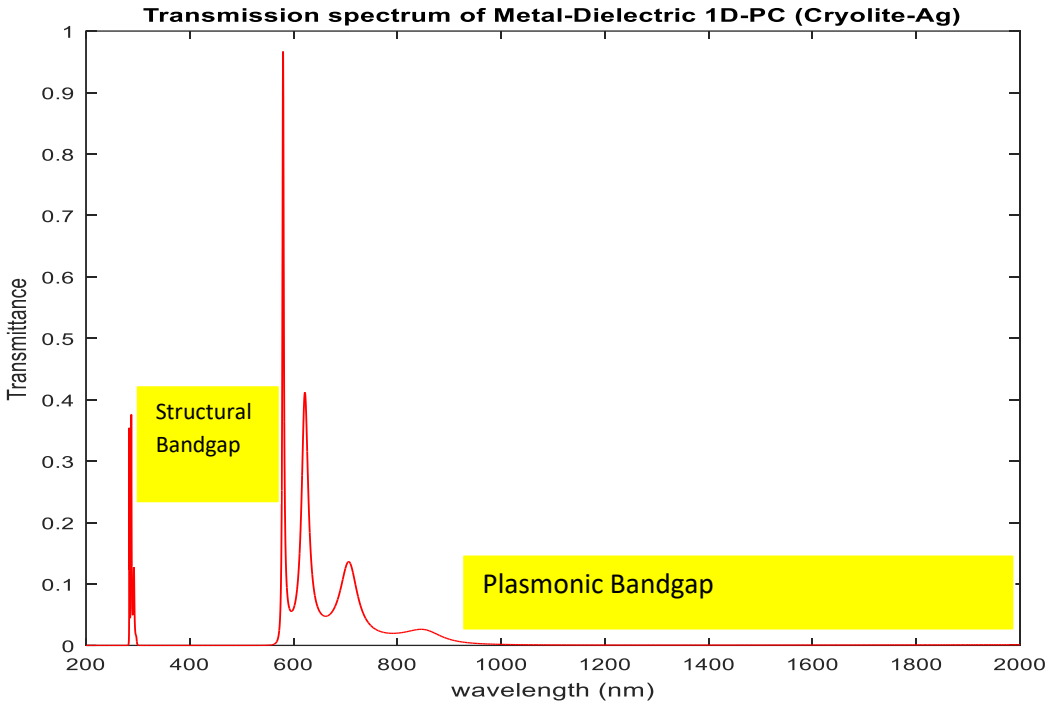


Figure 5.1: Transmittance spectrum for Metallo-Dielectric 1D-PC with $d_1$=200nm (Cryolite) $d_2$=10 nm (Ag)

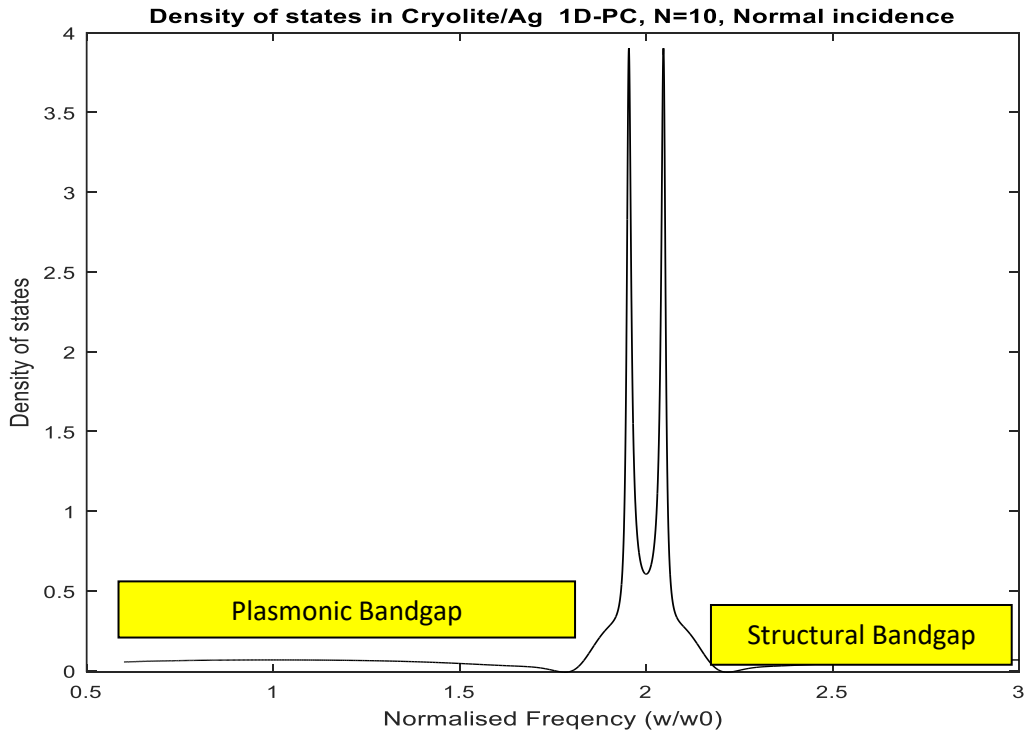


Figure 5.2 Density of states in Metallo-Dielectric 1D-PC with $d_1$=200 nm (Cryolite) $d_2$=10 nm (Ag)

## 5.3. EFFECT OF NUMBER OF LAYERS OF 1D-MDPC ON SPECTRAL RESPONSE

The effect of number of layers of 1D-MDPC is analysed and it was found that when the number of layers is decreased there is no change in the plasmonics band gap and structural bandgap, only the transmission peak decreases. The comparison of transmission spectrum for N=6, and N=10 is shown in Fig.5.3

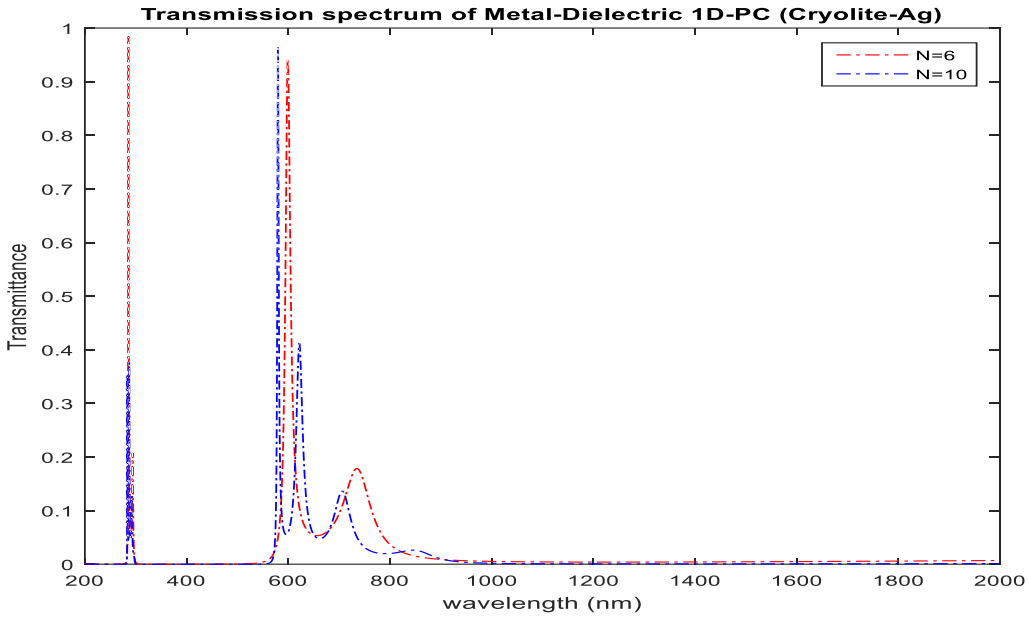


Figure 5.3: Spectral response of 1D-MDPC with change in number of layers

## 5.4. EFFECT OF THICKNESS FILL FACTOR OF Ag IN CRYOLITE/Ag 1D-MDPC

The ratio of thickness of Ag layer to thickness of unit cell of 1D-MDPC is known as thickness fill factor. The effect of thickness fill factor of metals in 1D-MDPC is studied with doubling the fill factor of Ag in Cryolite-Ag multilayer structure. It was found that the upper wavelength edge of transmission band is blue shifted while the lower wavelength transmission band edge remains unchanged as the fill factor is increased causing the shrinking of transmission band. The structural band gap and plasmonics band gap increases with increasing the fill factor as shown in Fig.5.4

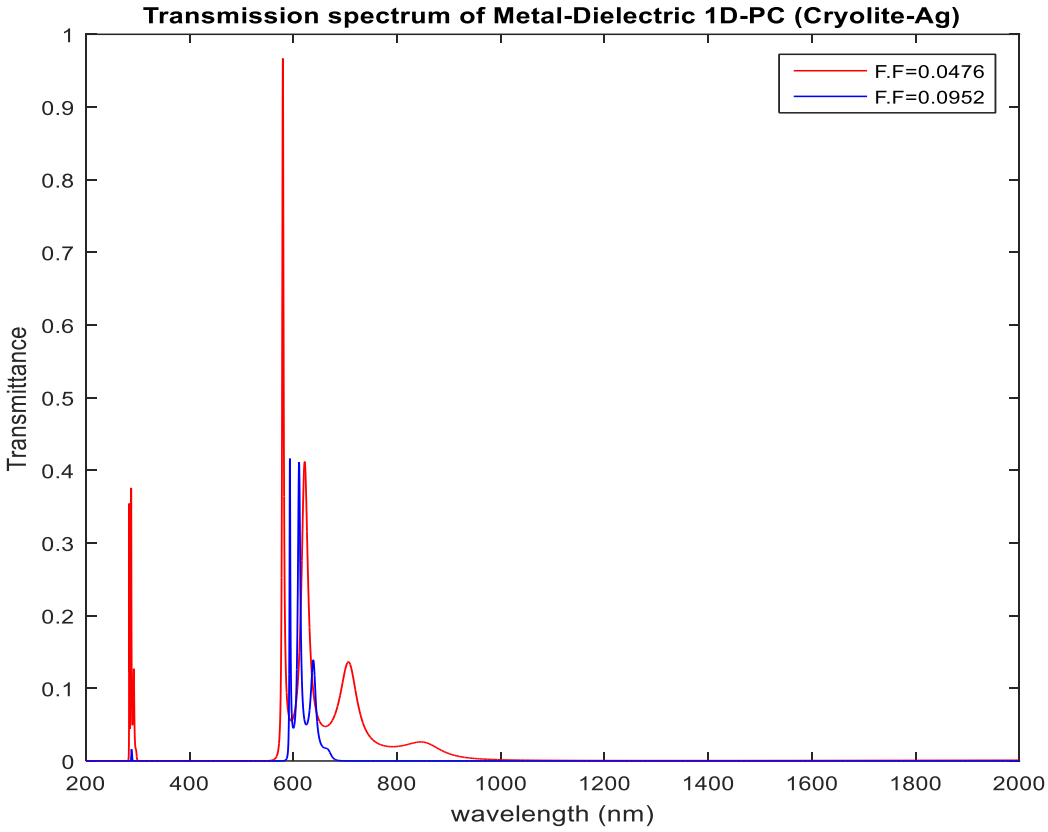


Figure 5.4: Spectral response of 1D-MDPC with change in thickness Fill-Factor of metal layer

**5.5. EFFECT OF ANGLE OF INCIDENCE ON SPECTRAL RESPONSE OF 1D-MDPC**

The effect of oblique incidence is also analysed in 1D-MDPCs with Cryolite-Ag multilayers. The increase in angle of incidence causes a blue shift of transmission band for both the polarisations as shown in Fig.5.5-5.6

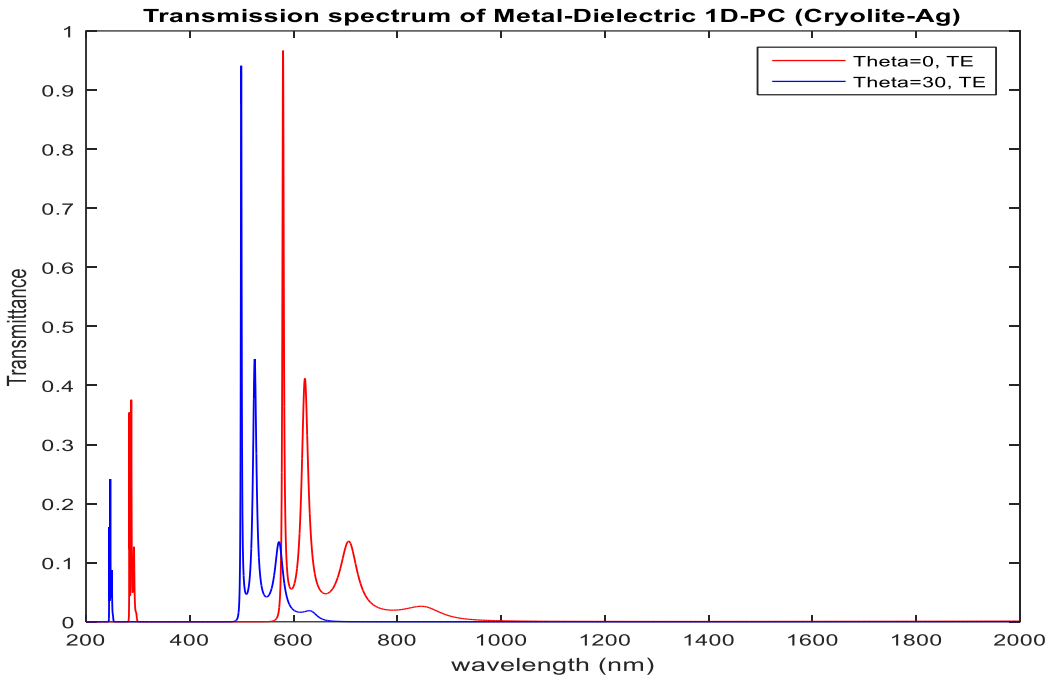


Figure 5.5: Spectral response of TE modes in 1D-MDPC with change in angle of incidence

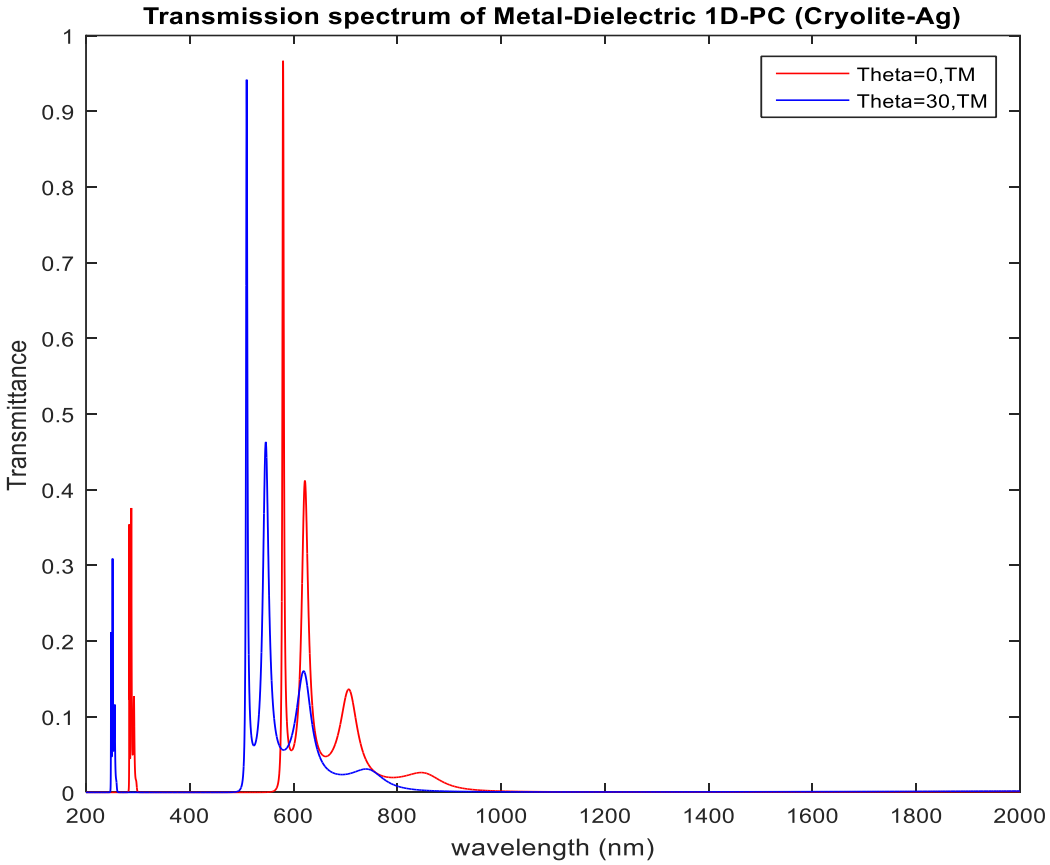


Figure 5.6: Spectral response of TM modes in 1D-MDPC with change in angle of incidence

## 5.6 EFFECT OF PLASMONIC FREQUENCY AND DAMPING COEFFICIENT

The effect of plasmonics frequency and damping coefficient is simulated by taking three different 1D-MDPCs with different metals (Silver, Gold and Aluminium). The plasmonic frequency and damping coefficient of Ag is 2175 THz and 4.35 THz and that for Au is 2175 THz and 6.5 THz respectively. The plasmonic frequency and damping coefficient of Al is 3750 THz and 19.4 THz. The plasmonics bandgap and structural bandgap of Cryolite-Ag and Cryolite-Au coincide with same width because both the metals are having almost same plasmonics frequency. Cryolite-Ag is having higher transmission peak than Au due to lower damping coefficient as shown in Fig.5.7. The transmission band width in Cryolite-Al is small in comparison to Cryolite-Ag due to large damping coefficient of Al. The width of structural bandgap and plasmonics bandgap is wider in Cryolite-Al 1D-MDPC as shown in Fig.5.8.

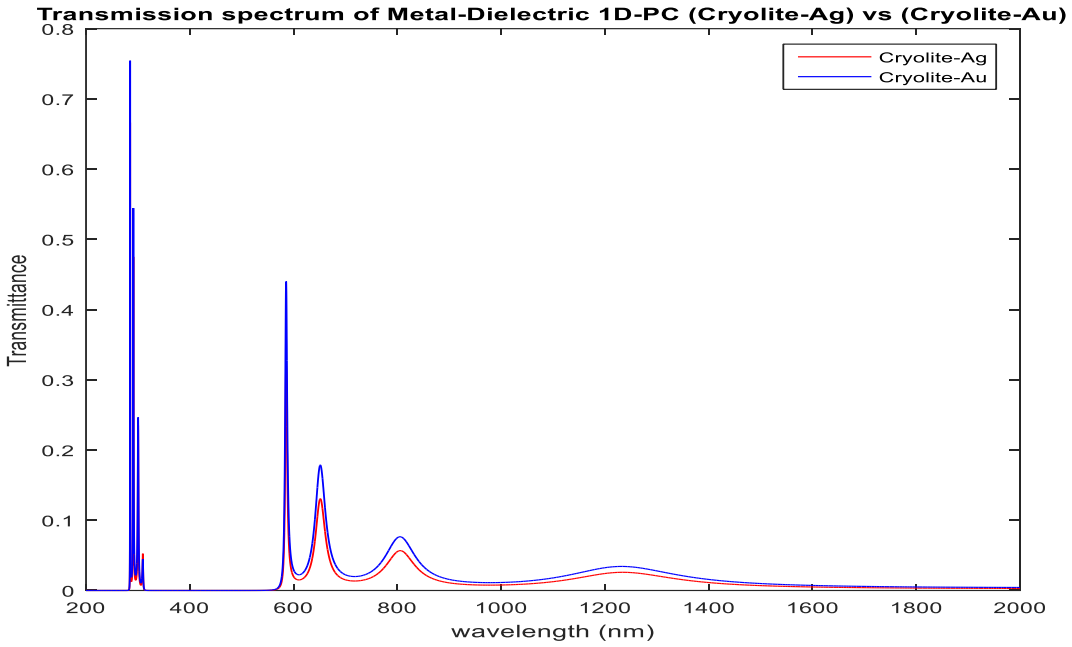


Figure 5.7: Comparative Spectral response of 1D-MDPC with Ag and Au

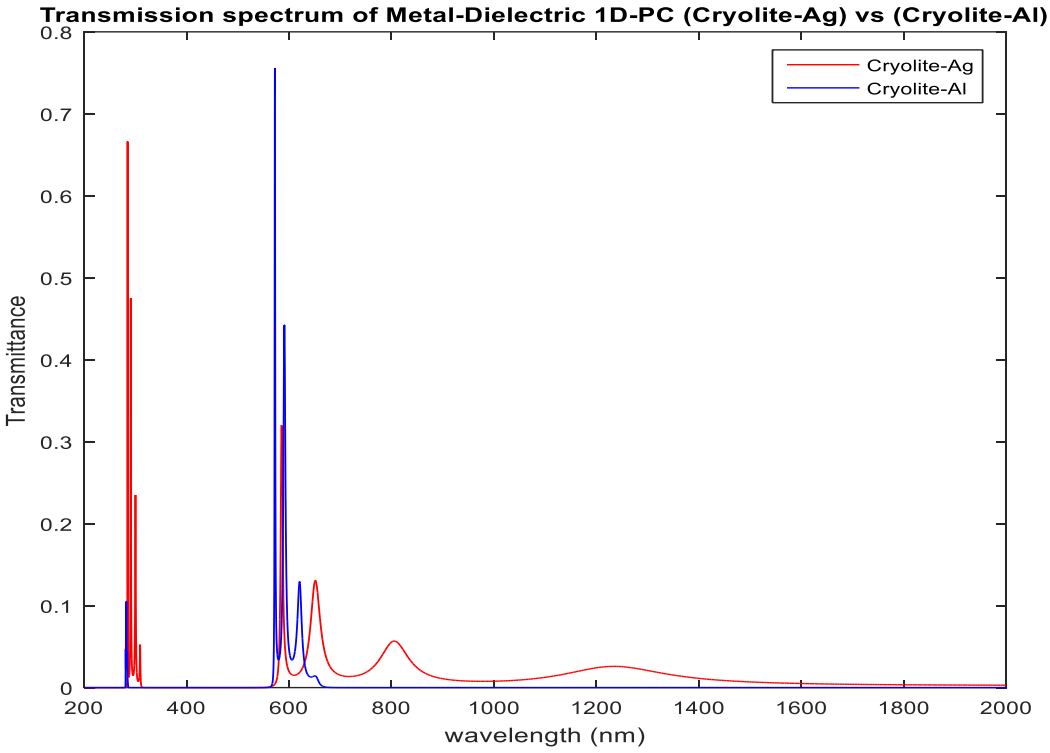


Figure 5.8: Comparative Spectral response of 1D-MDPC with Ag and Al

## CONCLUSIONS

We have designed 1D-MDPC using Ag and Cryolite as the constituent layers. The optical properties of the absorptive medium are deduced from Drude's model. The transmission spectrum of this structure shows there are structural and plasmonic bandgaps. The effect of various design parameters of 1D-MDPC like, number of layers and thickness fill factor on the structural and plasmonic bandgaps is analysed. The effect of plasmonic frequency and damping coefficient and angle of incidence is also studied for these structures. We have found that light can be transmitted through periodic, metallic structures, and by controlling the thickness of the dielectric or semiconductor sandwiched between the metal films, as well as the thickness of each metal film, the transparency regions can be tuned. The 1D-MDPC have induced transparency and shielding abilities which make them useful in transparent metal film device in a microwave oven door cavity, solar heat shields, laser safety goggles, sunglasses for protection from ultraviolet light, and other applications where transparent conductor oxides like indium tin oxide are required to ensure good transmission of light and good conductivity at the same time.

# CHAPTER-VI

# CONCLUSION AND FUTURE SCOPE OF WORK

## 6.1 CONCLUSIONS

1. One dimensional photonic crystal and their applications have been studied through literature review. The various tools for optical characterisation of 1DPCs were examined. The selected 1DPCs were studied by solving the Maxwell's equations in periodic medium. Transfer matrix method was used for simulations of reflection and transmission coefficients in 1DPCs. The expression for DOS, group velocity and effective index was analysed and it was observed that the group velocity and effective refractive index show abrupt variation at the PBG edges. The effect of various design parameters on the spectral response of selected 1DPCs were also studied. The 1DPCs create stop band filters and band pass filters which can be tuned according to the desired application in devices with change in design parameters.
2. ODRs were designed with selected 1DPCs and the effect of their design parameters were analysed. The enhancement in ODR band width have been proposed in selected 1DPCs with varying the thickness parameter using a gradual constant. ODR with PS/ Si 1DPC was designed and analysed for infiltration of liquids inside pores of PS. The structure showed a wide ODR band in the near infrared region and introduction of bio-chemicals in the pores of structure changed the ODR band and its width. The effect of material dispersion in multi-layered $ZnO/SiO_2$ ODR structure was explored and it was found that the material dispersion effects shrink the ODR band width from 79 nm to 30 nm. ODRs are used as high-quality mirrors in opto-electronic devices.
3. Microcavity structures were designed from 1DPCs using TMM and the Q-values with different defect layers were calculated. The Q-value of defect modes increased with increase in the refractive index contrast of 1DPC and the refractive index of defect layer. Two biochemical sensors with microcavity wavelength at 800 nm and 1200 nm were designed with porous Si layers. The shifts in microcavity wavelength due to introduction of analytes were used for sensing purpose. Effect of anisotropy was analysed on these structures and anisotropic 1DPC microcavity sensors were found to be more sensitive than isotropic 1DPC microcavity sensors.
4. 1D-MDPC structures were designed and their spectral response was analysed. The effect of various design parameters was studied for its optimisation. The designed 1D-

MDPC structures find applications in Radio and micro wave shields, transparent conductors, laser safety goggles, sunglasses for protection from UV rays etc.

## 6.2. FUTURE SCOPE OF WORK

1. The theoretical design of 1DPC can be realised experimentally with different design parameters to have the PBG in the desired region of application. It can act as band pass filter, stop band filter and selective wavelength filter in the desired application range.
2. Experimental work can be done to design ODR device which will be useful in many optoelectronic devices.
3. Experimentally the 1DPC microcavity structures can be designed using porous silicon layers. The device is useful in sensing applications of gasses, chemicals, bio-analytes and environmental pollutants.
4. 1D-MDPC can be designed experimentally which are transparent in visible region and blocking all other longer wavelengths. These transparent 1D-MDPCs find applications in devices like microwave open door cavity, solar heat shields, laser safety goggles, sunglasses for protection from UV rays.

# REFERENCES

[1.1] Yablonovitch, Eli. "Inhibited spontaneous emission in solid-state physics and electronics."Phys.Rev.Lett.,58,20:2059(1987).https://link.aps.org/doi/10.1103/PhysRevLett.58.2059

[1.2] S. K. Srivastava, S. P. Ojha, "Omnidirectional reflection bands in one-dimensional photonic crystal structure using fullerene films", Progress In Electromagnetics Research, PIER 74, 181–194, (2007)

[1.3] Born M., Wolf E., "Principles of Optics", (New York: Pergamon), (1980).

[1.4] Lipson R.H., and C. Lu, "Photonic Crystals : a unique partnership between light and matter", European Journal of Physics, 30, 4, pp. 33, (2009). https://doi.org/10.1088/0143-0807/30/4/S04

[1.5] Bykov V.P.,, "Spontaneous emission in a periodic structure", Soviet Physics JETP 35,269 (1972).

[1.6] P.Yeh, A Yariv, and Chi-Shain, " Hong electromagnetic propagation in periodic stratified media: A general theory", J. Opt. Soc. A 67,423 (1977).

[1.7] John S., "Strong localization of photons in certain disordered dielectric super lattices", Phys. Rev. Lett., Vol. 58, 2486–2489, (1987). https://doi.org/10.1103/PhysRevLett.58.2486

[1.8] K.M.Leung, and Y.F.Liu, "Full vector wave calculation of photonic bandgap structures in Face-centered-cubic dielectric media", Phys. Rev. Lett. 65, 2646 (1990).

[1.9] J.R.Wendt, G.A. Vawter, P.L.Gourley, T.M.Brennan, and B.E. Hammons," Nanofabrication of photonic lattice structures in GaAs/AlGaAs", J. of Vac. Sci. Technol. B 11, 2637 (1993).

[1.10] K.M.Ho, C.T.Chan, C.M.Soukoulis, R.Biswas, and M.Sigalas," Photonic bandgap in three dimensions: New layer by layer periodic structures", Sol. Sta. Communns. 89, 413 (1994).

[1.11] R.D. Meade, A. Devenyi, J.D. Joannopoulos, O.L.Alerhand, D.A.Smith, and K.Kash," Novel applications of photonic bandgap materials: low loss bends and high Q cavities", J.Appl. Phys. 75, 4753 (1994).

[1.12] A.Mekis, J.C.Chen, I.Kurland, S.Fan, P.R. Villeneuve. and J.D. Joannopoulos, " High transmissions through sharp bends in photonic crystal waveguides", Phys. Rev. Lett 77, 18, 3787, (1996).

[1.13] S.-Y. Lin, V.M.Hietala, L.Wang, and E.D.Jones, "Highly dispersive photonic bandgap prism", Opt.Lett. 21, 1771 (1996).

[1.14] H.Kosaka, T.Kawashima, A.Tomita, M.Notomi, T.Tamamura, T.Sato, and S. Kawakami, " Self collimating phenomena in photonic crystals", App. Phys. Lett. 74, 6951 (1999).

[1.15] J. O' Brien, O. Painter, C.C. Cheng, R.Lee, A. Scherer, and A.Yariv, " Lasers incorporating 2D photonic bandgap mirrors", Electron Lett. 32, 2243 (1996).

[1.16] I.Dajani, C.Vergien, C.Robin, and C.Zeringue, " Experimental and theoretical investigations of photonic crystal fiber amplifier with 260W output", Opt. Exp. 17, 24317 (2009).

[1.17] J.Rosenberg, R.V.Shenoi, S. Krishna, and O.Painter, " Design of plasmonic photonic crystal resonant cavities for polarization sensitive infrared photo detectors", Opt. Exp. 18, 3672 (2010).

[1.18] C.C. Cheng, V.A.Engles, A. Scherer, E. Yablonovitch, " Nanofabricated three dimensional photonic crystals operating at optical wavelengths", Phys. Scr. 17 (1996).

[1.19] S.Noda, K.Tomoda, N.Yamamoto, and A.Chutinan, " Full three dimensional photonic bandgap crystals at Near infrared wavelengths", 289, 604 (2000).

[1.20] S.Eyderman, A.Deinegaa, and S.Johnab, " Near perfect solar absorption in ultra-thin film GaAs photonic crystals", Journal of J.Mater.Chem. A 2, 761, (2014).

[1.21] Paul V.Barun et al.," Three dimensional self assembled photonic crystal with high temperature stability for thermal emission modification", Nat. Commun. 4, 2630 (2013).

[1.22] Y.Fink, J.N.Winn , S.H.Fan, C.Chen, J.Michel, J.D. Joannopoulos, and E.L.Thomas, " A dielectric omnidirectional reflector" , Science 282, 1679 (1998).

[1.23] M.Centini, C.Sibilia, M.Scalora, G.D.Aguanno, M. Bertolotti, M.J.Bloemer, C.M.Bowden and Nefedov, " Dispersive properties of finite , one dimensional photonic

bandgap structures : Applications to nonlinear quadratic interactions “, Phys. Rev.E 60, 4891, (1999).

[1.24] A.Bosco, M.Centini, L.Sciscione, C.Sibilia, E.Fazio, M. Bertolotti, A.Fiore, A.Convertino L. Cerri and M.Scalora, “Noncollinear type-II second harmonic generation in a $Al_{(0.3)}Ga_{(0.7)}As/Al_2O_3$ one dimensional photonic crystal”,Appl. Phys. Lett. 84, 3010 (2004).

[1.25] A.V.Andreev, A.V.Balakin, I.A.Ozheredov, A.P. Shkurinov, P.Masselin, G.Mouret, and D. Boucher, “Compression of femtosecond laser pulses in thin one dimensional photonic crystals”, Phys. Rev. E 63, 016602 (2000).

[1.26] D.V.Novitsky, “Pulse trapping inside a one dimensional photonic crystal with relaxing cubic nonlinearity”, Phys. Rev. A 81, 053814 (2010).

[1.27] F.Eilenberger, C.M.de Sterke, and B.J.Eggleton, “ Soliton mediated optical quantization in the transmission of one dimensional photonic crystals”, Opt. Exp. 18, 12708 (2010).

[1.28] Busch, K., C. T. Chan and C. M. Soukoulis, “Techniques for band structures and defect states in photonic crystals,” Photonic Band Gap Materials, NATO ASI Series, Series E: Appl. Sci., 315, 465-486, (1995).

[1.29] Ortowski, A., M. Rusek and J. Mostowski, “Localization of light in 2D random media,” Microcavities and Photonic Bandgaps: Physics and Applications, NATO ASI Series, Series E: Appl. Sci., 324, 165-174, (1995).

[1.30] Joannopoulos, J. D., P. R. Villeneuve and S. Fan, “Photonic Crystals,” Solid State Communs., 102, 2-3, 165-173, (1997).

[1.31] Jin, C. J., Z. W. Sun and B. Y. Cheng, “Microcavities composed of point defects and waveguides in photonic crystals,” Opt. Communs.,188, 5-6, 255-260, (2001).

[1.32] Johnson, S. G., S. Fan and A. Mekis, “Multipole-cancellation mechanism for high-Q cavities in the absences of a complete photonic band gap,” Appl. Phys. Lett., 78, 22, 3388-3390, (2001).

[1.33] Yamada, K., A. Shinya, C. Takahashi, and M. Notomi “Improved line-defect structures for photonic crystal waveguides with high group velocity,” Opt. Communs., 198, 4-6, 395-402, (2001).

[1.34] Wang, Y. Q., C. J. Jin and S. Z. Han, "Defect modes in two-dimensional quasi- periodic photonic crystal," Jap. J. of Appl. Phys. Part 1- 43, 4A, 1666-1671, (2004).

[1.35] De La Rue, R. M., and T. F. Krauss, "Strategies for the fabrication of photonic microstructures in semiconductors," Microcavities and Photonic bandgaps: Physics and Applications, NATO ASI Series, Series E: Appl. Sci., vol. 324, pp. 175-192, (1995).

[1.36] Fan, S., P. R. Villeneuve and J. D. Joannopoulos, "High extraction efficiency of spontaneous emission from slabs of photonic crystals," Phys. Rev. Lett., 78, 17, 3294-3297, (1997).

[1.37] Lin, S. Y., E. Chow, V. Hietala and J. D. Joannopoulos, "Experimental Demonstration of Guiding and Bending of Electromagnetic Waves in a Photonic Crystal," Science, 282, 5387, 274-276, (1998).

[1.38] Benisty, H., C. Weisbuch and D. Labilloy, "Optical and confinement properties of two-dimensional photonic crystals," J. of Lightwave Tech., 17, 11, 2063-2077, (1999).

[1.39] Temelkuran, B., and E, Ozbay, "Experimental demonstration of photonic crystal based waveguides," Appl. Phys. Lett., 74, 4, 486-488, (1999).

[1.40] Loncar, M., D. Nedeljkovic, T. Doll, J. Vuckovic, A. Scherer and T.P. Pearsall "Waveguiding in Planar Photonic Crystals," Appl.Phys. Lett., 77,13, 1937-1939, (2000).

[1.41] Loncar, M., T. Doll and J. Vuckovic, "Design and Fabrication of Silicon Photonic Crystal optical Waveguides," J. of Lightwave Tech, 18, 10, 1402-1411, (2000).

[1.42] Smith, C. J. M., H. Benisty, S. Olivier, "Low-loss channel waveguides with two-dimensional photonic crystal boundaries," Appl. Phys. Lett., 77, 18, 2813-2815, (2000).

[1.43] Olivier, S., H, Benisty, C. J.M. Smith, "Transmission properties of two-dimensional photonic crystal channel waveguides," Optical and Quantum Electronics, 34, 1-3,171-181, (2002).

[1.44] Baba, T., N. Fukaya and Y. Yonekuva, "Observation of light propagation in photonic crystal optical waveguides with bends," Elec. Lett. 35, 8, 654-655, (1999).

[1.45] Chutinan, A., S. Noda, "Waveguides and waveguide bends in two-dimensional photonic crystal slabs," Phys. Rev. B, 62, 7, 4488-4492,(2000).

[1.46] Chutinan, A., S. Noda, “Analysis of waveguides and waveguide bends in photonic crystal slabs with triangular lattice,” Jap. J. of Appl. Phy. Part 2-39, 6B, 595-596,(2000).

[1.47] Tokushima, M., H. Kosaka, A. Tomika and H. Yamada, “Light-wave propagation through a 120 degrees sharply bent single-line-defect photonic crystal waveguide,” Appl. Phy. Lett. 76, 8,952-954, (2000).

[1.48] Yamada, K., M. Notomi, A. Shinya and C. Takahashi, “Single mode light wave transmission in SOI-type photonic-crystal line-defect waveguides with phase-shifted holes,” Elec. Lett., 38, 2, 74-75, (2002).

[1.49] Yablonovitch, E., T. Gmitter and K. Leung, “Photonic band structure: The face- centred-cubic case employing nonspherical atoms”, Physical Review Letters, 67, 17, 2295-2298, (1991).

[1.50] Srinivasan, K., P.E. Barclay, O. Painter, J. Chen, A.Y. Cho and C. Gmachl, “Experimental demonstration of a high quality factor photonic crystal microcavity,”, Appl. Phy. Lett., 83,10,1915-1917, (2003).

[1.51] Knight, J. C., J. Broeng, T. A. Birks and P. S. Russell, “Photonic band gap guidance in optical fibers,” Science, 282, 5393, 1476-1478, (1998).

[1.52] Baba, T., N. Fukaya, and A. Motegi, “Clear correspondence between theoretical and experimental light propagation characteristics in photonic crystal waveguides,” Elec. Lett., 37, 12, 761-762, (2001).

[1.53] Painter, O., R. K. Lee, A. Scherer, A. Yariv, J. D. O’Brien, P. D. Dapkus and I. Kim, “Two Dimensional photonic band gap defect mode laser,” Science, 284,1819-1821,(1999).

[1.54] Villeneuve, P. R., S. Fan, J. D. Joannopoulos, K-Y. Lim, G. S. Petrich, L. A. Kolodziejski, and R. Reif, “Air-bridge microcavities,” Appl. Phy. Lett., 67 (2),167-169, (1995).

[1.55] Villeneuve, P., S. Fan and J. D. Joannopoulos, “Microcavities in photonic crystals,” Microcavities and Photonic Bandgaps: Physics and Applications, NATO ASI Series, Series E: Appl. Sci., 324,133-152, (1995).

[1.56] Konotop, V. V., “Waveguides in periodic structures with smoothly varying parameters,” Photonic Band Gap Materials, NATO ASI Series, Series E: Appl. Sci., 315, 547-554, (1995).

[1.57] Foresi, J. S., P. R. Villeneuve, J. Ferrera and J. D. Joannopoulos, “Photonic-bandgap microcavities in optical waveguides,” Nature, 390 (6656), 143-145, (1997).

[1.58] Baba, T., N. Fukaya and Y. Yonekuva, “Observation of Light propagation in Photonic Crystal optical Waveguides with bends,” Elec. Lett., 35, 8, 654-655, (1999).

[1.59] Hattori, T., N. Tsurumachi and N. Muroi, “Enhancement of optical nonlinearity in one-dimensional photonic crystals,” Progress in Crystal growth and characterization of materials, 33, 1-3, 183-186, (1996).

[1.60] Hattori, T., N. Tsurumachi and H. Nakatsuka, “Analysis of optical nonlinearity by defect states in one-dimensional photonic crystals,” J. of the Op. Soc. of Am. B Optical Physics, 14, 2, 348-355, (1997).

[1.61] Lau, W. T. and S. H. Fan, “Creating large bandwidth line defects by embedding dielectric waveguides into photonic crystal slabs,” Appl.Phy. Lett. 81, 21, 3915-3917, (2002).

[1.62] Leung, K. M., “Diamond like photonic band-gap crystal with a sizable band gap,” Phys. Rev. B, 56, 7, 3517-3519, (1997).

[1.63] Tsurumachi, N., S. Yamashita, N. Muroi and H. Nakatsuka, “Enhancement of nonlinear optical effect in one-dimensional photonic crystal structures,” Jap. J. of Appl. Phy., 38, 6302-6308, (1999).

[1.64] Soljacic, M., S. G. Johnson and S. H. Fan, “Photonic-crystal slow-light enhancement of nonlinear phase sensitivity,” J. of the Op. Soc. of Am. B Optical Physics, 19, 9, 2052-2059, (2002).

[1.65] Soljacic, M., C. Luo, J. D. Joannopoulos and S. Fan, “Nonlinear photonic crystal microdevices for optical integration,” Opt. Lett., 28, 8, 637-639, (2003).

[1.66] Fan, S., P. R. Villeneuve, J. D. Joannopoulos and H. A. Hans, “Channel drop tunneling through localized states,” Phy. Rev. Lett., 80, 960-963, (1998).

[1.67] Lousse, V., W. Suh, O. Kilic and S. Fan, “Angular and polarization properties of a photonic crystal slab mirror,” Opt. Exp., 12, 8,1575-1582, (2004)

[1.68] Chigrin, D.N., Lavrinenko, A.V., Yarotsky, D.A., Gaponenko, S.V., “Observation of total omnidirectional reflection from a one-dimensional dielectric lattice”, Appl. Phys. A , 68:25-28, (1999).Crossref

[1.69] Chigrin, D.N., Lavrinenko, A.V., Yarotsky, D.A., Gaponenko, S.V.,” All-dielectric one-dimensional periodic structures for total omnidirectional reflection and partial spontaneous emission control”, J. Light Wave Technol., 17:2018-2024, (1999).Crossref

[1.70] Winn, J.N., Fink, Y., Fan, S., Joannopoulos, J. D.” Omnidirectional reflection from a one-dimensional photonic crystal”, Opt. Lett. 23:1573-1575, (1998).Crossref

[1.71] Lee, H.Y., Yao, T.,” Design and evaluation of omnidirectional one dimensional photonic crystals”. J. Appl. Phys. 93:819-830,(2003),Crossref

[1.72] Lin, W., Wang, G.P., Zhang, S.,”Design and fabrication of omnidirectional reflectors in the visible range.” J. Mod. Opt. 52:1155-1160, (2005),Crossref

[1.73] K. Ben, Abdelaziz, J. Zaghdoudi, M.Kanzari and B.Rezg, “A broad omnidirectional reflection band obtained from deformed Fibonacci quasi-periodic one dimensional photonic crystals”, J. Opt. A: Pure Appl. Opt., 7, 10, (2005).

[1.74] T.,Yante, J.J Monzon, A.Felipe and L.L Sanchez-soto, “Optimizing omnidirectional reflection by multilayer mirrors”, J. Opt. A: Pure Appl. Opt., 6, 1, (2003).

[1.75] John Lekner, “Omnidirectional reflection by multilayer dielectric mirrors”, J. Opt. A: Pure Appl. Opt., 2, 349–352, (2000).

[1.76] Chen Zhao, Jiang, “Design and optimization of omnidirectional bandgap for one dimensional periodic and quasi-periodic photonic hetrostructures”, Chinese Phy. Lett. , 32, 1, (2015).

[1.77] Birks, T. A., D. M. Atkin, G. Wylangowski and P. St. Russell, “2D photonic band gap structures in fiber form,” Photonic Band Gap Materials, NATO ASI Series, Series E: Appl. Sci., 315, 437-444, (1995).

[1.78] Pechstedt, R. D., P. St. Russell and T. A. Birks, “Dispersion, tunability and applications of defect modes in photonic band-gap structures,” Photonic Band Gap Materials, NATO ASI Series, Series E: Appl. Sci., 315, 445-452, (1995).

[1.79] Cregan, R. F., B. J. Mangan, and J. C. Knight, “Single-mode photonic band gap guidance of light in air,” Science 285 (5433), 1537-1539, (1999).

[1.80] Russell, P., “Photonic crystal fibers”, Science, 299, 358-362, (2003).

[1.81] Russell, P. St. J., “Designing photonic crystals”, Electron and photon confinement in semiconductor nanostructures, IL Nuovo Cimento (editor), Amsterdam: IOS Press, 79-103, (2003).

[1.82] Zhaona Wang, Shujing Chen, Jing Zhou, and Dahe Liu, “Band-edge oscillations of the diffraction spectrum of a volume hologram investigated by the air-doping model,” Appl. Opt. 50, 2049-2054, (2011).

[1.83] J.-Y. Yeh, “Control analysis of the tunable phononic crystal with electrorheological material,” Physica B: Condensed Matter, vol. 400, no. 1-2, pp. 137–144, (2007).

[1.84] M. S. Kushwaha, P. Halevi, L. Dobrzynski, and B. Djafari-Rouhani, “Acoustic band structure of periodic elastic composites,” Physical Review Letters, vol. 71, no. 13, pp. 2022–2025, (1993).

[1.85] Y. Cao, Z. Hou, and Y. Liu, “Convergence problem of plane-wave expansion method for phononic crystals,” Physics Letters A, vol. 327, no. 2-3, pp. 247–253, (2004).

[1.86] D. L. Yu, G. Wang, Y. Z. Liu, J. H. Wen, and J. Qiu, “Flexural vibration band gaps in thin plates with two-dimensional binary locally resonant structures,” Chinese Physics, vol. 15, no. 2, pp. 266–271, (2006).

[1.87] A.Taflove, “ Advances in computational electrodynamics : the finite difference time domain method “, Norwood MA: Artech House (1998).

[1.88] C.T.Chan, Q.L. Yu, K.M.Ho, “ Order-N spectral method for electromagnetic waves”, Phys. Rev. B, 51, 16635 (1995).

[1.89] Bipin K. Singh, Mayank K. Chaudhari, and Praveen C. Pandey, “Photonic and Omnidirectional Band Gap Engineering in One-Dimensional Photonic Crystals Consisting of Linearly Graded Index Material”, Journal Of Lightwave Technology, Vol. 34, No. 10, (2016)

[1.90] F. Abeles, “ Recheerches sur la propagation des ondes electromagnetiques sinusoidales dans les milieu stratifies. Application aux couches minces”, Annales de Physique ,5596, 706 (1950).

[1.91] Keskin, O. Y., Dalmis, R., Birlik, I., & Ak Azem, N. F., “Comparison of the effect of non-metal and rare-earth element doping on structural and optical properties of CuO/TiO2 one-dimensional photonic crystals”, Journal of Alloys and Compounds, 153262, (2019). doi:10.1016/j.jallcom.2019.153262

[2.1] Yablonovitch, E. and Gmitter, T. J.,” Photonic band structure: The face-centered-cubic case”, Phys. Rev. Lett., vol 63, 18, pp 1950, (1989). https://link.aps.org/doi/10.1103/PhysRevLett.63.1950

[2.2] Z. Zhang and S. Satpathy, “Electromagnetic wave propagation in periodic structures: Bloch wave solution of Maxwell's equations”, Phys. Rev. Lett. 65, 2650, (1990). https://link.aps.org/doi/10.1103/PhysRevLett.65.2650

[2.3] O. K. Andersen, “Linear methods in band theory” , Phys. Rev. B 12, 3060, (1975). https://link.aps.org/doi/10.1103/PhysRevB.12.3060

[2.4] M. Born and E. Wolf, Principles of Optics, 7th ed., Cambridge University, Cambridge, England, (1999).

[2.5] W. J. Titus, “Solutions of the Kronig–Penney Models by the T-Matrix Method,” Am. J. Phys. 41, 512–516 (1973).

[2.6] C. Kittel, Introduction to Solid State Physics (Wiley, New York), 7th ed., p. 180, (1996).

[2.7] W. Ashcroft and N. D. Mermin, Solid State Physics ~Saunders, Philadelphia, p. 148, (1976).

[2.8] Subodha Mishra and S. Satpathy, “Kronig–Penney model with the tail-cancellation method”, Am. J. Phys. 69, 512 (2001); https://doi.org/10.1119/1.1326074

[2.9] C. M. Bowden, J. P. Dowling, and H. O. Everitt,” Development and Applications of Materials Exhibiting Photonic Band Gaps”, special issue of J. Opt. Soc. Am. B 10, 279 (1993).

[2.10] E.Yablonovitch, K.M.Leung, “Photonic band structure: Non-spherical atoms in the face-centered-cubic case”, Physica B: Condensed Matter, Volume 175, Issues 1–3, 1 December, Pages 81-86, (1991). https://doi.org/10.1016/0921-4526(91)90696-C

[2.11] John, Sajeev and Wang, Jian, “Quantum optics of localized light in a photonic band gap”, Phys. Rev. B. 43, 12772, (1991). https://link.aps.org/doi/10.1103/PhysRevB.43.12772

[2.12] Dowling, Jonathan P. and Bowden, Charles M, “Atomic emission rates in inhomogeneous media with applications to photonic band structures”, Phys. Rev. A. 46, 612, (1992). https://link.aps.org/doi/10.1103/PhysRevA.46.612

[2.13] Dowling, J. P., & Bowden, C. M. “Anomalous Index of Refraction in Photonic Bandgap Materials”, Journal of Modern Optics, 41(2), 345–351, (1994), https://doi:10.1080/09500349414550371

[2.14] Dowling, Jonathan P. and Bowden, Charles M., “Near dipole-dipole effects in lasing without inversion: An enhancement of gain and absorption less index of refraction”, Phys.Rev.Lett.70, 1421, (1993). https://link.aps.org/doi/10.1103/PhysRevLett.70.1421

[3.1] Yoel Fink, Joshua N. Winn, Shanhui Fan, Chiping Chen, Jurgen Michel, John D. Joannopoulos, Edwin L. Thomas, “A Dielectric Omnidirectional Reflector”, Science , 282,5394, pp. 1679-1682,(1998). https://doi:10.1126/science.282.5394.1679

[3.2] E. Yablonovitch,” Inhibited Spontaneous Emission in Solid-State Physics and Electronics”,Phys.Rev.Lett.58,2059(1987).
https://link.aps.org/doi/10.1103/PhysRevLett.58.2059

[3.3] J. D. Joannopoulos, R. Meade, J. N. Winn, Photonic Crystals: Molding the Flow of Light (Princeton Univ. Press, Princeton, NJ).(1995).

[3.4] Winn, J. N., Fink, Y., Fan, S., & Joannopoulos, J. D.” Omnidirectional reflection from a one-dimensional photonic crystal”, Optics Letters, 23(20), 573, (1998). https://doi:10.1364/ol.23.001573

[3.5] F. Abeles, Ann. Phys. Paris 5, 596 (1950).

[3.6] M. Born and E. Wolf, Principles of Optics (Pergamon, ed. 6), p. 67,(1980)

[3.7] Yeh, P., Yariv, A., & Hong, C.S., "Electromagnetic propagation in periodic stratified media I General theory", Journal of the Optical Society of America, 67(4), 423, (1977). https://doi.org/10.1364/JOSA.67.000423

[3.8] Canham L ,(1997)," Properties of Porous Silicon ", 1st edition (London: INSPEC) chapter 1.

[3.9] Cullis A G, Canham L T and Calcott P D J," The structural and luminescence properties of porous silicon", Journal of Applied Physics 82, 909 (1997).https://doi.org/10.1063/1.366536.

[3.10] Koshida N (ed) ,"Device Applications of Silicon Nanocrystals and Nanostructures" 1st edition (New York: Springer Science) chapter 10, (2009).

[3.11] W.Theiß," Optical properties of porous silicon", Surface Science Reports, Volume 29, Issues 3–4, Pages 91-93, 95-192, (1997). https://doi.org/10.1016/S0167-5729(96)00012-X

[3.12] Edoardo De Tommasi , Luca De Stefano , Ilaria Rea , Valentina Di Sarno , Lucia Rotiroti , Paolo Arcari , Annalisa Lamberti , Carmen Sanges and Ivo Rendina," Porous Silicon Based Resonant Mirrors for Biochemical Sensing", Sensors, 8(10), 6549-6556, (2008) https://doi.org/10.3390/s8106549

[3.13] Solanki C, " Study of porous silicon layers transfer for applications in thin film monocrystalline silicon solar cell" PhD Thesis Katholieke University Leuven, Belgium, chapter 2, (2007).

[3.14] Sharon M. Weiss,Philippe M. Fauchet," Electrically tunable porous silicon active mirrors",Physica status solidi a: applications and material science, 197, 2 ,Pages 556–560, (2003). https://doi.org/10.1002/pssa.200306562

[3.15] Thuy Chi Do, Huy Bui, Thuy Van Nguyen, The Anh Nguyen, Thanh Hai Nguyen and Van Hoi Pham, "A microcavity based on a porous silicon multilayer", Adv. Nat. Sci.: Nanosci. Nanotechnol. 2 , 035001 (5pp) , (2011). https://doi.org/10.1088/2043-6262/2/3/035001

[3.16] M. Khardani, M. Bouaïcha, B. Bessaïs, "Bruggeman effective medium approach for modelling optical properties of porous silicon: comparison with experiment", Physica status

solidi a:Current topics in solid state physics, 4, 6,Pages1986–1990, (2007). https://doi.org/10.1002/pssc.200674420.

[3.17] P N Patel , Vivekanand Mishra and A K Panchal," Theoretical and experimental study of nanoporous silicon photonic microcavity optical sensor devices", Adv. Nat. Sci.: Nanosci. Nanotechnol. 3 , 035016 (7pp), (2012). https://doi.org/10.1088/2043-6262/3/3/035016.

[3.18] Yuan K., Zheng X., Li C.L., and She W.L., "Design of omnidirectional and multiple channelled filters using one dimensional photonic crystals containing a defect layer with a negative refractive index" ,Phys. Rev. E, 71,066604:1–5,(2005). https://doi.org/10.1364/JOSAA.24.000A28

[3.19] Lopez, H. A., Linda Chen, X., Jenekhe, S. A., & Fauchet, P. M., "Tunability of the photoluminescence in porous silicon due to different polymer dielectric environments", Journal of Luminescence, 80(1-4), 115–118, (1998). https://doi.org/10.1016/s0022-2313(98)00078-7

[3.20] Chan, S., Horner, S. R., Fauchet, P. M., & Miller, B. L., "Identification of Gram Negative Bacteria Using Nanoscale Silicon Microcavities", Journal of the American Chemical Society, 123(47), 11797–11798, (2001). https://doi.org/10.1021/ja016555r

[3.21] Shimoda, Y., Ozaki, M., & Yoshino, K., "Electric field tuning of a stop band in a reflection spectrum of synthetic opal infiltrated with nematic liquid crystal", Applied Physics Letters, 79(22), 3627–3629, (2001). https://doi.org/10.1063/1.1421080

[3.22] V. V. Dvoyrin, V. M. Mashinsky, E. M. Dianov, A. A. Umnikov, and A. N. Guryanov, in 31st European Conference on Optics Communications, Glasgow, Scotland , 4, p. 949, (2005).

[3.23] E. M. Dianov, V. V. Dvoyrin, V. M. Mashinsky, A. A. Umnikov, and A. N. Guryanov, Quantum Electron. 35, 1083 (2005).

[3.24] Razdobreev, L. Bigot, V. Pureur, A. Favre, G. Bouwmans, and M. Douay, "Efficient all-fiber bismuth-doped laser", Appl. Phys. Lett. 90, 031103 (2007); https://doi.org/10.1063/1.2431762

[3.25] N. Bouchenak Khelladi, N.E. Chabane Sari: "Optical properties of ZnO thin film", Advances in Materials Science.,V. 13, No 1(35).- P. 21-29, (2013).

[3.26] Sun, X. W., & Kwok, H. S., " Optical properties of epitaxially grown zinc oxide films on sapphire by pulsed laser deposition", Journal of Applied Physics, 86(1), 408–411, (1999). https://doi.org/ 10.1063/1.370744

[3.27] M. Rosete-Aguilar, F.C. Estrada-Silva, N.C. Bruce, C.J. Roman-Moreno, and R. Ortega-Mart ´ ´ınez,"Calculation of temporal spreading of ultrashort pulses propagating through optical glasses", Rev.Mex. Fis, 54(2), 141-148 (2008). http://www.scielo.org.mx/pdf/rmf/v54n2/v54n2a10.pdf

[3.28] Hasegawa, H., Kobayashi, K., Takahashi, Y., Harada, J., & Inabe, T., "Effective band gap tuning by foreign metal doping in hybrid tin iodide perovskites", Journal of Materials Chemistry C, 5(16), 4048–4052, (2017). https://doi.org/ 10.1039/c7tc00446j

[3.29] Singh, J., Kumar, P., Hui, K. S., Hui, K. N., Ramam, K., Tiwari, R. S., & Srivastava, O. N.," Synthesis, band-gap tuning, structural and optical investigations of Mg doped ZnO nanowires", Cryst.Eng.Comm., 14(18), 5898, (2012) https://doi.org/ 10.1039/c2ce06650e

[3.30] E. Yablonovitch, "Photonic band-gap structures",Journal of the Optical Society of America B Vol. 10,Issue 2,pp. 283- 295,(1993) https://doi.org/10.1364/JOSAB.10.000283

[3.31] Y.L.HooW,JinJ,JuH.L..HoD.N.Wang,"Design of photonic crystal fibers with ultra-low, ultra-flattened chromatic dispersion", Optics Communications Volume 242, Issues 4–6, Pages 327-332,(2004). https://doi.org/10.1016/j.optcom.2004.08.030

[3.32] Bhat, S. V., & Deepak, F. L. ," Tuning the bandgap of ZnO by substitution with Mn2+, Co2+ and Ni2+", Solid State Communications, 135(6), 345–347, (2005) https://doi.org/10.1016/j.ssc.2005.05.051

[3.33] Lupan, O., Pauporté, T., Le Bahers, T., Viana, B., & Ciofini, I.,"Wavelength-Emission Tuning of ZnO Nanowire-Based Light-Emitting Diodes by Cu Doping: Experimental and Computational Insights", Advanced Functional Materials, 21(18), 3564–3572, (2011). https://doi.org/10.1002/adfm.201100258

[3.34] Congxin Xia, YuJia, MengTao, Qiming Zhang, "Tuning the band gap of hematite α-Fe2O3 by sulfur doping", Phys. Lett. A, 377,31–33, 1943-1947,(2013). https://doi.org/10.1016/j.physleta.2013.05.026.

[3.35] Jin, S., Yang, Y., Medvedeva, J. E., Wang, L., Li, S., Cortes, N., … Marks, T. J., "Tuning the Properties of Transparent Oxide Conductors. Dopant Ion Size and Electronic Structure Effects on CdO-Based Transparent Conducting Oxides. Ga- and In-Doped CdO Thin Films Grown by MOCVD", Chem. of Mater.", 20(1), 220–230, (2008). https://doi.org/10.1021/cm702588m .

[3.36] Vinod Chacko, Sonia Bansal, Aurangzeb Khurram Hafiz, "Effect of dispersion on omnidirectional reflection band in zinc oxide-based one-dimensional photonic crystal heterostructures" , J. of Nanophotonics, 12(2), 026012 (2018). https://doi.org/10.1117/1.JNP.12.026012

[4.1] Yablonovitch E., "Inhibited spontaneous emission in solid-state physics and electronics", Physics Review Letter, 58, pp 2059, (1987). https://link.aps.org/doi/10.1103/PhysRevLett.58.2059.

[4.2] Born M., Wolf E., "Principles of Optics", (New York: Pergamon), (1980).

[4.3] John S., "Strong localization of photons in certain disordered dielectric super lattices", Physics Review Letter, 58, pp 2486–2489, (1987). https://doi.org/10.1103/PhysRevLett.58.2486.

[4.4] Lipson R., Lu C., "Photonic Crystals: a unique partnership between light and matter", European Journal of Physics, 30, pp 33, (2009). https://doi.org/10.1088/0143-0807/30/4/S04.

[4.5] Banerjee A., "Enhanced refractometric optical sensing by using one dimensional ternary photonic crystals", Progress in electromagnetics research, 89, pp 11-22, (2009). https://doi.org/10.2528/PIER08112105.

[4.6] Hopman W.C.L., Pottier P., Yudistira D., Lith J., Lambeck P., De R., Rue L., Driessen A., Hoekstra H., De Ridder R., " Quasi-one dimensional photonic crystal as a compact building block for refractometric optical sensors ", IEEE journal of selected topics in quantum electronics, 11, pp 11-16, (2005). https://doi.org/10.1109/JSTQE.2004.841693.

[4.7] Ugale S.P., Mishra V., "Modeling and characterization of fiber Bragg grating for maximum reflectivity", Optik - international journal for light and electron optics, 122, pp 1990-1993, (2011). https://doi.org/ 10.1016/j.ijleo.2010.12.017

[4.8] Stefano L.D., Rendina I., Moretti L., Tundo S., Rossi A.M., “Smart optical sensors for chemical substances based on porous silicon technology”, Applied Optics , 43, pp 167-172, (2004). https://doi.org/10.1364/AO.43.000167

[4.9] Victor S.Y. L., Motesharei K., Dancil K.P.S., Sailor M.J., Ghadiri M.R., “ A porous silicon based optical interferometric biosensor”, Science ,278, pp 840-843, (1997). https://doi.org/10.1126/science.278.5339.840.

[4.10] Adachi, S., “Model dielectric constants of Si and Ge,” Physical Review B, 38, 18, pp.12966-12977,(1988).

[4.11] Busch, K., C. T. Chan and C. M. Soukoulis, “Techniques for Band-structures and Defect States in Photonic Crystals,” Photonic Band Gap Materials, NATO ASI Series, Series E: Applied Science,315, pp. 465-486, (1995).

[4.12] Chen, K. M., A. W. Sparks and H. C. Luan, “SiO2/TiO2 omnidirectional reflector and microcavity resonator via the sol-gel method,” Applied Physics Letters, 75, 24, pp. 3805-3807,(1999).

[4.13] De La Rue, R. M., and T. F. Krauss, “Strategies for the fabrication of photonic micro-structures in semiconductors,” Microcavities and Photonic Bandgaps: Physics and Applications, NATO ASI Series, Series E: Applied Science, 324, pp. 175-192,(1995).

[4.14] Foresi, J. S., P. R. Villeneuve, J. Ferrera and J. D. Joannopoulos, “Photonic-bandgap microcavities in optical waveguides,” Nature, 390 (6656), pp. 143-145, (1997).

[4.15] Jin, C. J., Z. W. Sun and B. Y. Cheng, “Microcavities composed of point defects and

wave-guides in photonic crystals,” Optics Communications, 188, No. 5-6, pp. 255-260, (2001).

[4.16] Jugessur, A. S., P. Pottier and R. M. De La Rue, “One-dimensional periodic photonic crystal microcavity filters with transition mode-matching features, embedded in ridge waveguides,” Electronics Letters, vol. 39, No. 4, pp. 367-369, (2003).

[4.17] Leigh C. (edited.), “Properties of porous silicon “, London: Institution of Electrical Engineers, 1st Edition, (1997). https://trove.nla.gov.au/version/29615055.

[4.18] Cullis A.G., Canham L.T., Calcott P.D., “The structural and luminescence properties of porous silicon “, Journal of Applied Physics, 82, 909 (1997); https://doi.org/10.1063/1.366536.

[4.19] Uhlir A. Jr., “Electrolytic shaping of germanium and silicon”, The Bell system technical journal, 35, pp 333-347, (1956). https://doi.org/10.1002/j.1538-7305.1956.tb02385.x.

[4.20] Theiss W., “Optical properties of porous silicon”, Surface Science Reports, 29, pp 91-93, (1997). https://doi.org/10.1016/S0167-5729(96)00012-X.

[4.21] Mazzoleni C., Pavesi L., “Application to optical components of dielectric porous silicon multilayers “, Applied Physics Letters, 67, 2983 (1995). https://doi.org/10.1063/1.114833.

[4.22] Lenshin A.S., Kashkarov V.M., Spivak Y.M., Moshnikov V.A., “Investigations of nanoreactors on the basis of p-type porous silicon: electron structure and phase composition,” Materials Chemistry and Physics, 135, pp. 293–297, (2012), https://doi.org/10.1016/j.matchemphys.2012.03.095.

[4.23] Spivak Y. M., Maraeva E.V., Belorus A.O., Molchanova A.V., Nigmadzyanova N.R.,” Preparation and investigation of porous silicon nanoparticles for targeted drug delivery”, Smart Nanocomposites; Hauppauge , 4, pp 115-118. (2013).

[4.24] Solanki C., Ph.D thesis, Katholieke University Leuven, Belgium (2007).

[4.25] Panchal A.K., Kale P.G., Solanki C., ICAER , 797, (2007).

[4.26] Hou X.Y., Fan H.L., Xu L., Zhang F.L., Li M.Q., Yu M.R., Wang X., “Pulsed anodic etching: An effective method of preparing light-emitting porous silicon”, Applied Physics Letters , 68, pp 2323 (1996). https://doi.org/10.1063/1.115845.

[4.27] Xiong Z.H., Liao L.S., Ding X.M., Xu S.H., Liu Y., Gu L.L., , Tao F.G. , Lee S.T., Hou X.Y., “Flat layered structure and improved photoluminescence emission from porous silicon microcavities formed by pulsed anodic etching”, Applied Physics A, 74, 807, (2002). https://doi.org/10.1007/s003390100977.

[4.28] Timoshenko V.Yu., Osminkina L.A., Efimova A.I., Golovan L.A., Kashkarov P.K., Kovalev D., Künzner N., Gross E., Diener J., Koch F., “Anisotropy of optical absorption in birefringent porous silicon”, Physics Review B, 67, 113405, (2003). https://doi.org/10.1103/PhysRevB.67.113405.

[4.29] Aktsipetrov O.A., Dolgova T.V., Soboleva I.V., Fedyanin A.A., “ Anisotropic photonic crystals and microcavities based on mesoporous silicon”, Physics of Solid State, 47, pp.156-158, (2005). https://doi.org/10.1134/1.1853468.

[4.30] Fesenko V.I., Sukhoivanov I.A., Shulga S.N., “Photonic crystals and microresonators based on the anisotropic mesoporous silicon”, Telecommunications and radio engineering, 70, pp 367-376, (2011). https://doi.org/ 10.1615/TelecomRadEng.v70.i4.60.

[4.31] Kovalev D., Polisski G., Diener J., Heckler H., Kunzner N., Timoshenko V.Yu., Koch F., " Strong in-plane birefringence of spatially nanostructured silicon", Applied Physics Letters ,78, pp.916-918, (2001). https://doi.org/10.1063/1.1343476.

[4.32] Fesenko V.I., Sukhoivanov I.A., Shulga S.N., Shi H.," One dimensional anisotropic photonic crystals based on anisotropic porous silicon", 12th International Conference on Mathematical Methods in Electromagnetic theory , Ukraine (2008).

[4.33] Cardona M., "Atomic structure and properties of solids", edited by Burstein E. (Academic, New York, pp 513) (1972).

[4.34] Hakshur K., Ruschin S., "Observation of a large optical birefringence effect in a (110) oriented porous silicon layer", Applied Physics Letters, 104, 051909 (2014). https://doi.org/10.1063/1.4863746.

[4.35] Genereux F., Leonard S.W., Van Driel H.M., Birner A., Gosele U., "Large birefringence in two-dimensional silicon photonic crystals", Physics Review B, 63, 161101(R), (2001). https://doi.org/10.1103/PhysRevB.63.161101.

[4.36] Alvarez J., Bettotti P., Suarez I., Kumar N., Hill D., Chirvony V., Pavesi L., Martinez Pastor J. , "Birefringent porous silicon membranes for optical sensing", Optics Express,19, pp 26106-26116, (2011). https://doi.org/10.1364/OE.19.026106.

[4.37] Alvarez J., Bettotti P., Suarez I., Kumar N., Hill D., Chirvony V., Pavesi L., Martinez Pastor J., "Highly-sensitive anisotropic porous silicon based optical sensors", proceedings 8212, Frontiers in Biological Detection: From Nanosensors to Systems IV, 821209 (2012). https://doi.org/10.1117/12.908214.

[4.38] Liu R., Schmedake T.A., Li Y.Y., Sailor M.J., Fainman Y., "Novel porous silicon vapour sensor based on polarization interferometry", Sensors and Actuators B: Chemical, 87, pp 58-62, (2002). https://doi.org/10.1016/S0925-4005(02)00217-4.

[4.39] Gross E., Kovalev D., Kunzner N., Timoshenko V.Yu., Diener J., Koch F., " Highly sensitive recognition element based on birefringent porous silicon layers", Journal of Applied Physics, 90, 3529 (2001); https://doi.org/10.1063/1.1391417.

[4.40] De Tommasi E., Rendina I., Rea I., Di Sarno V., Rotiroti L., Arcari P., Lamberti A., Sanges C., Stefano L.D.," Porous silicon based resonant mirrors for biochemical sensing", Sensors , 8, pp 6549-6556, (2008). https://doi.org/10.3390/s8106549.

[4.41] Rendina I., Rea I., Rotiroti L., Stefano L.D., "Porous silicon-based optical biosensors and biochips", Physica E: Low-dimensional Systems and Nanostructures, 38, pp 188-192.(2007). https://doi.org/10.1016/j.physe.2006.12.050.

[4.42] Ouyang H., Fauchet P.M.," Biosensing using porous silicon photonic bandgap structures" proceedings of SPIE Optics East, 6005, 600508 (2005). https://doi.org/10.1117/12.629961.

[4.43] Koshida N., (ed.), ""Nanocrystalline silicon ballistic electron emitter.", Device applications of silicon nanocrystals and nanostructures, pp 251, © Springer Science + Business Media, LLC 2009 DOI: 10.1007/978-0-387-78689-6_9.

[4.44] Kale P.G., Solanki C.S., "Synthesis of Si nanoparticles from freestanding porous silicon (PS) film using ultrasonication", 35th IEEE Photovoltaic Specialists Conference PVSC ,Honolulu, Hawaii, 5617016, pp 3692–3697 (2010) . http://dspace.library.iitb.ac.in/xmlui/handle/10054/15643.

[4.45] Dubey R.S., Gautam D.K., "Photoluminescence and surface morphology of nanostructured porous silicon", Chalcogenide Letters, 6, pp 523 – 528, (2009). http://www.chalcogen.ro/523_Dubey.pdf

[4.46] Mahdi M.A., Ramizy A.,Hassan Z., Ng S.S., Hassan J.J., Kasim S.J., "CdS nanocrystalline structured grown on porous silicon substrates via chemical bath deposition method ", Chalcogenide Letters , 9, pp 19 – 25, (2012).

[4.47] Dubey R.S., Gautam D.K.," Synthesis and characterization of nanocrystalline porous silicon layer for solar cells applications", Journal of Optoelectronics and Biomedical materials, 1, pp 8-14, (2009).

[4.48] Mortezaali A., Ramezani S.S., Javani F.J., "Correlation between porosity of porous silicon and optoelectronic properties", Journal of Non-Oxide Glasses, 1, pp 293 – 299, (2009).

[4.49] Ioanid A., Dieaconu M., Anothe S., "A semiempirical potential model for h-terminated functionalized surface of porous silicon", Digest Journal of Nanomaterials and Biostructures, 5, pp 947-957, (2010). http://chalcogen.ro/947_Ioanid-corectat-1.pdf.

[4.50] Saha H., "Porous silicon sensors- elusive and erudite", International journal on smart sensing and intelligent systems, 1, (2008). https://pdfs.semanticscholar.org/f138/820a83fb5d64d83f2a860ce53f842262f972.pdf

[4.51] Weiss S.M., Fauchet P.M., "Electrically tunable porous silicon active mirrors", Physica status solidi (a) 197, pp 556-560, (2003). https://doi.org/10.1002/pssa.200306562.

[4.52] Chi D.T., Bui H., Van Nguyen T., Anh Nguyen T., Hai Nguyen T., Hoi Pham V., "A microcavity based on a porous silicon multilayer", Advances in Natural Sciences: Nanoscience and Nanotechnology, 2, (2011), https://doi.org/10.1088/2043-6262/2/3/035001.

[4.53] Robbiano V., Paterno G. M., La Mattina A.A., Motti S.G., Lanzani G., Scotognella F., Barillaro G., "Room-temperature low-threshold lasing from monolithically integrated

nanostructured porous silicon hybrid microcavities", ACS Nano 12,pp 4536−4544 (2018). https://doi.org/10.1021/acsnano.8b00875.

[4.54] Ning H., Krueger N. A., Sheng X., Keurn H., Zhang C., Choquette K. D., Li X. L., Kim S., Rogers J. A., Braun P. V.," Transfer-printing of tunable porous silicon microcavities with embedded emitters", ACS Photonics, 1, pp 1144−1150, (2014). https://doi.org/ 10.1021/ph500230j.

[4.55] Wan Y., Krueger N. A., Ocier C. R., Su P., Braun P. V., Cunningham B. T., "Resonant mode engineering of photonic crystal sensors clad with ultralow refractive index porous silicon di-oxide", Advanced Optical Materials, 5, 1700605, (2017). https://doi.org/10.1002/adom.201700605.

[4.56] Khardani M., Bouaïcha M., Bessaïs B., "Bruggeman effective medium approach for modelling optical properties of porous silicon: comparison with experiment", Physica status solidi (a): Current topics in solid state physics, 4, pp 1986–1990. (2007), https://doi.org /10.1002/pssc.200674420.

[4.57] Patel P.N., Mishra V., Panchal A.K.," Theoretical and experimental study of nanoporous silicon photonic microcavity optical sensor devices", Advances in natural sciences. Nanoscience and Nanotechnology, 3, 035016 (pp 7), (2012). https://doi.org /10.1088/2043-6262/3/3/035016.

[4.58] Bruggeman D.A.G.,"Berechnung verschiedener physikalischer konstanten von heterogenen substanzen. i. dielektrizitatskonstanten und leitfahigkeiten der mischkorper aus isotropen substanzen", Annalen der Physik, 416, pp 636–664, (2006). https://doi.org /10.1002/andp.19354160705.

[4.59] Schubert M., "Polarization-dependent optical parameters of arbitrarily anisotropic homogenous layered systems", Physical Review B, 53, 8, (1996). https://doi.org/10.1103/PhysRevB.53.4265.

[4.60] Schubert M., "Generalized ellipsometry and complex optical systems", Thin Solid Films, 313-314, pp-323-332, (1998). https://doi.org/10.1016/S0040-6090(97)00841-9.

[4.61] Pochi, Y., "Optics of anisotropic layered media: a new 4 x 4 matrix algebra" Surface Science, 96, pp 41-53. (1980). https://doi.org/10.1016/0039-6028(80)90293-9.

[4.62] Berreman D.W., "Optics in stratified and anisotropic media: a 4 x 4 matrix formulation", Journal of the Optical Society of America, 62, pp 502-510, (1972). https://doi.org/10.1364/JOSA.62.000502.

[4.63] Stallinga S., "Berreman 4×4 matrix method for reflective liquid crystal displays ",Journal of Applied Physics 85, 3023 (1999); https://doi.org/10.1063/1.369638.

[4.64] Pavesi L., Mulloni V., “All porous silicon microcavities: growth and physics”, Journal of Luminescence, 80, pp 43-52, (1998). https://doi.org/10.1016/S0022-2313(98)00069-6.

[4.65] Mulloni V., Mazzoleni C., and Pavesi L.,” Elaboration, characterization and aging effects of porous silicon microcavities formed on lightly p-type doped substrates”, Semiconductor Science and Technology,14,1052, (1999). https://doi.org/10.1088/0268-1242/14/12/307.

[4.66] Nemec H., Duvillaret L., Quemeneur F., Kuzel P. , “Defect modes caused by twinning in one-dimensional photonic crystals”, Journal of the Optical Society of America B, 21, pp 548-553, (2004). https://doi.org/10.1364/JOSAB.21.000548.

[4.67] Xu K.Y., Zheng X., She W.L., “Properties of defect modes in one-dimensional photonic crystals containing a defect layer with a negative refractive index”, Applied Physics Letters, 85, 6089, (2004). https://doi.org/10.1063/1.1824175.

[4.68] Nemec H., Kuzel P., Garet F., Duvillaret L., “Time-domain terahertz study of defect formation in one-dimensional photonic crystals”, Applied Optics, 43, pp 1965-1970,(2004). https://doi.org/10.1364/AO.43.001965.

[4.69] Ma G., Shen J., Zhang Z., Hua Z., Tang S.H.,” Ultrafast all-optical switching in one-dimensional photonic crystal with two defects” Optics Express, 14, pp 858-865 (2006). https://doi.org/10.1364/OPEX.14.000858.

[4.70] Ha Y.K., Yang Y.C., Kim J.E., Park H.Y., Kee C.S., Lim H., Lee J.C.,” Tunable omnidirectional reflection bands and defect modes of a one-dimensional photonic band gap structure with liquid crystals”, Applied Physics Letters, 79, 15 (2001). https://doi.org/10.1063/1.1381414.

[4.71] Cos J., Ferre-Borrull J., Pallares J., Marsal L.F., “Tunable Fabry–Pérot filter based on one-dimensional photonic crystals with liquid crystal components”, Optics Communications, 282, pp 1220-1225, (2009). https://doi.org/10.1016/j.optcom.2008.11.074.

[4.72] Abeles F.,”Recherches sur la propogation Ci es ondes electromaetiques sinusoedales dans les milleux stratiries", Annales de Physique (Paris), 5, pp 596-706., (1950).

[4.73] Sarbey O.G., Frolova E.K., Fedorovich R.D., Dan’ko D.B., “Birefringence of porous silicon”, Physics of the solid state, 42, 7, pp 1240-1241, (2000). https://doi.org/10.1134/1.1131371.

[4.74] Aoqian Shi, Rui Ge, Jianjun Liu, “Side-coupled liquid sensor and its array with magneto-optical photonic crystal”, Journal of the Optical Society of America A, 37, 8, pp. 1244-1248, (2020).

[4.75] Vinod Chacko, Sonia Bansal, Aurangzeb Khurram Hafiz, “Effect of anisotropy on the spectral characteristics of one-dimensional porous silicon photonic crystal microcavity for optical sensing applications”, J. of Nanophotonics, 13(1), 016012 (2019). https://doi.org/10.1117/1.JNP.13.016012

[5.1] Kuzmiak, V., & Maradudin, A. A., “Photonic band structures of one- and two-dimensional periodic systems with metallic components in the presence of dissipation”, Physical Review B, 55(12), 7427–7444.(1997). doi:10.1103/physrevb.55.7427

[5.2] Sievenpiper, D. F., Sickmiller, M. E., & Yablonovitch, E,” 3D Wire Mesh Photonic Crystals”, Physical Review Letters, 76(14), 2480–2483.(1996) doi:10.1103/physrevlett.76.2480

[5.3] Sievenpiper, D. F., Yablonovitch, E., Winn, J. N., Fan, S., Villeneuve, P. R., & Joannopoulos, J. D, “ 3D Metallo-Dielectric Photonic Crystals with Strong Capacitive Coupling between Metallic Islands”, Physical Review Letters, 80(13), 2829–2832.(1998) doi:10.1103/physrevlett.80.2829

[5.4] McIntosh, K. A., Mahoney, L. J., Molvar, K. M., McMahon, O. B., Verghese, S., Rothschild, M., & Brown, E. R., “Three-dimensional metallo-dielectric photonic crystals exhibiting resonant infrared stop bands”, Applied Physics Letters, 70(22), 2937–2939. (1997). doi:10.1063/1.118749

[5.5] Suzuki, T., & Yu, P. K. L. “Complex photonic band structures of a conductive metal lattice by a quadratic eigensystem”, Optics Letters, 20(24), 2520. (1995). doi:10.1364/ol.20.002520.

[5.6] Ward, A. J., Pendry, J. B., & Stewart, W. J. ,“Photonic dispersion surfaces”, Journal of Physics: Condensed Matter, 7(10), 2217–2224. (1995).doi:10.1088/0953-8984/7/10/027

[5.7] Scalora, M., Bloemer, M. J., Pethel, A. S., Dowling, J. P., Bowden, C. M., & Manka, A. S. ,” Transparent, metallo-dielectric, one-dimensional, photonic band-gap structures”, Journal of Applied Physics, 83(5), 2377–2383, (1998). doi:10.1063/1.366996.

[5.8] Ahmed, A. M., & Mehaney, A., ”Ultra-high sensitive 1D porous silicon photonic crystal sensor based on the coupling of Tamm/Fano resonances in the mid-infrared region”. Scientific Reports, 9(1), (2019) . doi:10.1038/s41598-019-43440-y

[5.9] Andrey Vyatskikh, Ryan C. Ng, Bryce Edwards, Ryan M. Briggs, and Julia R. Greer," Additive Manufacturing of High-Refractive-Index, Nanoarchitected Titanium Dioxide for 3D Dielectric Photonic Crystals", : Nano Lett. 20, 3513−3520, (2020).

[5.10] Pinghui Wua , Zeqiang Chena, Huge Jileb , Congfen Zhangc , Danyang Xud , Li Lve," An infrared perfect absorber based on metal-dielectric-metal multi-layer films with nanocircle holes arrays ", Results in Physics 16 , 102952, (2020).

# LIST OF PUBLICATIONS OUT OF THESIS

List of Published Papers in Journals

| S.No | Title of Paper | Name of Journal where published | Volume & Issue | Year | Pages |
|---|---|---|---|---|---|
| 1 | Effect of anisotropy on the spectral characteristics of one-dimensional porous silicon photonic crystal microcavity for optical sensing applications | Journal of Nanophotonics (SCI Expanded/ Scopus, Impact Factor 1.415 ) | 13 (1) | 2019 | 016012 (1-17) |
| 2 | Effect of dispersion on omnidirectional reflection band in zinc oxide-based one-dimensional photonic crystal hetrostructures | Journal of Nanophotonics (SCI Expanded/ Scopus, Impact Factor 1.415 ) | 12(2) | 2018 | 026012 ( 1-16) |
| 3 | Broad Inhibition of Transmission Frequency in Multilayered Dielectric One Dimensional Photonic Crystal Nanostructure | International Journal of Science and Engineering | 13(1) | 2019 | (7-11) |
| 4 | Enhancement of omnidirectional bandgap in graphene based quasi-periodic one dimensional photonic crystal hetrostructures | Journal for Foundations and Applications of Physics | 5(2) | 2018 | (128-140) |
| 5 | Omnidirectional reflection band in multi-layered graphite film based one dimensional photonic crystal nanostructure | Journal for Foundations and Applications of Physics | 5(1) | 2018 | (35-48) |
| 6 | Optical Characteristics of multilayered Al2O3-Ti2O3 one dimensional photonic crystal structure as a suitable material for anti-reflection coatings | YMCAUST International Journal of Research | 1(1) | 2013 | (62-69) |

List of Published Papers in Conference

| S.No | Title of Paper | Name of Conference | Year |
|---|---|---|---|
| 1 | Optical characterization of TiO2 – Al2O3 one dimensional photonic crystal structure as suitable material for anti-reflection coatings | Workshop on Nanotechnology and Embedded systems", sponsored by ISTE, YMAUST, Faridabad. | 2012 |
| 2 | Omni Directional Reflection Band in Multilayered Porous Silicon (P-Si)-GaAs one dimensional photonic crystal structures | Proceedings in National Conference On Futuristic Trends In Mechanical Engineering And Nanotechnology, NCFTME | 2013 |
| 3 | Omni Directional Reflection Band in Multilayered Porous Silicon (P-Si)- Te one dimensional photonic crystal structures | Proceedings in National Conference On Recent Trends In Mechanical Engineering , NCRTME | 2015 |
| 4 | Omni Directional Reflection Band in Multilayered Na3AlF6-Si one dimensional photonic crystal structures | Proceedings in National Conference On Role of Science and Technology Towards 'Make in India' organized by YMCA University of Science and Technology, Faridabad, | 2016 |
| 5 | Omni Directional Reflection Band in Multilayered Na3AlF6-Ge one dimensional photonic crystal structures | Proceedings in International Conference On Sustainable Development Through Research In Engineering And Management (SDREM 2016) at YMCA University Of Science And Technology, Faridabad | 2016 |

# BRIEF PROFILE OF RESEARCH SCHOLAR

I have received M.Sc degree in Physics from IIT Roorkee in 2001 and M.Tech in Applied Optics from IIT Delhi in 2002. I have total teaching experience of 17 years. I have submitted my PhD thesis on one dimensional photonic crystal waveguides and devices to J.C. Bose University of Science and Technology, YMCA Faridabad. My research area of interest includes 1D photonic crystal, nanophotonics, optical sensors, omnidirectional reflectors, and photonic microcavities. I have published 6 papers in various international and national journals, out of which two papers are SCIE/ Scopus indexed. I have published 5 papers in various national and international conferences.